Local and Nonlocal Relaxation Dynamics of Hot Electrons in Au/Fe/MgO(001) Thin Films

Der Fakultät für Physik
der Universität Duisburg-Essen vorgelegte

Dissertation

zur Erlangung des akademischen Grades eines Doktors der
Naturwissenschaften
(Dr. rer. nat.)

von

Yasin Beyazit
aus Essen

Hiermit versichere ich, die vorliegende Dissertation selbstständig, ohne fremde Hilfe und ohne Benutzung anderer als den angegebenen Quellen angefertigt zu haben. Alle aus fremden Werken direkt oder indirekt übernommenen Stellen sind als solche gekennzeichnet. Die vorliegende Dissertation wurde in keinem anderen Promotionsverfahren eingereicht. Mit dieser Arbeit strebe ich die Erlangung des akademischen Grades Doktor der Naturwissenschaften (Dr. rer. nat.) an.

Essen, den 01.08.2023

Yasin Beyazit

_____

_____

Ort, Datum

Name

Acknowledgments

- To my lab and office colleagues with whom I shared a wonderful time during my Ph.D.: Dr. John Thomas, Marius Milnikel, Oscar Naranjo, Dr. Manuel Bridger, Dr. Fabian Brinks, Thies Albert, Dr. Jinghao Chen, Mahendra Kabbinahithlu, Hamed Abbasi, Newsha Vesalimahmoud, Dr. Isabella Avigo, Dr. Ishita Agarwal, Dr. Abdul Samad Syed, Dr. Muhammadmahdi Afshari, Dr. Jayita Patwari, Dr. Changji Pan, Dr. Eswara Vallabhaneni, Dr. Jesumony Jayabalan, Dr. Ljupka Stojchevska, Dr. Andrea Eschenlohr, Dr. Alexander Tarasevitch and Prof. Dr. Klaus Sokolowski-Tinten.

Persönliche Danksagung

Eine persönliche Danksagung geht an meine Familie und Freunde, die mich während meiner Promotion in allen Hinsichten motiviert und unterstützt haben. Insbesondere möchte ich mich bei meiner Frau Zühriye Beyazit, meinen Kindern Zümra und Halid, meinem Vater Bekir Beyazit, und meinen Schwiegereltern Nebiye und Şendoğan Cin bedanken. Ohne Eure Liebe, Geduld und Unterstützung wäre diese Arbeit niemals zustande gekommen. Vielen, vielen Dank!

Abstract

Photoexcited hot charge carriers exhibit excess energies that could be harnessed for a wide range of applications, such as in photovoltaic cells for the conversion of sunlight into energy. The energy of the charge carriers also leads to scattering mechanisms in the constituents or at the interfaces of heterostructures, which compete with their use in application devices. Therefore, the spatial, temporal, and energetic distribution of hot charge carriers is important for their efficient extraction and utilization. This work investigates the ultrafast local and nonlocal relaxation dynamics of hot electrons in epitaxially grown Au/Fe/MgO(001) thin films. Femtosecond time-resolved two-photon photoemission spectroscopy (tr-2PPE) was used to study the energy-dependent ultrafast electron dynamics in Au and Fe buried media/interfaces. Experiments were performed with two different geometries: (i) pump-probe at the Au surface (FP) and (ii) pumping Fe layer and probing at the Au surface (BP). The propagation of electrons from a ferromagnetic metal (FM) to a noble metal (NM) through the FM/NM interface is of particular interest in this work.

As a first step for investigating the energy-dependent hot electron relaxation dynamics in Au/Fe/MgO(001) thin films, femtosecond time-resolved 2PPE intensities as a function of Au thickness d_{Au} and intermediate state energy $E - E_{\mathrm{F}}$ are explored. It is found that optical excitation of the Fe layer leads to a temporal shift in the intensity built-up of the transient 2PPE yields. The thicker the Au layer, the more pronounced the temporal shift in the intensity built-up, which is attributed to transport effects. This nonlocal effect was not observed in the tr-2PPE measurements with the Au-side pump geometry. Analysis of the interplay among local and nonlocal relaxation dynamics led to the conclusion that hot electrons propagate from the Fe layer to the Au layer surface in a superdiffusive manner.

It is also shown in this work that the Fe-side pump geometry can separate the local scattering rates in the constituents of the Au/Fe heterostructure, which can not be inferred from the Au-side pump data analysis. However, tr-2PPE experiments with the Au-side pumping approach reveal the first image potential state IPS ($n =1$) at the Au(001) surface. Another spectral feature is observed by the Fe-side pumping approach, which is attributed to the excitation of d-band minority states in Fe, and, thus, demonstrates the sensitivity of the Fe-side pump geometry to the hot electron relaxation dynamics in buried media of metallic heterostructures.

This work establishes Fe-side pumping in femtosecond two-photon photoemission spectroscopy and demonstrates a tool for analyzing hot electron relaxation and transport dynamics in FM/NM heterostructures energy-resolved in the time domain.

Zusammenfassung

Photoangeregte heiße Ladungsträger weisen einen Energieüberschuss auf, der für eine Vielzahl von Anwendungen nutzbar gemacht werden könnte, wie z.B. in Photovoltaikzellen für die Umwandlung von Sonnenlicht in Energie. Die Nutzung der Energie der Ladungsträger konkurriert mit Streuereignissen in den Bestandteilen oder an den Grenzflächen von Heterostrukturen. Daher ist die räumliche, zeitliche und energetische Verteilung heißer Ladungsträger wichtig für deren effiziente Extraktion und Nutzung. In dieser Arbeit wird die ultraschnelle lokale und nichtlokale Relaxationsdynamik heißer Elektronen in epitaktisch gewachsenen Au/Fe/MgO(001)-Filmen untersucht. Es wurde Femtosekunden zeitaufgelöste Zwei-Photonen-Photoemissionsspektroskopie (tr-2PPE) verwendet, um die energieabhängige ultraschnelle Elektronendynamik in Au und Fe Volumen/Grenzflächen zu untersuchen. Die Experimente wurden mit zwei verschiedenen Geometrien durchgeführt; (i) Photoanregung und- Abfragung (pump-probe) an der Au-Oberfläche (FP) und (ii) Pumpen der Fe-Schicht und Probe an der Au-Oberfläche (BP).

Als erster Schritt zur Untersuchung der energieabhängigen Relaxationsdynamik heißer Elektronen in dünnen Au/Fe/MgO(001)-Filmen werden die Femtosekunden zeitaufgelöste 2PPE-Intensitäten als Funktion der Au-Dicke d_{Au} und der Zwischenzustandsenergie $E - E_{\mathrm{F}}$ untersucht. Es zeigt sich, dass die optische Anregung der Fe-Schicht zu einer zeitlichen Verschiebung des Intensitätsaufbaus der transienten 2PPE-Intensität führt. Je dicker die Au-Schicht ist, desto ausgeprägter ist die zeitliche Verschiebung des Intensitätsaufbaus, die auf Transporteffekte zurückgeführt wird. Dieser nichtlokale Effekt wurde bei den tr-2PPE-Messungen mit der FP-Geometrie nicht beobachtet. Die Analyse der inelastischen e-e Streuereignisse und der nichtlokalen Transporteffekte führte zu der Schlussfolgerung, dass sich heiße Elektronen auf superdiffusive Weise von der Fe-Schicht zur Au-Oberfläche propagieren. Es wird in dieser Arbeit auch gezeigt, dass die BP-Geometrie die lokalen Streuraten in den Bestandteilen der Au/Fe-Heterostruktur trennen kann, was aus der FP-Datenanalyse nicht abgeleitet werden kann. Darüber hinaus zeigen tr-2PPE-Experimente mit FP-Ansatz den ersten Bildladungszustand IPS ($n =1$) an der Au(001)-Oberfläche. Ein weiteres spektrales Merkmal wird mit der BP-Geometrie beobachtet, das auf die Anregung von d-Band-Minoritätszuständen in Fe zurückgeführt wird. Diese Arbeit etabliert das rückseitige Pumpen (BP) in der Femtosekunden zeitaufgelöste Zwei-Photonen-Photoemissionsspektroskopie und demonstriert eine neuartige Methode zur energie- und zeitaufgelösten Analyse der Relaxations- und Transportdynamik heißer Elektronen in FM/NM Heterostrukturen.

Abbreviations

Abbreviation	Denomination
2D	two-dimensional
2PPE	two-photon photoemission
2TM	two-temperature model
ARPES	angle-resolved photoelectron spectroscopy
AFM	atomic force microscope
BBO	β-barium-borate
BP	back-side pumping front-side probing or Fe-side pumping Au-side probing
BWL	bandwidth-limited
CCD	charge coupled device
CD	chromatic dispersion
CFD	constant-fraction discriminator
CM	chirped mirror
CPA	chirped pulse amplification
CR	count rate
CW	continuous-wave
DFT	density functional theory
DOS	density of states
e-e	electron-electron
e-m	electron-magnon
e-ph	electron-phonon
E_{F}	Fermi energy
FLT	Fermi liquid theory
FM	ferromagnetic metal
FP	front-side pumping front-side probing or Au-side pumping Au-side probing
FROG	frequency-resolved optical gating
FS	fused silica
fs	femtosecond
FWHM	full width at half maximum
GD	group delay
GDD	group delay dispersion
GVD	group velocity dispersion

Abbreviation	Denomination
IC	integrated circuit
ICAN	interdisciplinary center for analytics on the nanoscale
IMFP	inelastic mean free path
IPES	inverse photoemission
IPS	image potential state
LEED	low energy electron diffraction
LMIG	liquid metal ion gun
LPE	linear photoemission
MBE	molecular beam epitaxy
MCP	micro channel plate
NEQ	nonequilibrium
ND	neutral density
NIM	nuclear instrumentation module
NM	normal or nonmagnetic metal
NOPA	noncollinear optical parametric amplification
PES	photoelectron spectroscopy
PIC	particle-in-cell
ps	picosecond
QMS	quadrupole mass spectrometer
RegA	regenerative amplifier
SHG	second harmonic generation
S/N	signal-to-noise
SP	spin polarization
TDC	time-to-digital converter
TEM	transmission electron microscopy
THz	terahertz
Ti:Sa	Ti-doped sapphire
TOD	third-order dispersion
e-TOF	electron time-of-flight
p-e TOF	position-sensitive electron time-of-flight
TOF	time-of-flight
ToF-SIMS	time-of-flight secondary ion mass spectrometry
tr	time-resolved
UHV	ultra-high vacuum
UV	ultraviolet
VIS	visible

Contents

List of Figures

1. Introduction

1.1. Motivation

The modern, digitized world expects a multifaceted transformation with its rapid progress in high technology. With ambitious future projects in artificial intelligence (AI), autonomous driving, e-mobility, 5G/6G communication, and robotics, one will see changes in diverse aspects of social life. The electronic industry will continue to grow and, thus, demands more and more electrical power. This compelling demand for energy leads to a dilemma with the international mitigation strategies against the threat of climate change [1–3]. The mitigation measures include less usage of fossil fuel resources and reduction of greenhouse gas emissions, which have been a driving engine for innovation in renewable energy and related materials technology.

A rising global demand shows up for developing and commercializing technologies that can convert and harness energy efficiently. The European Union has pledged to become the first climate-neutral continent by 2050. It started the campaign Important Project of Common European Interest (IPCEI), where countries like Germany plan to invest several billion into the chip industry [4]. With innovative smart solutions for greener mobility and more energy-efficient products, it is aimed to reduce CO_2 emission and ultimately shift toward a low carbon economy. Here presents microelectronics one of the key technologies. In this case, a compelling development of powerful and energy-efficient devices is inevitable for a sustainable future. Thus, understanding the fundamentals of energy dissipation and transport in nanoscale structures is of great importance for designing energy-efficient circuits and energy-conversion systems.

The invention of the first transistor in 1948 [5] and its use for the first integrated circuit (IC) in 1958 by Kilby et al. paved the way for the first commercial microprocessor in 1971, the Intel 4004 [6–8]. Due to the interest in faster processing circuits, the density of transistors in ICs increased and led to the well-known Moore's Law, which predicted a doubling of the transistor density every 18 months [9]. Together with the Dennard scaling down to the nanometer scale, the performance and energy-efficiency in the circuits increased exponentially and, at the same time, reduced the cost per compute [10]. While Intel 4004 was capable of performing 92000 operations per second, nowadays, MediaTek's 5G smartphone system-on-chip (SoC) are now capable of performing 4.5 trillion operations per second. This vast development led to high-speed switching processors and revolutionized modern technol-

ogy [11–13].

Important physics for these high-speed switching circuits is the electron and hole dynamics in the transistors. Non-equilibrated hot charge carriers with an energy of about a few eV above the Fermi level E_F are intrinsically nonlocal and propagate from the source to the drain. They generate a current in the circuit, and the more efficiently the charge carriers can move through the lattice, the higher the performance. The transport proceeds faster and with less power dissipation, which is beneficial for the switching speed of ICs. Nevertheless, ICs usually suffer from carrier scattering processes within the transistors, such as inelastic electron-electron (e-e) and electron-phonon (e-ph) scattering mechanisms. These local relaxation dynamics occur for a few eV hot charge carriers above the Fermi energy E_F on femtosecond (fs) up to picosecond (ps) time scales and compete with the charge carrier transport[1] [14–17]. Both the local relaxation and nonlocal transport dynamics are determined by the electronic band structure of the material and, thus, show an energy-dependent inelastic mean free path (IMFP) of the hot charge carriers [18]. Therefore, the length scale of the channel in the transistors plays a crucial role in the propagation behavior of the hot charge carriers.

The fastest propagation behavior, ballistic propagation, is by definition a transport without charge carrier scattering. In contrast, many scattering events during spatiotemporal transport lead to diffusive propagation. Consequently, an ultrafast relaxation of hot electrons in the fs regime by inelastic e-e scattering leads to an ultrafast energy redistribution. After a few hundreds of fs, the high electron temperature T_e couples to the lattice and heats the materials system, leading to energy dissipation and lowering the performance of the transistor [19, 20]. Although the intrinsic speed of hot electrons in the transistors proceeds in the ballistic regime, scattering events reduce ultrafast electron speed. Due to this fact, it is of great interest to reduce charge carrier scattering in transistors as much as possible and sustain the high-speed ICs. Thinning further down the transistor might reduce e-ph coupling and minimize heat waste. However, lateral dimensions < 20 nm lead to serious leakage currents and increases in power consumption. Thus, the clock speed of processors has remained unchanged at a few GHz since 2000 and has not reached the THz range [21–23].

These material shortfalls at lower dimensions (< 20 nm) limit the Dennard scaling and forces Moore's Law to find new ways to sustain further. Different transistor geometries, such as FinFETs from the 5 nm node or implementing 2D materials with their ultrathin nature and high-quality interfaces into the ICs are some of the efforts [12, 24, 25].

Exploiting nonequilibrium charge carrier local relaxation and nonlocal transport processes in the constituents or at the interfaces of heterostructures might lead to cutting-edge technologies. Preventing hot charge carriers from energy loss by reducing scattering processes with

---

[1]For a homogeneous electron gas in bulk crystals of sp-metals, the inelastic e-e scattering time is determined in the framework of Fermi liquid theory (FLT) by $\tau_{e-e} \sim n^{5/6} (E - E_F)^{-2}$ with electron density n.

certain nanostructural material design could support extracting and harnessing the energy before it decays. The hot charge carriers energy could be used for 2D/3D hot electron transistors, photovoltaics, novel batteries, and heat management within electrical circuits [20,21,26]. In particular, spintronics is a fascinating field for ultrafast data processing and data storage in computers. The Fe/Au metallic heterostructure has spin filtering properties at the Fe/Au interface and can act as a THz emitter. Understanding the energy-dependent microscopic processes of local and nonlocal relaxation dynamics allows controlling and shaping the material properties in the NEQ state.

This thesis addresses the relevant ultrafast NEQ dynamics of photoexcited hot charge carriers in epitaxially grown Au/Fe/MgO(001) thin films and contributes to the fundamental research for energy-efficient, advanced materials technology. Especially the interplay among local relaxation and transport processes in the constituents or at the heterostructure interface is interesting for scientists and application engineers. By performing Fe-side pumping and Au-side probing fs time-resolved photoemission spectroscopy on Au/Fe/MgO(001) thin films, this thesis answers the questions:

- What kind of scattering mechanisms accompany the spatiotemporal transport of hot carriers? Moreover, what kind of propagation behavior is observable?

- What is the influence of the epitaxially grown Fe/Au interface on the hot electron relaxation dynamics?

The Fe-side pumping and Au-side probing experimental approach enabled exploring the questions and investigating the interplay among local and nonlocal relaxation dynamics energy-dependent in the time domain in Au/Fe/MgO(001) heterostructure. The following section presents the development of this pump-probe approach in time-resolved optical measurements.

1.2. Experimental approach

In the 1960s, the importance of transistors became more and more apparent. Scientists and companies sought to understand the physical processes in transistors better in order to improve computer processors. In this regard, gaining knowledge about local relaxation and nonlocal transport processes of charge carriers in applied materials was essential. The development of ultrashort laser pulses opened the way for studying ultrafast charge carrier dynamics in solid-state material systems. By finding the ultrafast time-resolved pump-probe technique with fs laser pulses one could deduce the ultrafast charge carrier dynamics in the femtosecond regime.

In 1987 Brorson et al. [27] presented the first evidence of ultrafast electronic transport on thin Au films after a laser pulse excitation. They performed an ultrafast optical pump-probe

reflectivity measurement for different Au thicknesses ranging from 50 nm to 300 nm. In order to measure the heat transport in thin Au films they employed front-side pumping and back-side probing. It represented a time-of-flight measurement of heat transport through the sample. By plotting the transit time as a function of sample thickness, they observed a transport velocity of the same order as the Fermi velocity $v_F = 1.4$ nm/fs [27]. The conclusion was a contribution of ballistic propagating hot electrons for this rapid transport. With this work, Brorson et al. introduced the measurement of ultrafast electron transport processes in the fs regime by employing ultrashort laser pulses in a pump-probe technique. The remarkable efficiency and the relatively low cost of this technique made it favorable for many researchers to address fs dynamics. Seminal work in this regard was the discovery of the fs laser-induced ultrashort demagnetization (sub-picosecond) of Ni thin films by Beaurepaire et al. [28] in 1996. To understand the impact of this discovery, one has to imagine the switching speed of a magnetic bit in hard-disk drives, which proceeds in several ns [29]. The employment of laser-induced magnetization suggested an increase of the switching speed by three orders of magnitudes. This intriguing finding and the purpose of continually increasing the speed and density of data storage with less energy consumption generated a lot of interest among researchers [30].

In 2008, Malinowski et al. described the fs laser-driven ultrafast demagnetization in a ferromagnet (FM)/ normal metal (NM) heterostructural thin films by spin-polarized hot electron transport effects [31]. Nevertheless, the decisive description was delivered in 2010 by Battiato et al. [32], which incorporated in addition to the spin-polarized hot electron transport the energy- and spin-dependent scattering mechanisms. This description led to the superdiffusive transport model, which describes the propagation behavior of photoexcited hot electrons in an intermediate regime between ballistic and diffusive transport accompanied by a few scattering events. With this model, Battiato et al. succeeded in explaining the ultrafast demagnetization process in Ni/Al heterostructure during the first few hundred femtoseconds. In FM as Ni, Fe and Co, the transport behavior, lifetime, inelastic mean free path and velocity of excited hot electrons are highly energy- and spin-dependent. Hot majority electrons from the sp-band are much more mobile and have a larger inelastic mean free path with respect to minority electrons from the 3d-band [33].

In order to experimentally verify this theory, Melnikov et al. performed in 2011 magnetization sensitive nonlinear optical measurements on epitaxially grown Au/Fe/MgO(001) thin films out [34]. By photoexciting hot electrons in the Fe layer and probing a transient spin polarization at the Au surface with the optical second harmonic generation, they proved the existence of a spin-polarized current of hot carriers propagating from the Fe toward the Au layer [30]. Together with observing a superdiffusive propagation behavior of hot electrons, Melnikov and his collaborators corroborated the superdiffusive spin transport model for FM/NM thin films. This pioneering work was followed and further applied on different

material systems. It enriched the insights in the ultrafast magnetization dynamics induced by photoexcited spin-polarized hot carrier dynamics [29,33,35,36]. The benefit of this fundamental research was finding spin filtering properties of Fe/NM interfaces. In the case of the Fe/Au system, the spin current probed at the Au surface was mainly caused by an injection of hot majority electrons from the ferromagnetic Fe film into the adjacent Au layer. The Fe/Au interface exhibits high transmittance for majority electrons, attributed to the well-matched sp-bands in Fe and Au above the Fermi energy. However, for minority electrons and majority electrons at lower energies, the average transmittance is low due to the significant density of d-states in Fe. Accordingly, the Fe/Au interface acts as an efficient spin filter for non-thermalized electrons optically excited in Fe [37]. Moreover, the resulting ultrashort spin current pulse at the Fe/Au interface propagates with a velocity of the order of 1 nm/fs in Au and can generate a terahertz electromagnetic pulse (THz), which opened the door for THz spintronics devices [33,38,39].

The relevance of spin-dependent charge carrier transport in femtosecond magnetization dynamics has spurred the use of back-side pumping in optical pump-probe experiments [34,36,40], which provide energy- (and momentum)-integrated information. However, due to the energy- and spin-dependence nature of carrier dynamics at the buried media/interfaces, researchers have been actively pursuing energy-resolved measurements in the ultrafast time domain to gain deeper insights [41].

A suitable method for this is time- and angle-resolved photoelectron spectroscopy (tr-ARPES) with sensitivity to hot charge carriers energy and momentum at the surface. This tool is based on a pump-probe approach and has been used for exploring the relaxation dynamics of hot charge carriers energy-resolved in the time domain. [42–45]. Two well-established PES variants are the linear photoemission (LPE) and the nonlinear two-photon photoemission (2PPE) technique.

In the case of time-resolved LPE, an intense fs pump laser pulse photoexcites the ground-state of a system and monitors the transient evolution of occupied states by direct photoemission with a time-delayed probe pulse. The photoexcitation of hot electrons above the Fermi edge E_{F} is accompanied by a depletion of electrons below E_{F} which is referred to as holes. Thus, time-resolved LPE enables the study of the ultrafast relaxation dynamics of photoexcited electrons and holes in the NEQ state and their coupling to quasi-particles such as phonons in the vicinity of E_{F}.

Further insights have been achieved by employing time-resolved 2PPE spectroscopy, which directly accesses the electron energy relaxation dynamics in the unoccupied part of the electronic band structure. Various measurements with this nonlinear photoemission method combined with theoretical calculations have shown that transport effects have to be taken into account to describe the observed hot electron relaxation times fully [17, 46–48]. All these LPE and 2PPE measurements are based on the conventional front-pump front-probe

experimental configuration and have been delivering energy-resolved information about the transient energy distribution of excited charger carriers at the surface.

Although the PES method provides energy-resolved information, the peculiarity of this method is that it is surface sensitive, which in turn is a significant limitation for the study of hot carrier dynamics in buried media/interfaces of heterostructures. So far, local relaxation dynamics at the surface and nonlocal contributions, e.g., due to transport, were indirectly distinguished by analyzing relaxation at surfaces [16, 46, 47, 49, 50]. The ultrafast relaxation and transport processes occur on similar time scales, and, thus, the disentanglement of both processes remains challenging. Separating these local and nonlocal contributions is essential to obtain a microscopic understanding of the underlying processes. In order to overcome this limitation of the surface sensitivity, back-side pump front-side probe PES has been suggested for studying the interplay among local and nonlocal hot charge carrier relaxation dynamics energy-resolved in the time domain. Time-resolved 2PPE was performed on Au/Fe/MgO(001) thin films using Fe-side pumping Au-side probing (BP) and Au-side pumping and probing (FP) experimental geometries, which are shown in Figure **1-1**.
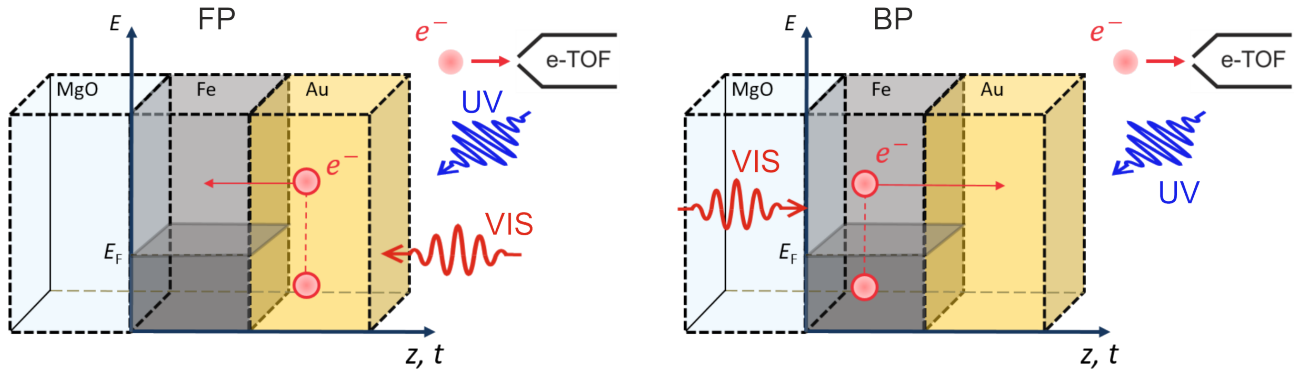
Figure 1-1: Sketch of time-resolved pump-probe photoelectron spectroscopy with FP and BP geometries on epitaxially grown Au/Fe/MgO(001) thin films. FP: Hot electrons photoexcited by an ultrashort VIS laser pulse at the Au surface propagate toward the Fe layer. A time-delayed UV laser pulse probes the remaining population of hot electrons at the Au surface. BP: Photoexcited hot electrons in the Fe layer up to a few eV above the Fermi level E_F undergo transport processes toward the Au surface where they can be probed by a time-delayed UV pulse. The photoemitted electrons are detected and analyzed with an e-TOF spectrometer.

By using a fs time-resolved back-pump front-probe experimental configuration the hot electrons are excited above E_F in the Fe layer by a VIS fs laser pulse. The photoexcited electrons experience a spatiotemporal transport from the Fe layer through Fe/Au(001) interface toward the Au surface. A time-delayed ultrashort UV pulse probes the hot electron at the surface. The photoemitted electrons will be detected and subsequently analyzed by an

electron time-of-flight (e-TOF) spectrometer. In the case of front-side pumping front-side probing, the photoexcitation and probing by a time-delayed UV pulse occur both at the Au surface. The propagation of hot electrons occurs in this case from the Au surface through Au/Fe interface toward the Fe layer but is not directly observed.

Insights gained from time-resolved 2PPE on epitaxially grown Au/Fe/MgO(001) thin films with both Au-side pump (FP) and Fe-side pump (BP) experimental configurations: In contrast to the conventional measurements in the front-pump configuration, the back-pump configuration allowed the analysis of the interplay among local and nonlocal relaxation dynamics in an energy-resolved manner in the time domain. It opened the door for distinguishing local relaxation dynamics in the constituents of the MgO(001)/Fe/Au heterostructure. Moreover, by varying the Au thicknesses from 5 to 70 nm, nonlocal electron dynamics were observed and I concluded a superdiffusive propagation behavior of hot electrons. Another aspect is the observation of the first image potential state IPS ($n =1$) at the Au(001) surface with the FP experimental approach. Furthermore, excitation of unoccupied Fe-minority states has been observed with the BP geometry.

2. Theoretical background

The research field of hot electron dynamics in metallic thin films includes various processes occurring on ultrafast time scales from femtoseconds (fs) to a few picoseconds (ps). In this chapter, we present the theoretical background of hot electron local relaxation and nonlocal transport phenomena in metallic thin films, and the effect of the interface in ferromagnetic/normal metal (FM/NM) heterostructures. To define the terms *local* and *nonlocal* relaxation dynamics, the following aspects are mentioned for metallic heterostructures: While the local relaxation dynamics of photoexcited electrons refers to scattering events in a single constituent, the nonlocal effect is related to the hot electron spatiotemporal transport across the interface between the constituents of a heterostructure, see Figure **2-1**.
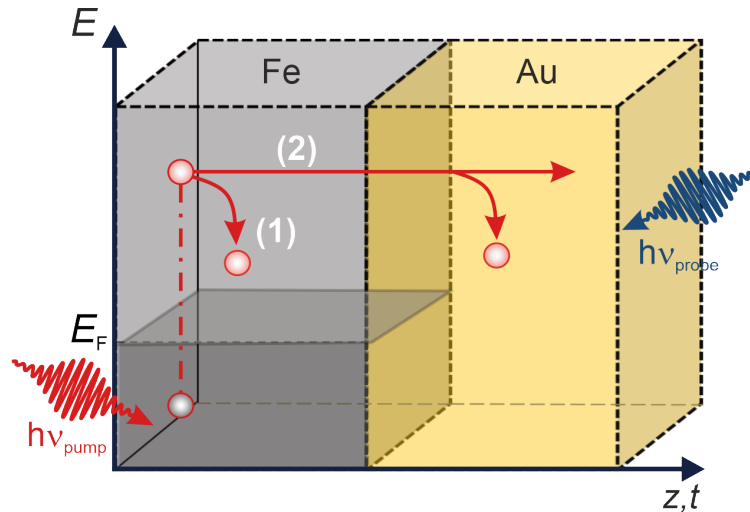
Figure 2-1: Pump-probe photoelectron spectroscopy with BP geometry on Fe/Au heterostructures. Hot electrons photoexcited by an ultrashort VIS laser pulse in the Fe layer up to a few eV above the Fermi level E_F undergo two possible processes: (1) local relaxation dynamics occurring through inelastic e-e scattering processes in a single constituent (Fe or Au) of the heterostructure, or (2) nonlocal transport of hot electrons between the two constituents across the Fe/Au interface.

In the first section, the band structures of the studied Au and Fe material system is presented, which determine the local and nonlocal relaxation dynamics in the Au/Fe/MgO(001) heterostructure. However, in FM/NM heterostructures, spin-dependent dynamics must be taken into account due to the splitting of the energy band into majority and minority sub-

bands in FMs. Therefore, spin-dependent bulk and interface effects in FM/NM heterostructures are predicted and are described here. Moreover, the observation of the lowest image potential state (IPS, $n = 1$) at the Au(001) surface by the 2PPE technique (discussed in chapter 4) leads to the introductory discussion of this particular state in section 2.1.

The second section describes the process of laser light absorption in metals. We show here the photon energy dependent absorption of laser pulses in the visible region for Fe and Au. In addition, the inter- and intraband transitions in combination with the excitation scheme in sp-metal Au and 3d-metal Fe are discussed. Lambert-Beer's law is presented to provide a theoretical basis for the absorption profiles in chapter 4.

The third section deals with the ultrafast phenomena of photoexcited electrons in the nonequilibrium state (NEQ) in condensed matter. The time scales for the elementary scattering processes of hot electrons such as the inelastic e-e, e-ph, or e-defect interaction range from femtoseconds to a few picoseconds. Furthermore, these ultrafast local scattering mechanisms are in direct competition with ultrafast nonlocal transport phenomena of hot electrons. Consequently, the energy-dependent interplay of local and nonlocal relaxation dynamics of hot electrons is discussed.

Then, in the fourth section, an overview of previous scientific works reporting on the local and nonlocal relaxation dynamics of hot electrons is given [27, 34, 46, 49, 51]. Based on these studies, the film thickness effect and the influence of the excitation schemes such as front-side pumping (FP) or back-side pumping (BP) geometry are reported. In addition, previous optical experiments on Au/Fe/MgO(001) with BP geometry are described, which paved the way for our time- and energy-resolved PES measurements. In particular, spin-dependent relaxation and transport properties of hot electrons and interfacial effects in Au/Fe heterostructure are discussed.

The last section of this chapter describes the fundamental principles of photoelectron spectroscopy (PES). The two variants in PES, linear photoemission (LPE) and two-photon photoelectron emission (2PPE) are compared and described. Since the 2PPE method is applied within this thesis work, the main focus will be on the 2PPE technique. It represents a state-of-the-art technology to gain insights into ultrafast electron dynamics in unoccupied states of the band structure in condensed matter.

2.1. Electronic band structure of Au and Fe

The band structure of solid-state materials determines, among other aspects, the optical properties and the charge carrier relaxation dynamics of the material system. Therefore, knowledge of the band structure and the DOS of the material is essential for understanding
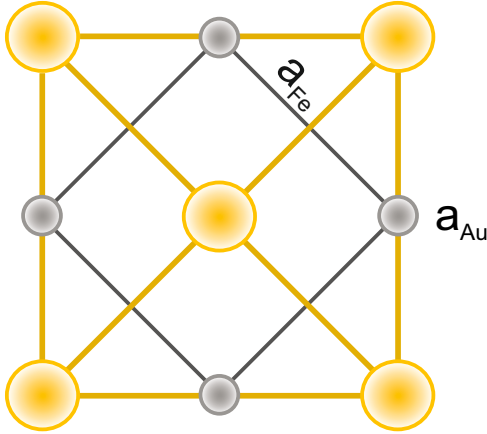
Figure 2-2: Illustration of epitaxially grown fcc-Au(001) on bcc-Fe(001): Large yellow and small gray circles indicate Au and Fe atoms, respectively. The rotation of the in-plane axes of both layers by 45° to each other leads to lattice-match with the lattice constants $a_{Au}/\sqrt{2} = 2.88$ Å and $a_{Fe} = 2.86$ Å.

and elucidating the fundamental microscopic processes behind the observed dynamics. The epitaxially grown Au/Fe heterostructure here consists of an fcc-Au and a bcc-Fe lattice with the crystalline orientation (001). It is particularly well lattice-matched if the in-plane axes of both layers are rotated by 45° to each other and thus differ only by 0.5% at lattice constants $a_{Au}/\sqrt{2} = 2.88$ Å and $a_{Fe} = 2.86$ Å, as shown in Figure **2-2** [52–54].

(i) Electronic band structure of Au

The noble metal Au represents an sp-metal whose electronic band structure calculated by Rangel et al. is presented in Figure **2-3**. The (001) high-symmetry line in a cubic fcc lattice extends from the high-symmetry point Γ to X; Γ → X. The states of the sp-like bands are shown as black (blue) lines for the occupied (unoccupied) part of the band structure. Thus, the sp-like band crosses the Fermi edge E_F and exhibits a steep curve. In contrast, many d-like bands below E_F tend to have a flat structure. The upper d-band edge (red line) shows the 5d band roughly at 2.5 eV below the Fermi level E_F, which is reflected in the *ab initio* DOS with a steep d-band edge at 2.4 eV in Figure **2-3**(b) [55]. Consequently, for photon energies $h\nu < 2.4$ eV, sp-like bands play a crucial role in the charge carrier relaxation dynamics.

Moreover, spectral features such as image potential states (IPS) in front of the Au surface were proposed by Echenique et al. in 1978 [57] and identified by Straub et al. in 1984 [58] using inverse photoemission (IPES) experiments. One year later, in 1985, Giesen et al. proved the existence of IPS at Cu(111) and Ag(111) crystal surfaces by two-photon photoemission [59]. Compared to intrinsic surface states such as the Tamm and Shockley surface states, which are localized in the surface atomic layers, the electrons in image potential states are trapped a few Angstroms in front of the surface [60]. An electron that is excited out of the crystal in front of the surface leads to the formation of an electric field induced by the image charge of the electron at the sample surface, see Figure **2-4** top.
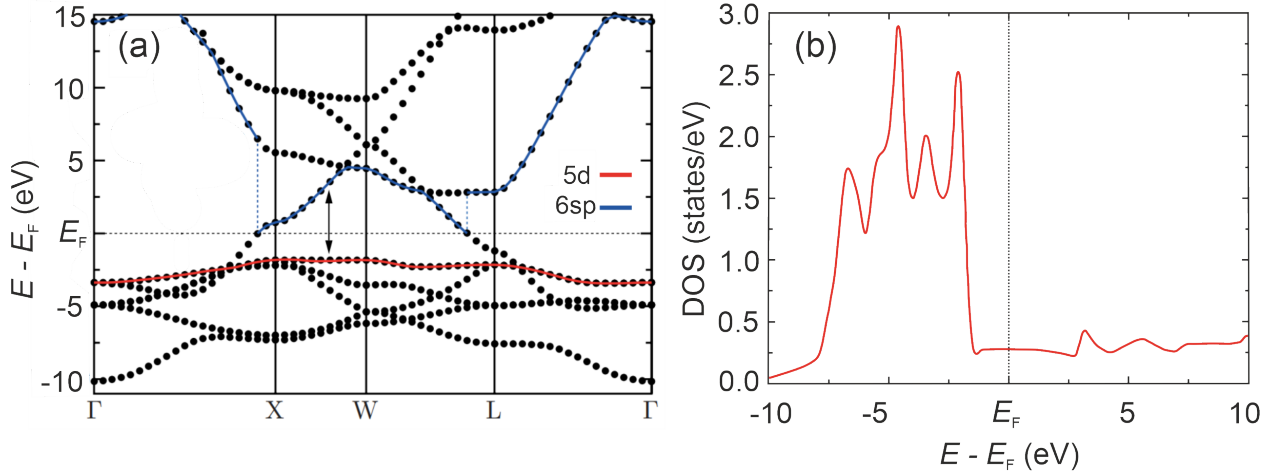
Figure 2-3: (a) Electronic band structure of Au calculated using *ab initio* many-body perturbation theory. The Fermi level E_F is set to 0 (dashed black line). The red line shows the 5d-character topmost occupied d-band, while blue (black) lines indicate the 6sp-like lowest empty bands. Slightly modified and reprinted with permission from Rangel et al. Band structure of gold from many-body perturbation theory. *Phys. Rev. B* 86, 125125 (2012). DOI: https://doi.org/10.1103/PhysRevB.86.125125. Copyright © 2012 by the American Physical Society. Ref. [56]. (b) *Ab initio* calculation of density of states (DOS) of Au. Slightly modified and reprinted with permission from Hopkins et al. Contribution of d-band electrons to ballistic transport and scattering during electron-phonon nonequilibrium in nanoscale Au films using an ab initio density of states. *J. Appl. Phys.* 106, 053512 (2009). DOI: https://doi.org/10.1063/1.3211310. Copyright © 2009 by AIP Publishing. Ref. [55].

A potential well induced by the attractive Coulomb potential of the image charge and the repulsive lattice potential generates image potential states localized in the vacuum region of the metal surface. By analogy with the hydrogen model, these image potential states form a Rydberg-like series converging to E_vac with discrete energies

$$E_n = E_\mathrm{vac} - \frac{0.85 \text{ eV}}{(n+a)^2} \tag{2-1}$$

numbered by $n = 1, 2, 3, \ldots$ [42]. Parameter a represents a quantum defect that depends on the crystal surface of interest. Figure **2-4** (bottom) shows the two lowest IPS ($n = 1, 2$) and the squares of the wavefunctions in front of the sample surface. Earlier theoretical calculations in 1999 by Chulkov et al. showed that the first IPS ($n = 1$) of Au(100) is 0.64 eV below the vacuum energy [62].
Moreover, using high energy-resolved 2PPE spectroscopy, Nakazawa et al. proved in 2016 the existence of the first image potential state IPS ($n = 1$) at the Au(001) surface with a binding energy of 0.765 eV to the vacuum energy E_vac [63]. In section 4.2.1, we show the distinct spectral feature of the first IPS ($n = 1$) on the Au(001) surface excited by the Au-side pump (FP) time-resolved 2PPE experiments.
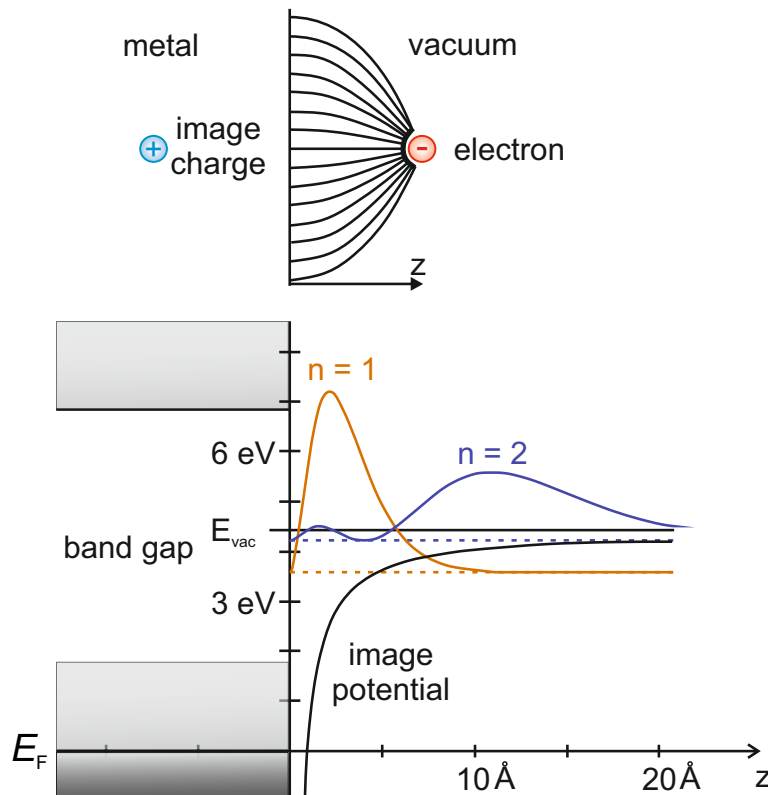
Figure 2-4: Top: The electric field of an electron that is localized a few Angstroms Å in front of a metal surface can be described by the concept of an image charge. Bottom: The corresponding attractive image potential leads to a series of bound states if the electron cannot penetrate the material due to a band gap caused by the negative electron affinity of the solid metal surface. The image potential states form a Rydberg-like series of unoccupied states. For the lowest two image potential states $n = 1, 2$ (orange and blue dashed lines), the squares of the wavefunctions (orange and blue solid lines) are shown. Reprinted with slight modifications with permission from T. Fauster, W. Steinmann. Two-photon photoemission spectroscopy of image states. *Phot. Prob. Surf.* Ch. 8, pp. 347-411 (1995). DOI: https://doi.org/10.1016/B978-0-444-82198-0.50015-1. Copyright © 1995, with permission from Elsevier. Ref. [61].

(ii) Electronic band structure of Fe

The ferromagnet Fe represents a d-band transition metal with the electron configuration $3d^6 4s^2$. It belongs to the 3d ferromagnets formed by Fe, Co, and Ni, all of which contain sp-like and d-like orbitals in the valence band. The electronic band structure of Fe, depicted in Figure **2-5**(a), exhibits exchange-split bands with majority and minority spin characters[1]. The dispersion of the electron bands for both minority and majority electrons has been
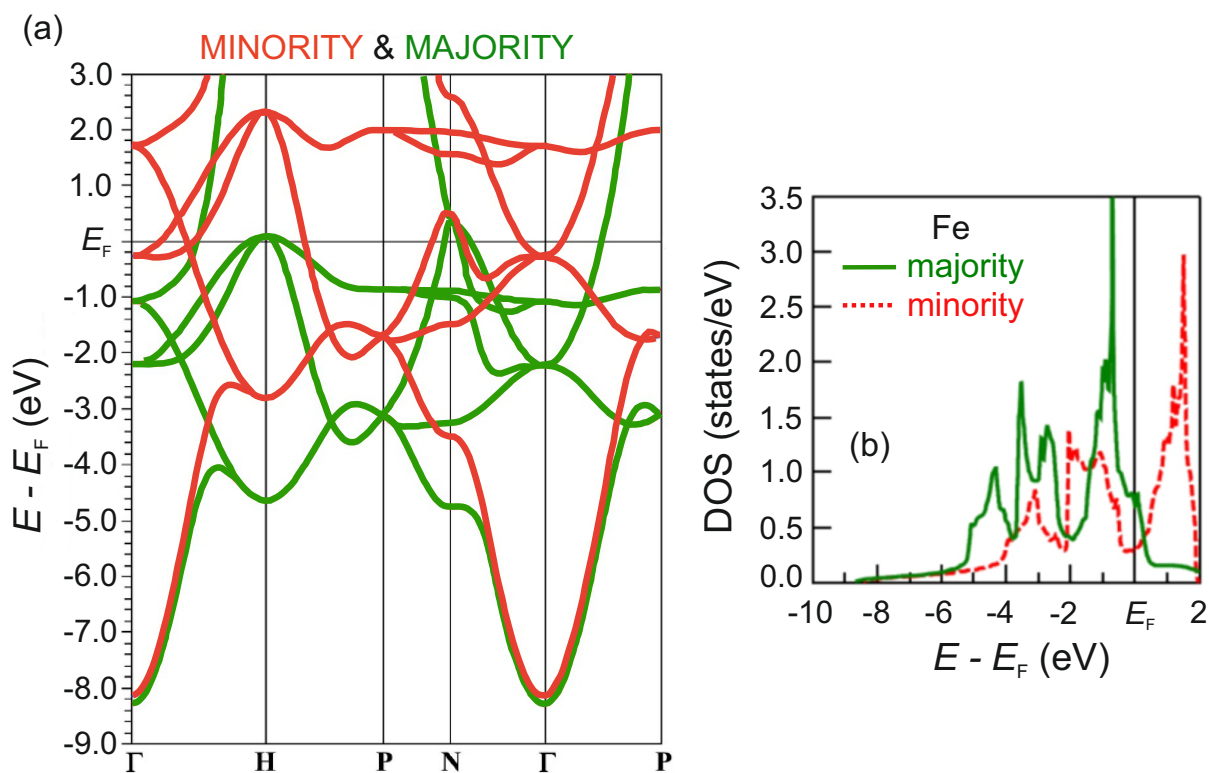
Figure 2-5: (a) The Fe band structure for minority and majority spin electrons with a red and green solid line, respectively. The exchange splitting is energy- and k-dependent. Reprinted with permission from Schäfer et al. Fermi surface and electron correlation effects of ferromagnetic iron. *Phys. Rev. B* 72, 155115 (2005). DOI: https://doi.org/10.1103/PhysRevB.72.155115. Copyright © 2005 by the American Physical Society. Ref. [66]. (b) The density of states of Fe for majority and minority electrons in the dependence of intermediate state energy $E - E_F$ redrawn based on Ref. [29] with permission from Dr. A. Alekhin.

---

[1]The Stoner model of the ferromagnetic metals is the simplest band-like model, which accounts for the interplay between itinerant electrons and an atomic-based direct interaction between electrons of opposite spin [64]. The comprehensive discussion of the energy band split into minority and majority sub-bands can be taken from [65].
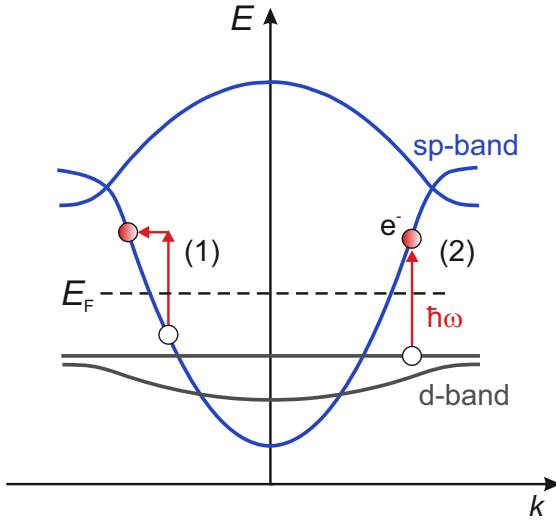
Figure 2-6: Energy-momentum $E(k)$ diagram showing (1) intra- and (2) interband transition processes by photon absorption in metals with sp- and d-bands (e.g. Cu, Au). Direct (interband) absorption occurs from one band to a second, provided the photon energy $\hbar\omega$ is sufficient to excite an electron from the occupied d-band to the unoccupied sp-band above the Fermi level E_F. Indirect (intraband) transitions are also possible at lower energies and require an additional scattering process, e.g., with a phonon, to ensure the conservation of momentum k.

calculated by Schäfer et al. with DFT [66]. The (001) high symmetry line in a bcc lattice ranges from the high symmetry point Γ to H. Note that below E_F the states are dominantly occupied by majority bands while above E_F minority bands prevail. This is also reflected in the DOS of bcc-Fe for majority (green) and minority (red) spins in Figure **2-5**(b). The high DOS of minority electrons at $E - E_F > 0.4$ eV provides a large phase space for inelastic scattering processes and consequently represents more localized d-band minority electrons. In contrast, majority electrons at $E - E_F > 0.4$ eV show a more sp-like character and less phase space for inelastic scattering processes.

2.2. Absorption of light in metals

The application of ultrashort laser pulses is a common approach in solid-state physics to analyze the dynamics of hot charge carriers. The energy of an ultrashort laser pulse irradiated onto the surface of a solid can be absorbed by free charge carriers, e.g. electrons in the conduction band absorb photons and are excited to energy states above the Fermi edge E_F. Figure **2-6** illustrates the free-electron intra- and interband transition processes upon single-photon absorption of metals with sp- and d-bands (e.g. Cu, Au). The intraband transition process describes the photoexcitation of a free electron from an occupied state below the Fermi level E_F to an unoccupied state at higher energies above E_F within a single band, e.g., the sp-band. In comparison, the interband transition process represents the excitation from occupied to unoccupied states between two different bands, for example, the d- and sp-bands. Both processes are common in metallic nanostructures, provided that the photon energy $\hbar\omega$ is sufficient for the excitation from occupied d-band to unoccupied sp-band states.

As shown in the previous section 2.1, the electronic band structure of Au exhibits an upper

d-band edge at about 2.5 eV below the Fermi level E_F. Therefore, the optical properties of Au at photon energies $\hbar\omega < 2.4$ eV are mainly determined by collective excitations of free carriers in sp-like bands. This causes a high reflectivity and negligible absorption at $\hbar\omega < 2$ eV. In contrast, Fe d-bands are located around the Fermi level E_F and promote the intra- and interband optical transitions, which explains the low reflectivity and large absorption at 2 eV. Considering the Fe-side pumping approach (BP) with pump photon energies $\hbar\omega < 2.4$ eV on Au/Fe/MgO(001) thin films, the influence of hot electrons excited by the pump pulse in Au can be neglected. In contrast, hot electrons are mainly excited in Fe due to strong absorption. For photon energies above 2.4 eV, the absorption in Au is expected to increase due to interband transitions.

The propagation of a plane electromagnetic wave in medium to the positive direction z can be described by the oscillating electric field

$$E(z,t) = E_0 \cdot e^{i(kz - \omega t + \Phi)}, \tag{2-2}$$

with angular frequency ω, amplitude E_0 and phase Φ of the electric field in the point $z = 0$ at the time $t = 0$, and $k = k' + ik'' = \frac{\omega}{c}(n' + in'')$ the wave-vector inside the medium. In absorbing matter, the amplitude of the electric field decreases with distance by $e^{-k''z}$, and the intensity of the electromagnetic wave, which is proportional to $|E_0 \cdot e^{-k''z}|^2$, is governed by the Lambert-Beer's law

$$I(z,\omega) = I_0 \cdot e^{-\alpha(\omega)z}, \tag{2-3}$$

where I_0 is the initial intensity of the electromagnetic wave at $z = 0$ and $\alpha(\omega) = 2k'' = 2\omega n''/c$ the absorption coefficient with the extinction coefficient n''. A femtosecond laser pulse has a relatively wide spectrum and differs from monochromatic light with a single frequency ω. Different parts of the spectrum of the ultrashort laser pulse may have different absorption coefficients $\alpha(\omega)$. However, if $\alpha(\omega)$ does not vary much within the broad spectrum, it can be replaced by an average value. In section 4.1 we show the absorption profiles for Au/Fe/MgO(001) heterostructures with different Au thickness d_Au.

2.3. Elementary electron relaxation processes

Absorption of ultrashort laser pulses by metallic nanostructures leads to a NEQ distribution of hot charge carriers. The initial energy relaxation of hot electrons above the Fermi level E_F is collectively governed by the photon energy $h\nu$ and the band structure of the metal [17, 26, 67]. In this section, we will discuss the elementary scattering processes between quasi-particles in photoexcited solids. The central quantity is the lifetime τ (inversed scattering rate) of a state, which represents the passed time between two scattering processes. Consequently, the energy relaxation or population decay at a specific state proceeds

exponentially with a time constant τ. In spectroscopy, a finite lifetime of a state is expressed as the linewidth that corresponds to

$$\tau = \hbar/\Gamma. \tag{2-4}$$

Several processes such as inelastic e-e, e-ph scattering, or electron-magnon (e-m) interactions with the respective energy-dependent decay rates Γ_{e-e}, Γ_{e-ph}, and Γ_{e-m} play a role in the fast equilibration of the non-thermal hot electrons on an ultrafast timescale ($t \approx \text{fs} - \text{ps}$). According to the Matthiessen rule, the rate of individual processes such as Γ_i can be added to the total decay rate $\Gamma = \sum_i \Gamma_i$ if the scattering mechanisms are independent [17, 68]. Figure **2-7** gives an overview of the various processes and their typical covered linewidth range (top axis), and ultrafast time scales (bottom axis) where the elementary scattering dynamics take place and contribute to the decay.
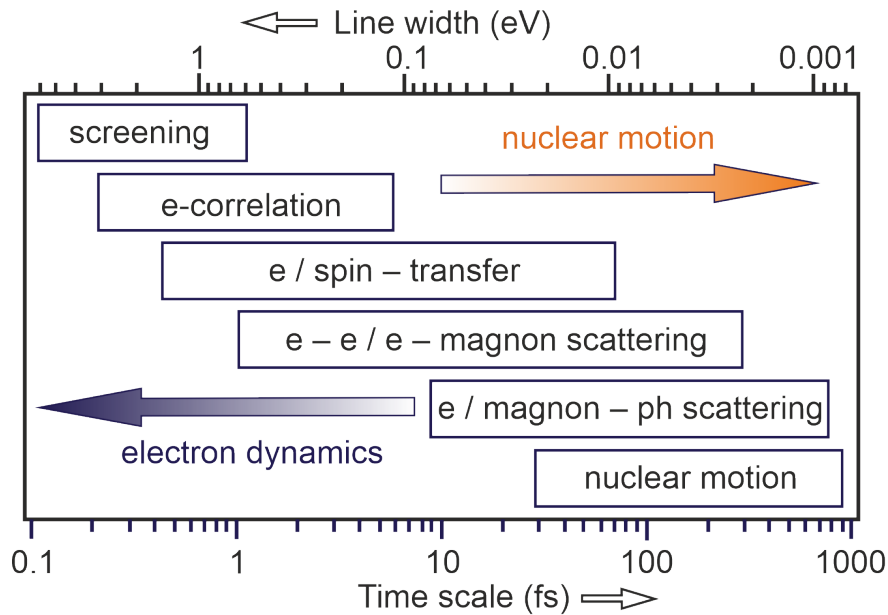
Figure 2-7: Ultrafast phenomena: Typical time scales and energy bandwidth of elementary excitation and decay processes in solid materials. The figure is redrawn based on Ref. [17] and printed with permission from U. Bovensiepen et al. Elementary relaxation processes investigated by femtosecond photoelectron spectroscopy of two-dimensional materials. *Las. & Phot. Rev.* 6, 589-606 (2012). DOI: https://doi.org/10.1002/lpor.201000035. Copyright © 2012 by John Wiley and Sons.

Next to the fastest processes of screening and e-correlation effects in the time range of atto- and femtosecond are dephasing processes at which the photoexcited electrons start to scatter elastically. In this case the phase relation is lost, but the population of the state does not decrease. Inelastic e-e or e-m scattering represents a decay channel of excited electrons and

proceeds in time scales of several fs to a few 100 fs. The scattering of electrons or magnons with phonons happens in time scales between a few ten fs to ps and leads to transient energy distribution between different degrees of freedom in solids [17]. For a general overview of the common scattering processes in PES, electron-electron scattering, electron-phonon scattering, and electron-defect scattering are briefly discussed below.

Electron-electron scattering: For large excitation energies $E - E_\mathrm{F} \gg k_\mathrm{B}T$ and ultrashort time scales (< 1 ps) the hot electron energy distribution in metals is dominated by inelastic e-e scattering dynamics. The interaction between hot and "cold" electrons below the Fermi level E_F leads to energy transfer and secondary electrons occupying the energy states near E_F due to the equal mass of the collision partners. In the case of elastic e-e scattering the excited electrons experience momentum change without energy transfer. The phase is lost (dephasing), which broadens the linewidth Γ with an additional dephasing time τ_0 by $\Gamma = \hbar/\tau + \hbar/(2\,\tau_0)$ [69].

Electron-phonon scattering: At low hot electron energies, a few 10 meV above E_F, the electrons scatter with the lattice by absorption or emission of phonons. For hot electrons (a few eV above E_F), e-ph scattering processes can be seen as a quasi-elastic process, which leads to a large change of parallel momenta such that the propagation of an excited electron is efficiently changed.

Electron-defect scattering: Imperfections in the crystal structure, such as defects, impurities or potential corrugations at interfaces may lead to hot electron scattering processes, which change the electron energy and momentum. This scattering process can be approximated to be a quasi-elastic redistribution of momenta [70].

Based on our analysis of hot electron relaxation dynamics via 2PPE spectroscopy in chapter 4, we will present next the inelastic e-e scattering processes in more detail, which was the main contributor in hot electron local scattering processes in Au/Fe/MgO(001) thin film heterostructure.

2.3.1. Inelastic electron-electron scattering

The inelastic e-e scattering is described within a system of interacting Fermions, the Fermi liquid. The theoretical approach, known as the Landau theory of Fermi liquids (FLT), deals with the quasi-particle lifetimes of an excited electron or hole considering e-e scattering [71–73]. In case of the photoexcitation of bulk sp-metal crystals, for low excitation densities ($< 10^{-3}$ e$^-$) of an excited single electron at given energy $E - E_\mathrm{F}$ (~ 0.1 to a few eV) above the Fermi level E_F, the relaxation time is determined by inelastic scattering processes and is generally well described by the Fermi liquid theory (FLT). The inelastic e-e relaxation time
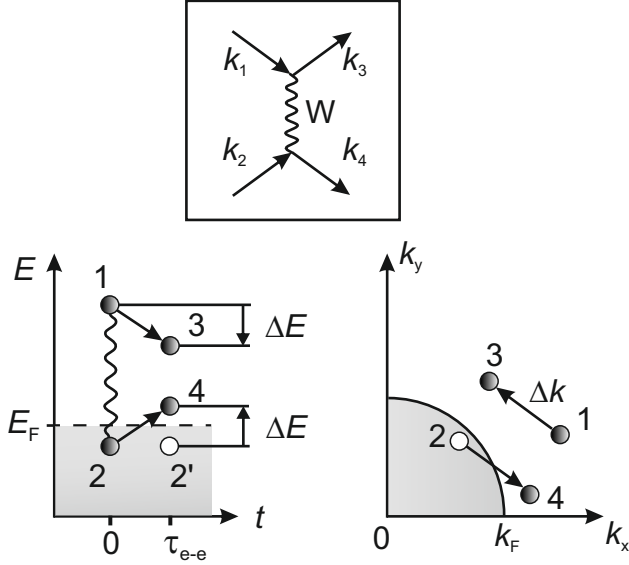
Figure 2-8: Schematic of electron-electron scattering. At the top is the Feynman diagram and at the bottom left is the energy diagram. An electron 1 scatters with an electron 2 of the Fermi gas and transfers the energy ΔE to its collision partner. Subsequently, two excited electrons 3 and 4 and a hole 2' are generated. Overall, such scattering processes cause the number of excited electrons to increase near the Fermi level and decrease at higher energies. Bottom right: The reciprocal space in which conservation of momentum and momentum transfer Δk become clear. The Figure is redrawn based on Ref. [75] with permission from Dr. M. Lisowski.

τ_{e-e} scales with the inversed squared intermediate state energy with respect to the Fermi level E_F

$$\tau_{e-e} \sim \frac{1}{(E - E_F)^2}. \tag{2-5}$$

Accordingly, τ_{e-e} decreases with increased intermediate state energy $E - E_F$ due to the increased available phase space for inelastic e-e scattering processes [72–74].

For illustration, Figure **2-8** depicts the case of the inelastic e-e scattering process between two electrons. Upon photoexcitation of a metallic surface, a single electron 1 is excited from an occupied state below the Fermi level E_F to an unoccupied state above E_F; $E_1 > E_F$. The photoexcited electron 1 with momentum $\vec{k}_1$ scatters inelastically with a 'cold' electron 2 of momentum $\vec{k}_2$ from an occupied state in the Fermi sea; $E_2 < E_F$. An energy and momentum transfer of ΔE and $\vec{q}$ occurs between both participating electrons, resulting in the creation of two excited electrons 3 and 4 with momenta k_3 and k_4, and a remaining hole 2'. Due to the occupied states below E_F, the Pauli exclusion principle only allows scattering into final states k_3 and k_4, which are unoccupied states above E_F; E_3, $E_4 > E_F$. The screened Coulomb interaction W mediates the scattering process, which must conserve energy and momentum:

$$\begin{aligned} E_1 + E_2 &= E_3 + E_4 \\ &= (E_1 - \Delta E) + (E_2 + \Delta E) \end{aligned} \tag{2-6}$$

$$
\begin{aligned}
\vec{k}_1 + \vec{k}_2 &= \vec{k}_3 + \vec{k}_4 \\
&= (\vec{k}_1 - \vec{q}) + (\vec{k}_2 + \vec{q})
\end{aligned}
\tag{2-7}
$$

While excited electron 1 loses the energy of ΔE due to the inelastic scattering process with electron 2, producing an electron 3 ($1 \to 3$) in the unoccupied state, "cold" electron 2 gains energy of ΔE, leading to electron 4 ($2 \to 4$) and a hole 2'. Electron 4 represents secondary electrons, which populate the intermediate energy states close to E_F and contribute to the population effect of these low unoccupied energy states. In contrast, the high-energy electrons experience a population decay. The energy regime of interest for secondary electron lies $< h\nu/2$. Thus, the measured relaxation times at these energy states are not occurring purely due to the relaxation of this state but also due to the additional in-scattering effect of secondary electrons.

2.3.2. Interplay of scattering & transport dynamics

In photoelectron spectroscopy, metallic surfaces are irradiated by ultrashort laser pulses in order to excite hot charge carriers and investigate the energy-dependent ultrafast relaxation dynamics [15, 45]. Hot electron relaxation and transport in metallic nanostructures involve many ultrafast processes whose interplay is determined by the band structure and the properties of the employed fs laser pulses [77]. Hohlfeld et al. present a scheme in [76] showing the energy-dependent competition between local relaxation and nonlocal transport processes, see Figure **2-9**. It shows the time evolution of hot electron relaxation dynamics after the photoexcitation of a metal. A non-photoexcited metal, at time $t < 0$, is initially in thermal equilibrium in which the electrons follow the Fermi-Dirac statistics with the distribution function

$$
f(E, \mu, T_\mathrm{e}) = \frac{1}{\exp\left[\frac{E-\mu}{k_\mathrm{B} T_\mathrm{e}}\right] + 1},
\tag{2-8}
$$

known as the Fermi-Dirac distribution with the chemical potential μ, electron temperature T_e and the Boltzmann constant k_B.

Fig. **2-9**(a, left) demonstrates that after photon absorption at time $t = 0$, nonequilibrium, hot electrons are excited within the optical penetration depth and a transient non-thermal electron distribution is created, which is not described by a Fermi-Dirac statistic. The electrons are energetically lifted up and populate the unoccupied part of the band structure above E_F. The density of hot electrons increases in the highest energy states, and hot electron transport occurs due to the gradient of energy density at the metal surface, see Fig. **2-9**(a, right). Initially, the hot electrons propagate deeper in the sample with ballistic velocities $v \sim 10^6$ m/s (1 nm/fs) until they are scattered by e-e interaction[2].

---

[2]Hot electron transport can be either ballistic or diffusive, depending on the ratio between inelastic scattering length and sample size [54].
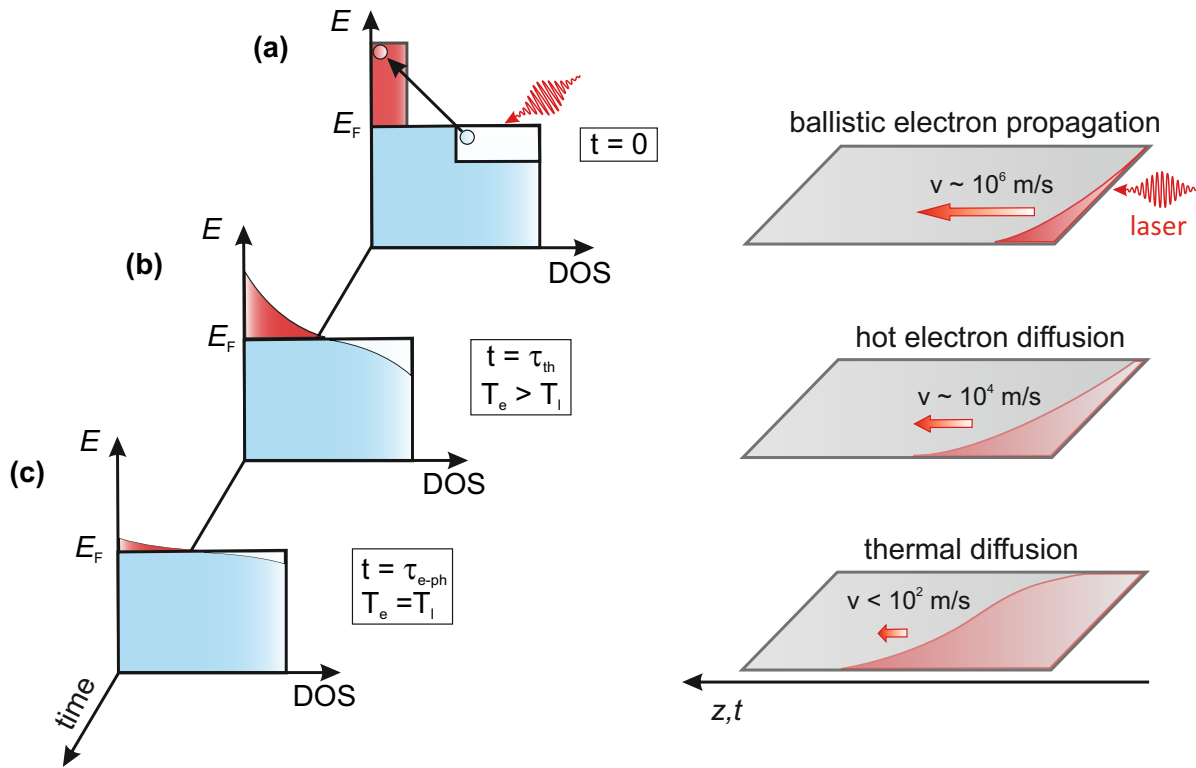
Figure 2-9: Nonequilibrium dynamics of hot electrons after photoexcitation of metallic surface by an ultrashort laser pulse: Three different relaxation phases of optically excited electrons in metals. The figure is modified and reprinted with permission from J. Hohlfeld et al. Electron and lattice dynamics following optical excitation of metals. *Chem. Phys.* 251, 237-258 (2000). DOI: https://doi.org/10.1016/S0301-0104(99)00330-4. Copyright © 2000 by Elsevier. Ref. [76].

Fig. **2-9**(b, left) shows the case, in which non-equilibrated electrons will again tend toward thermal equilibrium by scattering processes. The duration from optical excitation to a thermal distribution is denoted as the thermalization time τ_{th}. There is no uniform definition for this, and in fact, there are a number of different criteria [45, 49]. However, during thermalization hot electron density at higher-lying energy states decreases due to down-scattering events, which increases the population at lower-lying unoccupied and occupied states. Simultaneously, upwards-scattered secondary electrons are generated and contribute to the increase in hot electron density near the Fermi edge E_F, as sketched in Fig. **2-8** bottom. A Fermi distribution is formed with a well-defined electron temperature T_e, which is initially very different from the lattice temperature T_l according to the two-temperature model[3].

---

[3]This concept of separate, transient electron and lattice temperatures, T_e and T_l, provides the basis of the well-known two-temperature model (2TM).

The electron temperature T_e is defined by the electron heat capacity and the absorbed pulse energy. As the electron heat capacity is 1-2 orders of magnitude smaller compared to the lattice, the electron temperature T_e can reach several thousand Kelvin within 1 ps while the lattice remains relatively cold, $T_e > T_l$ [49, 76]. In terms of electron transport, see Fig. **2-9**(b, right), the e-e scattering processes impede the ballistic propagation, and diffusive hot electron propagation occurs at a lower velocity ($v < 10^4$ m/s) than ballistic motion.

Fig. **2-9**(c, left) shows the case where the electron temperature cools due to e-ph coupling and the electrons reach equilibrium with the lattice temperature ($T_e = T_l$) at $t = \tau_{e-ph}$. As a result, multiple scattering occurs, and energy transport occurs by very slow thermal diffusion in the lattice ($v < 10^2$ m/s), as illustrated in Fig. **2-9**(c, right).

Transport from the sample surface, where electrons are probed in 2PPE, to the interior of the sample is an important relaxation channel for hot electrons competing with e-e scattering. It has been reported that at time scales $t < 100$ fs, hot electron transport in sp-metals proceeds in the ballistic region with a Fermi velocity $v_F \approx 1$ nm/fs [27, 78, 79]. In noble metals such as gold (Au), ballistic propagation can extend to the mean free path of $\lambda_{bal}(Au) \approx 100$ nm [76]. Further calculations have shown that the approximate mean free path of other sp-band metals corresponds to $\lambda_{bal}(Cu) \approx 70$ nm and $\lambda_{bal}(Ag) \approx 70$ nm [14, 76]. In the case of d-band transition metals, the estimated mean free path λ_{bal} is drastically reduced due to the large phase space for electron scattering, e.g., $\lambda_{bal}(Fe) \approx 3 - 5$ nm, $\lambda_{bal}(Ni) \approx 10$ nm, and $\lambda_{bal}(Cr) \approx 14$ nm [80]. Moreover, it can be concluded that the electron-phonon coupling is stronger in transition metals, so the energy transfer from the electronic system to the lattice is probably faster [76].

However, one of the differences between noble metals and 3d ferromagnets (FM) lies in the exchange splitting in the band structure of 3d FM such as Fe, Co, and Ni [14, 80]. Electron majority and minority sub-bands are generated so that optical pumping leads to the excitation of majority $e^\uparrow$ and minority $e^\downarrow$ electrons to the states with different binding energies, lifetimes, velocities and ballistic electron mean free path λ_{bal}. Thus, the values mentioned above for the electron mean free path has to be treated cautiously and an energy dependence has to be considered. Calculations by Zhukov et al. [80] and Battiato et al. [32] show the energy- and spin-dependent lifetime, velocity, and inelastic mean free path λ_{bal} of hot charge carriers for different metals. Furthermore, Battiato et al. have constructed a theoretical model describing the energy- and spin-dependent interplay among local relaxation and nonlocal transport dynamics in FM/NM heterostructure thin films, as shown below.

2.3.3. Superdiffusive hot electron transport

Battiato et al. introduced a superdiffusive transport model, which incorporated the energy- and spin-dependency of hot electron scattering mechanisms, lifetime, inelastic mean free

path, and transport behavior [32]. It describes the measured ultrafast demagnetization processes in FM/NM heterostructures [28, 81]. The computed spin dynamics show that upon laser excitation of the ferromagnetic layer, a superdiffusive spin current is injected into the adjacent metallic layer. The transport exhibits anomalous behavior that can not be attributed to a ballistic or diffusive regime. To distinguish ballistic, superdiffusive, and diffusive electron transport behavior, Battiato et al. [82] discussed, as shown in Equation 2-9, the variance σ^2 of the displacement of a single-particle distribution with density n in space along a direction z and t:

$$\sigma^2(t) = \int n(t, z) \, (z - z_0)^2 \, dz. \tag{2-9}$$

It should be noted that the calculation of dispersion in this equation is only in the z-direction, while the transport of particles is three-dimensional in all directions. The dynamical particle distribution $\sigma^2(t)$ is defined, as shown in Equation 2-10, by the generalized diffusion coefficient K_w and the anomalous diffusion exponent d_w:

$$\sigma^2(t) = K_w \, t^{2/d_w}. \tag{2-10}$$

Figure **2-10** shows the calculated transient evolution of the anomalous diffusion coefficient d_w, which Battiato et al. used to describe the transport behavior of photoexcited hot electrons in FM/NM heterostructures for time scales from 1 fs to about one ps. Thermal diffusion processes are characterized by a σ^2 that grows linearly with time, i.e., $d_w = 2$. For sufficiently short times, $t \ll \tau$, with τ the scattering time (or inverse scattering rate), the particle distribution spreads ballistically because no scattering has yet occurred. This regime can be described by $d_w = 1$. With increasing time, particles experience single scattering events, leading to a transition from ballistic to diffusive propagation. This transition range is referred to as the superdiffusive regime and is characterized by $1 < d_w < 2$. For times $t \gg \tau$, the number of scattering events increases, and the propagation becomes diffusive once the electron distribution has thermalized. Additionally, noteworthy is the research conducted by Nenno et al. [83], where they employed a spin-dependent particle-in-cell PIC model to investigate the spin- and energy-dependent relaxation dynamics of hot electrons in the Au/Fe heterostructure. Their findings also supported the observation of superdiffusive transport behavior of hot electrons.

Previous experimental works have explored the local and nonlocal relaxation dynamics of hot electrons in the constituents or at the interfaces of metallic nanostructures [27, 46, 47]. Experiments with different metal layer thicknesses on the nanometer scale showed the important role of transport effects in the relaxation dynamics of hot electrons, which will be discussed below.
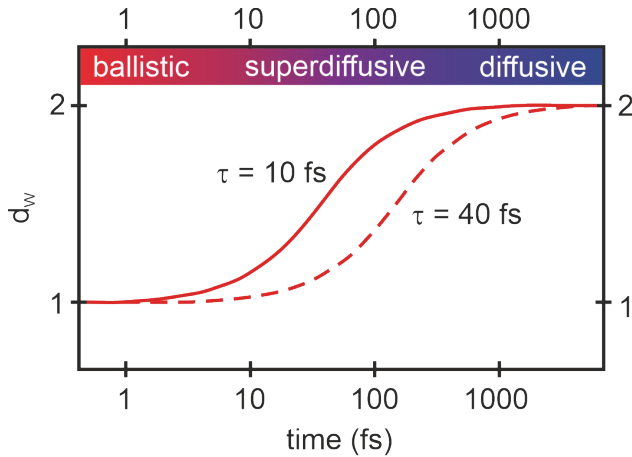
Figure 2-10: Time evolution of the anomalous diffusion coefficient d_w for the lifetime $\tau = 10$ fs (solid curve) or $\tau = 40$ fs (dashed curve) and the three different transport regimes. While the transport of hot electrons is initially ballistic, it changes to superdiffusive or diffusive transport behavior after a few or many scattering events, respectively. The figure is modified with additional text to highlight the transport regimes and reprinted with permission from Battiato et al. Theory of laser-induced ultrafast superdiffusive spin transport in layered heterostructures. *Phys. Rev. B*, 86, 024404 (2012). DOI: https://doi.org/10.1103/PhysRevB.86.024404. Copyright © 2012 by the American Physical Society. Ref. [82].

2.4. Hot electron relaxation dynamics & film thickness effect

Time-resolved optical and PES experiments were used to investigate the local and nonlocal relaxation dynamics of photoexcited hot charge carriers in thin metal films. It has been revealed that a significant thickness dependence occurs in the energy-dependent relaxation dynamics [27, 34, 46, 47, 69, 78, 84]. Based on those previous studies, this section showcases the film thickness dependence and the influence of the excitation schemes such as front-side pumping (FP) or back-side pumping (BP) on the scattering and transport dynamics of non-equilibrated electrons in thin metallic films.

Front-side pump approach and relaxation dynamics

Many studies have analyzed the dynamics of hot electron relaxation based on the FP experimental geometry [46, 47, 78]. The irradiation of a metallic surface by an ultrashort laser pulse leads, within the optical penetration depth λ_{opt} of the laser light[4], to the excitation of hot electrons near the surface region. The gradient in hot electron density at the metallic surface leads to electron transport into the bulk. For a typical electron velocity of $v \sim 1$ nm/fs, the characteristic distance of 10 nm is covered within 10 fs, which resembles a time scale comparable to the inelastic lifetime at optical excitation energies [69]. The crucial param-

---

[4]The optical penetration depth λ_{opt} for visible laser light is of the order of 10 nm in metals.

eter for the relevance of transport in a tr-2PPE experiment is the electron mean free path $\lambda_{bal} = \tau_{e-e}\, v$, which is governed by elastic, quasi-elastic and inelastic scattering dynamics. These transport processes decrease the excited population in the surface region probed in the tr-2PPE experiment and affects the detected lifetime signal [67].
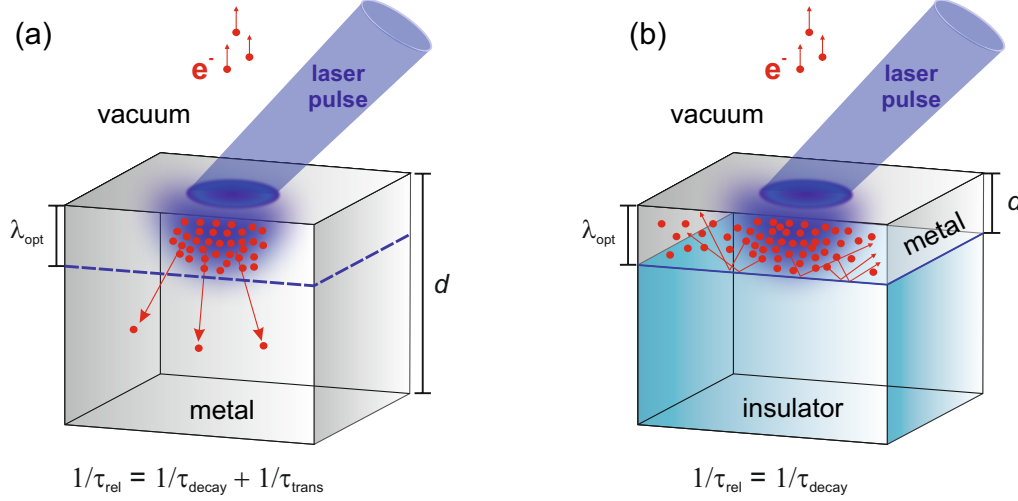
Figure 2-11: Thickness-dependent effects on hot electron relaxation dynamics: (a) Schematic representation of the transport effect in a 2PPE experiment for a thick sample $(d > \lambda_{opt})$. Hot electrons (red circle) are able to propagate out of the sample surface toward the bulk. (b) Thin metallic film $(d \leq \lambda_{opt})$ on an insulator leads to reduced or even suppressed transport processes.

Figure **2-11** showcases the hot electron relaxation dynamics for (a) thick and (b) thin metallic films. In thicker films, where the film thickness d exceeds the optical penetration depth λ_{opt} of the laser light $(d > \lambda_{opt})$, the photoexcited electrons (red circles) move out of the surface region toward the bulk. These transport processes out of the probed surface region affect the lifetime by representing an additional decay channel for hot electrons at the sample surface. Thus, if refilling processes (cascade and Auger electrons) are excluded, and separate mechanisms for decay and transport are assumed in a first-order approximation, we can add the measured decay rate according to the Matthiessen rule:

$$\frac{1}{\tau_{rel}} = \frac{1}{\tau_{trans.}} + \frac{1}{\tau_{decay}} \tag{2-11}$$

For thin metal films in the order of the optical penetration depth $(d \leq \lambda_{opt})$, as shown in Figure **2-11**(b), transport out of the surface region is inhibited by an insulating substrate. Thus, the hot electrons remain in the optical probing depth, and the effective relaxation rate is given by

$$1/\tau_{rel} = 1/\tau_{decay}. \tag{2-12}$$

The film thickness-dependent hot electron relaxation dynamics are reflected in the measured lifetimes of epitaxial Cu films on Si(111)-7×7 heterostructures obtained by Lisowski et al. [46]. The measured lifetimes are plotted as a function of the intermediate state energies $E - E_F$ for different Cu thicknesses, see Figure **2-12**.

The increasing Cu film thickness shows a significant decrease in hot electron lifetime. This relaxation behavior shows an enhanced energy distribution in thicker films due to the transport of excited carriers into the bulk. A similar thickness-dependent relaxation dynamics of hot electrons in Au layers was observed by Aeschlimann et al. [47]. In this study tr-2PPE data from Au were compared with simulations that considered, within a Boltzmann equation approach, secondary electrons and transport. The simulations confirm the increase in the lifetime as the film thickness decreases. Both works [46] and [47] see the hot electron
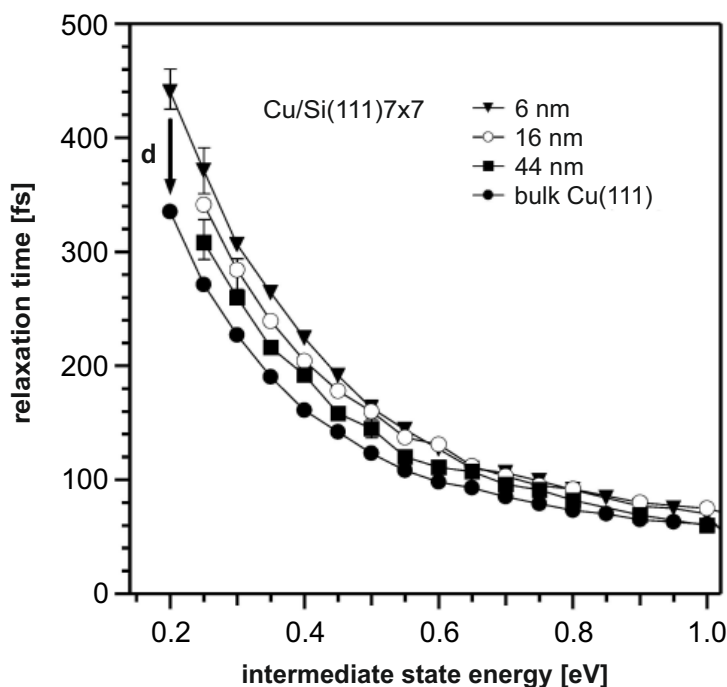
Figure 2-12: Relaxation times of photoexcited electron distributions in Cu/Si(111)-7×7 films and bulk Cu. Reprinted with permission from Lisowski et al. Femtosecond dynamics and transport of optically excited electrons in epitaxial Cu films on $Si(111) - 7 \times 7$. *Appl. Phys. A* 79, 739–741 (2004). DOI: https://doi.org/10.1007/s00339-004-2591-4. Copyright © 2004 by Springer Nature. Ref. [46].

transport as a scattering-out phenomenon, which leads to hot electron population decay at the sample surface and, thus, showcases an additional decay channel beside the pure relaxation time of the specific energy state. Noteworthy to mention, secondary electrons may play a significant role in the population dynamics as scattering-in processes, particularly at intermediate state energies $E - E_F < h\nu/2$, as discussed in section 2.3.
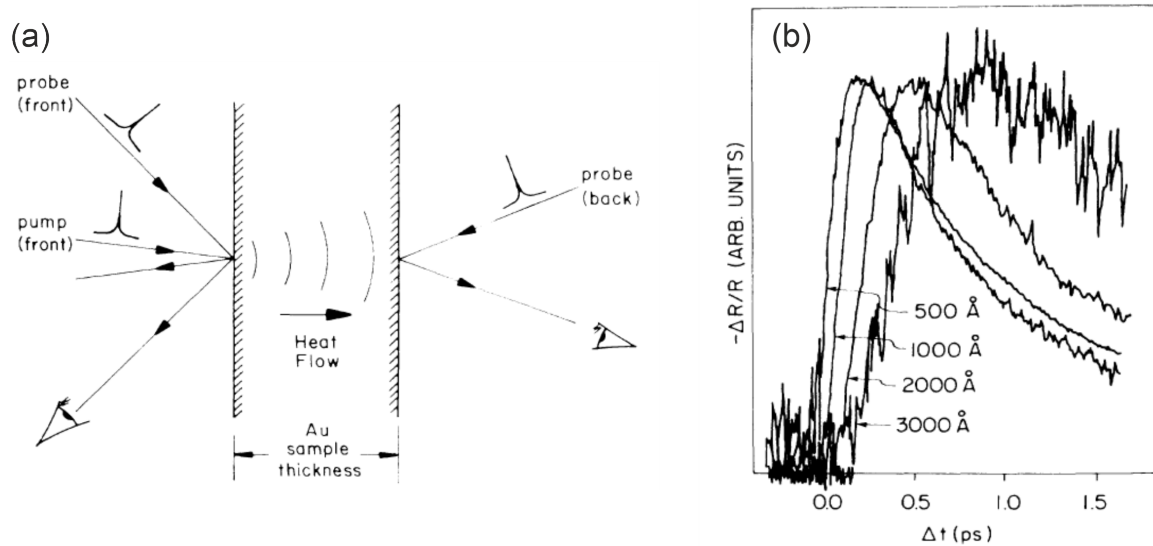
Figure 2-13: Front-side pumping back-side probing on Au thin films. (a) Schematic of the experimental setup for pumping on the front surface, and the front- or back-side probed surface. (b) The transient change in reflectivity $\Delta R/R$ for various Au film thicknesses. Both figures are reprinted with permission from Brorson et al. Femtosecond electronic heat-transport dynamics in thin gold films. *Phys. Rev. Let.* 59, 1962 (1987). DOI: https://doi.org/10.1103/PhysRevLett.59.1962. Copyright © 1987 by American Physical Society. Ref. [27].

Until now, the local relaxation dynamics at the surface and the nonlocal transport processes determined by the experimental FP configuration had to be indirectly distinguished by additional theoretical calculations [47, 49, 78]. To disentangle both processes that occur on the same time scale is challenging. A direct way to measure and observe hot electron transport processes in metallic thin films was introduced by Brorson et al. with the BP experimental configuration [27], presented below.

Back-side pump approach and relaxation dynamics

The study by Brorson et al. from 1987 [27] represents the first measurement of ultrafast electronic transport in Au thin films after laser pulse excitation. Figure **2-13**(a) shows that ultrafast time-resolved optical reflectivity measurement was performed for various Au thicknesses from 50 to 300 nm using front-side pumping and back-side probing experimental geometry.

This experimental geometry allowed measurements of the fast 'heat' transport from the front-side to the back-side of the sample. This was a time-of-flight measurement, as depicted in Figure **2-13**(a). The thickness-dependent measurement shows a time shift of the rising edge in the transient reflectivity changes $\Delta R/R$ curves. From the analysis of the travel

time as a function of sample thickness, they inferred a ballistic propagation behavior of hot electrons with a velocity on the order of the Fermi velocity $v_F \approx 1.4$ nm/fs. The technique of Brorson et al. of front-side pumping and back-side probing introduced a novel tool for studying electronic transport processes in the fs range with ultrashort laser pulses.
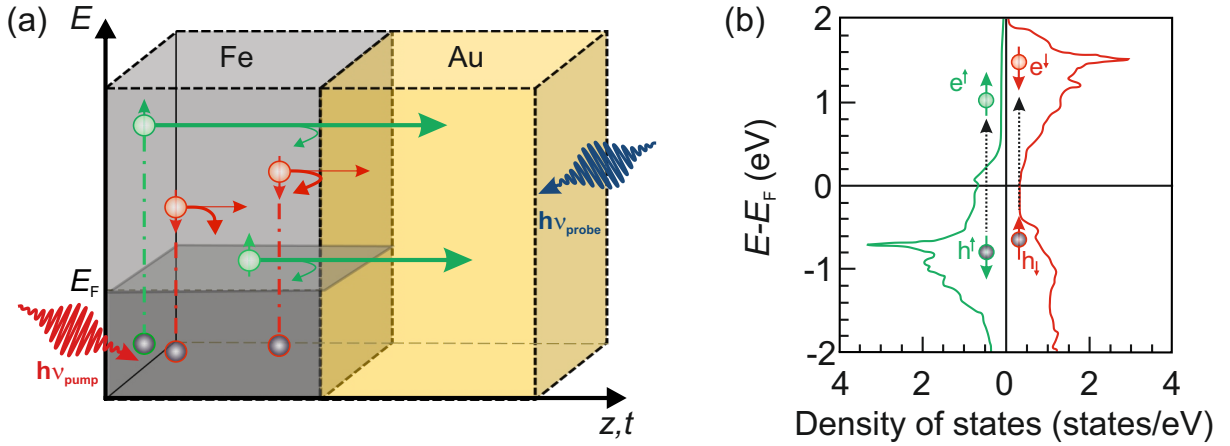
Figure 2-14: (a) Scheme of back-side pumping tr-2PPE on Fe/Au heterostructure and the generation of nonlocal spin transport and local scattering processes in the constituents or at the interface of the Fe/Au heterostructure. Hot majorities $e^\uparrow$ (green) and minorities $e^\downarrow$ (red) are excited above E_F by a VIS pump pulse (vertical dashed lines). The photoexcited charge carriers experience transport effects toward the Au surface, which are represented by horizontal arrows. The thickness of the arrows shows the dominating relaxation process in the constituent or at the interface of the Fe/Au heterostructure. The nonlocal transport process towards the Au surface results in the accumulation or filling of hot electron population in the vicinity of the probed region.(b) Electronic density of states (DOS) of Fe in the majority (green) and minority (red) sub-bands redrawn based on Ref. [29] with permission from Dr. A. Alekhin. Photoexcitation (dashed black arrows) of majority $h^\uparrow$ and minority $h^\downarrow$ holes below the Fermi energy E_F, and majority $e^\uparrow$ and minority $e^\downarrow$ electrons above the Fermi energy E_F.

This preliminary work was followed by studies that built on this experimental approach. Melnikov et al. performed magnetization-sensitive nonlinear optical measurements on epitaxially grown Au/Fe/MgO(001) thin films [34]. Their results indicate the optically induced spin-dependent transport of Fe-majority $e^\uparrow$ and -minority $e^\downarrow$ electrons, as sketched in Figure **2-14**(a). According to their work, during time-resolved pumping on the Fe-side and probing on the Au-side, hot $e^\uparrow$-majority and $e^\downarrow$-minority electrons are excited in the Fe layer and propagate in different manners across the Fe/Au interface to the Au surface. They attributed, due to the larger $e^\uparrow$-transmission compared to the $e^\downarrow$-transmission across the Fe/Au
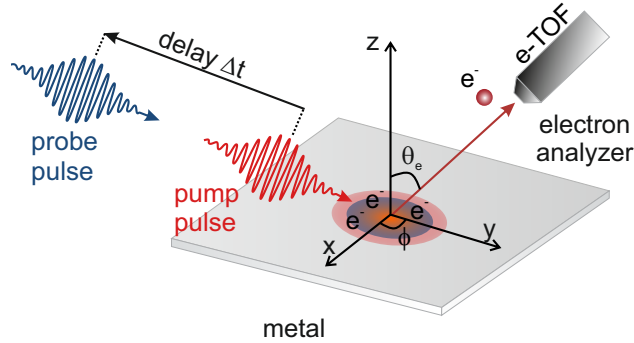
Figure 2-15: Schematic representation of time-resolved pump-probe photoelectron spectroscopy on a metallic surface. A pump pulse photoexcites a hot electron, which is subsequently photoemitted by a time-delayed UV probe pulse, whereupon the kinetic energy E_{kin} is analyzed by an electron time-of-flight spectrometer (e-TOF). The electron photoemission proceeds in a certain direction with respect to the sample surface defined by the angles θ_{e} and ϕ.

interface [35], the detection of an ultrafast spin current at early times to hot majority $e^{\uparrow}$ electrons from the sp-band. The velocity of this ultrafast spin current was of the order of the Fermi velocity $v_{\mathrm{F}} \sim 1.4$ nm/fs in Au and thus represented ballistic transport behavior. Moreover, a second, temporally broader spin current pulse was detected at later times and interpreted as a diffusive contribution of minority electrons $e^{\downarrow}$ from the Fe d-band. However, optical pump-probe experiments provide energy- and momentum-integrated information about the relaxation dynamics of hot electrons. Due to the energy-dependent dynamics of hot electrons, pump-probe photoemission experiments, such as Fe-side pumping Au-side probing tr-2PPE, can provide energy-resolved information on local scattering and nonlocal transport effects. Figure **2-14**(b) illustrates the DOS of majority (green) and minority electrons (red) in Fe, which will be important in understanding the studied energy-dependent electron relaxation dynamics in Fe/Au heterostructure in chapter 4. Note that in the case of tr-2PPE with Au-side pumping (FP) geometry, the transport process refers to the decay of the hot electron population at the probed Au surface region. On the other hand, in the case of Fe-side pumping (BP), the nonlocal transport process acts as a filling mechanism for hot electrons. In the next section, we will discuss the fundamentals of photoelectron spectroscopy.

2.5. Photoelectron spectroscopy

The theoretical explanation of the photoelectric effect by Albert Einstein in 1905 [85], building on the earlier observations by Heinrich Hertz in 1887 [86] and the experimental work of Philipp Lenard in 1902 [87], paved the way for the development of the time-resolved pump-probe technique with ultrashort laser pulses and the state-of-the-art technology of ultrafast pump-probe photoelectron spectroscopy (PES).
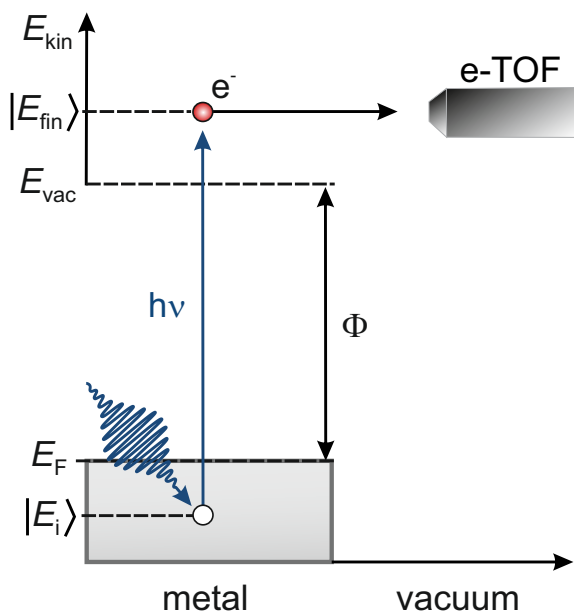
Figure 2-16: Energetic representation of the direct photoemission process when a metallic surface is irradiated by a laser pulse. When the photon energy $h\nu$ exceeds the work function Φ and the binding energy of the excited electron, direct photoemission occurs. The electron is emitted from an occupied initial state $|E_i\rangle$ below E_F to a final state $|E_{fin}\rangle$ above the vacuum energy level E_{vac} and propagates out of the sample into vacuum, where it is detected by a e-TOF analyzer.

As shown in Figure **2-15**, in time-resolved PES, hot electrons are photoexcited at a metallic surface by a VIS pump pulse, which are subsequently photoemitted by a time-delayed UV probe pulse. This technique enables the study of ultrafast charge carrier relaxation dynamics in condensed matter energy-resolved in the time domain [88, 89]. Moreover, angle-resolved photoelectron spectroscopy (ARPES) measurements allow imaging of electronic band structure in momentum-space [89]. Among the PES variants, there are two well-established techniques: Linear photoemission (LPE) and nonlinear two-photon photoemission (2PPE). This section is mainly concerned with the latter, which is used in this work.

2.5.1. Principles of photoelectron spectroscopy

The irradiation of a metallic surface by a photon with the energy $h\nu$ leads to the excitation of hot electrons to higher-lying energy states above the Fermi energy level E_F. If the photon energy $h\nu$ exceeds the sample work function Φ and the binding energy E_i of an initial occupied state with respect to E_F, the electrons are excited above the vacuum level E_{vac} into final states and no longer bound to the crystal atoms, see Figure **2-16**. The photoexcited electrons propagate in the solid to the surface[5], whereby the mean free path length determines the surface sensitivity to be 5 - 100 Å. The photoemitted electrons leave the sample with kinetic energy

---

[5]Three-step model of photoemission: (1) Photoexcitation of electrons, (2) propagation to the sample surface and (3) photoemission of an electron into the vacuum and propagation to the detector. In comparison, the 1-step model explains photoemission as the excitation of an electron wave from a Bloch state in the solid that propagates to the vacuum but decays away from the surface into the solid [89, 90].

$$E_{\text{kin}} = h\nu - \Phi - (E_{\text{i}} - E_{\text{F}}). \tag{2-13}$$

The kinetic energies E_{kin} are detected and analyzed by an electron TOF spectrometer, which provides together with a calculation program an energy-resolved photoemission spectrum. Hence, in angle-resolved measurements such as ARPES, a band structure of the investigated sample can be mapped out in the momentum-space k. This is possible since PES conserves the in-plane (parallel) momentum $\vec{k}_{\parallel}$[6], given by

$$k_{\parallel}(E_{\text{kin}}, \theta_{\text{e}}) = \frac{\sqrt{2m_e E_{\text{kin}}}}{\hbar} \sin\theta_{\text{e}}, \tag{2-14}$$

with the electron mass m_e, the reduced Planck constant $\hbar$ and the emission angle θ_{e} of the photoelectron. The reason is the translation invariance parallel to the surface, which is given by the periodic lattice structure. By measuring the angle at which the electrons leave the sample and considering their kinetic energy, the initial momentum component $k_{\parallel}$ parallel to the surface can be determined. Since the translational symmetry perpendicular to the surface is broken by the potential difference between the vacuum and the solid, the perpendicular momentum $k_{\perp}$ component changes as the electrons leave the surface. Therefore, $k_{\perp}$ can only be accurately determined by knowing the exact change in potential. This is not the subject of this work and is explained in detail in [89].

The photoemission intensity is described by

$$I(\vec{k}_{\parallel}, E_{\text{kin}}) = M\, f(E, T)\, A(\vec{k}_{\parallel}, E), \tag{2-15}$$

with transition dipole matrix element M, the Fermi-Dirac distribution function f with temperature T, and single particle spectral function $A(\vec{k}, E)$ which is directly connected to the Green's function

$$A(\vec{k}, E) = \frac{1}{\pi}\text{Im}(G(\vec{k}, E)) = \frac{1}{\pi}\frac{\Gamma}{(E - E_{\text{i}})^2 + \Gamma^2}. \tag{2-16}$$

The last term is the spectral function in the case of a single quasi-particle signature with binding energy E_{i} and intrinsic linewidth Γ. The photoemission process demonstrates an electron removal spectroscopic technique, which does not directly measure the electron energies of the unperturbed N particle system but the energy of N-1 particle system, where one electron has been removed. The description of the photoemission process is rather complex, yet theoretical approximations make it feasible to describe the ultrafast process. At the heart of all theories of photoemission is the so-called sudden approximation. This approach assumes that the photoemission process, which connects the initial N-particle to the final

---

[6]The photoemission process conserves the parallel momentum as long as the momentum of the photon is smaller than the Brillouin zone $2\pi/a$ (lattice constant a) and there is no scattering in the final state.

N-1 electron state, occurs much faster than the relaxation of the excited N-1 electronic state [70, 89].
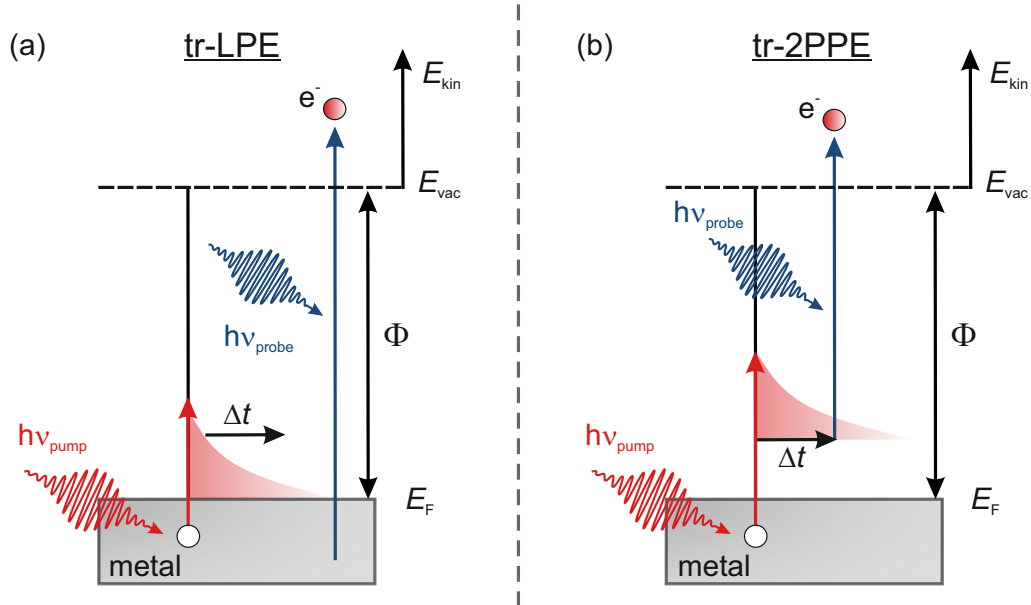
Figure 2-17: (a) Time-resolved LPE: An intense visible (VIS) pump pulse $h\nu_{\text{pump}}$ generates hot electrons above E_{F}. A time-delayed UV pulse with $h\nu_{\text{probe}} > \Phi$ probes the transient change of the occupied band structure and the unoccupied states in the vicinity of E_{F}. (b) Time-resolved 2PPE: In contrast to LPE, the pump and probe photon energies are smaller than the work function Φ. Hence, the hot electrons are excited to higher NEQ states and probed by a time-delayed UV pulse.

The linear photoemission technique (LPE) in Figure **2-17**(a) represents a PES variant based on the direct photoemission technique and enables the analysis of occupied and unoccupied states in the vicinity of E_{F} of the electronic band structure. In direct photoemission, only one photon is needed to excite the electron from below E_{F} to above E_{vac}. Thus, an essential condition is a photon energy that exceeds the work function and the binding energy with respect to E_{F} of the occupied state; $h\nu > \Phi + E - E_{\text{F}}$.

In time-resolved LPE, the ground state of a system is photoexcited by an intense fs pump laser pulse, and the transient evolution of the occupied states is monitored by direct photoemission with a time-delayed probe pulse. Photoexcitation of hot electrons above the Fermi edge E_{F} is accompanied by depletion of electrons below E_{F}, which are called holes. Thus, time-resolved LPE allows the study of ultrafast relaxation dynamics of photoexcited electrons and holes in the NEQ state and their coupling with quasi-particles such as phonons near E_{F} [54, 91–93]. However, in this work, the results are obtained only by the time-resolved nonlinear 2PPE technique, as outlined in Figure **2-17**(b). This technique facilitates the study of hot electron relaxation dynamics in unoccupied states in Au/Fe/MgO(001) thin

film heterostructures. Therefore, the 2PPE method is the subject of the following section and will be described in more detail.

2.5.2. Two-photon photoelectron spectroscopy

Electronic states in solids and at solid surfaces have been studied comprehensively and extensively by photoemission measurements. The equilibrium electronic band structure is broadly studied by direct photoemission. For analyzing the unoccupied part of the electronic band structure, a well-known spectroscopic technique is the inverse photoemission (IPES) [94]. However, the limited energy resolution of this technique prompted the search for another method with better resolution. The two-photon photoemission technique offers high energy resolution and applicability to the range between E_{F} and E_{vac} [59, 61, 95]. Subsequently, two-photon photoelectron spectroscopy has been successfully applied in various measurements and developed into a powerful tool for investigating hot charge carrier relaxation dynamics in the nonequilibrium state [15, 46, 47, 61, 84, 96, 97].

Within the 2PPE process, an ultrashort pump pulse ($h\nu_{\mathrm{pump}} < \Phi$) excites a cold electron from the occupied states below the Fermi level E_{F} to the intermediate state energies above E_{F}. A second probe pulse ($h\nu_{\mathrm{probe}} < \Phi$) photoemitts the hot electrons into states above the vacuum level E_{vac}, which is subsequently analyzed by an electron time-of-flight spectrometer (e-TOF). Thus, the stringent conditions for a 2PPE process are that (i) the pump and probe photon energies have to be smaller than the work function, and on the other hand, the sum of both photon energies has to overcome the work function:

$$h\nu_{\mathrm{pump,probe}} < \Phi \ \text{ and } \ h\nu_{\mathrm{pump}} + h\nu_{\mathrm{probe}} > \Phi. \tag{2-17}$$

Consequently, direct photoemission processes are prohibited and only second (or higher order) processes can be detected, which involve intermediate unoccupied states. Thereby, involves the two-step nature of the 2PPE process different excitation mechanisms of the intermediate states $|im\rangle$ as shown in Figure **2-18** based on [70].

1. Resonant excitation: A real intermediate state $|im\rangle$ is resonantly and directly excited if the energy of the pump photon is equal to the energy between the occupied initial state $|i\rangle$ and the unoccupied intermediate state $|im\rangle$: $h\nu_{\mathrm{pump}} = E_{\mathrm{im}} - E_{\mathrm{i}}$. A second pulse probes the intermediate state, which generally shows an enhanced peak in the 2PPE spectrum, like the IPS state observed in our tr-2PPE experiment.

2. Non-resonant excitation: Indirect excitation of an intermediate state $|im\rangle$ is enabled by inelastic carrier scattering leading to occupation effects from another intermediate state. Such an excitation scheme is typical of a continuum of initial states and dispersion states, which allow excitation over a wide range of $k_{\parallel}$ and can lead to subsequent inter- and intraband scattering processes.
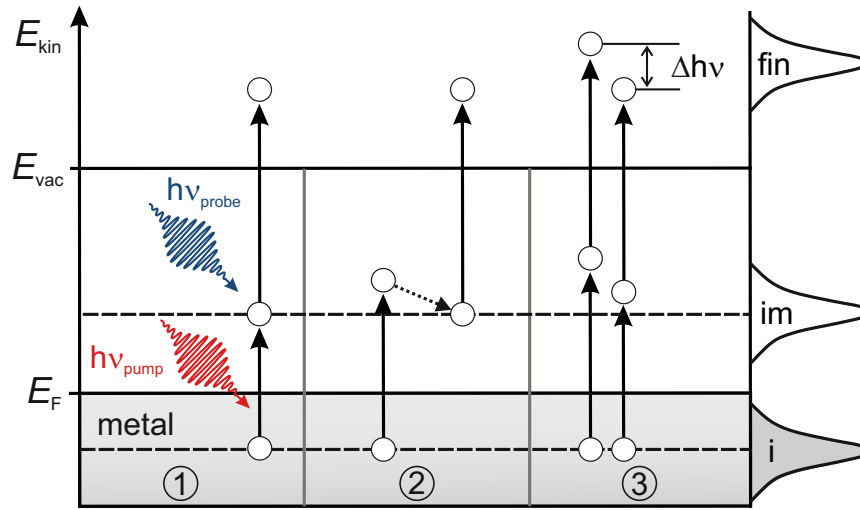
Figure 2-18: Excitation mechanisms of 2PPE involving discrete initial, intermediate and final states, noted with i, im and fin, respectively. (1) Resonant excitation, (2) Non-resonant excitation, (3) photoemission via virtual intermediate states. The figure is redrawn based on Ref. [70] with permission from Dr. P. Kirchmann.

3. Photoemission via virtual intermediate states occurs when both laser pulses in the 2PPE process overlap in time and a direct, non-resonant excitation process takes place. A characteristic of such virtual intermediate states is their infinitesimally short lifetime.

To determine whether a peak in a 2PPE spectrum originates from an initial, intermediate, or final state of the 2PPE process, one can vary the pump and probe photon energies independently and analyze the energy difference between the final states excited by $h\nu_{\text{pump}}$ and $h\nu_{\text{probe}}$. Here, $\Delta h\nu = h\nu_{\text{probe}} - h\nu_{\text{pump}}$ serves as a reference for identifying the origin of the measured spectral feature in a 2PPE spectrum:

- Initial state $|i\rangle$: If the peak in the 2PPE spectrum arises from an occupied initial state, photoemitted via virtual intermediate states, the electron kinetic energy scales linearly with each photon pulse, which would result in a final state energy difference of $2 \times \Delta h\nu$.

- Intermediate state $|im\rangle$: The kinetic energy of the photoemitted electrons from real intermediate states does not depend on the pump pulse energy and scales only linearly with the energy of the probe pulse, which would lead to an electron kinetic energy difference of $\Delta h\nu$.

- Final state $|fin\rangle$: The finale state energy is independent of the pump and probe photon energies, and thus no energy difference is expected; $0 \times \Delta h\nu$.

Energy scales in 2PPE
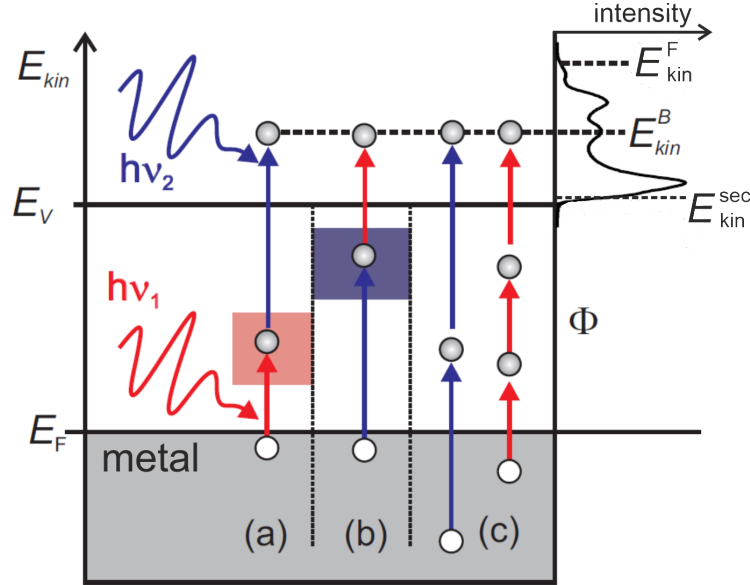
Figure 2-19: Static 2PPE photoemission processes with photon energies $h\nu_{1,2}$ less than the sample work function Φ; $h\nu_{1,2} < \Phi$. Bichromatic 2PPE processes with (a) VIS-pump ($h\nu_1$) and UV-probe ($h\nu_2$) sequence in which the excited unoccupied states are closer to E_F (red shaded area) with respect to (b) in which the pump-probe sequence is inverted and the excited unoccupied states are closer to the vacuum level E_V. (c) Monochromatic 2PPE and 3PPE for UV ($h\nu_2 = 4.2$ eV) and VIS ($h\nu_2 = 2.1$ eV) light pulses, respectively, in case of a sample work function $\Phi > 4.2$ eV. Top right: Static 2PPE spectrum with spectral features at kinetic energies excited from the Fermi edge E_{kin}^F, the initial occupied state with E_{kin}^B and low-energy cutoff at the secondary edge. The figure is adapted based on Ref. [98] with the permission by Dr. M. Sandhofer.

Figure **2-19** shows the 2PPE processes with different photon energies $h\nu_{1,2}$. The pump-probe mechanisms in Fig. **2-19**(a) and (b) represent the bichromatic 2PPE. In (a), a VIS pump pulse $h\nu_1$ excites an electron from initial occupied states $|E_i\rangle$ to unoccupied intermediate state energies $|E_{im}\rangle$. Subsequently, a second pulse $h\nu_2$ (UV) probes the photoexcited electron out of the sample to the final state $|E_{fin}\rangle$ above the vacuum level. The kinetic energy of the photoemitted electrons is then detected, and an energy-resolved photoemission intensity distribution can be displayed, as shown in Fig. **2-19** top right. In (b), the pump-probe sequence is inverted so that the UV light acts as the pump and the VIS light as the probe pulse. Depending on the initial energy state $|E_i\rangle$ from which the electron is excited, it can populate various unoccupied states. This process is illustrated by the red shaded area in the case of a VIS pump-UV probe sequence. In the case of the UV pump-VIS probe scheme, a photoexcited electron can populate unoccupied states at higher lying intermediate state energies $|E_{im}\rangle$, see the blue shaded area in (b). The available energy window of the

unoccupied nonequilibrium states (red or blue shaded area) can be calculated as follows

$$E_{\mathrm{kin}}^{\mathrm{F}} - E_{\mathrm{kin}}^{\mathrm{sec}} = h\nu_{\mathrm{pump}} + h\nu_{\mathrm{probe}} - \Phi \tag{2-18}$$

It is also worth noting that from this Equation 2-18 one can calculate the work function Φ of the sample. Figure **2-19**(c) shows the monochromatic 2PPE or three-photon processes for UV and VIS light pulses, respectively. These processes occur only for the respective VIS and UV pulses and contribute as a background signal to the time-correlated photoemission signal, which is briefly described in the following section on time-resolved 2PPE. The 2PPE spectrum in the top right of Fig. **2-19** shows different spectral features as a function of the kinetic energy E_{kin} of photoemitted electrons. The position of the secondary edge at $E_{\mathrm{kin}}^{\mathrm{sec}}$ stems from scattered secondary electrons that have just overcome the work function Φ. The electrons photoemitted from virtual intermediate states near the Fermi edge E_{F} exhibit the photoelectrons with the highest kinetic energy $E_{\mathrm{kin}}^{\mathrm{F}}$ in the spectrum. To determine the correct binding energy of an intermediate state, one must know the pump-probe sequence in the 2PPE process. The sequence of the pump-probe scheme with VIS and UV light can be derived by time-resolved 2PPE measurements, which are shown below.

2.5.3. Time-resolved two-photon photoemission

Electrons excited to unoccupied states a few eV above the Fermi energy E_{F} experience ultrafast scattering processes in the fs time regime [17,88]. Time-resolved 2PPE spectroscopy provides the tools for studying ultrafast hot electron dynamics with its fs-resolved pump-probe technique. It allows the recording of a correlated signal as a function of the pump-probe time delay t, which is varied by changing the optical path length between the pump and probe pulses with a delay step. To determine the intermediate state energy $E - E_{\mathrm{F}}$ of the photoemitted electron, one needs to know the pump-probe sequence involved in the 2PPE process. Figure **2-20** demonstrates the bichromatic time-resolved 2PPE with different pump-probe sequences. For neg-

Figure 2-20: Time-resolved 2PPE scheme with different pump-probe sequences, adapted from Ref. [70] with permission from Dr. P. Kirchmann.

ative delay times the UV pump pulse, $h\nu_2$, excites the hot electrons and the subsequent VIS pulse, $h\nu_1$ probes the transient hot electron population dynamics. In the reversed positive

delay times, the pump-probe sequence is inverted and the VIS pulse precedes the UV pulse. A prerequisite for obtaining the correlated signal in time-resolved 2PPE experiments is the spatiotemporal overlap of the VIS and UV pulses on the sample, as described in chapter 3. Figure **2-21**(a) shows the time-correlated 2PPE yield as a function of the pump-probe time delay t and the intermediate state energy $E - E_F$ for Au thickness $d_{\mathrm{Au}} = 10$ nm in the case of the FP experimental geometry. The time zero, $t = 0$ fs, is defined by considering the first detected electrons in the e-TOF spectrometer, which represent the photoelectrons with the highest kinetic energy. Performing a Gaussian fit to the hot electrons with the highest intermediate state energy $E - E_F \approx 2.1$ eV (red axis) gives time zero and full width at half maximum (FWHM) of the cross-correlation (XC) of both laser pulses.

Based on the direction in which the population decays, the pump-probe sequence for a spectral feature can be determined in the false-color plot. For example, at $E - E_F \approx 3.9$ eV (blue axis), an image potential state (IPS, n = 1) appears that decays to negative time delays, which was also observed in our previous work in Au/Fe/MgO(001) [84]. It should be noted that time zero in the case of BP was determined in the same way as for the FP 2PPE data to ensure consistency. We note that there is some ambiguity in this choice of time zero. In the case of Fe-side pumping (BP), a certain propagation time of the excited electron through the layer stack occurs before the electron is detected at the Au surface. For Au-side pumping (FP), the spectrally broad IPS feature at $E - E_F = 3.90$ eV could extend up to the top end of the spectrum. Consequently, the chosen time zero could be shifted to negative time delays due to the finite decay time of the IPS convoluted with the pulse duration, resulting in an effective shift of the intensity maximum, as the trailing part of the probe laser pulse contributes to the signal. To estimate this potential inaccuracy in the determination of time zero, we indicate in Figure **2-21**(a) the intensity maxima as a function of time delay for all energies by a solid red line. At $E - E_F = 1.5$ to 1.0 eV the maximum is shifted to $+10$ fs without a clear decay. We consider in the following that the actual time zero is uncertain within this interval of 0 to 10 fs.

Figure **2-21**(b) shows the transient population dynamics as a function of delay time t for different intermediate state energies $E - E_F = 3.9, 2.1, 1.0$ and 0.6 eV[7]. The transient XC traces were obtained by integration over the energy intervals of 100 meV. In general, the time-resolved 2PPE intensity $I^{\mathrm{2PPE}}(E, \Delta t)$ curves can be described by the

$$I^{\mathrm{2PPE}}(E, \Delta t) \propto \int F_{\mathrm{XC}}(t - \Delta t) R(E, t) \, dt, \qquad (2\text{-}19)$$

---

[7]Describing transient population dynamics of excited continuum metallic states is very complicated and can hardly be done within analytical models. However, quantization of the band structure and discrete states allows the description of a 3-level-system consisting of initial, intermediate and final states. Especially in non-resonant excitation, the Bloch equations simplify to a set of classical, coupled rate equations [70]. For a more detailed description of this approach, we refer to the works of [70, 99].
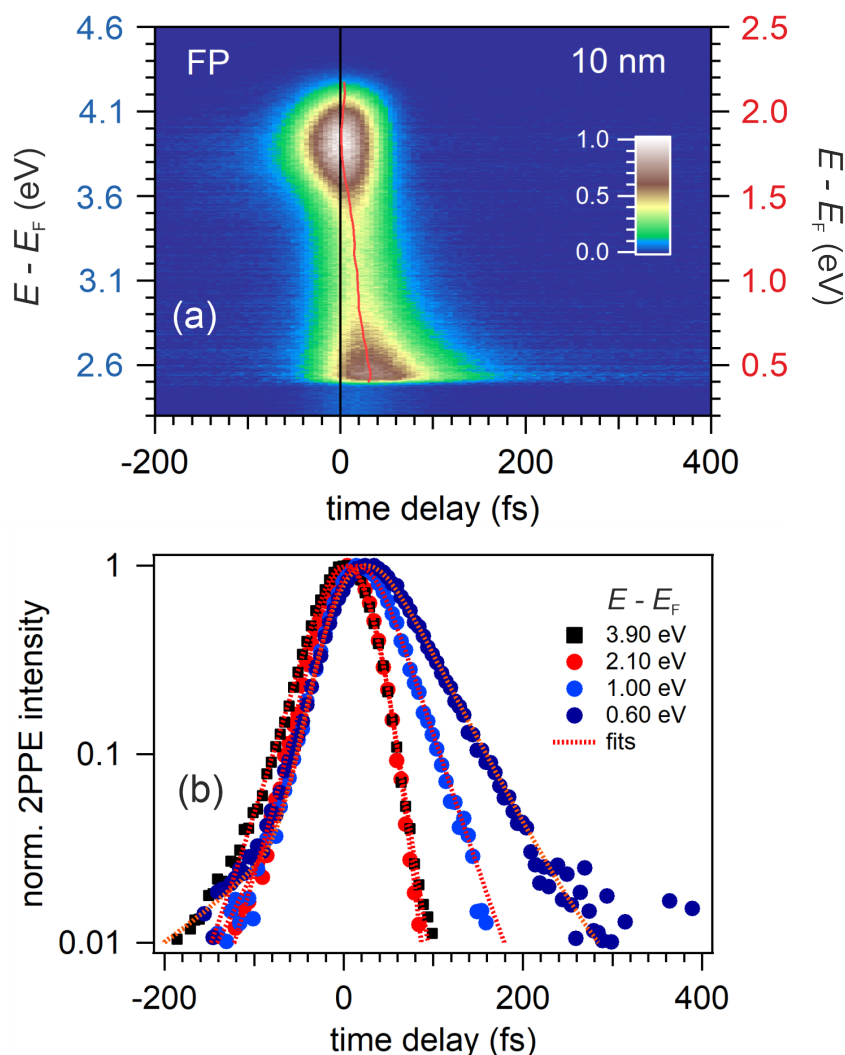
Figure 2-21: Time-resolved 2PPE on 10 nm Au/7 nm Fe/MgO(001) with FP geometry: (a) Time-correlated 2PPE yield as a function of pump-probe time delay (horizontal axis) and intermediate state energy $E - E_F$ (vertical axis) in a false-color representation. Normalization of the false-color map is done by dividing each 2PPE intensity by the maximum intensity. For negative time delays, $t < 0$ fs, the intermediate states are excited by the UV pulse ($h\nu_{UV} = 4.13$ eV), see blue vertical axis. For positive time delays, $t > 0$ fs, the pump-probe sequence is reversed and thus intermediate state energies are generated by the VIS pulse ($h\nu_{VIS} = 2.1$ eV), see the red vertical axis. On the right, the color bar shows the false-color scheme of the transient photoemission intensity. The red, solid line indicates the 2PPE intensity maxima for different energies with time delay. (b) Transient 2PPE intensity traces for different intermediate state energies $E - E_F = 0.6$, 1.0, 2.1 and 3.9 eV ($\blacksquare$: IPS, $n = 1$) extracted from the false-color plot in (a). Traces are fitted by a convolution of a Gaussian (XC function F_{XC}) and exponential decay function (dotted lines), which provides with $\tau(E)$ and time offset t_0 the observables for local and nonlocal relaxation dynamics, respectively.
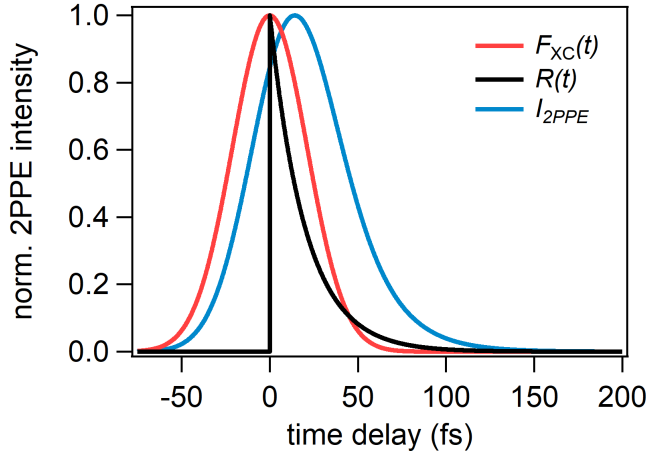
Figure 2-22: According to Equation 2-19; simulation of a time-resolved 2PPE yield $I_{2\text{PPE}}(\Delta t)$ as a function of pump-probe time delay Δt, which is obtained by a convolution of an exponential response function $R(t)$ (decay $\tau = 20$ fs) and a Gaussian laser pulse cross-correlation F_{XC} with FWHM = 50 fs.

whereby F_{XC} is the convolution of the two laser pulses assumed to be Gaussian[8] in time and $R(E, t)$ is the response function of the material under study at a specific energy E. As mentioned above, the XC function F_{XC} is determined by a Gaussian fit at large excess energies $E - E_{\text{F}} \approx 2$ eV. This is feasible since the excitation proceeds via virtual intermediate states without a finite lifetime. If the lifetime is infinitely small, the response function of the system is a δ-function. For the analysis of the 2PPE transients at specific intermediate state energies $E - E_{\text{F}}$ the response function is assumed to be an exponential decay function:

$$R(E, t) = \exp(-t/\tau(E)). \tag{2-20}$$

Figure **2-22** demonstrates a simulation of the transient 2PPE yield $I_{2\text{PPE}}$ (blue curve). This is obtained by a convolution of an exponential decay function $R(t)$ (black curve) with decay time $\tau = 20$ fs and a Gaussian XC function F_{XC} (red curve) with FWHM = 50 fs. The resulting transient 2PPE curve is temporally broader and its maximum is shifted toward positive delay times, which increases with an increased decay time τ. The measured 2PPE transients were fitted by a convolution of the XC function F_{XC} and two exponential decay functions, see the fits (red dotted lines) in Figure **2-21**(b). One of the exponential decays, toward negative Δt, accounts for the contribution excited by 4.2 eV photon, and the other one, decay toward positive Δt, excited by 2.1 eV photons. The data discussed in this thesis work will be analyzed by such fits for different Au film thicknesses d_{Au} and different experimental configurations. As shown in chapter 4 the analysis delivers intriguing insights into the hot electron local and nonlocal relaxation dynamics in Au/Fe/MgO(001) thin films.

---

[8]Ultrafast amplifiers provide laser pulses with Gaussian profiles [70].

3. Sample preparation and experimental details

In this work, the local and nonlocal relaxation dynamics of hot electrons in epitaxially grown Au/Fe/MgO(001) thin films are investigated energy-resolved in the time domain. To access these ultrafast dynamics, time-resolved two-photon photoelectron emission spectroscopy (tr-2PPE) was employed using fs pump-probe laser pulses with FP and BP experimental geometries. The measured 2PPE spectra obtained with both geometries are compared and analyzed as a function of Au layer thickness d_{Au}. This chapter provides insight into the preparation and characterization of the Au/Fe/MgO(001) thin film, the photoelectron spectrometer, and the laser setup with FP and BP experimental configurations. After describing the experimental setup in general, a novel approach (in our group AG Bovensiepen) to compress the laser pulses and the analysis by frequency-resolved optical gating (FROG) are presented.

3.1. Au/Fe/MgO(001) thin film preparation and characterization

Epitaxially grown Au/Fe/MgO(001) heterostructures with layer thicknesses of $d_{\mathrm{Au}} = 7 - 70$ nm and $d_{\mathrm{Fe}} = 7$ nm represent a suitable material system for the study of hot charge carrier local and nonlocal relaxation dynamics owing to the similar inelastic mean free path and layer thicknesses [34, 35, 80, 84]. An optically transparent MgO(001) substrate for an ultrashort laser pulse with the photon energy of $h\nu_1 = 2.10$ eV facilitates the Fe-side pumping and Au-side probing time-resolved 2PPE measurements. This drives the propagation of photoexcited electrons from Fe toward the Au layer surface across the Fe/Au interface. While the Fe layer acts as the optically excited electron emitter, the Au layer serves as the acceptor hosting electron propagation. A well-defined, sharp Fe/Au interface is expected to suppress inelastic processes such as hot electron scattering by lattice inhomogeneities.

The Au/Fe/MgO(001) thin films employed for the time-resolved 2PPE measurements with the FP and BP geometry were epitaxially grown by J.P. Meyburg, F. Kühne, and Dr. D. Diesing at the University of Duisburg-Essen in the department of Physical Chemistry. Two Au/Fe/MgO(001) samples have been prepared simultaneously. Firstly, a commercially

(b) Sketch of the material system with the wedge structure used for the AFM.

acquired MgO(001) substrate from MaTecK GmbH with the dimensions 10 mm × 10 mm × 0.5 mm thickness was cleaned in ultrasonic baths of ethanol, isopropanol, and acetone. Subsequently, it was put into an ultra-high vacuum and exposed to O_2 at a partial pressure of $2 \cdot 10^{-3}$ mbar at a temperature of 540 K to remove carbon contamination. By using the molecular beam epitaxy (MBE) under ultra-high vacuum (UHV, $\leq 10^{-9}$ mbar) conditions, Fe(001) and Au(001) thin films were grown on the MgO(001) substrate according to the procedures described in [100–102]. A sharp crystalline Au/Fe interface is achieved by well-matched lattice constants $a_{Fe} \approx 286$ pm and $a_{Au} \approx 288$ pm since the fcc-Au lattice is rotated by 45° with respect to the (001) in-plane of the bcc-Fe [34, 101, 103]. The resulting excellent interface qualities of the Au/Fe/MgO(001) thin films were shown by Melnikov et al. [34] using scanning transmission electron microscopy.

Furthermore, in Figure **3-1**(a) atomic force microscopy (AFM) image of the Au surface topography shows the growth of a 40 nm Au layer on Fe (right) compared to the growth on bare MgO substrate (left). F. Kühne has prepared the Fe layer as a wedge with linearly increasing d_{Fe} up to 7 nm as sketched in Figure **3-1**(b). While the Au topography on bare MgO(001) exhibits a relatively large surface roughness $\Delta_{rms} = \pm 12$ nm, the deposition of Au on Fe(001) shows a smoother Au surface with roughness $\Delta_{rms} = \pm 2$ nm. The crystalline (001)-orientation of Au is mainly achieved on the Fe(001) film, whereas on bare MgO the (111)-orientation prevails, as shown in reciprocal space maps in Mattern et al. [103].

3.1.1. Thickness determination of Fe and Au thin film layers

Figure **3-2** shows the schematic of the stepwise Au/Fe/MgO(001) sample, which has been employed for the time-resolved 2PPE measurements in this thesis work. The Au layer thickness d_{Au} varies between 5 to 70 nm, while the Fe layer thickness was kept constant at $d_{\mathrm{Fe}} = 7$ nm. The Fe layer thickness $d_{\mathrm{Fe}} = 7$ nm was measured by a commercial AFM (Bruker Dimension FastScan) with a deviation less than 10%, as was discussed in Florian Kühne's master thesis [104]. The determination of d_{Au} is based on time-of-flight secondary
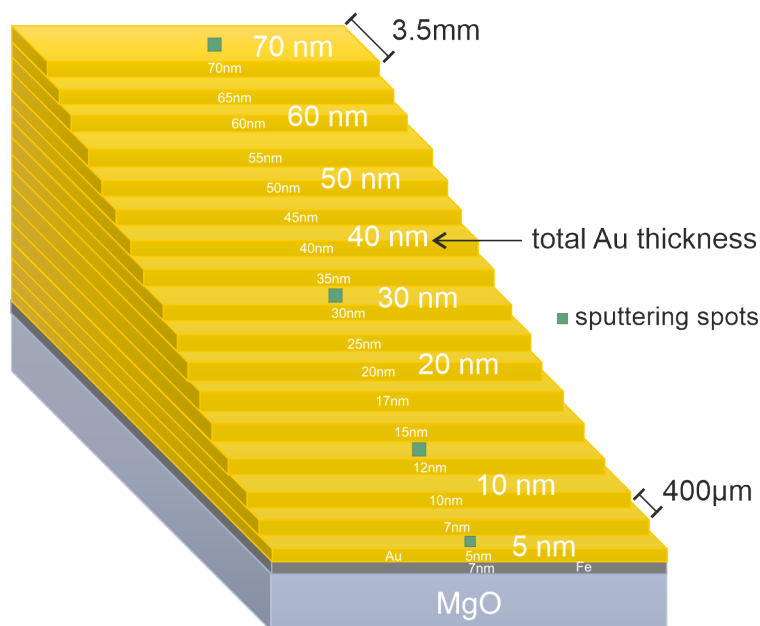
Figure 3-2: The stepwise design of the Au/Fe/MgO(001) sample with Au thicknesses $d_{\mathrm{Au}} = 5 - 70$ nm and a constant Fe thickness $d_{\mathrm{Fe}} = 7$ nm. The widths of the Au steps are 400 μm except at the 70 nm Au layer with 3.5 mm. Green sputtering spots: Measurement of Au thickness by ToF-SIMS technique. The image is designed by F. Kühne.

ion mass spectrometry ToF-SIMS, representing a powerful surface analysis technique with depth profiling capability [105, 106]. It can display the depth distribution of elements with a sub-nm resolution which is beneficial for layer thickness measurements of heterostructure material systems. The ToF-SIMS on Au/Fe/MgO(001) was conducted with the TOF.SIMS 5-100 instrument from ION-TOF GmbH (Münster, Germany) [107] in the interdisciplinary center for analytics on the nanoscale ICAN by Dr. Nils Hartmann. A dual beam depth profiling technique enabled the measurement of the layer thicknesses d_{Au}. Under UHV conditions, the sample surface is targeted by two ion beams. The first pulsed, high-energy ion beam (10 - 30 keV) is the analysis beam responsible for sputtering a crater and generating secondary ions. The secondary ions are then accelerated by an electric field and travel over a drift path toward a detector. Measuring the flight time for each secondary ion determines its mass-to-charge ratio, and information on the chemical compositions of the sample surface

is obtained. This reveals the material sensitivity of the ToF-SIMS technique.

For depth profiling in dual-beam mode, a second low-energy ion beam with a few hundred eV up to a few keV is used, the so-called sputter beam. It is employed to analyze the sample crater bottom and depth profiling progressively. Alternatingly turned-on analysis and sputter beams result in a series of mass spectra acquired at different depth points. The recorded mass peaks and their intensity as a function of sputter time t_{sp} can be converted into a depth scale. A constant sputter rate S (measured in nm/s) is required to convert the sputtering time t_{sp} into a depth z with

$$z = S \cdot t_{\mathrm{sp}}. \tag{3-1}$$

In this thesis work, the analysis and sputter ion beam sources were mounted to the sample at an angle of 45°. The surface analysis gun of the ToF-SIMS 5-100 was a 15 keV liquid metal ion gun (LMIG) emitting bismuth Bi^+ pulsed ion beams on a sample surface of $100 \times 100~\mu m^2$. The sample sputtering was performed by a monoatomic, low-energy oxygen beam (O_2^+) with 0.5 and 1 keV separately on a surface of $300 \times 300~\mu m^2$. In order to neutralize the charge build-up at the sample surface, low-energy electron flooding was applied between the pulsed analysis and the sputter beam. The high-energy, pulsed primary analysis beam sustains a high mass resolution, while the low-energy sputter beam provides a high depth resolution in the sub-nm range. Thus, the ToF-SIMS represents an appropriate technique for measuring the thickness of the Au and Fe layer in the nm range.

Figure **3-3**(a) shows the sputtering craters at different Au layer thicknesses on the Au/Fe sample. Different numbers are assigned to the multiple squared craters generated with the sputter ion beam (spot size of $300 \times 300~\mu m^2$), which are smaller than the widths of the Au layers (400 μm). Different crater numbers indicate the sputtering at different Au layer thicknesses. Figure **3-3**(b) and (c) illustrate the crater depth profiles of craters 1 and 2, which have been taken by a profilometer (BRUKER DektakXT stylus surface profiler). A diamond-tipped stylus with a radius of 12.5 μm was in contact with the sample surface, and the lateral movement of 800 μm through the crater center allowed the recording of the depth profile. The depth from the top Au layer to the bottom is equivalent to the Au thickness d_{Au}. The data analysis at crater 1 exhibits an Au thickness of 73 ± 7 nm, while at crater 2 it is 36 ± 5 nm. In both depth profiles of the craters, crater walls are observable, arising out of the crater center due to the sputtering procedure. However, this represents an error source in determining the Au thickness that can still be handled. Craters 1 and 2 represent an example for all Au layer thickness measurements and reveal the rough deviation of up to 10% between the nominally specified and measured d_{Au}. The deviation of the nominally indicated Au thicknesses d_{Au} and the determined error bars for d_{Au} ($\Delta d_{\mathrm{Au}} \approx 10-14\%$) from the profilometer data are taken into account in the 2PPE data analysis in chapter 4.
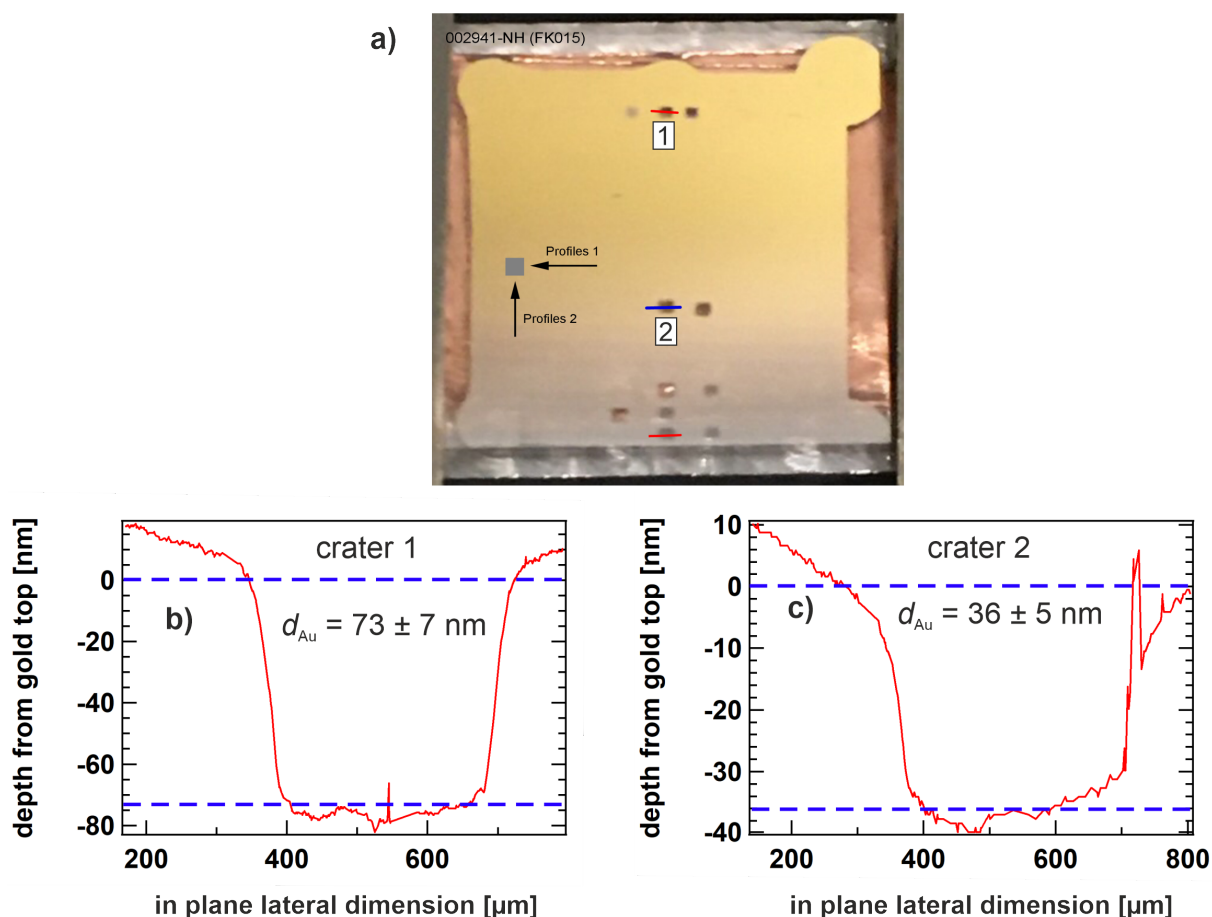
Figure 3-3: (a) Photo of an Au/Fe/MgO(001) heterostructure with sputter craters created using the ToF-SIMS technique at the Interdisciplinary Center for Nanoscale Analytics (ICAN). Profile measurements on sputter craters 1 and 2 were taken laterally through the crater center (horizontal lines). (b) and (c) profilometry depth profiles of craters 1 and 2, respectively. The blue dashed lines mark the difference between the gold top and bottom of the crater.

3.2. UHV chamber and the photoelectron spectrometer

The UHV chamber is an indispensable part of PES measurements. The undisturbed photoelectron signal is detectable at the lower pressure p in the UHV chamber because fewer residual gas atoms are adsorbed on the sample surface. Consequently, the mean free path of the photoemitted electrons becomes larger than the drift distance in the TOF spectrometer. To perform photoelectron spectroscopy, UHV conditions with a pressure $p \sim 10^{-10}$ mbar are established in the laboratory at University Duisburg-Essen, Faculty for Physics, in the working group of Prof. Dr. Bovensiepen.

The whole UHV setup consists of the following parts; the load lock, sample magazine, and the two upper and lower chambers for sample preparation and for spectrometer level, re-

spectively. The schematic of the upper and lower chambers are shown in Figure **3-4**(a) and (b). The load lock and magazine are connected to a turbo pumping station with a
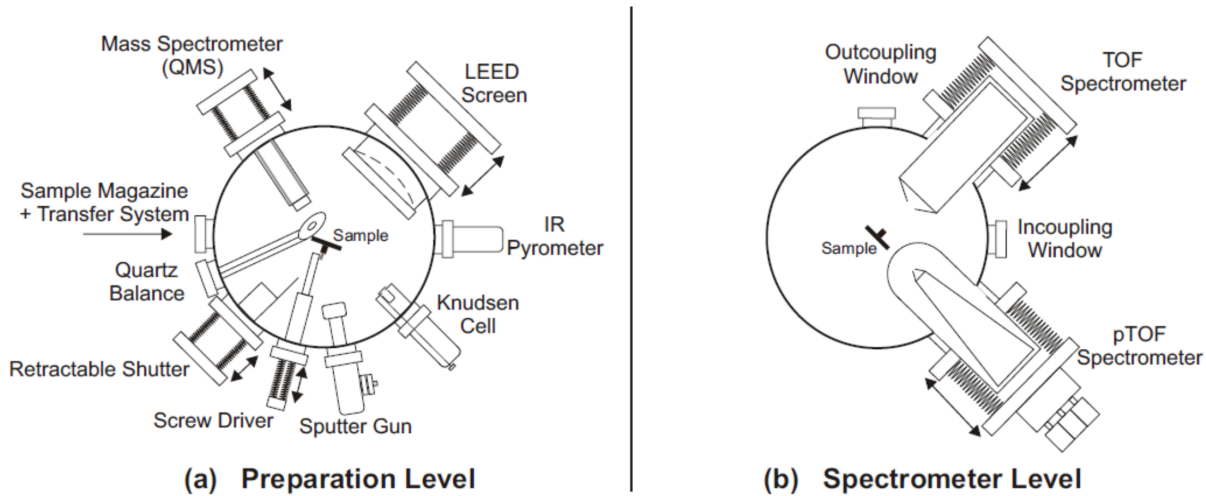
Figure 3-4: (a) Surface preparation and characterization tools in the upper part of the UHV chamber. (b) Spectrometer level in the lower part of the chamber for performing the photoelectron spectroscopy measurements. The schematic is taken from Ref. [108] with the permission by Dr. L. Rettig.

diaphragm roughing pump (Pfeiffer, HiCube 80 ECO) and an additional turbo-molecular pump (Pfeiffer, TPD 020) merely for the magazine to ensure a pressure of $p \sim 10^{-10}$ mbar[1]. The load lock is the first stage for inserting the sample into the UHV system. The sample boat is attached to a transfer line and then moved to the magazine (sample). The samples are heated up to 80 ℃ for degassing.

The next stage is the main chamber, divided into the preparation and spectrometer levels, as shown in Figure **3-4**(a) and (b). The preparation level is evacuated to $p \sim 10^{-10}$ mbar by baking-out procedures (110 ℃) and the employment of a turbo-molecular pump (Pfeiffer, HiPace 700), which is connected to a pre-vacuum line of $p \sim 10^{-6}$ mbar. This pre-vacuum is obtained by a drag-turbo pump and a four-stage membrane pump. The Au/Fe/MgO(001) sample is attached to a sample manipulator allowing for 400 mm vertical and ± 12.5 mm lateral movements. Furthermore, a differentially pumped rotation feedthrough enables the free rotation of 360° around the vertical axis of the manipulator. The linear movements are equipped with PC-controlled stepper motors, which allow for sample positioning with 10 μm precision.

---

[1]Before transferring the Au/Fe/MgO(001) sample into the UHV system, the Au surface and the MgO(001) surface are blown with He gas to remove contaminants such as dust grains.

The lower chamber is separated from the upper chamber by a gate valve. An ion get-ter pump and a titan sublimation pump are employed for evacuating the lower chamber to $p \sim 9 \cdot 10^{-11}$ mbar, ensuring clean sample surfaces over several hours up to days. In addition, the lower chamber contains the two time-of-flight (TOF) spectrometers applied for detecting the photoelectrons. The conventional electron TOF (e-TOF) spectrometer was not used in this thesis work. In contrast, the position-sensitive e-TOF (p-e TOF) spectrometer has been used to establish the front-side pumping front-side probing (FP) and back-side pumping front-side probing (BP) experimental configurations, see section 3.3. The working principles of the conventional e-TOF spectrometer represent the basis for the p-e TOF spectrometer, and thus both instruments constitute essential components in time-resolved photoelectron emission spectroscopy [96, 109, 110]. Compared to the conventional e-TOF spectrometer, the p-e TOF allows simultaneous analysis of low-energy electrons photoemitted from solid surfaces in an energy- and angle-resolved manner. However, in this work, the p-e TOF is used only to detect the kinetic energy of the photoemitted electrons. By combining PES with the time-resolved pump-probe technique, the correlated signal can be recorded as a function of the pump-probe delay time. The p-e TOF spectrometer was developed and built at the Freie Universität Berlin and described in detail by Kirchmann et al. in [110].

By placing the sample in front of the spectrometer, electrons will be photoemitted to the entrance tip with an aperture of 1.9 mm. The electrons propagate within a flight time t through the field-free Al drift tube with a length of $L = 200$ mm toward a chevron-mounted microchannel plate (MCP) stack of 80 mm active diameter. Correspondingly, when the p-e TOF spectrometer axis is oriented parallel to the sample surface normal, the acceptance angle spans $\pm 11°$. The p-e TOF spectrometer has a hexanode delay line behind the MCP stack, which simultaneously determines the photoelectron's hitting position on the hexanode. A calculation program makes it possible to map the photoelectron energy distribution in time and momentum simultaneously; see for a more detailed description [110]. However, in this thesis work, the momentum information is not considered, and a signal out of the MCP stack was taken to measure the photoelectrons' time-of-flight. The outcoupled signal from the MCP with a few mV amplitudes and a few ns pulse duration is amplified in a broad-band amplifier (ATR19 by RoentDek). Since the outcoupled signals from the MCPs show a broad amplitude distribution, a constant-fraction discriminator (CFD) (Ortec, QUAD 935) was employed to discriminate signals not on a fixed threshold but a constant fraction of the total peak height. Subsequently, nuclear instrumentation module (NIM) pulses are generated and fed into a time-to-digital converter (TDC, FAST Comtec GmbH) with a time resolution of 250 ps. The TDC measures the time difference t between the start signal t_{start} from a fast photodiode in the optical beam path and the stop signal t_{stop} of the CFD.
The kinetic energy of the non-relativistic electrons, with mass m_e, is determined by

$$E_{\text{kin}} = \frac{1}{2}m_e v^2 = \frac{m_e L^2}{2(t - t_0)^2}, \qquad (3\text{-}2)$$

with the constant field-free drift distance L and the time offset t_0, which has to be considered due to the different propagation times between the optical and electrical signal to the timing device. The spectrometer and its components, such as the drift tube and the tip, are coated with Graphite to present a homogeneous work function of ~ 4.3 eV. The entire spectrometer is housed in a 1.5 mm thick μ-metal casing to shield residual magnetic fields, which might disturb the photoelectron trajectories. The μ-metal shield has cut-outs where the laser beam can enter with a 45° angle on the sample and photoexcites the electrons.

If the sample and the spectrometer are directly connected, the Fermi levels $E_{\mathrm{F}}^{\mathrm{sample}}$ and the $E_{\mathrm{F}}^{\mathrm{spec.}}$ of both objects are aligned. Due to the difference in the work functions Φ_{sample} and $\Phi_{\mathrm{spec.}}$ a potential gradient arises between the sample and the spectrometer, as shown in a potential diagram in Figure **3-5**. The electrons must overcome the potential barrier $e_0 U$ and an applied bias voltage U_{bias}

$$e_0 U = \Phi_{\mathrm{sample}} - \Phi_{\mathrm{spec.}} + e_0 U_{\mathrm{bias}}. \tag{3-3}$$

The low-energy cutoff of the photoemission spectrum and the kinetic energy E_{kin} of the photoelectrons are determined by the vacuum energy levels $E_{\mathrm{vac}}^{\mathrm{sample}}$ and $E_{\mathrm{vac}}^{\mathrm{spec.}}$, respectively. Accordingly, offsetting the difference between the vacuum energy levels by applying a bias voltage of $e_0 U_{\mathrm{bias}} = -(\Phi_{\mathrm{sample}} - \Phi_{\mathrm{spec.}})$ is essential to ensure a field-free region between the sample and the spectrometer and thus unperturbed electron trajectories.

For reliable e-TOF spectra, the time offset t_0 from Equation 3-2 is determined by recording different TOF spectra with different bias voltages U_{bias}. The correct timing t_0 is defined by adjusting it as a free parameter so that the Fermi edge of the different spectra overlaps. Considering Equation 3-4, it is apparent that the achievable energy resolution ΔE_{kin} of the p-e TOF spectrometer depends on the experimental accuracy Δt in the TOF analysis and the drift length L according to

$$\Delta E_{\mathrm{kin}} = \sqrt{\frac{8 E_{\mathrm{kin}}^3}{m_e}} \frac{\Delta t}{L}. \tag{3-4}$$

For kinetic energies of photoelectrons with $E_{\mathrm{kin}} \leq 0.5 - 2.5$ eV, a drift length of $L = 200$ mm and time resolution $\Delta t \leq 1$ ns provide an energy resolution of $\Delta E_{\mathrm{kin}} \leq 20$ meV [96, 110]. Nevertheless, due to the spectral bandwidth of $10 - 50$ meV for femtosecond laser pulses, time-resolved 2PPE experiments do not necessarily profit from the much higher energy resolution of the spectrometer. The following section will describe the available laser system for performing photoemission experiments.

3.3. Laser setup and laser pulse overlap

A commercially available amplified laser system (Coherent) has been used for the time-resolved photoemission experiments. This system is based on a femtosecond mode-locked
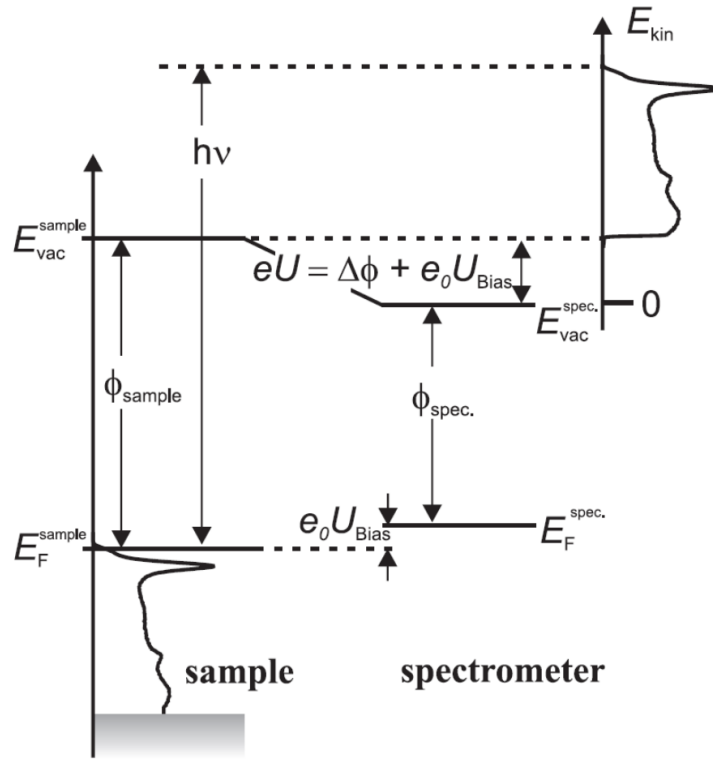
Figure 3-5: Potential gradients between sample and spectrometer. In order to avoid electric fields between the sample and the spectrometer entrance, which is essential for the detection of unperturbed photoelectrons, a bias voltage U_{bias} with a finite value can be applied (on the sample) to compensate the difference in the sample and spectrometer vacuum energies $E_{\text{vac}}^{\text{sample}}$ and $E_{\text{vac}}^{\text{spec.}}$. The kinetic energy is measured with respect to the spectrometer's vacuum level $E_{\text{vac}}^{\text{spec.}}$, while the sample's vacuum level $E_{\text{vac}}^{\text{sample}}$ determines the low-energy cutoff in the photoemission spectrum. The figure is taken from Ref. [70] with the permission from Dr. P. Kirchmann.

Ti:Sa oscillator (Micra) and a regenerative amplifier (RegA), whereby the chirped pulse amplification (CPA) technique provides intense, femtosecond ultrashort laser pulses [111]. Figure **3-6** shows the generation of the VIS and UV pulses with the photon energies $h\nu_1 = 2.1$ eV and $h\nu_2 = 4.2$ eV by noncollinear optical parametric amplification (NOPA), respectively.

A continuous-wave (CW) green diode laser (Coherent Verdi V-18, 532 nm) is used for pumping the laser system by 18 W. The Ti-doped sapphire (Ti:Sa) crystal in the oscillator cavity (Coherent Micra-5) is pumped by 5 W, which delivers fs laser pulses with a central wavelength of $\lambda_0 = 800$ nm a pulse duration of 40 fs at a pulse energy of ~ 3 nJ. This pulse energy is insufficient to generate VIS pulses by NOPA. Hence, chirped pulse regenerative amplification (Coherent RegA 9040) is employed using 13 W of the Verdi-18 pump laser, see top left in Figure **3-6**. After the amplification by RegA, IR pulses with an energy of
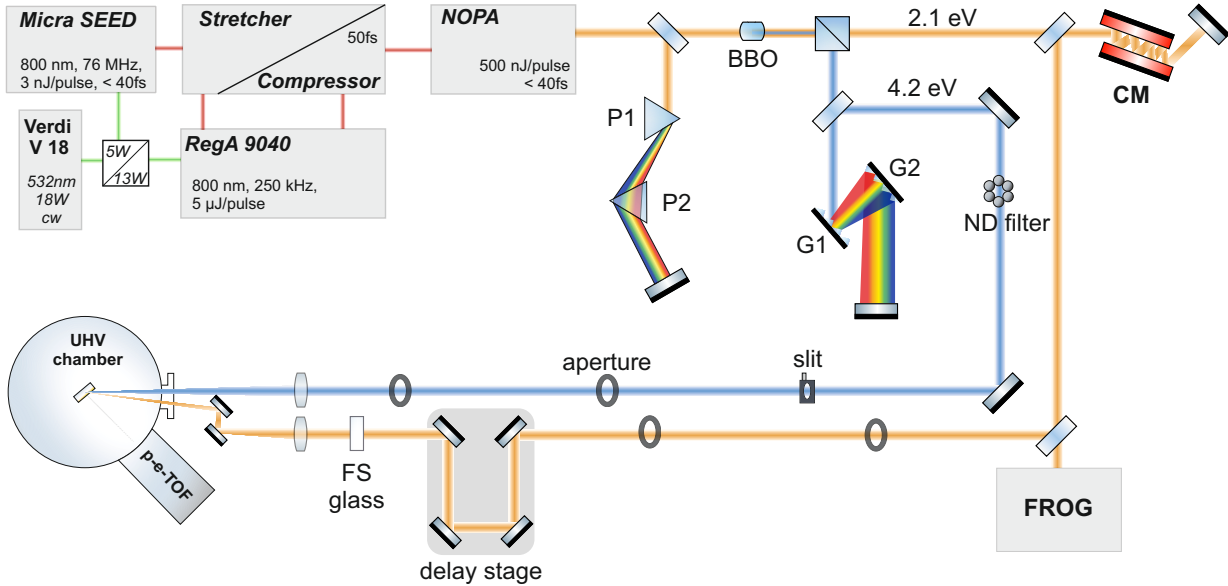
Figure 3-6: Top left: Sketch of the amplified laser system; femtosecond IR laser pulses are generated in the Ti:Sa oscillator Micra and subsequently amplified by RegA. The ultrashort RegA output (~ 6 μJ) is sent to the NOPA for generating a VIS laser pulse with a photon energy of $h\nu_1 = 2.1$ eV. Top right: Optical setup for generating UV laser pulses with a photon energy of $h\nu_2 = 4.2$ eV. Additionally, prisms ($P_{1,2}$), gratings ($G_{1,2}$), and chirped mirrors (CM) are used for compressing the laser pulse duration. Bottom right: A FROG device is employed for performing SHG-FROG measurements characterizing the VIS light in the spectral and time domain. Bottom left: Optical beam paths for coupling the VIS and UV laser beams into the UHV chamber over a pump-probe delay stage. A 5 mm FS plate in the pump beam path and a slit in the probe beam path are used to compensate for the chirped pulses.

~ 6 μJ per pulse and a repetition rate of 250 kHz are provided. These IR pulses are sent to a grating compressor and are gain compressed in time to a pulse duration of 40 fs. The ultrashort RegA pulses reached after compression a maximum output power of $P_{\mathrm{RegA}} = 1.60$ W. Subsequently, the NOPA is fed with 50% of the P_{RegA}, and a VIS ultrashort laser pulse with photon energy $h\nu_1 = 2.1$ eV, and less than 40 fs pulse duration is generated. In order to understand the generation of ultrashort VIS laser light by NOPA in more detail, see [112–115].

After NOPA, the fundamental beam $h\nu_1$ is passed to a BK7 prism-pair compressor ($P_{1,2}$) to compensate for group velocity dispersion (GVD) and then compress the beam in time (see Figure **3-6**, top right). After compression, the fundamental beam $h\nu_1$ is focused by a curved mirror onto a β-barium-borate (BBO) crystal (birefringent) with thickness $d_{\mathrm{BBO}} = 30$ μm to generate second harmonic generation (SHG) with frequency-doubled light of $h\nu_2 = 4.2$ eV. A

second curved mirror served as a collimator and sent the fundamental VIS and SHG light to a dichroic beam splitter, which separates the beam. The SHG process of type I in the BBO crystal gives rise to a rotation of the polarization axis, which occurs in uni-axial crystals by 90°, as reported in [116]. Subsequently, the second harmonic light is sent to a periscope to flip the polarization back from s to p.

The next station for the SHG is a parallel aligned grating compressor ($G_{1,2}$) to compensate the GVD caused in the dispersive optical elements. The grating compressor is designated by a blaze wavelength $\lambda_{blaze} = 300$ nm, blaze angle $\theta_{blaze} = 1.2°$ and a grove density of 300 l/mm for laser pulses with the central wavelength $\lambda = 300$ nm. The distance between the grating pair is adjusted by monitoring the full width at half maximum of the cross-correlation FWHM(XC) at high energies of the correlated signal in the time-resolved 2PPE measurements. The shortest FWHM(XC) is achieved at a grating pair distance of $d_{grating} = 13.2$ cm with ~ 60 fs. Subsequently, the ultrashort second harmonic light $h\nu_2$ is sent toward the UHV chamber. The advantage of compensating the high-order dispersion in the UV pulses by optimizing the grating compressor is shown in section 3.5.

Due to the positive dispersion at the dispersive optical elements of the VIS beam $h\nu_1$, it is directed to a compressor of rectangular chirped mirrors (Thorlabs GmbH, Germany), see Figure **3-6** top right. This CM pair is parallel aligned to each other, and the VIS light is reflected 24 times between these two parallel mirrors. Each reflection causes a negative chirp on the VIS beam $h\nu_1$ and is thus initiated due to a re-compression of a bandwidth-limited laser pulse. Eventually, after the compression of the VIS and UV laser pulses by the chirped mirror and grating compressors, respectively, they are guided toward the UHV chamber for the time-resolved 2PPE experiments. In section 3.5 a thorough comparison of the pulse dispersion compensation among the different compressor systems is provided.

Overlap of the VIS and UV pulses on the sample surface

Figure **3-7** and **3-8** show the beam paths for the VIS and UV beams in time-resolved 2PPE with front-side pumping / front-side probing (FP) and back-side pumping / front-side probing (BP) experimental configurations, which will be now described for both geometries. After compressing the UV light by a grating compressor – as described above – a neutral density (ND) filter wheel is inserted in the UV beam path. The ND filters used here are a combination of 0.04 and 0.10 strengths. One reason for reducing the power of the UV beam is to control the 2PPE signal count rate (CR) generated by UV only. In order to get a decent signal-to-noise (S/N) ratio in the two-color 2PPE measurements, it is beneficial if a CR ratio of $CR(h\nu_1)/CR(h\nu_2) = 1/3$ exists, which is controlled by the ND filters. Afterward, both beams are sent through a pair of mechanical laser shutters, which have the task of blocking the pump and probe beam separately after each delay scan and acquiring spectra of the
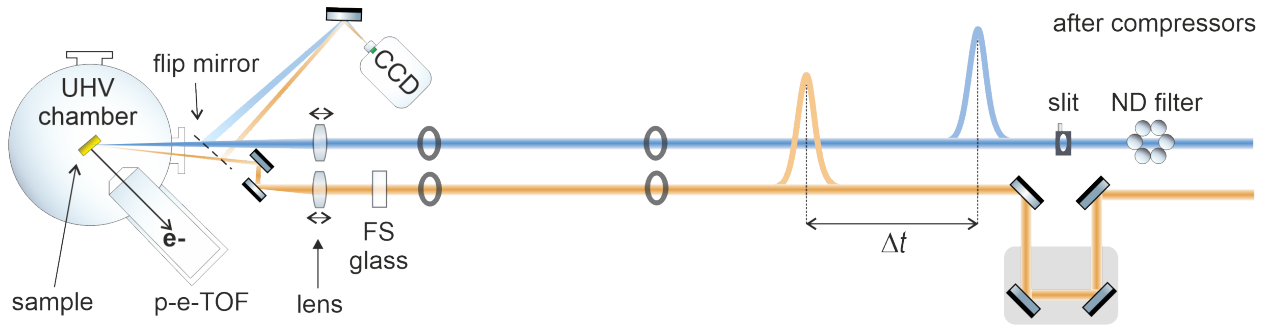
Figure 3-7: Incoupling of the pump and probe beams into the UHV chamber in case of front-side pumping and probing (FP) experimental configuration: Pumping and probing proceeds on the Au-side with $h\nu_1 = 2.1$ eV and $h\nu_2 = 4.2$ eV, respectively. Pulses are delayed to each other by Δt with a delay stage for the VIS pump beam. Beam profiles and spatial overlap of pump and probe beam are obtained by a UV sensitized CCD camera. A 5 mm FS plate in the pump beam path and a slit in the probe beam path are used to compensate for the chirped pulses.

2PPE of UV and VIS only. Before sending the beams to a detachable breadboard, where the optics for guiding the beams to the UHV chamber are located, the beams are sent through alignment apertures in order to get a well-aligned optical axis.

Time-resolved 2PPE with Au-side pump geometry

Intending to perform the time-resolved pump-probe 2PPE in the FP geometry, both beams with the photon energies $h\nu_1 = 2.1$ eV and $h\nu_2 = 4.2$ eV are sent toward the UHV chamber as depicted in Figure **3-7**. The UV laser pulse, $h\nu_2$, is guided through alignment apertures and Al mirrors toward a lens with a focal length of $f = 500$ mm and consequently focused on the sample in the UHV chamber. The beam coupling window at the UHV chamber is made of UV-transmitting CaF_2. A digitally controlled delay stage with a positioning accuracy of 0.1 fs in the path of the VIS beam supports time-resolved measurements by introducing a delay between the VIS and UV laser beams. The VIS pump beam is then guided through alignment apertures and Ag mirrors toward a separate lens ($f = 500$ mm) focused on the sample in the UHV chamber, as described for the UV probe beam. The focusing lenses are on translation stages to focus the beams on the same spot on the sample surface with quasi-collinear incidence to avoid interferometric conditions and minimize the temporal broadening due to a non-collinear geometry. Necessary to mention is the insertion of a 5 mm thick fused silica (FS) glass plate in the beam path of the VIS light. Using a flip mirror in front of the UHV chamber window, the beams are sent into a CCD camera to measure the beam profile. The distance from the flip mirror to the CCD camera chip is the same as the distance from the flip mirror to the sample. Thus, the measured beam profiles on the CCD chip correspond to the same on the sample surface. A LabView program

developed by Dr. Ping Zhou is used to determine the spot sizes of the laser beams, as shown in Figure **3-9**. In a 2PPE measurement, it is desirable to have a similar VIS and UV spot size to suppress the uncorrelated background signal.[2]

A prerequisite for obtaining a correlated signal in time-resolved 2PPE measurements is the spatiotemporal overlap of the VIS and UV pulses. Before setting the spatial overlap of the two beams, it is ensured that the beams are guided through the coupling mirrors on the Au/Fe/MgO(001) sample surface with the desired Au thickness d_{Au}. Finding a nice spot with a well-defined and reliable photoemission spectrum produced by each beam is important. As mentioned in chapter 2, the photoemission signal can also appear due to monochromatic 2PPE and 3PPE with UV ($h\nu_2 = 4.2$ eV) and VIS ($h\nu_1 = 2.1$ eV) light pulses. This signal represents a background signal for the time-correlated signal and must be controlled by monitoring the photoexcited spectra. Then, the spatial overlap is adjusted by overlapping the two beams on the CCD camera. Adjusting the temporal overlap of the VIS and UV pulses requires a preliminary step before monitoring the 2PPE signal. The temporal overlap of the two beams is first adjusted with a fast photodiode and a broadband oscilloscope within a time window of 50 ps with an accuracy of 15 ps.

Once the spatial and rough temporal overlap of the two beams is aligned, the correlated signal is acquired by scanning the delay stage with 3 fs time steps while simultaneously monitoring the tr-2PPE signal. In a 2PPE experiment, the correlated signal is easily detectable as it increases up to three orders of magnitude for an optimum VIS-UV overlap[3]. As already shown in previous works, the employment of tr-2PPE measurements with the FP experimental configuration enabled measuring local hot electron relaxation dynamics at the metallic sample surfaces [17, 47, 67, 69, 117]. By involving theoretical calculations within these works, ultrafast nonlocal hot electron transport from the surface into the bulk has been concluded. Using BP geometry – Fe-side pumping and Au-side probing – has opened the door to direct measurement of the local and nonlocal hot electron relaxation dynamics.

Time-resolved 2PPE with Fe-side pump geometry

Figure **3-8**(a) shows the time-resolved pump-probe alignment with the BP geometry on the Au/Fe/MgO(001) sample. While the UV probe beam path is kept the same as in FP geometry, the VIS pump beam path has to be guided by a flip mirror onto a window on the back-side of the UHV chamber. Right after the laser beam shutter for the VIS light, a flip mirror reflects the beam toward a delay stage. From there on, the VIS beam reflects to a 4 mm thick FS glass plate for compensating the chirp in the VIS pump pulse. Subsequently,

---

[2]In contrast to 2PPE measurements in time-resolved ARPES, a smaller UV probe beam is more favorable than the VIS pump beam to ensure a homogeneously excited sample surface.

[3]By contrast, in the case of tr-ARPES measurements, the correlated signal is significantly weaker and requires many scans. Optimizing the spatial overlap is achieved by fine-tuning the coupling mirrors to achieve a maximum correlated signal.

the beam propagates toward a lens ($f = 500$ mm), staying on a translation stage for adjusting the focus on the back-side of the sample. The angle of incidence of VIS pump and UV probe beams on the sample was close to 45°, so a nearly 90°-alignment between both beams has been established. This alignment is crucial to overlap both wavefronts of the VIS and UV pulses in time and space on each point of the Au/Fe/MgO(001) sample and maintain the time resolution, see Figure **3-8**(b). Accordingly, the smallest FWHM(XC) can be reached, and a distortion of the spatiotemporal overlap is avoided, which might lead to FWHM(XC) compression limited at larger values.
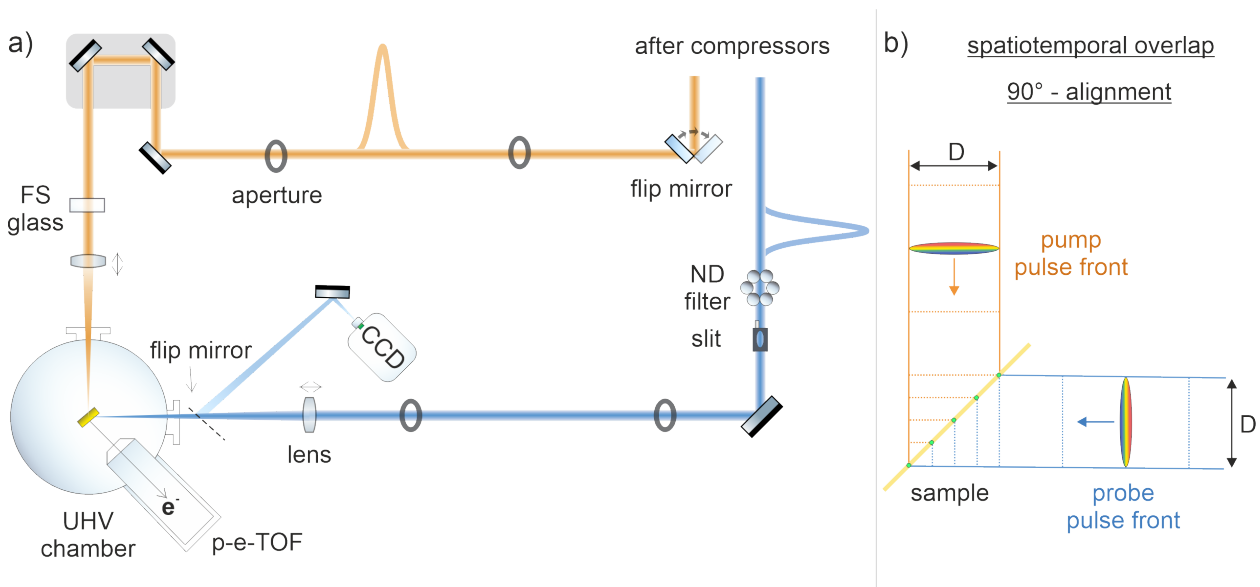
Figure 3-8: (a) BP experimental geometry: Pumping on the Fe-side and probing on the Au-side with $h\nu_1 = 2.1$ eV and $h\nu_2 = 4.2$ eV, respectively. (b) Spatiotemporal overlap of pump and probe beams with diameter D: Temporally chirped pulse fronts propagate toward the Au/Fe/MgO(001) sample. Assuming an angle of incidence of 90° between both pulse fronts leads to spatiotemporal overlap at every point of the sample; see green dots on the sample for illustration.

Due to the similar optical path lengths in both experimental configurations – FP and BP – for the VIS beam, a fast photodiode and broadband oscilloscope in BP geometry are not used to adjust the temporal overlap. Adjusting the spatial overlap of both beams in the BP geometry is a bit more challenging compared to the FP geometry. For the BP geometry, the spatial overlap is adjusted with a CCD camera outside the UHV chamber and the coupling mirrors of both beams. The CCD camera monitors the beam spots of the UV and VIS lights on the sample surface. The laboratory room had to be darkened entirely, and the exposure time of the CCD camera had to be increased in order to see the UV probe beam on the sample surface. After observing the UV beam's scattered light on a monitor showing the sample surface, it is marked on the monitor. Subsequently, the transmitting VIS light from

the Fe back-side to the Au surface is directed to the marked UV position on the monitor, and hereafter the spatial overlap is obtained.

The tr-2PPE measurement as described for FP shows a tr-correlated 2PPE yield. The correlated signal contrast has been improved by optimizing the spatial overlap by the coupling mirrors of both beams according to the maximum signal contrast. In the case of BP experimental configuration, the finding procedure of the correlated signal is usually done at the thinnest Au film thickness where the transmitting VIS beam is observable, and the signal contrast is relatively high compared to the signal contrast at thicker Au layers.

3.4. Pulse characterization

Figure **3-9**(a) and (b) show the intensity distributions of the focal spot profiles for the VIS and UV light. The profiles are measured by the CCD camera, which has been used to adjust the spatial overlap. The camera window is taken out to measure the UV beam spot so that the camera chip is sensitive to UV radiation. ND filters diminished the intense VIS pump and UV probe beam to avoid damage to the CCD camera chip. The focal spot sizes are evaluated by a 2D Gaussian fit of the horizontal (H) and vertical (V) intensity profiles, as shown in Figure **3-9**(c) and (d) for VIS pump and UV probe beams, respectively. This fitting procedure yields the full width at half maximum (FWHM) of the spot profiles. Denoted as H × V for the horizontal and vertical parts of the focal spot profiles, the beam spot sizes are 125×165 μm for the VIS and 75×95 μm for the UV light, calculated with a pixel size of ~ 5.5 μm. The laser fluence – deposited pulse energy per unit area on the sample – is measured by

$$F = \frac{TP}{R} \frac{4\cos(\alpha)}{\pi ab}, \tag{3-5}$$

whereby $T = 0.95$ is the transmission of the incoupling window, P the average power, $R = 250$ kHz the repetition rate, a and b the FWHM of the laser focal spot profile, and $\alpha = 45°$ the angle of incidence on the sample. The average power of $P \approx 3.3$ mW is measured right before the UHV chamber window and correspondingly led to typical fluences in the range of $50 - 70$ μJ/cm^2 for the VIS and $1 - 2$ μJ/cm^2 for the UV pulses in the 2PPE experiments. However, the precise determination of the absolute fluence is limited by the sensitivity of the power meter (0.1 mW) and the error in determining the beam diameter.

The usage of a mobile spectrometer (Ocean Optics, HR 4000CG-UV-NIR) with a broad spectral measurement range of $200 - 1100$ nm enabled the detection of the fundamental (VIS) and its frequency-doubled SHG (UV) beam simultaneously. The respective spectra of both beams are depicted in Figure **3-10**(a) and (b). The VIS pump beam with a central wavelength of $\lambda_{\text{VIS}} = 593$ nm corresponds to a photon energy of $h\nu_1 = 2.09$ eV. The spectral
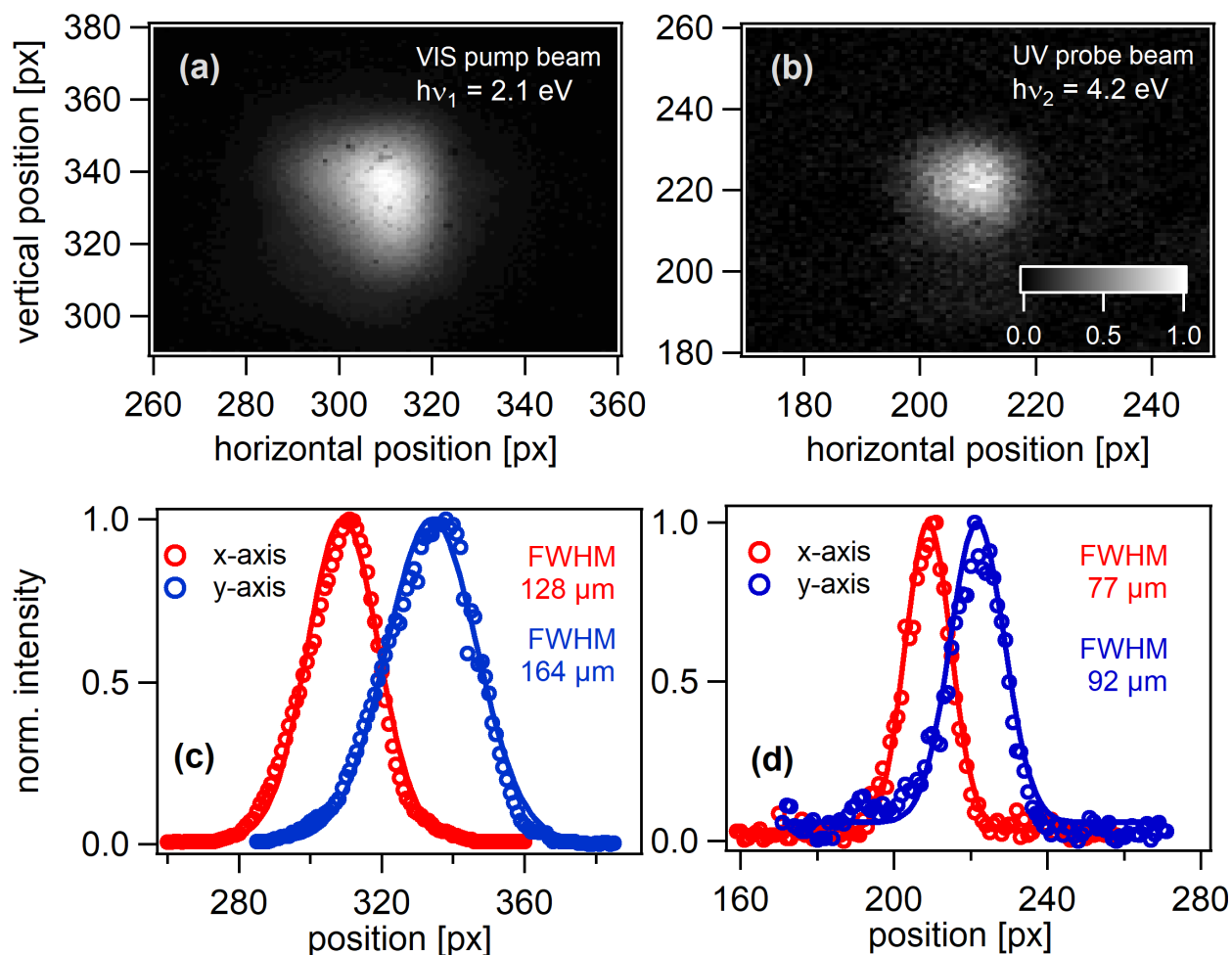
Figure 3-9: CCD camera images of the intensity distribution of focal spot profiles for (a) VIS pump and (b) UV probe beams. The focal spots' horizontal and vertical intensity profiles are shown in panels (c) and (d) for pump and probe beams, respectively. The intensity profiles (markers) are fitted by a Gaussian (solid line) to determine the focal spot sizes.
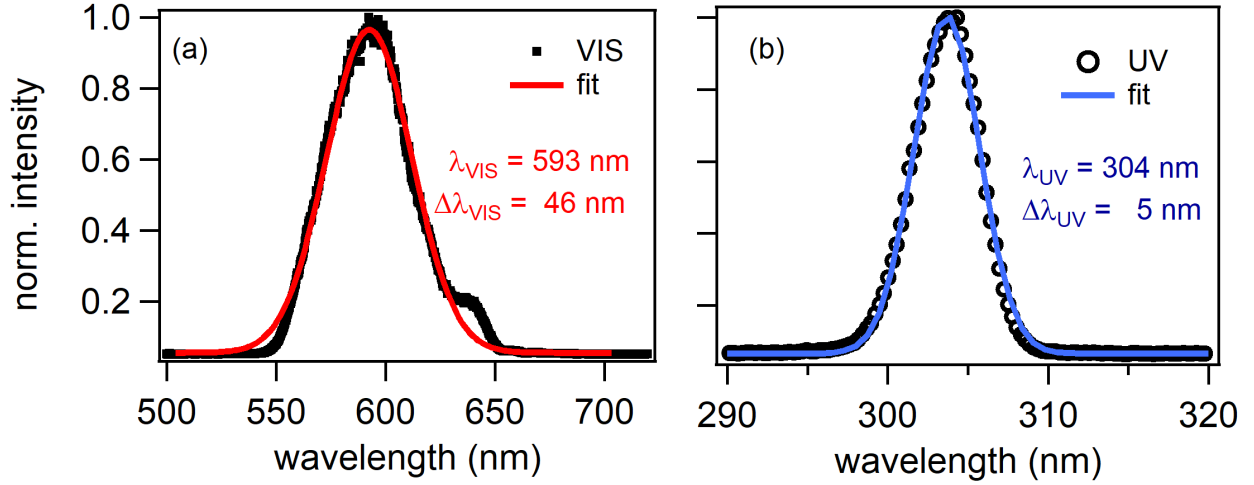
Figure 3-10: (a) Laser spectrum of the NOPA output VIS pulse with $\lambda_{\mathrm{VIS}} = 593$ nm and a spectral width of $\Delta\lambda_{\mathrm{VIS}} = 46$ nm. (b) Laser spectrum of the frequency doubled UV beam with $\lambda_{\mathrm{UV}} = 304$ nm and a spectral width of $\Delta\lambda_{\mathrm{UV}} = 5$ nm.

width is $\Delta\lambda_{\mathrm{VIS}} = 46$ nm corresponding to an energy bandwidth of 170 meV. In comparison, the UV pulse has a central wavelength of $\lambda_{\mathrm{UV}} = 304$ nm, which is equivalent to a photon energy of $h\nu_2 = 4.08$ eV. The spectral width amounts $\Delta\lambda_{\mathrm{UV}} = 5$ nm corresponding to energy bandwidth of 70 meV. The broadband and the wing toward the red part in the VIS light spectrum might have caused undesired dispersion effects in tr-2PPE measurements. A spatiotemporally chirped pulse could lead to distortion and broadening of the FWHM(XC). The solution of closing the apertures for the VIS beam and cutting a part of the UV beam with a slit will be shown in section 3.5.

3.5. Compression of VIS and UV laser pulses

In this thesis work, the investigation is mainly focused on ultrafast hot electron local and nonlocal relaxation dynamics in Au/Fe/MgO(001) thin films. The elementary scattering rates τ^{-1} of hot electrons a few eV above the Fermi level E_{F} are mainly determined by e-e scattering processes, which typically range from several fs to a few 100 fs [14, 15, 17]. Thus, ultrashort laser pulses with fs pulse durations are essential to perform appropriate time-resolved 2PPE measurements. In this regard, the compression of ultrashort laser pulses is inevitable due to group velocity dispersion (GVD) effects in dispersive optical elements.

As shown in the laser setup in Figure **3-6**, the VIS pump and UV probe beam have to pass optical components such as prisms, lenses, mirrors, and glass, representing dispersive media for the ultrashort laser pulses, which is problematic in ultrafast laser applications.

Short pulse durations characterize ultrashort laser pulses in the order of pico-, femto- and attoseconds. Bandwidth-limited (BWL) ultrafast laser pulses reaching the lower limit of their pulse duration have a broad wavelength bandwidth. The propagation of these ultrashort laser pulses through optical media generates a chromatic dispersion (CD) and lengthens the pulse duration, which is disadvantageous for the ultrafast tr-2PPE measurements. The dispersion can be quantified based on a Taylor expansion of the spectral phase $\psi(\omega)$ as a function of the angular frequency ω around the carrier frequency ω_0 of the pulse[4]

$$\psi(\omega) \approx \sum_{m=0}^{\infty} \frac{1}{m!} \psi_m (\omega - \omega_0)^m \tag{3-6}$$

with $\psi_m = \frac{d^m \psi(\omega)}{d\omega^m}\big|_{\omega_0}$ [118, 119]. Different m-order of dispersion $\frac{d^m \psi(\omega)}{d\omega^m}$ induce different effects on the temporal profile of the pulse. The zero-order term ψ_0 describes a typical phase shift, while the first-order term ψ_1 refers to the group delay (GD). Both terms express the time delay without affecting the pulse shape in the time domain. In contrast, second- and higher-order dispersion are more interesting since they cause frequency-dependent shifts. For our analysis of the pulse dispersion, the second-order dispersion ψ_2, known as group delay dispersion (GDD), and the third-order dispersion ψ_3 (TOD) are relevant. A more detailed description of the dispersion in ultrashort laser pulses is given in Appendix A.

3.5.1. Characterization of pulses in time and frequency domain

The dispersion of an ultrashort laser pulse can be controlled by changing the relative optical path of the different spectral components. Suitable setups in this regard consist of prisms, gratings, chirped mirrors, spatial light modulators, etc. [119, 120]. The fundamental VIS beam $h\nu_1$ generated by the NOPA is in our setup positively chirped. The most common way to compensate for positively chirped pulses is by introducing a negative chirp with prism-, grating- or chirped mirror compressors. This will be presented and analyzed using a time-frequency laser pulse analyzer for different compressors.

The measurement of ultrashort laser pulses in the time-frequency domain using the frequency-resolved optical gating technique (FROG) is an established method [118, 119]. The single-shot SHG-FROG traces of the VIS pump beam are taken by a laser pulse analyzer which is called FEMTOS (Polytec GmbH, Germany) and developed by Dr. Ping Zhou. In order to find out the best compression system for shortening the VIS pulse duration, three different compressors are employed; compression by (i) only prism compressor, (ii) prism compressor in combination with chirped mirror compressor, and (iii) grating compressor, see Figure **3-11**. The three cases will be discussed in detail with the FROG traces in Figure **3-12**, **3-13** and **3-14**.

---

[4]The electric field of an ultrashort laser pulse in the frequency domain can be described by $E(\omega) = \varepsilon(\omega)e^{i\psi(\omega)}$, with $\varepsilon(\omega)$ as the envelope in the frequency domain and $\psi(\omega)$ as the spectral phase.
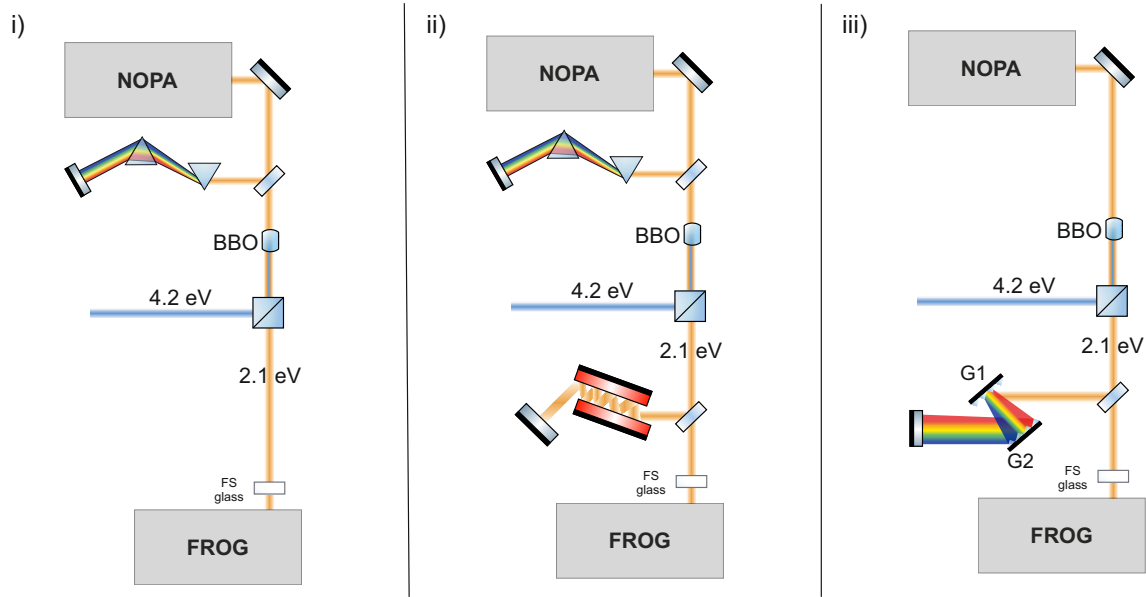
Figure 3-11: Schematic of the applied compressing systems (i) - (iii) for the analysis of the VIS laser pulse by single-shot SHG-FROG measurements. Application of (i) merely prism-pair compressor, (ii) prism-pair compressor in combination with chirped mirrors compressor after the BBO crystal, and (iii) parallel aligned grating-pair compressor.

(i) Only prism compressor

The prism compressor, used for compensating the positive chirp in the VIS pulse, is depicted in Figure **3-11**(i). The compressor consists of two BK7 prisms, which are suitable for compensating the chirp of VIS light compared to SF11 prisms, see [121]. By entering the prism pair compressor, the VIS pulse undergoes an angular dispersion for its spectral components and thus experiences a temporal negative chirp. Subsequently, the spectral phase velocities are coming closer and the pulse duration shortens. After the prism compressor, the VIS beam propagates through a BBO crystal ($d = 30$ μm) and generates by second harmonic generation (SHG) a UV beam. A beam splitter separates the VIS beam from the UV beam so that only the VIS beam is sent toward the SHG-FROG setup. Before entering the FROG setup, the beam is sent through a piece of fused silica (FS) to simulate a similar situation as in the tr-2PPE experiments. Placing a 5 mm FS directly in front of the lens of the VIS light enabled the compensation of the chirp in the pulses and resulted in a very short FWHM(XC) at about 60 fs.

The respective single-shot SHG-FROG trace is shown in Figure **3-12**(a). The measured time-wavelength trace is fed into a sophisticated phase retrieval algorithm [122] that delivers the reconstructed FROG trace, see Figure **3-12**(b). The extracted retrieved pulse in Figure **3-12**(c) shows a pulse duration of 25 ± 1 fs and some low-intensity contribution after the main optical pulse at later times. Compared with the BWL pulse duration of 13 ± 1 fs, the measured
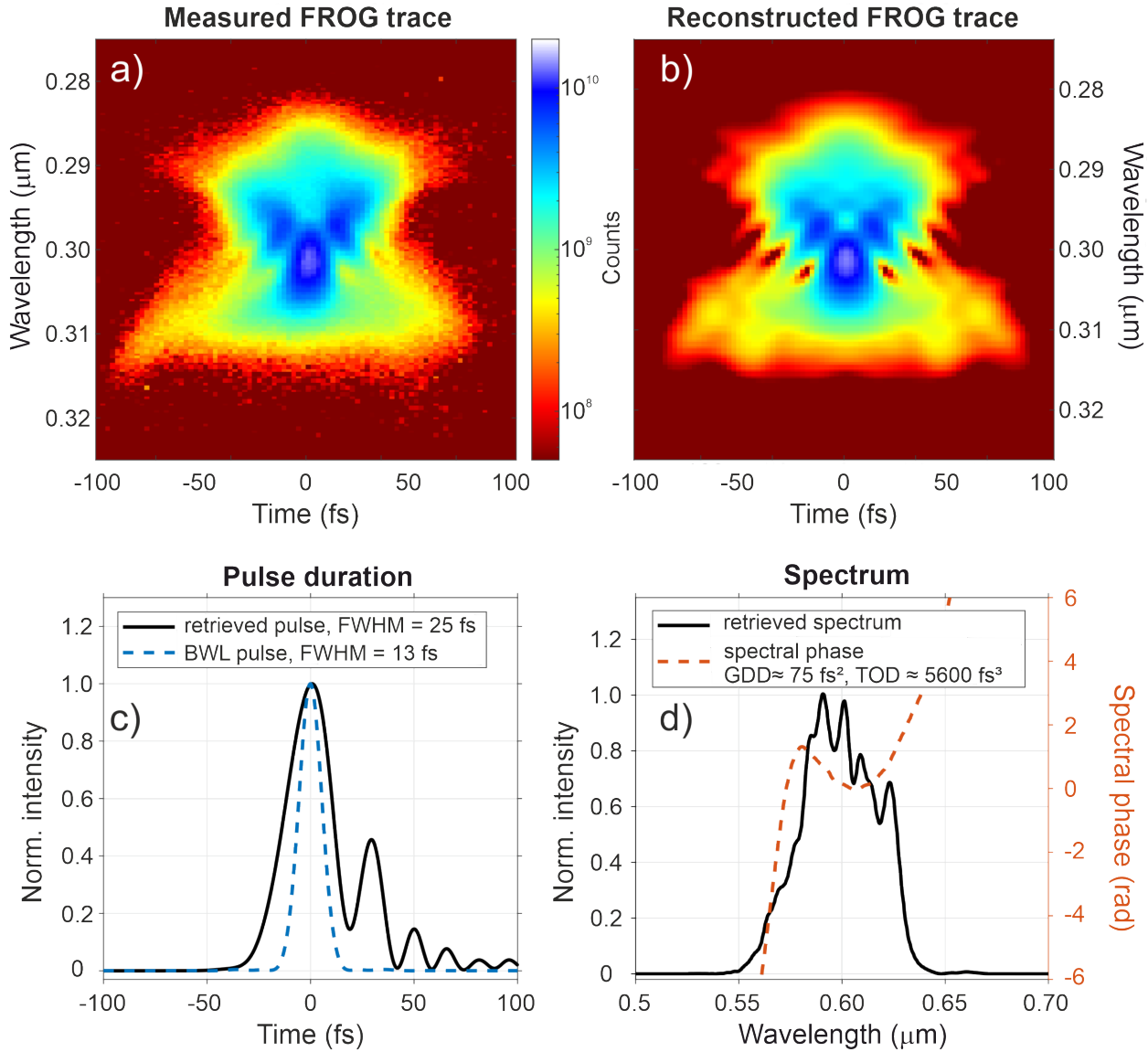
Figure 3-12: Second harmonic FROG intensity of 2.1 eV or 593 nm VIS beam pulse compressed by a prism compressor: (a) measured and (b) reconstructed FROG traces on logarithmic scale. (c) Retrieved time-dependent pulse (solid black line) and calculated BWL pulse (dashed blue line) with FWHM = 25 and 13 fs, respectively. (d) Retrieved spectrum (solid black line) and spectral phase (dashed orange line) with GDD = 75 fs^2 and TOD = 5600 fs^3.

longer pulse duration arises due to high-order dispersion. The appearance of low-intensity pulses at later times and the retrieved cubic spectral phase in Figure **3-12**(d) indicate the dominating third-order dispersion TOD. Applying a fit procedure, developed by Dr. A. Tarasevitch and O. A. Naranjo-Montoya enabled the extraction of GDD and TOD with 75 fs^2 and 5600 fs^3, respectively. Using only prism compressor and the resulting considerable TOD in the VIS pulse poses a critical limitation for proper tr-2PPE measurements with ultrashort laser pulses. The 30 μm thick BBO crystal after the prism compressor introduces an additional positive chirp in the VIS laser pulse. An additional compressing system, such as a chirped mirror compressor, was constructed to overcome this issue and compensate for the GDD and TOD.

(ii) Prism and chirped mirror compressor

The fundamental VIS beam must be negatively chirped after the SHG process in the BBO crystal where the beam was positively chirped. An additional chirped mirror compressor was inserted in order to compensate the chirp in the pulse, see Figure **3-11**(ii). A dispersive chirped mirror results in a negative GDD at long wavelengths than at short wavelengths, compressing the positively chirped pulse to a short pulse [123, 124]. Thus, the fundamental NOPA pulse is sent to the negatively chirped mirror compressor (suitable for 500 nm, Thorlabs GmbH) and is 24 times reflected to get the shortest laser pulse. The obtained and retrieved FROG traces by a combination of prism and chirped mirror compressor are shown in Figure **3-13**(a) and (b). The retrieved pulse in Figure **3-13**(c) shows a different pulse shape than the one obtained by only the prism compressor in Figure **3-12**(c). The additional chirped mirror compressor leads with 16$\pm$1 fs to a shorter pulse duration and a shorter BWL pulse of 12 $\pm$ 1 fs. Moreover, fewer low-intensity pulses appear beside the main optical pulse in the time domain. The analysis of the retrieved spectral phase in Figure **3-13**(d) delivers the values for GDD ≈ -32 fs^2 and TOD ≈ 4500 fs^3. Thus, the use of the 24-reflection chirp mirror compressor helped to significantly compensate for the TOD obtained by using the prism compressor alone.

(iii) Parallel aligned reflection grating compressor

Another possibility to compress laser pulses is the reflection grating compressor in the double-pass configuration, as shown in Figure **3-11**(iii). The grating compressor consists of two parallel aligned ruled gratings (Edmund Optics GmbH, Germany) with blaze wavelength $\lambda_{\text{blaze}} = 500$ nm, blaze angle $\theta_{\text{blaze}} = 2.13°$ and a groove density $g = 300$ l/mm. The first grating decomposes the VIS laser pulse into its spectral components so that the long wavelengths travel a longer optical path than the shorter wavelengths, which leads to a negative chirp or negative GDD [125, 126]. The parallel aligned second grating recollimates the beam and compensates the angular dispersion, so the pulse is temporally compressed but spatially chirped. The original beam is recovered by using a mirror that reflects the beam. Applying
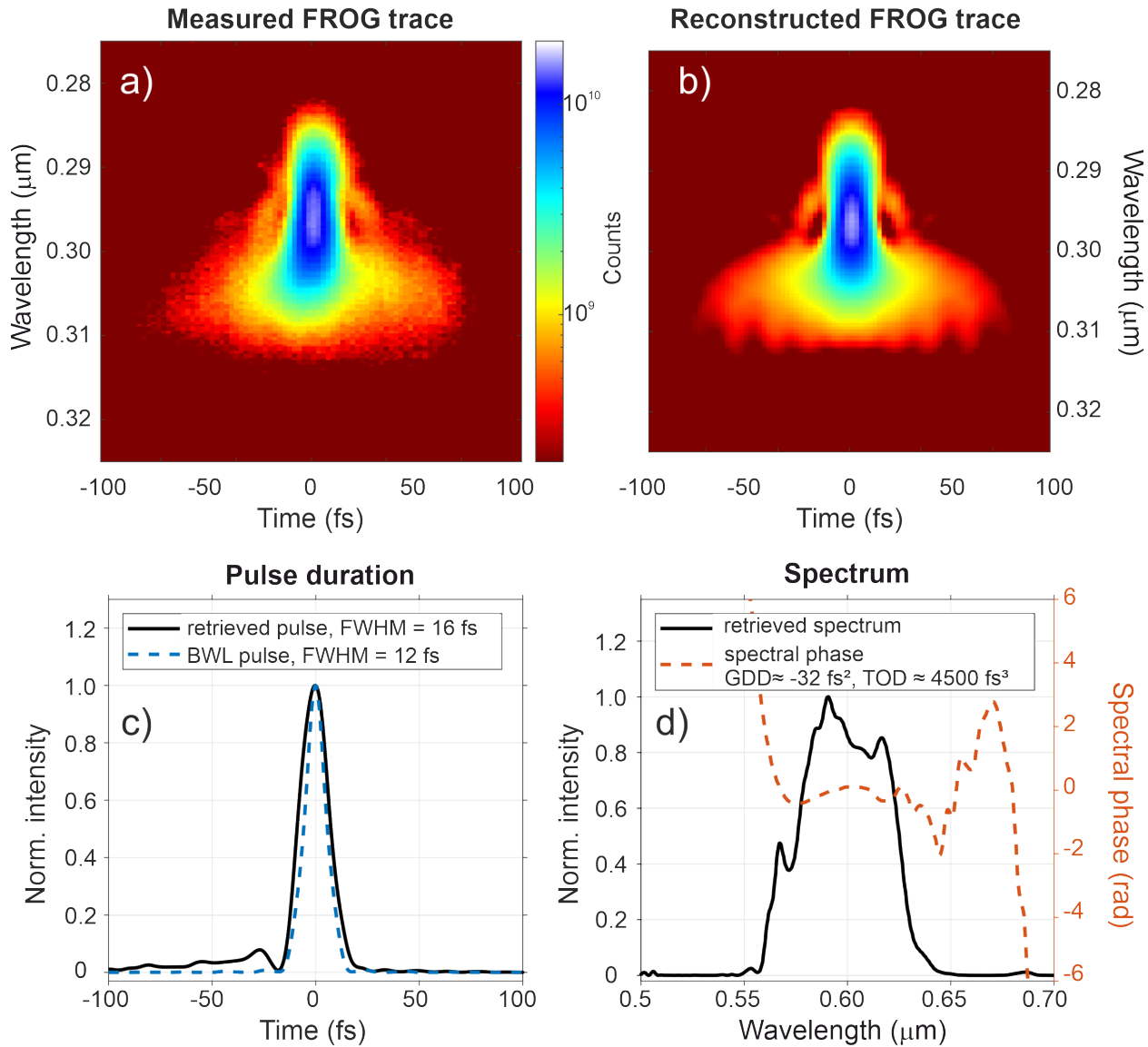
Figure 3-13: Second harmonic FROG intensity of 2.1 eV or 593 nm VIS beam pulse compressed successively by prisms and chirped mirrors: (a) measured and (b) reconstructed FROG traces on logarithmic scale. (c) Retrieved time-dependent pulse (solid black line) and calculated BWL pulse (dashed blue line) with FWHM = 16 and 12 fs, respectively. (d) Retrieved spectrum (solid black line) and spectral phase (dashed orange line) with GDD = -32 fs^2 and TOD = 4500 fs^3.
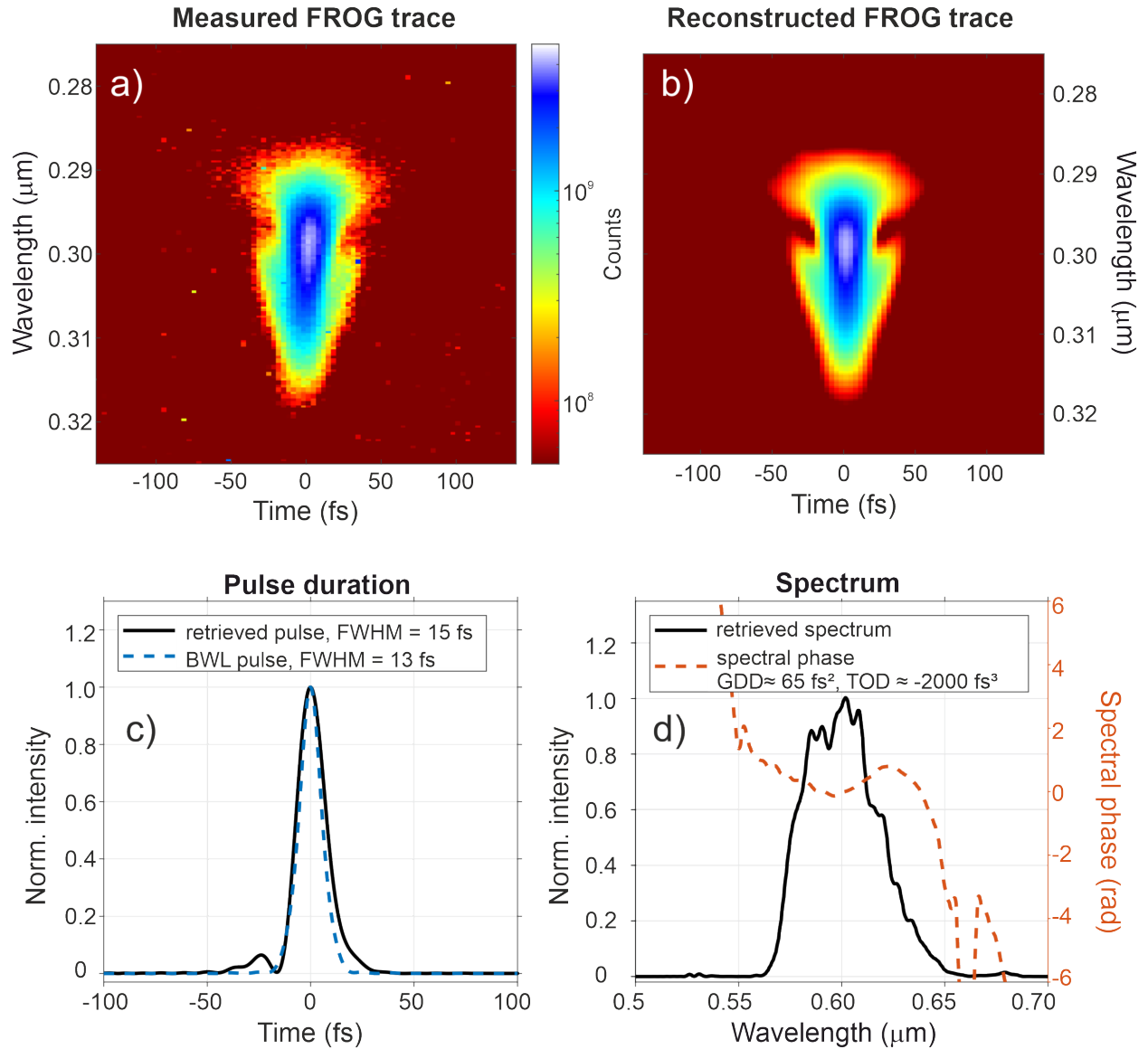
Figure 3-14: Second harmonic FROG intensity of 2.1 eV or 593 nm VIS beam pulse compressed by a grating compressor: (a) measured and (b) reconstructed FROG traces on a logarithmic scale. (c) Retrieved time-dependent pulse (solid black line) and calculated BWL pulse (dashed blue line) with FWHM = 15 and 13 fs, respectively. (d) Retrieved spectrum (solid black line) and spectral phase (dashed orange line) with GDD = 65 fs^2 and TOD = -2000 fs^3.

only the grating compressor to the VIS beam and performing a FROG measurement provided the measured and reconstructed FROG traces in Figure **3-14**(a) and (b). The retrieved pulse in Figure **3-14**(c) reveals a pulse width of 15 ± 1 fs, whereas the calculated BWL pulse shows a reachable pulse width of 13 ± 1 fs. The low-intensity pulse before the main optical pulse in the retrieved pulse indicates a certain amount of third-order dispersion. Figure **3-14**(d) displays the spectral phase and the values for the GDD $= 65$ fs^2 and TOD $= -2000$ fs^3. The opposite sign in TOD indicates the over-compression with the grating compressor compared to the other compressing systems (i) and (ii).

A non-negligible observation is the tilt of the measured FROG trace in Figure **3-14**(a). This tilt appears due to a lateral dispersion of the spectral components of the VIS beam. The spatial chirp leads to an appearance of the spectral components at different time delays at the FROG spectrometer. Nevertheless, the phase retrieval algorithm can not only deliver the pulse shape; it also performs a consistency check and corrects the lateral dispersion. The lateral dispersion constitutes a severe problem for the time-resolved pump-probe 2PPE experiments. The spatiotemporal chirped pulse causes at different spots on the sample at different times arriving spectral components, which broadens the FWHM(XC) or even distorts the actual hot electron dynamics in the sample. Closing the apertures for the VIS beam and a slit for the UV beam so that the highest intensity center (main optical pulse) could pass through the apertures resulted in a spatiotemporal overlap leading to the shortest FWHM(XC) ~ 60 fs.

Application of the compressing systems in the time-resolved 2PPE experiments

Different setups have been used to analyze the dispersion in the VIS beam by the FROG measurement technique. By gaining knowledge about the retrieved pulse durations and the spectral phases, it is possible to compare the optical pulse compression systems in Figure **3-11**(i)-(iii). The data clearly indicates that relying solely on a prism compressor does not yield sufficiently short pulses with reduced high-order dispersion. The shortest pulse is obtained when a chirped mirror compressor is added to the prism compressor after the BBO crystal. This double optical compression system takes much place on the optical table and restricts the flexibility in the arrangement of the setup.

In contrast, the grating compressor requires less space on the optical table, but the disadvantage here is the low output power (< 5 mW) after compression of the VIS pulse. The low output power would have provided an insufficient pump fluence $F < 50$ μJ/cm^2 for the time-resolved 2PPE measurements. This led to the use of a prism compressor and a chirped mirror compressor for the VIS pump beam. The grating compressor was used for the UV probe beam where the output power was sufficient. All these efforts allowed to improve the FWHM of the XC by ~ 20 fs, compared to the FWHM(XC) ~ 80 fs in the previous tr-

2PPE measurements published in [84]. The shorter pulse durations allowed a more detailed analysis with smaller error bars, facilitating a comprehensive understanding of the local and nonlocal relaxation dynamics of hot electrons in Au/Fe/MgO(001) thin films, as discussed in chapter 4.

4. Relaxation dynamics of hot electrons analyzed via tr-2PPE

The ultrafast hot electron local and nonlocal relaxation dynamics in the unoccupied states of the band structure have been studied by performing femtosecond time-resolved two-photon photoemission (2PPE) with two different experimental configurations. In Figure **4-1**(a) are both experimental configurations depicted. In case of the front pump-front probe (FP)
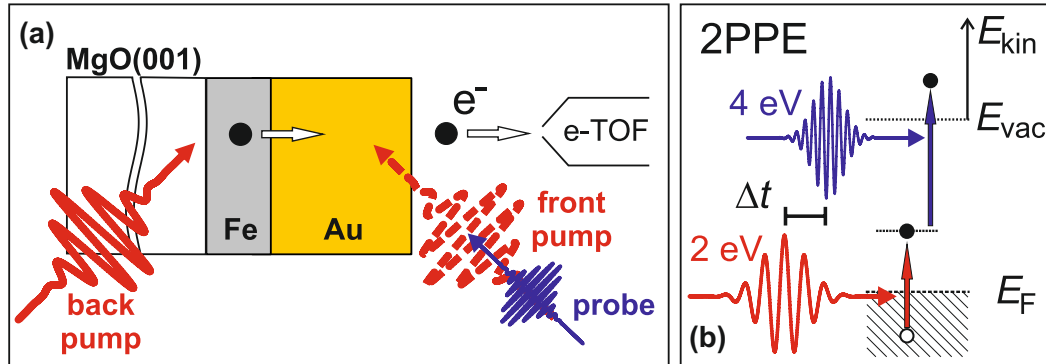
Figure 4-1: (a) Sketch of the excitation schemes for tr-2PPE on Au/Fe/MgO(001) thin films: In the case of the front-pump-front-probe geometry, excitation is performed by a VIS pump pulse (dashed red) and investigation by a UV pulse (blue) on the Au surface. In the case of the back pump-front probe configuration, excitation occurs in the Fe layer and probing occurs at the Au layer surface. The photoexcited electron (black circle) is injected from the Fe layer into the Au layer across the Fe/Au interface. The electron arriving at the Au surface is photoemitted by the UV pulse and detected by an electron time-of-flight (e-TOF) spectrometer. (b) Illustration of the two-color 2PPE process as a function of energy for the absorption of a 2 eV and 4 eV photon. The electron is excited into the energy region of the intermediate state by a 2 eV pump pulse and probed by a time-delayed 4 eV pulse above the E_{vac} level [84].

scheme on Au/Fe/MgO(001) thin films, the photoexcitation of hot electrons by a VIS pump pulse and the probe by a time-delayed UV pulse proceeds on the Au surface of the sample. A VIS pump pulse with the photon energy $h\nu_1 = 2$ eV photoexcites hot electrons around 2 eV above the Fermi level E_F in the Au layer. The photoexcited hot electrons experience

transport to the Fe layer across the Au/Fe interface. Ultrafast propagating hot electrons with the Fermi velocity v_F of approximately 1.4 nm/fs [27] leads to a depletion of high energy electrons at the Au surface. The remaining non-equilibrated electrons on the Au surface are probed by a time-delayed UV pulse with a photon energy of $h\nu_2 = 4$ eV. Photoemitted electrons out of the sample are then detected by a (p-e TOF) spectrometer.

The same photon energies $h\nu_1$ and $h\nu_2$ are also used in the back-side pumping front-side probing (BP) experimental configuration. The 0.5 mm MgO(001) crystal is transparent for the VIS pump pulse due to its band gap of 7.8 eV [127], thus the photoexcitation of hot electrons takes place in the Fe layer. The excited electrons undergo spatiotemporal transport from the Fe layer toward the Au surface across the Fe/Au interface. At the Au surface, arriving electrons are photoemitted by a time-delayed UV pulse. As in the front pump-front probe geometry, the analysis of photoemitted electrons is conducted by the p-e TOF spectrometer.

In Figure **4-1**(b), a schematic of the time-resolved two-color 2PPE process is shown. In this process, the work function Φ of the sample is larger than the applied photon energies $h\nu_1$ and $h\nu_2$, so at least two photons are required to photoemit electrons from the sample. A visible 2 eV pump pulse photoexcites electrons from occupied states into unoccupied states above the Fermi level E_F. Subsequently, a time-delayed UV pulse with 4 eV probes the hot electrons above the vacuum energy level E_{vac}. The front-side pumping front-side probing time-resolved 2PPE has so far allowed the analysis of transport processes in noble metals indirectly by analyzing the measured hot electron relaxation times. This analysis involves studying the measured relaxation times of hot electrons and employing theoretical calculations based on the Boltzmann equation [47,128,129]. Because of the strong interaction between local relaxation and transport processes, it is desirable to separate the contributions experimentally to circumvent the limitations of the theory.

It has been proven in time-resolved optical measurements that the back-side pumping front-side probing scheme is a well-suited approach to study transport processes of non-equilibrated electrons [27,34,35]. Applying this unconventional pump-probe scheme in combination with ultrafast time-resolved photoelectron spectroscopy (PES) opens the chances for exploring the interplay among local relaxation and transport processes of non-equilibrated electrons energy-resolved in the time domain. It might support an understanding of the elementary processes of non-equilibrated electrons and bring novel insights into the propagation behavior of hot electrons in Au/Fe/MgO(001) thin films and electron dynamics inside such heterostructures.

4.1. Absorption profiles in Au/Fe/MgO(001)

In previous works, experimental approaches such as tr-optical measurements and tr-PES have been established to investigate the transient hot charge carriers dynamics in metallic

thin films [15, 27, 28, 48, 109]. This research field has evolved and initiated the analysis of transient electron dynamics in metallic heterostructure thin films [35, 46, 54, 81, 84]. Due to the excitation of hot charge carriers by ultrashort laser pulses in the different layers, it is essential to calculate the absorption depth in the respective constituents of the heterostructure to infer the electron dynamics.

For a comprehensive understanding of the hot electron dynamics in Au/Fe/MgO(001) thin films, pump-laser absorption depth profiles in the Au and Fe layers have been calculated for the Fe-side (BP) and Au-side (FP) pumping geometries. The amount of laser light reaching the Au and Fe layers is determined by the Lambert-Beer law (in differential form) and the IMD software developed by Windt et al. [130]. It is developed for modeling the optical properties (reflectance, transmittance, electric-field intensity, etc.) of multilayer thin films and is based on applying Fresnel equations. The intensity distribution in the sample system is estimated by $I(z) = |E(z)|^2 = I_0 e^{-\alpha z}$ with the depth z, initial intensity I_0 and electric field E. The absorption coefficient is given by $\alpha = 4\pi k/\lambda$ with the extinction coefficient k and optical wavelength λ. The transmitted power $P(z)$ in the individual layers is given by the real part of the Poynting vector [131], resulting in

$$P(z) = n(z)I(z) = n(z)|E(z)|^2 = n(z)I_0 e^{-\alpha z}, \tag{4-1}$$

with the refraction index $n(z)$ of the material at the respective photon energy.

In Figure **4-2**, the depth profiles of differential absorption $dP_A(z)$ and relative absorbed power $P_A(z)$ are shown for the two excitation schemes (a) Fe-side and (b) Au-side pumping with $d_{Au} = 7$, 30, and 70 nm at constant $d_{Fe} = 7$ nm. The differential absorption power dP_A – absorbed power per length unit – is calculated by $dP_A(z) = n(z)\alpha|E(z)|^2$. The relative absorbed power is obtained by subtracting the transmitted power and normalizing the incoming intensity to 1 due to the interest in the attenuation of the field by absorption. The absorption depth profiles are determined by using the IMD software with the following optical parameters; pump photon energy $h\nu_{pump} = 2.1$ eV, angle of incidence $\Theta = 45°$, p-polarization of the light, refractive indices $n_{Au}(2.1 \text{ eV}) = 0.25$, $n_{Fe}(2.1 \text{ eV}) = 2.91$ and the extinction coefficients $k_{Au}(2.1 \text{ eV}) = 3.07$, $k_{Fe}(2.1 \text{ eV}) = 3.02$ [132].

For Fe-side pumping, the depth profiles for the absorption density show clearly that the absorption proceeds mainly in the Fe layer; 96% for $d_{Au} = 7$ nm, 94% for $d_{Au} = 70$ nm. A sharp attenuation of dP_A at the Fe/Au interface appears due to the high reflectance (88%) of Au for a photon energy of 2.1 eV. Due to the efficient light absorption in Fe compared to Au, hot electrons generated in the Au layer by the pump laser pulse will be neglected in the analysis of transport effects.

In case of Au-side pumping in Figure **4-2**(b), different absorption profiles appear; for the
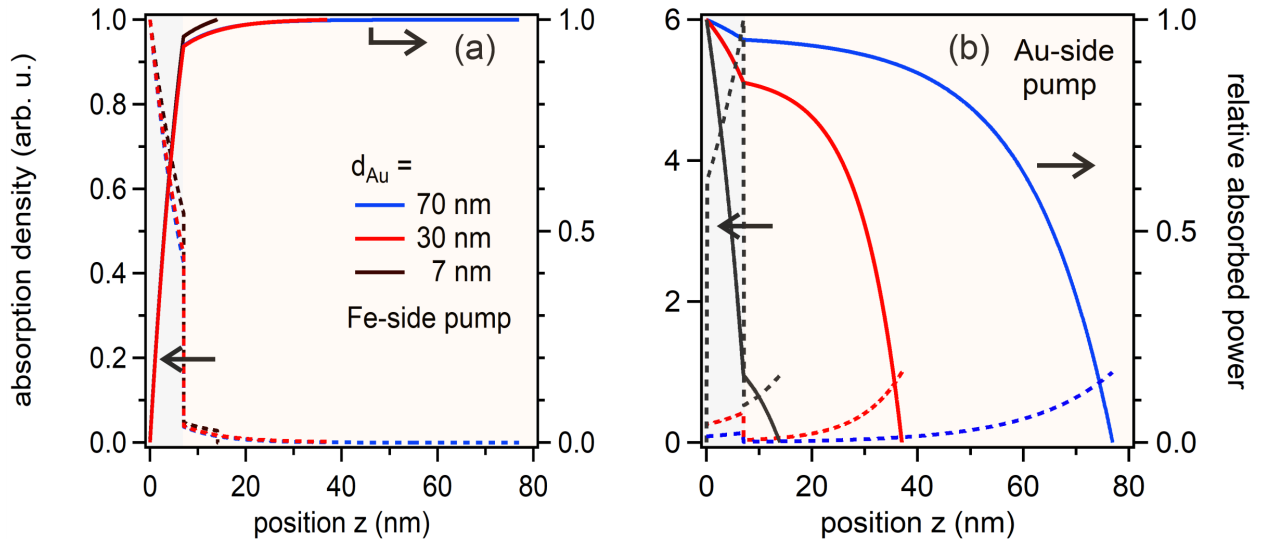
Figure 4-2: Absorption depth profiles for Au thicknesses $d_{Au} = 7$, 30 and 70 nm (yellow shaded area) at constant Fe-thickness layer of $d_{Fe} = 7$ nm (gray shaded area) with (a) Fe-side pumping and (b) Au-side pumping experimental geometries. Calculation of differential power absorption $dP_A(z)$ (left axis) and relative absorbed power P_A (right axis). In case of Fe-side pumping in (a): Quantities normalized to 1 at $z = 0$ for dP_A and at $z = \infty$ for P_A. For Au-side pumping in (b): $dP_A(z)$ normalized to 6 at $z = 0$, while P_A normalized to 1 at $z = \infty$.

thinnest Au film with $d_{Au} = 7$ nm, the excitation occurs mainly in the Fe layer in which 84% of the laser power is absorbed. In the thicker Au films $d_{Au} = 30$ and 70 nm the influence of the excitation scheme is apparent. Due to the 85% absorbed power in the Au layer at 30 nm and 95% at 70 nm the excitation in the Fe layer falls short. As a result, in the case of Au-side pumping geometry, the excitation in the Fe layer becomes less pronounced as the thickness of the Au layer increases.

The calculation and presentation of the absorption depth profiles in the Au/Fe/MgO(001) thin films as a function of Au thickness will support the discussion and understanding of the dynamics of photoexcited hot electrons in the following sections. The results from Figure **4-2** indicate that the absorption of the laser light in the respective constituents depends on the excitation geometry and the Au thickness d_{Au}, which will be useful in the data analysis.

4.2. Time-resolved 2PPE data analysis

Performing femtosecond time-resolved 2PPE spectroscopy on Au/Fe/MgO(001) thin films for various Au thicknesses d_{Au} and fixed Fe film thicknesses d_{Fe} using the FP and BP pump-probe schemes resulted in the 2PPE data shown in Figure **4-4**. Note that the data shown are only a selection of many more with different Au thicknesses. Here, one can investigate

the dynamics of transiently populated intermediate states energies for the Au thicknesses $d_{Au} = 7$, 30, and 70 nm.
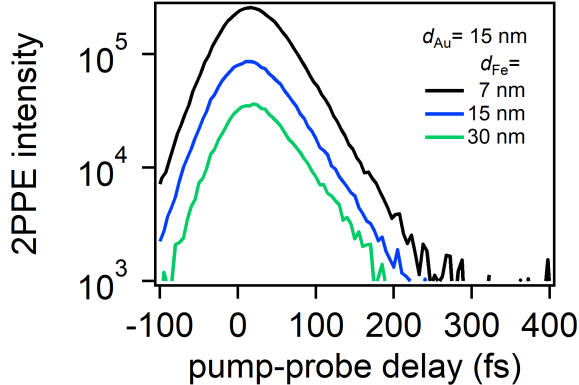
Figure 4-3: Time-dependent 2PPE intensity upon back-side pumping at $E - E_F = 1.0$ eV shown for different Fe thicknesses d_{Fe} and fixed Au thickness $d_{Au} = 15$ nm [84].

The Fe layer thickness is kept constant at $d_{Fe} = 7$ nm for each measured Au layer thickness. The reason is the signal-to-noise (S/N) ratio. Our results in Figure **4-3** obtained by our back pump-front probe measurements on Au/Fe/MgO(001) thin films show that a thicker Fe layer encompasses a decrease in the S/N ratio. This drop in the S/N ratio is mainly due to the short inelastic mean free path of the hot electrons in Fe with $\lambda_{Fe} \approx 2$ nm [36, 80]. The hot electrons scatter to lower intermediate state energies $E - E_F < 0.5$ eV and are not observable in our measured energy range. Thus, to maintain the S/N ratio in the presented experiments as high as possible, the Fe layer thickness is kept at $d_{Fe} = 7$ nm. Further insights about the Fe film thickness effect on hot charge carrier dynamics in Au/Fe/MgO(001) thin films can be taken from [29].

4.2.1. Analysis of Au-side pump time-resolved 2PPE data

In Figure **4-4**(a)-(c) one can see the 2PPE intensities in the dependence of time delay t (horizontal axis) and intermediate state energy $E - E_F$ (vertical axis) acquired by the Au-side pumping (FP) scheme on Au/Fe/MgO(001). The measurements are carried out on seven different Au thicknesses, which range from 7 to 70 nm. The results with $d_{Au} = 7$, 30 and 70 nm are shown to describe the transient non-equilibrated hot electron dynamics as a function of Au thickness d_{Au}. The white color in these false-color maps represents the peak intensity, while dark blue is the lowest intensity in the 2PPE yield, as the color scale shows. The colors are not quantitatively comparable due to the individual normalization[1] of each plot. Nevertheless, the relative intensities can be compared qualitatively, which will be shown in the further sections of the analysis. The time zero, where the time delay is $t = 0$ fs, is determined by performing a Gaussian fit at the highest intermediate state energy electrons, which stands for the first detected signal with negligible small decay times. Thus, the fit at $E - E_F = 2.10$ eV with an energy window of 100 meV delivered an ultrashort cross-correlation width of FWHM(XC) = 60 fs, as presented in detail in section 3.5.

---

[1]Normalization of the false-color maps is done by dividing each 2PPE intensity by the maximum intensity in the respective false-color map.
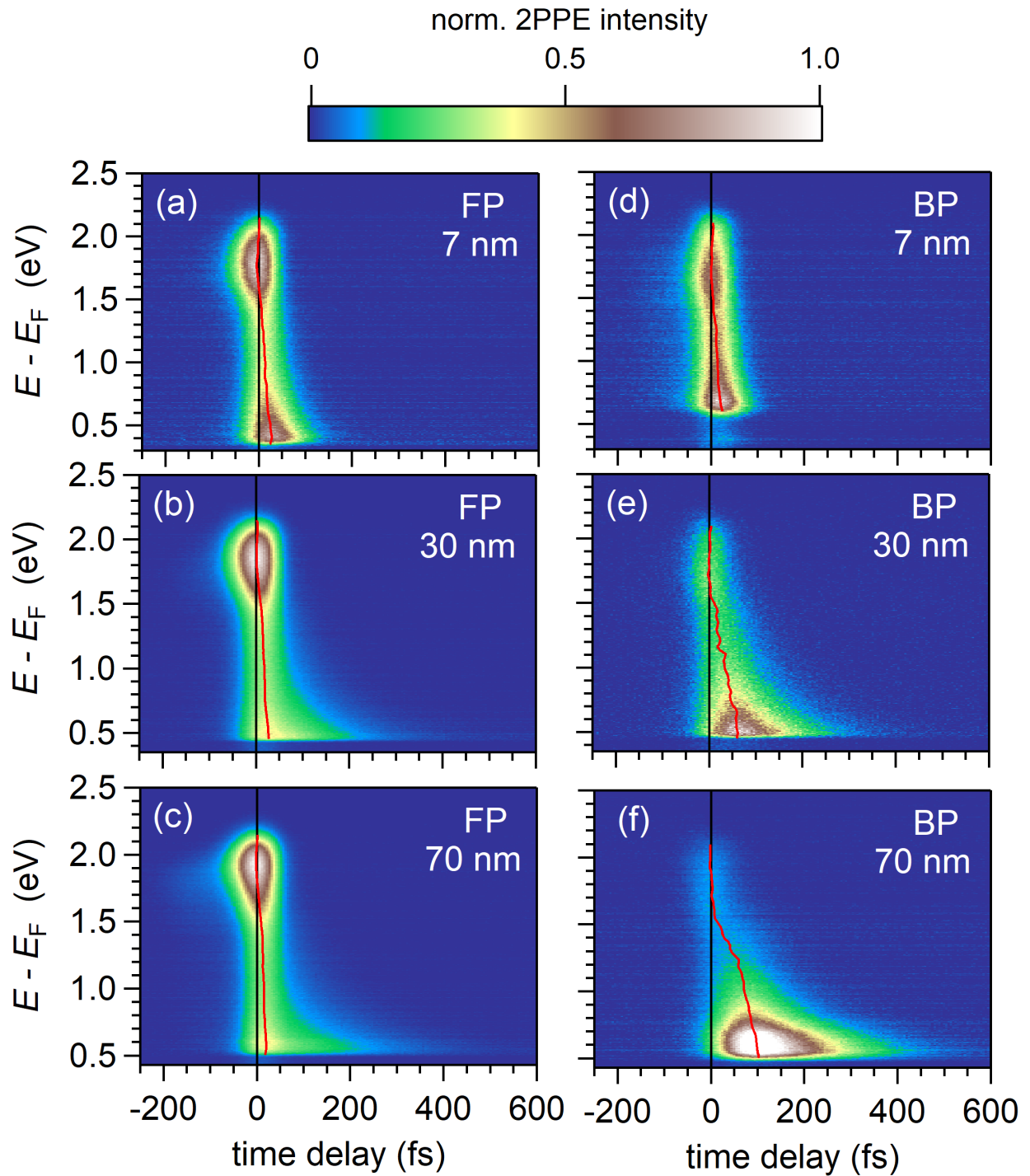
Figure 4-4: False-color maps of time-resolved 2PPE yields for Au thicknesses d_{Au} as indicated and constant $d_{Fe} = 7$ nm; (a)-(c) front pump-front probe geometry and (d)-(f) back pump-front probe experimental configuration. The red lines correspond to the maximum 2PPE intensity at each energy window as a function of time delay.
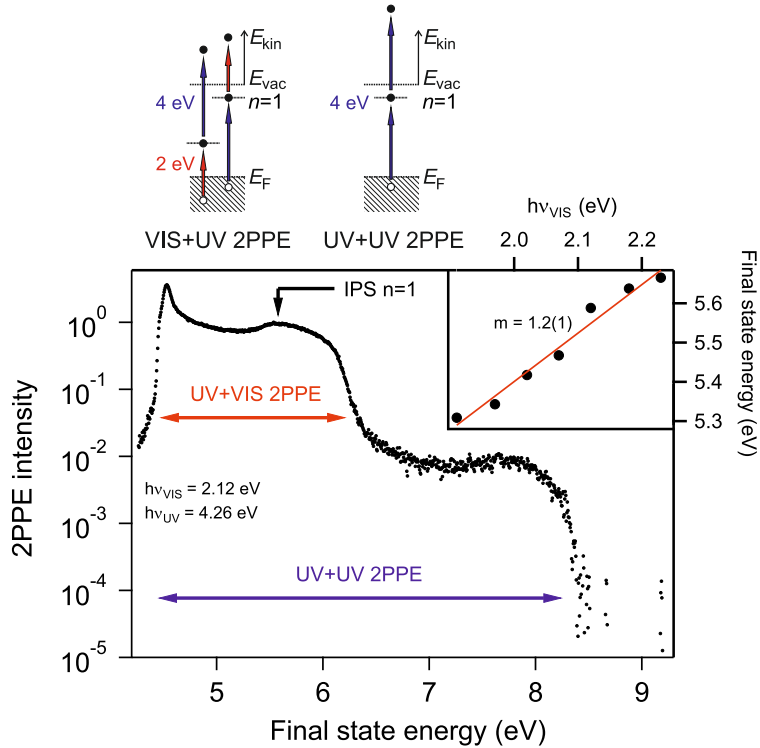
Figure 4-5: 2PPE spectrum taken at the temporal overlap of visible (VIS) and ultraviolet (UV) femtosecond laser pulses shown as a function of final state energy with respect to the Fermi energy. Two- and one-color contributions are indicated. The inset shows the photon energy dependence of the peak's final state energy labeled IPS ($n = 1$). The dependence is fit by a linear equation with a proportionality constant m as indicated.

Image potential state at the Au(001) surface

In Figure **4-4**(a)-(c) appears a high-intensity peak around the intermediate state energy $E - E_{\mathrm{F}} \approx 1.75$ eV. The transient population of this state decays toward negative time delays and indicates a UV-VIS pump-probe sequence. Accordingly, this UV-excited feature is actually around the intermediate state energy $E - E_{\mathrm{F}} \approx 3.75$ eV and represents the first image potential state (IPS, $n = 1$) with a binding energy of 0.8 eV to the vacuum level E_{vac} [63, 133]. This assignment of the lowest IPS ($n = 1$) at Au(001) surface is going to be explained as follows: Figure **4-5** shows a two-photon photoemission (2PPE) spectrum, which allows distinguishing between one-color (UV+UV) and two-color (UV+VIS) absorption of two photons and photoelectron generation. The low energy cutoff is determined by the vacuum energy E_{vac}. The high energy cutoffs in UV and UV+VIS are set by the Fermi energy of the Au surface plus the respective photon energy of the two photons. See also the 2PPE energy diagram in Figure **4-1**(b). An acceleration voltage of $U_{\mathrm{B}} = 0.1$ V was applied to detect the full spectrum including the low energy cutoff.

We identify a peak at 5.6 eV, which matches the energy of the first image potential state (IPS, $n = 1$) with a binding energy of 0.8(1) eV with respect to E_{vac} [63, 133]. Photon energy dependent measurements with determined peak energies given in the inset of Figure **4-5** support this assignment. The rather broad linewidth of the IPS indicates electron scattering at the Au surface assigned to residual gas adsorption occurring during sample exposition to ambient conditions while mounting the sample or defects at the surface. The lifetime of the image potential state IPS ($n = 1$) at the Au(001) surface is estimated by a fit of the XC
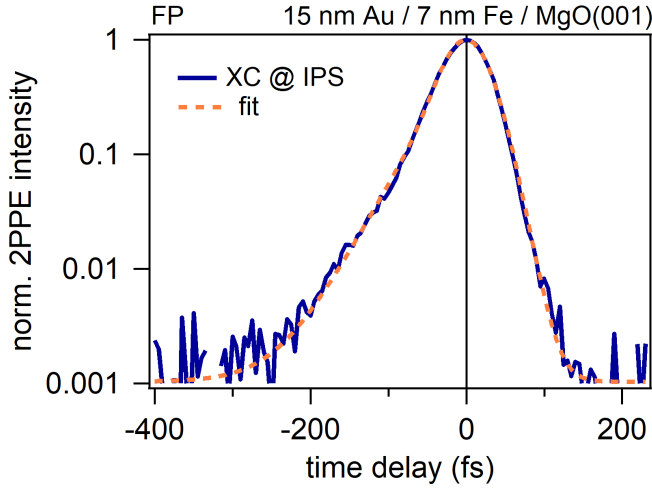
Figure 4-6: Tr-2PPE spectroscopy on 15 nm Au / 7 nm Fe / MgO(001) with FP geometry: Time-dependent 2PPE signal (blue solid line) of the IPS ($n = 1$) with the fit (orange, dashed line), which delivers a lifetime of $\tau = 36 \pm 3$ fs.

transient, as depicted in Figure **4-6**. The extracted lifetime amounts $\tau = 36 \pm 3$ fs, which is in good agreement with the lifetime of IPS state ($n = 1$) at Cu(001) surface [43].

Transient hot electron relaxation dynamics

The focus of this thesis work is mainly on the transient hot electron population dynamics at positive pump-probe time delays, with excitation by the VIS light pulse $h v_1 = 2.10$ eV and the probing of these photoexcited electrons by a time-delayed UV pulse $h v_2 = 4.13$ eV, as outlined in Figure **4-1**(b). The transient 2PPE intensity distribution for $d_{\mathrm{Au}} = 7$ nm in Figure **4-4**(a) shows a relatively fast relaxation for the intermediate state energy window between 2.1 eV and 0.4 eV. This relative fast relaxation is evident compared to the thicker Au layers $d_{\mathrm{Au}} = 30$ nm and $d_{\mathrm{Au}} = 70$ nm in Figure **4-4**(b) and (c), respectively. The decay slows down for all three thicknesses from high intermediate state energies $E - E_{\mathrm{F}}$ toward the Fermi level E_{F}.

Another observation in Figure **4-4**(a)-(c) is that a temporal shift of the peak intensity occurs toward lower intermediate state energies. To analyze this temporal shift in peak intensity as a function of Au thickness, a red line has been drawn over the maximum intensity of each energy window. For Au thicknesses $d_{\mathrm{Au}} = 7$, 30 and 70 nm, the temporal shifts of the peak traces were similar with a shift of about 25 fs, thus showing no d_{Au} dependence. These temporal shifts arise mainly from the local relaxation of hot electrons and secondary electrons and, thus, are not due to the delayed arrival of electrons.

However, this is different for Fe-side pumping and Au-side probing on Au/Fe/MgO(001). With this experimental geometry, it is possible to analyze the transport effects of hot electrons by photoelectron spectroscopy. This observation opens up new opportunities to study directly the interplay of relaxation and transport processes in an energy-resolved manner in the time domain.

4.2.2. Analysis of Fe-side pump time-resolved 2PPE data

Time-resolved 2PPE measurements with BP experimental configuration are performed on Au/Fe/MgO(001) thin films with 13 different Au thicknesses d_{Au} ranging from 5 to 70 nm with a constant Fe thickness d_{Fe} of 7 nm. In Figure **4-4**(d)-(f), we show the energy-resolved population dynamics of hot electrons for $d_{Au} = 7$, 30 and 70 nm. We find a difference in the width of the 2PPE spectra for 7 nm Au, 30 and 70 nm Au. The 2PPE spectrum width for 7 nm Au amounts to 0.2 eV smaller than for 30 and 70 nm Au thickness. This observation indicates a difference in the work functions Φ originating due to the different surface potentials for different surface structures.

As observed in the false-color plots for FP data, in case of tr-2PPE with BP geometry a spectral signature arises around $E - E_F \approx 1.8$ eV, see Figure **4-4**(d)-(f). However, a decay to negative time delays is not observable and thus does not seem to represent a UV-excited IPS state of Au(001). Recent spin- and layer-resolved time-dependent DOS calculations for Au/Fe heterostructures by Elaheh Shomali (AG Prof. Dr. Rossitza Pentcheva) indicate a spectral feature in the DOS of Fe-minority electrons $e^{\downarrow}$ at $E - E_F = 1.8$ eV. The hot electrons are excited mainly in Fe to these unoccupied minority states (d-band) and undergo ultrafast local and nonlocal relaxation dynamics. For thicker Au layers, e.g., $d_{Au} = 70$ nm, the intensity (population) at these Fe minority states decreases, which is due to enhanced inelastic e-e scattering processes during propagation over a longer distance. The ultrafast scattering leads to an increased population of lower intermediate energy states at later time delays, as shown in the plots in Figure **2-21**(e) and (f) for $d_{Au} = 30$ and 70 nm, respectively. The observation of these excited Fe-minority d-band states with the BP geometry demonstrates the sensitivity of this experimental approach to bulk and buried media in metallic heterostructures. This is a novelty in photoelectron spectroscopy which is primarily known for its surface sensitivity with the FP experimental approach.

The similar ultrafast relaxation behavior among the BP and FP data for 7 nm Au arise most likely due to the small dimension of the heterostructure 7 nm Au / 7 nm Fe/MgO(001). The optical excitation happens mainly in the Fe layer, as shown in Figure **4-2**(a,b). Therefore, the photoexcited electrons in the Fe layer play a significant role in the hot electron dynamics. This explains as well the faster decay behavior in thin Au layers compared to the thicker Au layers such as 30 and 70 nm Au in both experimental approaches FP and BP. Moreover, from the false-color plots for 7, 30, and 70 nm Au thickness in Figure **4-4**(d)-(f) it can be seen that the transient 2PPE intensity decays slower by increasing the Au thickness d_{Au}. Additionally, slower decay behavior appears in the transient 2PPE intensity toward lower intermediate state energies $E - E_F$ for all Au thicknesses in the BP data as it is observed for FP data.

A decisive difference arises in the red peak traces in the tr-2PPE data for back-side and

front-side pumping. The temporal shift of the peak traces starts between intermediate state energies of 1.5 and 1.6 eV for all Au thicknesses and increases toward lower intermediate state energies $E - E_{\mathrm{F}}$. An intriguing effect is that the maximal temporal peak shift increases with the Au thickness d_{Au}. While the shift of the peak trace at $E - E_{\mathrm{F}} = 0.6$ eV for 7 nm Au is about 23 fs, it is 58 and 98 fs for 30 and 70 nm, respectively. This dependence of the time shift of peak intensity on Au thickness is attributed to the transport effects of photoexcited, non-equilibrated electrons. For comparison, the difference between the time shift of peak intensity in 70 nm Au-side and Fe-side pump data is about 75 fs. This originates due to the interaction/ competition among ultrafast transport and scattering processes of hot electrons. While photoexcited, non-equilibrated hot electrons propagate quasi-ballistic from the Fe layer toward the Au layer surface, the electrons experience inelastic e-e scattering processes. These inelastic e-e scattering processes lead to the generation of secondary electrons which populate the low intermediate state energies and thus increase the time-dependent 2PPE yield at lower $E - E_{\mathrm{F}}$ with the Au thickness d_{Au}.

In summary, the temporal shift of the peak intensity traces increases with Au thickness d_{Au}. Moreover, a spectral feature was observed in the energetic region of the unoccupied d-band states. The Fe-minority electrons of the d-band $e^{\downarrow}$ populate lower intermediate energy states with a later time delay due to ultrafast inelastic e-e scattering processes. The observations suggest evidence for energy-resolved local and nonlocal relaxation dynamics in space and time. Thus, tr-2PPE spectroscopy with the Fe-side pump geometry represents a technique sensitive to bulk and buried media that is new to PES measurements. In the next section, analysis of the time-dependent 2PPE intensities will highlight the strength of this back-side pumping experimental approach on Au/Fe/MgO(001) thin films.

4.3. Electron dynamics in Fe/Au heterostructure

A variety of energy-dependent ultrafast scattering processes play an important role in the relaxation and transport dynamics of hot electrons in nanostructures. The interplay among local and nonlocal hot electron relaxation dynamics has been investigated for decades [27,46–48,84]. To unravel these energy-dependent spatiotemporal processes, time-dependent 2PPE intensities are analyzed for various parameters, such as the Au thickness d_{Au} and the energy $E - E_{\mathrm{F}}$. The tr-2PPE measurements have been carried out with the back-side (BP) and front-side (FP) pumping experimental geometries. We begin with the presentation of the time-dependent 2PPE intensities and describe them with emphasis on the intensity relaxation behavior and the temporal shift of the peak intensity as observed in the previous section for 2PPE data with BP geometry. Fitting processes were used to analyze the relaxation dynamics quantitatively. These fits provide the relaxation time τ and time offset t_0, which are the observables for local relaxation and transport processes. The propagation behavior of hot electrons from the Fe layer across the Fe/Au interface to the Au surface is found to

be superdiffusive. Furthermore, it is presented that the local relaxation of hot electrons in the constituents of Fe and Au can be distinguished from each other in the heterostructure.

4.3.1. Time-dependent 2PPE intensity relaxation behavior

With the purpose of quantitatively analyzing the local and nonlocal relaxation dynamics of hot electrons energy-resolved in the time domain, the cross-correlation (XC) traces are taken from the data in Figure **4-4** and are presented in Figure **4-7**.

In Figure **4-7**(a)-(c) are time-dependent 2PPE intensities for the FP and in Figure **4-7**(d)-(f) for the BP geometries depicted, whereby the intermediate state energies $E - E_{\mathrm{F}}$ range from 2.10 to 0.60 eV. The following relaxation behavior of the transient 2PPE yields are observed:

1. The decay of the transient intensities becomes slower toward E_{F} for all Au thicknesses d_{Au} and for both experimental configurations FP and BP.

2. Au thickness dependent relaxation behavior; the thicker the Au layer, the slower the relaxation of the transient 2PPE yield.

3. If one compares the XC traces for FP and BP data, the temporal shift of the XC intensity built up is more pronounced in BP data and at lower intermediate state energies $E - E_{\mathrm{F}}$. Moreover, the shift increases with Au thickness d_{Au}. Therefore, this effect is attributed to the delayed arrival of excited electrons at the Au-vacuum interface.

In Figure **4-8**(a), the time-dependent normalized 2PPE intensities for different Au thicknesses at $E - E_{\mathrm{F}} = 1.00$ eV depicts the nonlocal hot electron transport dynamics. The shift in time delay of the intensity built up increases with increasing d_{Au}. Looking at the normalized 2PPE peak intensity, we see between the time delay of the intensity built up for 5 and 70 nm Au a difference of 58 fs.

Another insight is the influence of the Au layer thickness on the 2PPE intensity dynamics range. We published in [84] that an increasing Fe thickness layer d_{Fe} results essentially in a loss of 2PPE intensity within the measured intermediate state energy range, as shown in Figure **4-3**. Such a loss of intensity is also observed with increasing d_{Au}, see Figure **4-8**(b). It presents the transient 2PPE intensity obtained with the BP experimental configuration for different Au thicknesses d_{Au} and a constant Fe thickness $d_{\mathrm{Fe}} = 7$ nm in Au/Fe/MgO(001) heterostructures. A reduction in the 2PPE intensity with an increasing d_{Au} is explained as follows. Photoexcited hot electrons injected from the Fe into the Au constituent propagate toward the Au surface [2]. These electrons relax by inelastic scattering processes with a larger probability in thicker Au layers than in thinner ones. Only those electrons can be detected at

---

[2]Transport phenomena arise from driving forces such as gradients in occupation number. A gradient in the hot electron density, which can be excited by optical absorption of femtosecond laser pulses within the optical absorption depth, drives electron currents [54].
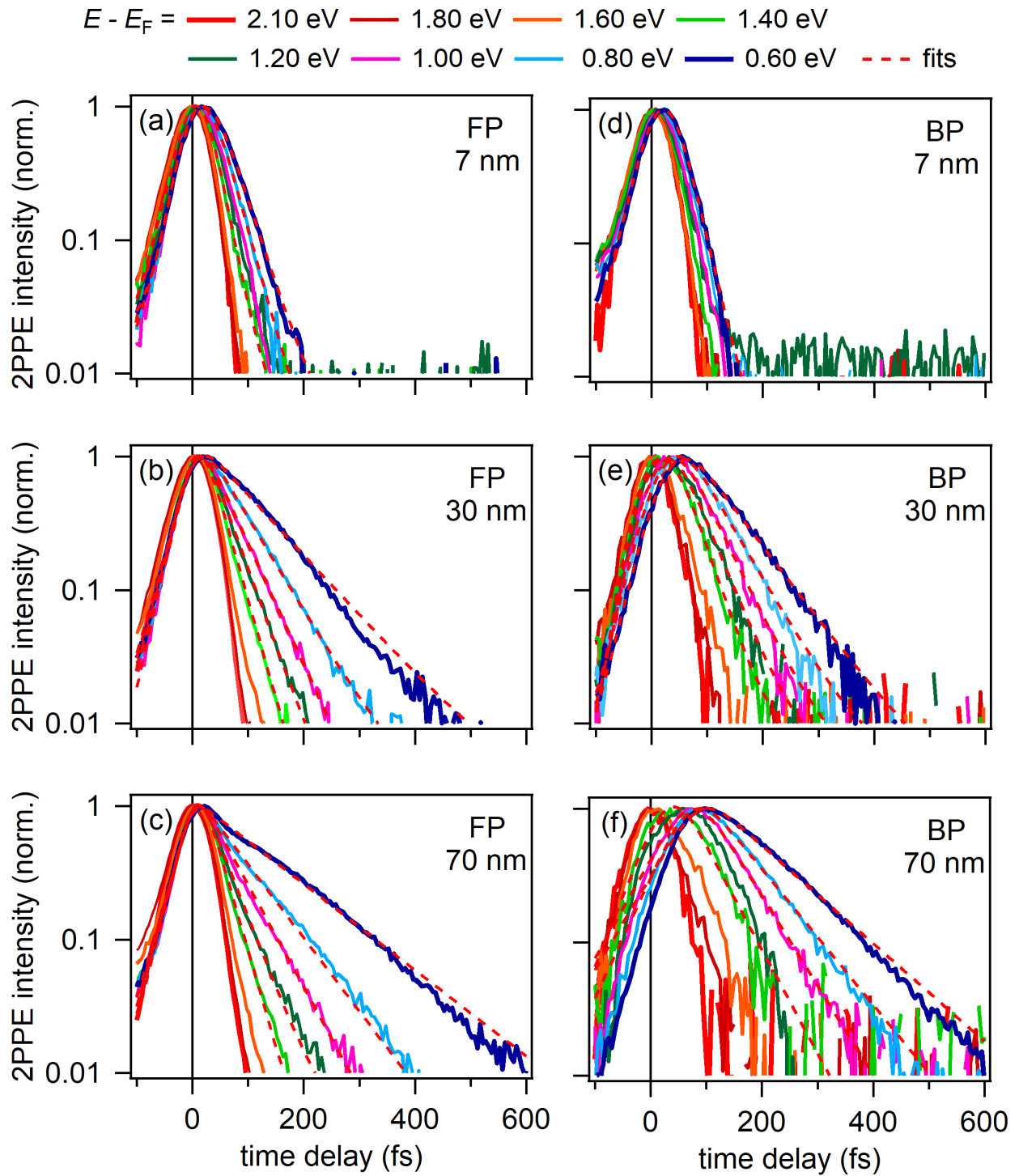
Figure 4-7: Normalized time-dependent 2PPE intensity on a logarithmic scale for (a)-(c) front and (d)-(f) back-side pumping with the fits (red dashed lines) at indicated energies above the Fermi level E_F.
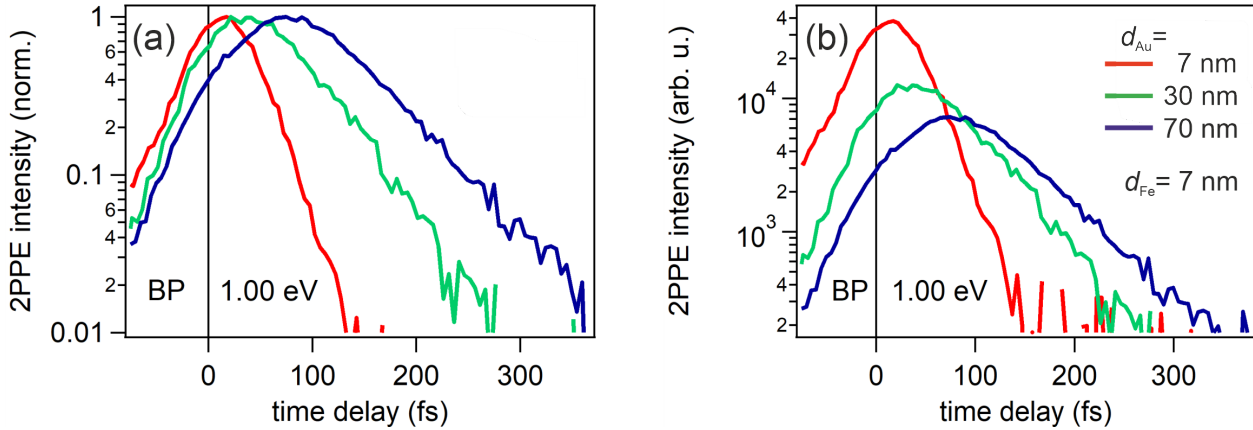
Figure 4-8: 2PPE intensity in the dependence of pump-probe time delay at intermediate state energy $E - E_F = 1.00$ eV for various Au-thicknesses d_{Au} and a fixed Fe-thickness $d_{Fe} = 7$ nm obtained by the back-side pumping experimental configuration; (a) normalized and (b) non-normalized 2PPE intensity.

the Au surface, which arrive at the analyzed energy and at the surface. Since we detect the 2PPE intensity as a function of energy $E - E_F$ the 2PPE intensity can indeed be expected to decrease with d_{Au}. A detailed analysis is not attempted because small variations of the pump-probe overlap might influence the 2PPE intensity.

Moreover, a temporal broadening of the time-dependent 2PPE intensities occurs for thicker Au layers, see Figure **4-8**(a). The thicker the Au layer, the longer becomes the transient 2PPE signal. Figure **4-7** demonstrates the energy-dependence in the temporal broadening. The effect is more pronounced at lower intermediate state energies than at higher intermediate states, which has already been predicted by Nenno et al. [83].

Figure **4-9** displays in a simplified picture the spatiotemporal evolution of the hot electron density profile in case of Fe-side pumping and Au-side probing experiment on Au/Fe/MgO(001) heterostructure. The photoexcited hot electrons in the Fe layer are elevated by a VIS pump pulse into energy states above the Fermi level E_F. These primary excited electrons experience a spatiotemporal transport from the Fe layer across the Fe/Au interface toward the Au layer surface, where they are probed by a time-delayed UV pulse. The ballistic propagation behavior of high energy electrons at short time scales ($t < \tau$) alternates at later time scales due to scattering events ($t \geq \tau$) the propagation behavior to superdiffusive or even at longer time scales ($t \gg \tau$) to diffusive transport behavior. Thus, owing to the inelastic e-e scattering processes, the velocity of the hot electrons becomes effectively reduced and a velocity distribution arises. The down-scattering of high-energy electrons to lower intermediate state energies $E - E_F$ and the upward-scattering of secondary electrons leads together with slower electrons to a longer/broader hot carrier density profile in space and time. Thus, i.e., a pure
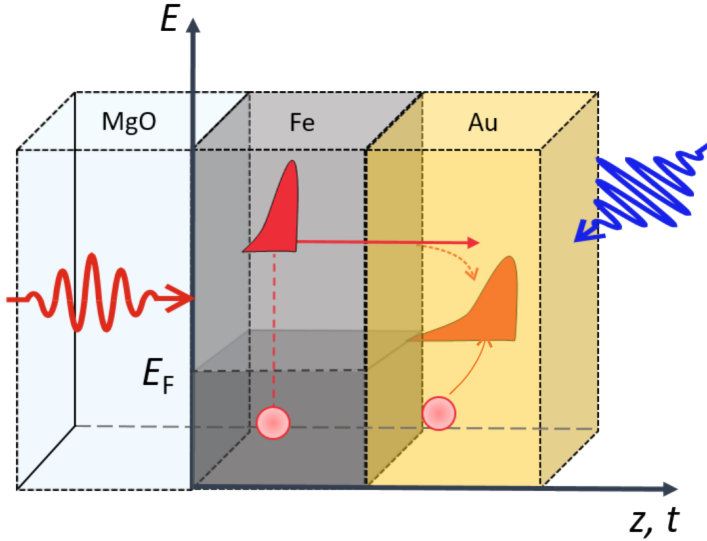
Figure 4-9: Sketch of Fe-side pumping and Au-side probing experimental configuration on Au/Fe/MgO(001) heterostructure; the interplay among transport and scattering processes of excited electrons causes a broadening of the hot carrier density distribution in space and time.

ballistic propagation behavior without a scattering of hot electrons is not apparent for the intermediate state energy $E - E_F = 1.00$ eV.

In order to quantify the local relaxation dynamics and investigate the transport behavior of the hot electrons, a fit procedure has been performed. Time-dependent 2PPE intensities for both geometries were fitted by two exponential decays convolved with the XC of the laser pulses as determined by 2PPE at maximum kinetic energy. Examples of such fits are plotted in Fig. **4-7** as red dashed lines. This fitting determines energy-dependent, inelastic relaxation times $\tau(E)$ and time offsets $t_0(E)$, representing observables for local and nonlocal relaxation dynamics. In the following the analysis of $\tau(E)$ and $t_0(E)$ for the Au thicknesses $d_{Au} = 7$, 30 and 70 nm with a constant $d_{Fe} = 7$ nm will be shown and discussed.

4.3.2. Interplay of local relaxation and transport processes

Hot electron relaxation and transport in nanostructures involve a multitude of energy-dependent ultrafast processes, such as the inelastic e-e, e-ph or e-m scattering and the hot electron propagation whose interplay is not fully understood [77]. To unravel these energy-dependent spatiotemporal processes tr-2PPE data are analyzed for a variety of parameters. Thus, subsection 4.3.2 is going to present the analysis of the relaxation time $\tau(E)$ and the time offset t_0 as a function energy $E - E_F$ and Au film thickness d_{Au} with two experimental approaches FP and BP. In subsections (a) to (c) are the observables for the Au thicknesses $d_{Au} = 7$ nm, 30 nm and 70 nm presented and described. This is followed by a discussion of (i) relaxation times $\tau(E)$ and (ii) time offsets $t_0(E)$. The discussions will show the influence of various parameters on the relaxation and transport dynamics of photoexcited electrons in Au/Fe/MgO(001) thin film heterostructures.

(a) 7 nm Au/7 nm Fe/MgO(001)
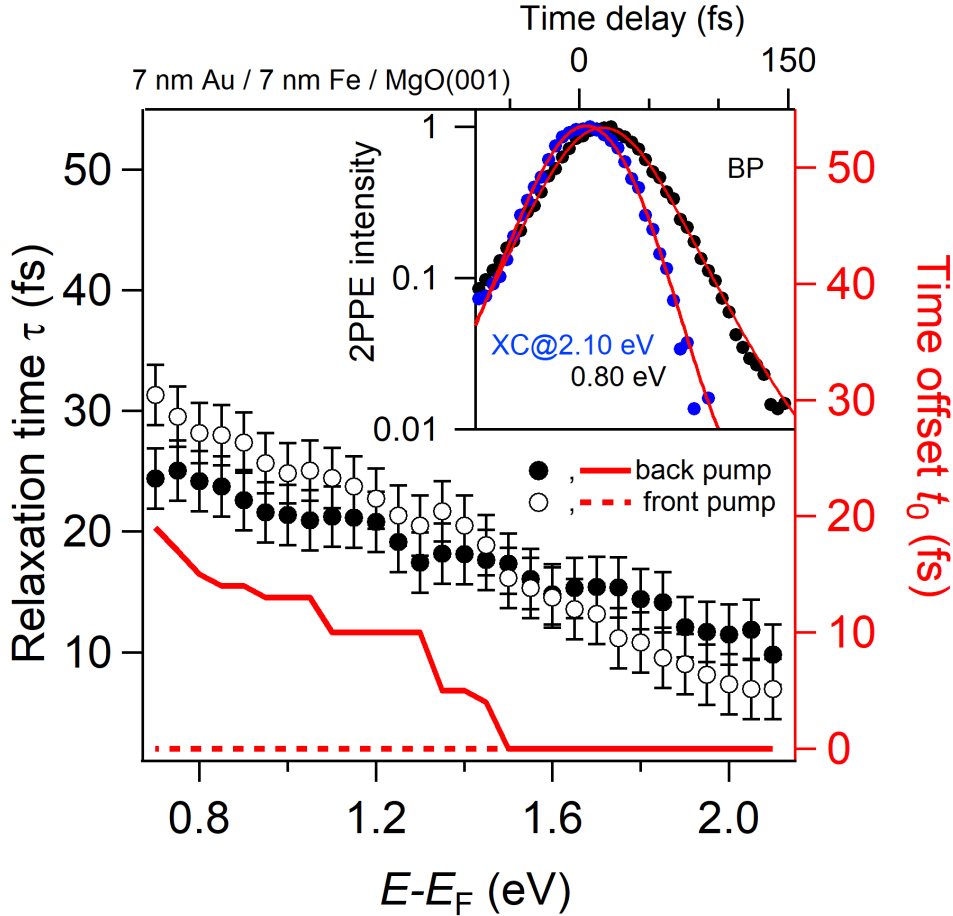
Figure 4-10: Left axis: Relaxation times τ of hot electrons at energies $E - E_\mathrm{F}$ for 7 nm thick Au films on 7 nm Fe on a MgO(001) substrate. Right axis: Time offset t_0. Both quantities are determined by fitting and are given for front- and back-side pumping as indicated. Error bars for t_0 are ± 6 fs at 0.8 eV and decrease to ± 2 fs at 2.1 eV. Inset: Fits of the transient 2PPE intensities at $E - E_\mathrm{F} = 2.1$ and 0.8 eV obtained by BP experimental approach.

Figure **4-10** shows the energy-dependent observables relaxation time $\tau(E)$ (left, black axis) and time offset $t_0(E)$ (right, red axis) obtained for $d_\mathrm{Au} = 7$ nm at $d_\mathrm{Fe} = 7$ nm. In the inset are the fits for the intermediate state energies 2.10 eV and 0.80 eV plotted and matched appropriately with the time-dependent 2PPE intensity data points[3]. The relaxation times $\tau(E)$ for BP and FP deliver the following results; for BP the relaxation times increase from $\tau = 10 - 25$ fs for the intermediate state energy range $E - E_\mathrm{F} = 2.1 - 0.6$ eV. In comparison, the relaxation times obtained in the FP data analysis increase from $\tau = 7 - 32$ fs for the

---

[3]The fits in the inset at $E - E_\mathrm{F} = 0.8$ and 2.1 eV are an example of fits in the range of 0.6 to 2.0 eV with 0.1 eV intervals.

same energy regime. In both cases is an increase in the relaxation times $\tau(E)$ toward the Fermi level E_F observable. Despite the similar values within the error bars of ± 2 fs for both relaxation times, an energy-dependent difference is observable. The relaxation time τ_{7nm}^{FP} for the energy regime $E - E_F = 2.1 - 1.6$ eV is shorter with respect to τ_{7nm}^{BP}, while the reverse occurs below $E - E_F = 1.4$ eV.

The time offsets for front pump $t_0^{FP}(7 \text{ nm})$ remain the same at 0 fs for the intermediate state energy range. At first, this seems controversial to the observations from Figure **4-7**(a)-(c), in which a temporal shift, albeit small, in the FP transients appears. Here one has to realize that this temporal shift arises due to the relaxation time τ. As was discussed in Figure **2-22**, the convolution of an exponential decay function with a Gaussian laser pulse cross-correlation produces a temporal shift in the XC curve of the 2PPE data. Therefore, a negligible temporal shift can be observed, which does not affect the time offset $t_0^{FP}(7 \text{ nm})$.

However, in back-side pumping data an increase in $t_0^{BP}(7 \text{ nm})$ from 0 to 22 fs is revealed. While the time offset with $t_0^{BP}(7 \text{ nm})$ between $E - E_F = 2.10 - 1.50$ eV remains with 0 fs the same, below 1.5 eV a significant increase appears. This rise in time offset $t_0^{BP}(7 \text{ nm})$ between 1.5 and 0.6 eV intermediate state energies shows the sensitivity of time-resolved 2PPE back-side pumping experimental configuration in detecting transport effects, even in thin films like the 7 nm Au/7 nm Fe/MgO(001) heterostructure.

(b) 30 nm Au/7 nm Fe/MgO(001)

Figure **4-11** shows the energy-dependent relaxation times $\tau(E)$ and time offsets $t_0(E)$ for 30 nm Au/ 7 nm Fe/ MgO(001). The inset reveals the exemplary fits for the 2PPE intensities of the intermediate state energies $E - E_F = 2.10$ and 0.80 eV. The relaxation time for back-side pumping at the energy 2.10 eV amounts to $\tau_{30nm}^{BP} = 20$ fs and increases up to 85 fs at low energy 0.55 eV. This energy-dependence of increased relaxation time at lower intermediate state energies is also observed for front pump relaxation time τ_{30nm}^{FP}, rising from 10 to 103 fs for the same intermediate state energies. The front-side pumping relaxation times reveal a nearly inversed quadratic energy scaling with respect to the E_F level, $\tau \sim (E - E_F)^{-2}$, as predicted by FLT [14, 72, 134]. In contrast to this inverse quadratic scaling of relaxation time τ and intermediate state energy $E - E_F$, back-side pumping relaxation times τ_{30nm}^{BP} exhibit an anomaly around $E - E_F = 1.4 - 1.9$ eV and amount between 30 to 40 fs. This anomaly in relaxation time τ_{30nm}^{BP} deviates from FLT, which will be analyzed and discussed in section 4.4. Nevertheless, between $E - E_F = 2.10$ and 1.2 eV is $\tau_{30nm}^{BP} > \tau_{30nm}^{FP}$ and below $E - E_F = 0.8$ eV this reverses again, as it was observed for $d_{Au} = 7$ nm in Figure **4-10**. This observation arises due to an interplay between the propagation direction of the hot electrons and the detection volume by the probe pulse at the Au surface, which will be discussed in subsection 4.3.3 with Figure **4-17**.
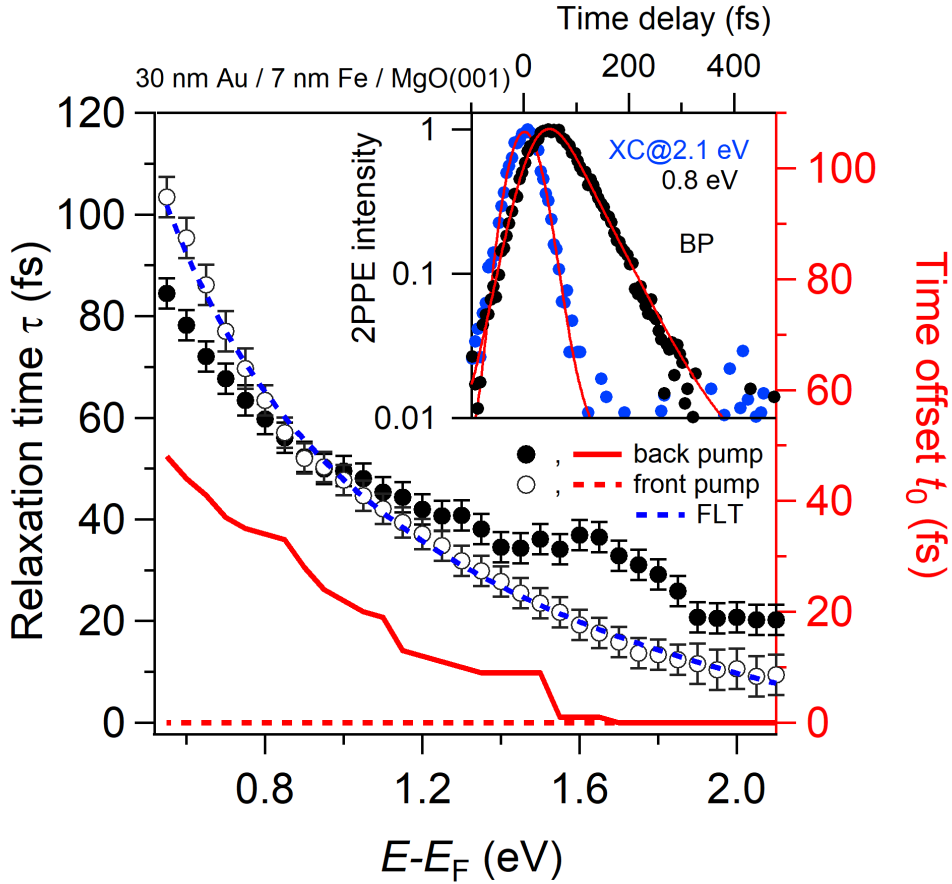
Figure 4-11: Left axis: Relaxation times τ of hot electrons at energies $E - E_F$ for 30 nm thick Au films on 7 nm Fe on a MgO(001) substrate. The blue dashed line shows the FLT behavior of τ_{FP}. Right axis: Time offset t_0. Both quantities are determined by fitting and are given for front- and back-side pumping as indicated. Error bars for t_0 are ± 8 fs at 0.8 eV and decrease to ± 2 fs at 2.1 eV. Inset: Fits of the transient 2PPE intensities at $E - E_F = 2.1$ and 0.8 eV obtained by BP experimental approach.

The energy-dependent time offset $t_0(E)$ for Au-side pumping 2PPE keeps at 0 fs for the energy window $E - E_F = 2.10 - 0.55$ eV. In case of the Fe-side pumping 2PPE data analysis, the time offset $t_0^{BP}(30\text{ nm})$ is 0 fs between 2.10 and 1.70 eV and increases from 1.65 eV to 0.55 eV up to $t_0^{BP}(30\text{ nm}) = 48$ fs.

(c) 70 nm Au/7 nm Fe/MgO(001)

The energy-dependent relaxation time $\tau_{70\text{nm}}^{BP}$ and time offset $t_0^{BP}(70\text{ nm})$ for the Au-side and Fe-side pumping 2PPE on 70 nm Au/ 7 nm Fe/MgO(001) are depicted in Figure **4-12**. As seen in $\tau_{30\text{nm}}^{FP}$ the relaxation time $\tau_{70\text{nm}}^{FP}$ also scales similar to the inverse quadratic intermediate state energy, $\tau \sim E - E_F^{-2}$. For the energies from 2.1 to 0.6 eV the relaxation
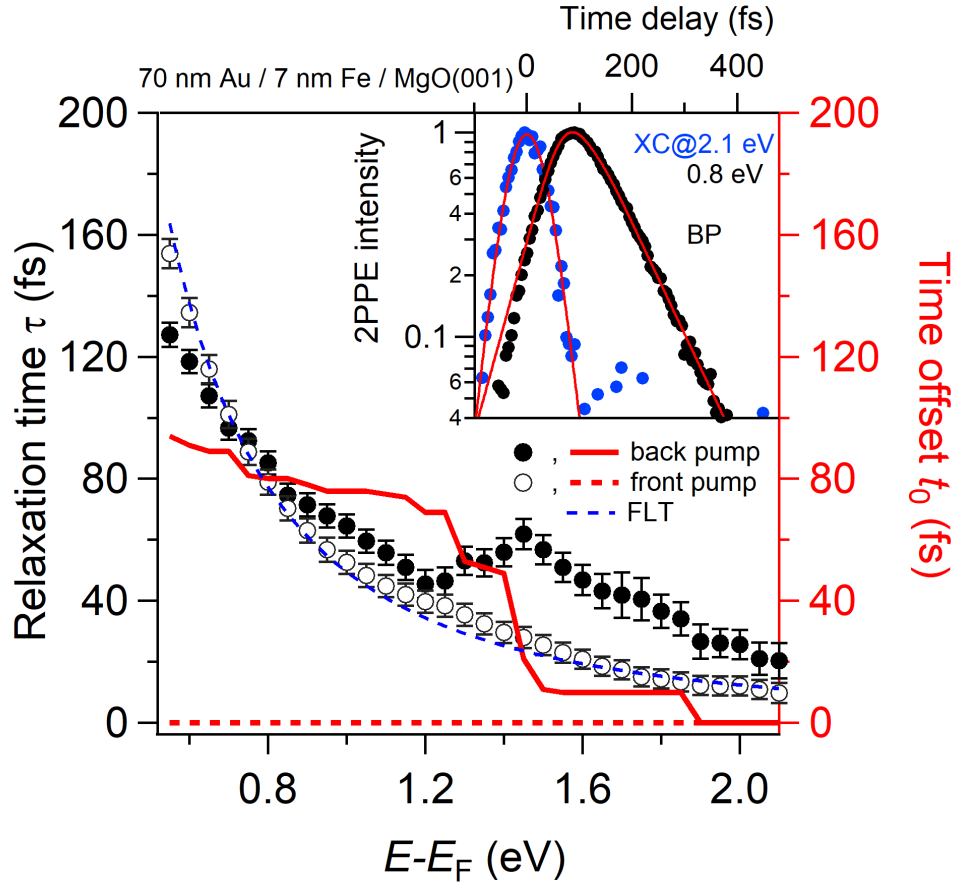
Figure 4-12: Left axis: Relaxation times τ of hot electrons at energies $E - E_F$ for 70 nm thick Au films on 7 nm Fe on a MgO(001) substrate. The blue dashed line shows the FLT behavior of τ_{FP}. Right axis: Time offset t_0. Both quantities are determined by fitting and are given for front- and back-side pumping as indicated. Error bars for t_0 are ± 11 fs at 0.8 eV and decrease to ± 3 fs at 2.1 eV. Inset: Fits of the transient 2PPE intensities at $E - E_F = 2.1$ and 0.8 eV obtained by BP experimental approach.

times $\tau_{70\mathrm{nm}}^{\mathrm{FP}}$ increase from 10 to 135 fs. The relaxation time for back-side pumping data corresponds to $\tau_{70\mathrm{nm}}^{\mathrm{BP}} = 20 - 118$ fs for the same energies. Between $E - E_F = 2.10 - 1.2$ eV the relaxation times of back pump exceeds with $\tau_{70\mathrm{nm}}^{\mathrm{BP}} = 20 - 47$ fs the relaxation time of front pump $\tau_{70\mathrm{nm}}^{\mathrm{FP}} = 9 - 38$ fs. Thereby is again, as for $\tau_{30\mathrm{nm}}^{\mathrm{BP}}$ recognized, an anomaly in the relaxation time observable. The maximum relaxation time within this intermediate state energy regime $E - E_F = 2.10 - 1.2$ eV, where the anomaly is pronounced, is $\tau_{70\mathrm{nm}}^{\mathrm{BP}} = 62$ fs at 1.45 eV, which is in comparison to the anomaly in 30 nm with $\tau_{30\mathrm{nm}}^{\mathrm{BP}} = 37$ fs at 1.60 eV larger and shifted in energy. This anomaly in the relaxation times τ_{BP} arises due to an issue in the fitting procedure, which will be discussed in more detail in section 4.4.

The time offset for front-side pumping does not change with $t_0^{\mathrm{FP}}(70\text{ nm}) = 0$ fs for the energy regime $E - E_F = 2.10 - 0.60$ eV and highlights the non-observation of nonlocal

relaxation effects by the front-side pumping experimental configuration. Contrary to this, the back pump time offset increases by decreased energy with $t_0^{\mathrm{BP}}(70 \text{ nm}) = 0 - 91$ fs for $E - E_{\mathrm{F}} = 2.10 - 0.60$ eV, which is larger with respect to the obtained $t_0^{\mathrm{BP}}(7 \text{ nm})$ and $t_0^{\mathrm{BP}}(30 \text{ nm})$ for the same energy range. Consequently, this observation emphasizes the d_{Au}-dependency in the local and nonlocal relaxation dynamics. Moreover, for 70 nm Au/ 7 nm Fe/ MgO(001) between the intermediate state energies 1.35 to 0.90 eV the back-side pumping time offset $t_0^{\mathrm{BP}}(70 \text{ nm})$ exceeds the relaxation time $\tau_{70\mathrm{nm}}^{\mathrm{BP}}$, which has not been observed for $d_{\mathrm{Au}} = 7$ and 30 nm in Figs. **4-10** and **4-11**, respectively.

(i) Discussion of the relaxation times τ

The study of the relaxation times $\tau(E)$ for different Au thicknesses d_{Au} with a constant $d_{\mathrm{Fe}} = 7$ nm in Au/Fe/MgO(001) thin films has yielded the following results. By comparing the energy-dependent relaxation times $\tau(E)$ for all Au thicknesses d_{Au}, as shown in the Figure **4-10**, **4-11** and **4-12**, $\tau(E)$ decreases with increasing energy. This is explained by the fact that, according to the FLT, at higher energies the phase space for inelastic e-e scattering increases and leads to faster decay since there are more states to scatter into. Nevertheless, for 7 nm Au thickness the relaxation times $\tau(E)$ for back and front-side pumping 2PPE spectroscopy exhibit no inversed quadratic energy scaling with respect to the energy above E_{F}, see Figure **4-10**. Yet, this scaling law $\tau \sim (E - E_{\mathrm{F}})^{-2}$ is revealed for the relaxation times τ_{FP} measured on the Au thicknesses 30 and 70 nm as shown in Figures **4-11** and **4-12**, respectively. In the case of BP, τ_{BP} deviates from the scaling $\tau \sim (E - E_{\mathrm{F}})^{-2}$, and instead, an anomaly is observed in the relaxation time that shows sensitivity to both energy and the thickness of the Au layer d_{Au}. This anomaly leads to longer relaxation times for BP compared to FP, particularly evident in thicker Au layers; $\tau_{\mathrm{BP}} > \tau_{\mathrm{FP}}$ for the energy range $E - E_{\mathrm{F}} = 2.1 - 1.3$ eV. In contrast, no anomaly in τ_{BP} and τ_{FP} was observed for the 7 nm thin Au film. However, it becomes evident that the excitation geometry (FP or BP) and the Au layer thickness d_{Au} significantly influence the relaxation dynamics. A detailed discussion of the observed anomaly in relaxation times τ_{BP} will be presented in section 4.4.

An interesting observation is as well the Au thickness dependence of $\tau(E)$ in Au/Fe/MgO(001) film. If compared at identical energies, τ is larger for thicker Au films than for thinner ones. For instance, at an intermediate state energy $E - E_{\mathrm{F}} = 1.0$ eV, the relaxation times are $\tau_{\mathrm{FP}} = 21, 51,$ and 65 fs for $d_{\mathrm{Au}} = 7, 30,$ and 70 nm, respectively. This d_{Au}-dependency of energy-dependent hot electron relaxation time is due to the opposite thickness dependence of $\tau(E)$ quite remarkable in comparison to previous studies [46–48]. Cao et al. [48] performed front-side pumping time-resolved 2PPE on an Au(111) single crystal and on films with different thicknesses. They could not find any significant thickness dependence in the energy-dependent relaxation times of photoexcited electrons. In contrast, in time-resolved 2PPE on Au films by front-side pumping, Aeschlimann and co-workers ob-

served a thickness dependence of $\tau(E)$ of hot electrons due to ultrafast transport effects [47]. They measured shorter relaxation times $\tau(E)$ with increased Au thickness. This opposite behavior, with respect to our observation, in the thickness dependence of $\tau(E)$ was also observed by Lisowski et al. with front-side pumping time-resolved 2PPE on Cu/Si(111)-7×7 [46]. The reason is the fundamentally different relaxation dynamics of hot electrons in the Au/Fe/MgO(001) heterostructure compared to Au(111) or Cu/Si(111)-7×7 films. Thus, considering all three material systems with the FP time-resolved 2PPE technique, the following local and nonlocal relaxation dynamics are obtained in the material system.

For [47] and [46] the employed substrates were insulating materials. Thus, nonlocal transport processes of hot electrons through the metal/insulator interface are hindered and subsequently do not escape, in case of thin metallic films, from the probing depth near the surface region. This leads to longer relaxation times in thin films. In thicker Au(111) and Cu(111) films, the photoexcited electrons propagate from the sample surface deeper toward the bulk. Consequently, a population decay in the near-surface region occurs, which leads to shorter relaxation times.

In case of Au/Fe/MgO(001) heterostructure, the Fe layer plays a decisive role in the observed Au thickness dependent relaxation times. Since Fe exhibits d-bands in the relevant energy range, the inelastic e-e scattering phase space is large, which leads to short relaxation times $\tau_{\mathrm{Fe}} \approx 2 - 5$ fs [69]. In comparison, Au shows mainly sp-bands in the same unoccupied energy states and due to the large inelastic electron mean free path $\lambda_{\mathrm{Au}} \approx 57 - 100$ nm the relaxation time ranges between $\tau_{\mathrm{Au}} = 60 - 110$ fs [34,80]. Accordingly, in time-resolved 2PPE on thin Au layers, as $d_{\mathrm{Au}} = 7$ nm, short relaxation times $\tau = 10 - 20$ fs refer to the pronounced contribution of the Fe layer in the detected 2PPE signal. For thicker Au layers the contribution of the Fe layer becomes considerably weaker. It can be inferred that the excitation density profile (section 4.1) and optical penetration depth λ_{opt} governs the contribution of the heterostructure constituents to the photoemission signal, which determines the relaxation times $\tau(E)$ of the hot electrons.

(ii) Discussion of the time offsets t_0

With Fe-side pumping time-resolved 2PPE variations in $t_0(E)$ occur up to 22, 48 and 91 fs for $d_{\mathrm{Au}} = 7$, 30 and 70 nm, respectively. In case of Au-side pumping $t_0(E)$ do not vary. The observed $t_0(E) > 0$ fs for Fe-side pumping is a nonlocal effect and quantifies the time required for the transport of electrons excited in Fe, injected into Au across the Fe-Au interface, and propagation through Au toward the Au-vacuum interface, where they are probed in 2PPE. Following bulk optical constants, above 90% of the absorbed pump pulse intensity excites the 7 nm Fe layer, and the 2PPE signal detected for X nm Au/ 7 nm/MgO(001) (X = 5 to 100 nm) with the respective Au thickness X is dominated by electrons propagating through Au. This assignment is supported by the increase in t_0 and τ for the larger d_{Au} compared

to the thinner one; see Figure **4-10**, **4-11** and **4-12**. Since relaxation times of hot electrons in metals at few eV energy above E_F are determined by inelastic e-e scattering [69], the similar trend of increasing t_0 and τ with decreasing energy indicates that t_0 is determined by inelastic e-e scattering as well. On this basis, the electron transport through Au is concluded to proceed in a superdiffusive regime, which occurs before hot electrons have thermalized by subsequent e-e scattering events [82], as discussed in chapter 2.

In this work, a superdiffusive transport behavior is identified by comparing the propagation time t_0 and the inverse scattering rate τ, which are found in Figure **4-10**, **4-11**, and **4-12** to be of the same order of magnitude. This implies individual scattering events during the hot electron spatiotemporal transport and differs from ballistic and diffusive regimes. The latter requires many scattering processes starting from an optically excited electron distribution. Ballistic propagation, on the other hand, would occur for absent relaxation, which disagrees with the observed temporal broadening in time-dependent 2PPE intensities while the electrons propagate through Au, see Figure **4-8**. Given the weak variation of the electron group velocity with respect to the Fermi velocity in Au [83] ballistic propagation is also incompatible with the increase in t_0 observed with decreasing energy. Scattering might increase the covered distance to the surface and a determination of the electron's propagation velocity $v = d_{Au}/t_0$, which results for $d_{Au} = 30$ nm at $E - E_F = 1.0$ eV in $v = 1.35$ nm/fs – a value close to v_F in Au – has to be treated with care. We note that we cannot exclude ballistic propagation of electrons $E - E_F \geq 1.7$ eV where we find $t_0 = 0$ fs for $d_{Au} = 30$ nm, which is set by the time zero determination.

For Fe-side pumping 2PPE analysis, the comparison of the time offsets $t_0(E)$ for the Au thicknesses 7, 30, 70 nm show a thickness- and energy-dependency in rising $t_0 > 0$ fs, see Figure **4-10**, **4-11** and **4-12**. While the time offset in 7 nm Au becomes $t_0^{BP}(7 \text{ nm}) > 0$ fs first at $E - E_F = 1.45$ eV, it already happens for 30 and 70 nm at $E - E_F = 1.65$ and 1.85 eV, respectively. As a result, the thicker the Au layer, the more likely one sees a change in time offset $t_0(E)$ at higher hot electron energies. Accordingly, at higher intermediate state energies, the propagating hot electrons are more prone to inelastic e-e scattering in thicker Au layers than in thin layers. Time offset $t_0 > 0$ fs in thicker Au layers at higher intermediate state energies, might indeed show that at energies, where $t_0 = 0$ fs, a ballistic propagation appears. However, it is crucial to exercise caution while interpreting these observations, and further investigations are warranted to fully understand the underlying mechanisms governing the observed behavior.

The investigation of hot electron propagation behavior in MgO(001)/Fe/Au has been done as well by other researchers such as Melnikov et al. [34], and Alekhin et al. [35, 37]. They performed Fe-side pumping time-resolved optical measurements on a series of Fe/Au layers with various Au thicknesses (≤ 130 nm). It is claimed that the transport of hot electrons

to the Au surface was observed at a velocity of about 1.3 nm/fs, which is close to the Fermi velocity in Au $v_{\mathrm{F}} = 1.4$ nm/fs [27] and represents the ballistic transport behavior. However, optical pump-probe experiments provide energy- and momentum-integrated information about the relaxation dynamics of hot electrons. Due to the energy-dependent dynamics of hot electrons, pump-probe photoemission experiments, such as Fe-side pumping Au-side probing 2PPE, can provide energy-resolved information on local scattering and nonlocal transport effects. As shown above in Figure **4-10**, **4-11**, and **4-12**, a few scattering events during spatiotemporal transport of hot electrons in Au indicate the superdiffusive transport behavior.

4.3.3. Separation of e^- dynamics in the individual Fe/Au constituents

By investigating hot electron dynamics for $d_{\mathrm{Au}} = 5 - 70$ nm, thickness dependent relaxation time $\tau = \tau(d_{\mathrm{Au}})$ has been identified, see Figure **4-10**, **4-11** and **4-12**, which is for thinner films smaller than in bulk Au [69]. Figure **4-13** shows $\tau(d_{\mathrm{Au}})^{-1}$ for different energies. To understand this thickness dependence, a continuum approach to scattering in the heterostructure is considered, which assumes that the individual thicknesses d_{Au}, d_{Fe}, and the extension of the interface $d_{\mathrm{Au-Fe}}$ are comparable with the respective scattering lengths $\lambda_i \approx \tau_i \cdot v_{\mathrm{F},i}$, which are ≈ 50 nm in Au and ~ 2 nm in Fe [36,80]. The integral scattering probability of electrons propagating in the interface normal direction z increases linearly with d_{Au}, d_{Fe}, and $d_{\mathrm{Au-Fe}}$:

$$\int\limits_0^{d_{\mathrm{Fe}}+d_{\mathrm{Au-Fe}}+d_{\mathrm{Au}}} \frac{dz}{\tau(z)} = \frac{d_{\mathrm{Fe}}}{\tau_{\mathrm{Fe}}} + \frac{d_{\mathrm{Au-Fe}}}{\tau_{\mathrm{Au-Fe}}} + \frac{d_{\mathrm{Au}}}{\tau_{\mathrm{Au}}}. \tag{4-2}$$

In the 2PPE back-side pump front-side probe experiment, the variation of d_{Au} allows separation of two independent processes, see Appendix B, described by

$$\frac{1}{\tau(d_{\mathrm{Au}})} = \frac{1}{\tau_1} + \frac{1}{\tau_2} = A + \frac{B}{d_{\mathrm{Au}}}. \tag{4-3}$$

Figure **4-13**, depicts fits[4] following Equation 4-3 with A and B being the intercept with the ordinate and slope as a function of $1/d_{\mathrm{Au}}$, respectively. Note that both A and B/d have the dimension of a rate. Our analysis determines relaxation times τ_1 and τ_2 which are plotted in Figure **4-14** in comparison with literature values for hot electron lifetimes in bulk Au and Fe $\tau_{\mathrm{Au}}, \tau_{\mathrm{Fe}}$, respectively, taken from Ref. [69]. Given the agreement of the measured data with these literature values, it is concluded to have distinguished the electron dynamics in the two constituents and thereby demonstrate sensitivity to the buried Fe film.

---

[4]For small d_{Au} of the order of $d_{\mathrm{Fe}} = 7$ nm, we observe systematic deviations of the linear fit from the experimental data. The fit tends to overestimate the measured relaxation rates. In our recently submitted work, we discussed this problem and corrected it with a nonlinear fitting approach [100].
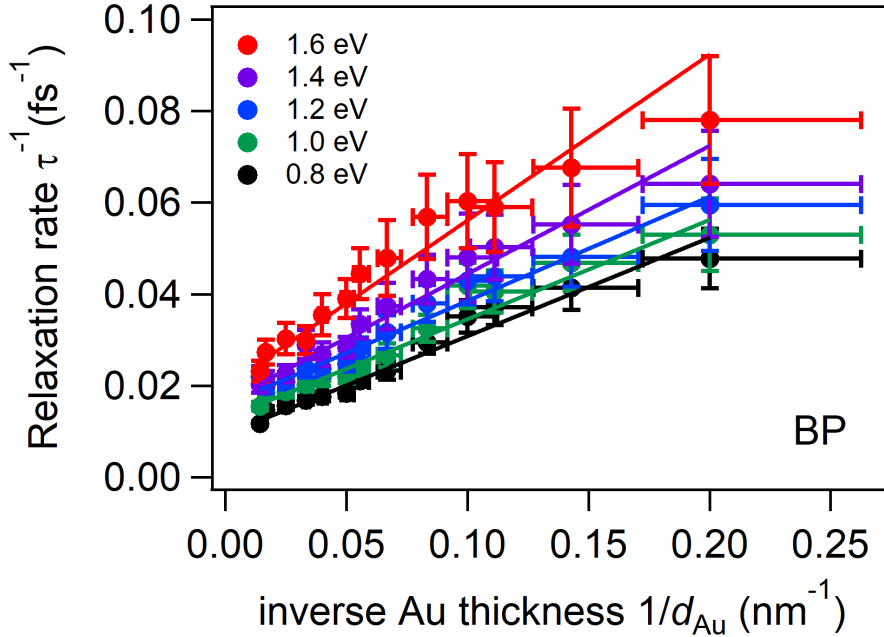
Figure 4-13: Relaxation rates τ^{-1} as a function of d_{Au}^{-1} for different electron energies above E_F obtained by BP experimental configuration. Lines represent linear fits. Slopes and intercepts determine the two relaxation rates discussed in the text.

The observation of τ_{Au} is straightforward to understand. A hot electron injected into Au at the Fe-Au interface propagates through the Au film and reaches the surface where it is photoemitted. During the propagation, it experiences inelastic e-e scattering with rates of bulk Au and transfers energy to a secondary electron. This scattering is detected by the time-dependent reduction of 2PPE intensity at the energy of interest at which the electrons were injected into Au. Secondary electrons were not taken into account because the energy scale is restricted to rather high values $E - E_F$, where primary electrons dominate [46]. Secondary electrons start to contribute at half the primary energy [69], which is $E - E_F < 1$ eV for the highest energy electrons at 2.1 eV studied here. For sufficiently thick Au films, the second term in Equation 4-3 vanishes, and scattering in Au dominates. Understanding the determination of τ_{Fe} in buried Fe requires consideration of all processes that may contribute to B in Equation 4-3. Following Equation 4-2 scattering in Fe and at the Au-Fe interface has been taken into account. Since within the experimental uncertainty $\tau_2 = \tau_{Fe}$ is found, scattering at the interface does not contribute. In the investigated epitaxial heterostructure, electron injection across the interface can be assumed to proceed by coherent propagation of a wavepacket in Bloch states which conserves energy and momentum across the interface [35, 50]. Therefore, the injection process across the Au-Fe interface is ballistic and violates the above assumption $d_{Au-Fe} \approx \lambda_{Au-Fe}$, which might be a reason for not detecting it.

In addition, the back-side pumping front-side probing approach provides opportunities to
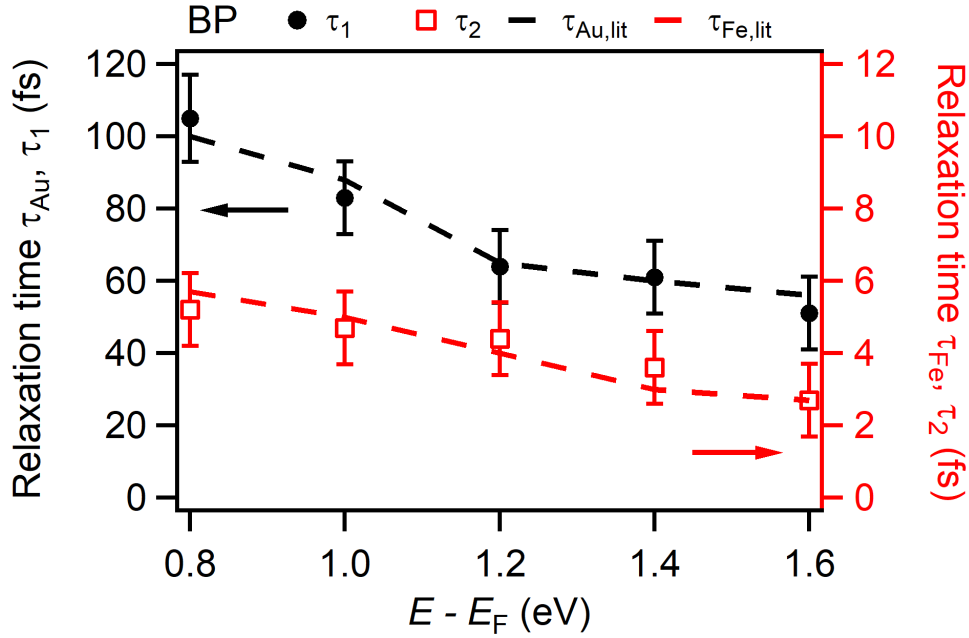
Figure 4-14: BP data analysis: Determined relaxation times τ_1 ($\bullet$) and τ_2 ($\square$) as a function of $E - E_F$ in comparison with literature data for hot electron lifetimes τ_{Au} and τ_{Fe} from Ref. [69] shown by dashed lines.

analyze scattering at buried interfaces originating from (i) electronic interface states and (ii) scattering at non-epitaxial interfaces for heterostructures in general. While (i) might be in analysis following Equation 4-3 through the appearance of anomalies in the energy-dependent relaxation times $\tau(E)$ and lead to the deviations from the smooth variation reported in Figure **4-14**, the impact of (ii) can be determined by changing the thickness of both constituents as introduced in Equation 4-2. As detailed in Appendix B, this would lead to an additional term in Equation 4-3 representing scattering at the interfaces.

This distinguishing of hot electron local relaxation dynamics in the individual constituents of Au/Fe/MgO(001) heterostructure by back-side pumping front-side probing approach was also achieved in the previous work by Beyazit et al. [84]. However, the measured relaxation times obtained within this thesis work show a better accuracy with respect to [84]. The reason might lie in the fact that in the new experiments, the employed FWHM(XC) of the laser pulses was roughly 60 fs, while in [84] it was broader with FWHM(XC) = 75 fs. Consequently, the shorter laser pulses improved the error bars for $\tau_1 = \tau_{Au}$ and $\tau_2 = \tau_{Fe}$ by factors 3 and 2, respectively. The bulk or buried media/interface sensitivity of the Fe-side pumping experimental configuration allowed the separation of local electron dynamics in the Au/Fe/MgO(001) heterostructure constituents. This raises the question of whether the same sensitivity can be achieved with the same analysis (Matthiesen's rule) for the relaxation times obtained by Au-side pumping geometry.

Separation of e$^-$ dynamics fails for Au-side pumping geometry

Figure **4-15** shows the relaxation rates τ_{FP}^{-1} as a function of the inverse Au thickness $1/d_{\mathrm{Au}}$ obtained from the inverse of the relaxation time τ_{FP}, which are attained by the analysis of front-side pumping 2PPE data.
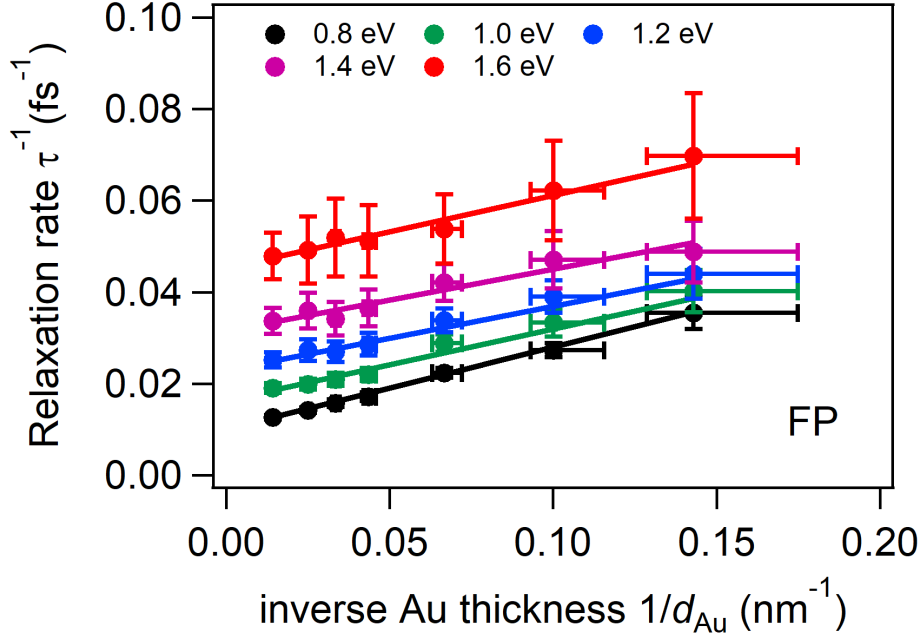
Figure 4-15: Relaxation rates τ^{-1} as a function of d_{Au}^{-1} for different electron energies above E_{F} obtained by FP experimental configuration. Lines represent linear fits. Slopes and intercepts determine the two relaxation rates discussed in the text.

The relaxation rates for different intermediate state energies in the range of $E - E_{\mathrm{F}} = 0.80 - 1.60$ eV are fitted by the same linear Ansatz (Matthiessen's approach) as for back-side pumping analysis, see Equation 4-3. From the intercept with the ordinate A and the slope B of the linear fitting curves the corresponding τ_1 and τ_2 have been determined and depicted together with literature values for τ_{Au} and τ_{Fe} as a function of $E - E_{\mathrm{F}}$ in Figure **4-16**. Comparing τ_1 and τ_2 with τ_{Au} and τ_{Fe}, respectively, yields a different result here for the Au-side pump data analysis than for the Fe-side pump. The relaxation times τ_1 and τ_2 obtained by Matthiesen's rule approach demonstrate no agreement with the literature values τ_{Au} and τ_{Fe} for the energy range $E - E_{\mathrm{F}} = 1.0 - 1.6$ eV, respectively. Only at $E - E_{\mathrm{F}} = 0.8$ eV appears a consistence with $\tau_1 = \tau_{\mathrm{Au}}$ and $\tau_2 = \tau_{\mathrm{Fe}}$. To be more accurate, one sees that toward lower $E - E_{\mathrm{F}}$ the differences between τ_1 and τ_2 decrease with respect to literature values τ_{Au} and τ_{Fe}. The error bars of the individual relaxation times also decrease toward the Fermi level E_{F}. However, despite using the same analytical approach, we fail to separate the local dynamics of hot electrons in the constituents of Au/Fe/MgO(001) for the experimental configuration of Au-side pumping.
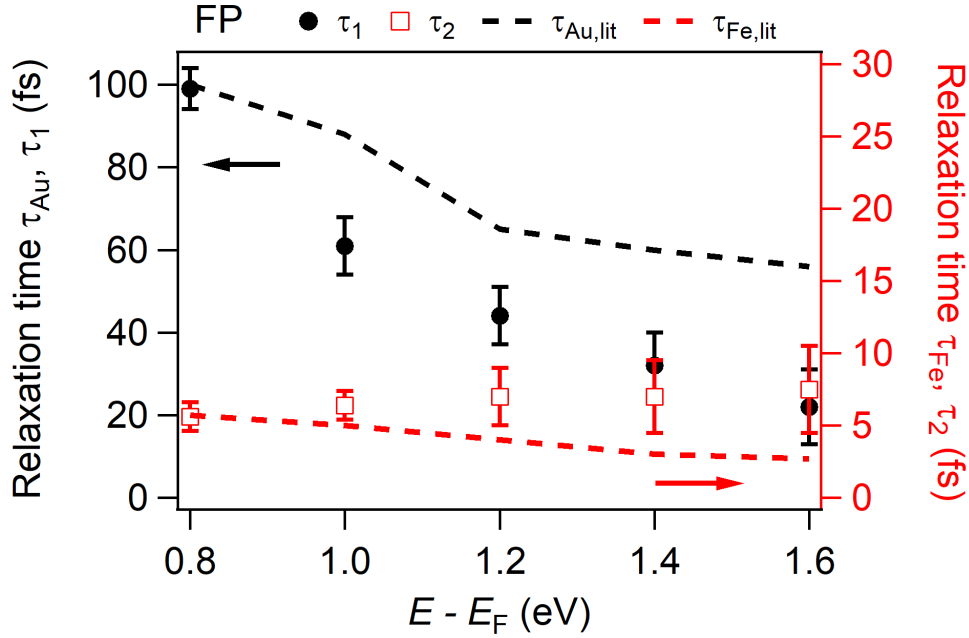
Figure 4-16: Analysis of FP data: Plot of the determined relaxation times τ_1 ($\bullet$, left axis) and τ_2 ($\square$, right axis) as a function of $E - E_F$ in comparison with literature data for hot electron lifetimes τ_{Au} and τ_{Fe} from Ref. [69] shown by black and red dashed lines, respectively.

Effect of photoexcitation geometry and optical penetration depth λ_{opt}

Hot electron dynamics follow different relaxation patterns, given the different photoexcitation conditions among the front- and back-side pumping time-resolved 2PPE on Au/Fe/MgO(001) heterostructure. The hot electron relaxation dynamics are mainly determined by the electronic band structure of the involved material in the pump-probe scheme. In the case of back-side pumping, the photoexcitation of hot electrons occurs in the ferromagnetic Fe layer, while the excitation in front-side pumping happens at the Au surface. Thus, different local and nonlocal relaxation dynamics are expected for both cases.

After photoexciting hot electrons in Fe, roughly 2 eV above the Fermi level E_F the hot electrons propagate toward the Au surface, where they are probed by a time-delayed UV pulse with a photon energy of $h\nu_2 \approx 4$ eV. The Fe layer serves as an injection layer of hot electrons into the Au layer.

However, in the case of front-side pumping, the hot electrons are excited at the Au surface and propagate toward the Fe layer across the Au-Fe interface, whereby the roles are exchanged so that the Fe layer serves as a sink layer. The different transport directions of the hot electrons influence the entire relaxation dynamics, which is observable in the relaxation times $\tau(E)$ in Figure **4-10**, **4-11** and **4-12**. The relaxation times $\tau(E)$ show clearly a thickness dependence d_{Au} and an influence of the time-resolved 2PPE experimental configuration. The relaxation times at $d_{Au} = 7$ nm for front- and back-side pumping particularly do not change and are

within the error bars similar. However, the relaxation times for $d_{\mathrm{Au}} = 30$ and 70 nm look different. A significant thickness- and energy-dependence between τ_{FP} and τ_{BP} is visible; at higher intermediate state energies $E - E_{\mathrm{F}} = 2.10 - 1.2$ eV is basically $\tau_{\mathrm{FP}} < \tau_{\mathrm{BP}}$, while at low energies $E - E_{\mathrm{F}} = 0.75 - 0.50$ eV a reverse appears so that $\tau_{\mathrm{FP}} > \tau_{\mathrm{BP}}$. These differences in the quantitative analysis between back- and front-side pumping can be explained by the different pump absorption profiles in the Au/Fe/MgO(001) heterostructure, which varies with Au layer thickness d_{Au}, see Figure **4-2**(a, b). Since the electronic transport processes are determined by gradients in excitation density and electronic temperature [76], the velocity distributions and the corresponding transient electron densities will differ for the two pumping geometries. To describe this, Figure **4-17** shows a sketch of the hot electron nonlocal dynamics and the effect of the photoexcitation density and the optical penetration depth λ_{opt}.
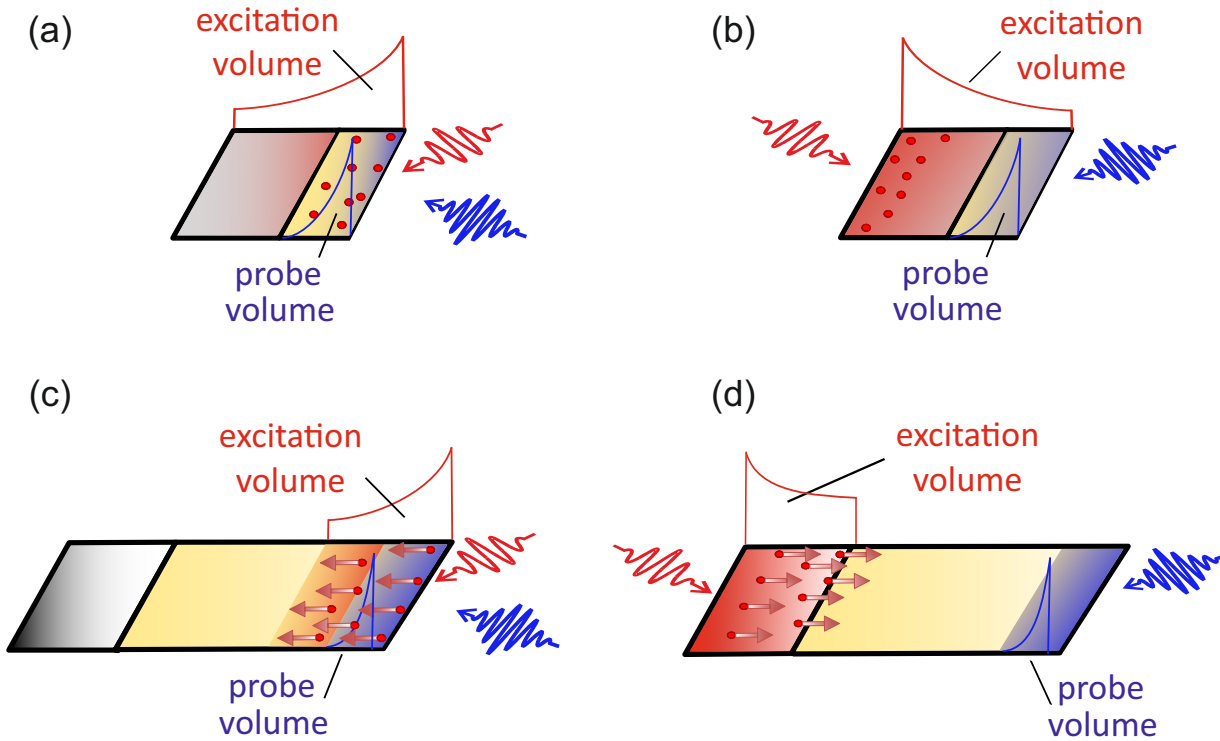
Figure 4-17: Sketch of the penetration depth of the pump pulse and of the probe pulse. Photoexcited electrons leave the surface of the excited layer due to transport effects. (a) & (c) for thin and thick Au layers with FP excitation scheme. (b) & (d) for thin and thick Au layers with BP excitation scheme.

At the top of Figure **4-17** are the thin Au/Fe heterostructures with (a) the front- and (b) the back-side pumping experimental pump-probe schemes. When the Au layer is as thin as the optical penetration depth ($d_{\mathrm{Au}} \sim \lambda_{\mathrm{opt}}$), homogeneous excitation of the heterostructure

occurs, resulting in insensitivity for transport regardless the experimental configuration. In case of thick Au layers ($d_{\mathrm{Au}} > \lambda_{\mathrm{opt}}$), the situation changes, and an inhomogeneous excitation of the heterostructure makes it sensitive to transport effects in the Au- and Fe-side pumping experimental configurations see Figure **4-17** (c) and (d), respectively. According to the universal curve of the electron mean free path length is the penetration depth for the VIS light with a photon energy of $h\nu_1 = 2.10$ eV roughly 10 nm. In comparison, the probe depth for the UV light with a photon energy of $h\nu_2 = 4.13$ eV is only around 4 nm [135,136]. This small probing depth plays a significant role in the difference between τ_{FP} and τ_{BP}.

For front-side pumping geometry in Figure **4-17**(c), upon exciting the Au surface, a large number of hot electrons with $E - E_{\mathrm{F}} = 2.10 - 1.20$ eV move within a few tens of femtosecond out of the near-surface probe region. The propagation proceeds with a velocity close to the $v_{\mathrm{F}} = 1.4$ nm/fs into the bulk Au toward the Fe layer, where the hot electrons undergo many inelastic e-e scattering processes ($\tau_{\mathrm{Fe}} \approx 3$ fs) due to the large phase space in Fe d-bands [69,83]. Consequently, the Fe layer serves as a sink layer for hot electrons. The ultrafast hot electron population decay at the near-surface probe region due to quasi-ballistic transport effects and the ultrafast energy relaxation of hot electrons in the Fe layer lead to the observation of $\tau_{\mathrm{FP}} < \tau_{\mathrm{BP}}$ for $E - E_{\mathrm{F}} \approx 2.10 - 1.20$. In contrast, note that in case of back-side pumping, the hot electrons populate by propagating superdiffusively to the probe region at the Au surface, see Figure **4-17**(d). At low intermediate state energies $E - E_{\mathrm{F}} = 0.80 - 0.60$ eV the relaxation time τ_{FP} becomes larger than τ_{BP}. Presumably, the low-energy electrons are too slow to escape the probing depth at the Au surface shortly after excitation. Another scenario is the repopulation of the near-surface region after the spatiotemporal transport of reflected hot electrons at the Au/Fe interface. Both aspects might lead to the slower relaxation of the transient population at lower intermediate state energies in the case of front-side pumping. For back-side pumping, the low energy electrons might not reach the Au surface due to an increased inelastic e-e scattering so that a population reduction at the near-surface region appears, which leads to $\tau_{\mathrm{FP}} > \tau_{\mathrm{BP}}$ at $E - E_{\mathrm{F}} = 0.80 - 0.60$ eV.

These findings are supported by previous front-side pumping time-resolved photoemission measurements on thin Au, Ag, and Cu thin films with various thicknesses [47,117,137]. They reported a significant impact of transport effects on the hot electron relaxation dynamics, which provides an additional decay component to the photoexcited electron population at the sample surface. The mean escape depth amounts to a few nm in the experiments and results discussed here. Thus, the front-side pumping front-side probing time-resolved 2PPE represents a bulk and surface-sensitive technique. Yet, it was not able to distinguish the local relaxation dynamics at the Au/Fe/MgO(001) heterostructure, as one can see the insights $\tau_1 \neq \tau_{\mathrm{Au}}$ and $\tau_2 \neq \tau_{\mathrm{Fe}}$ for front-side pumping 2PPE in Figure **4-16**. By using the back-side pumping front-side probing time-resolved 2PPE technique, it has been accomplished to distinguish the local relaxation dynamics in the individual constituents of the Au/Fe/MgO(001)

heterostructure. Moreover, another feature in τ_{BP} has been observed around $E - E_{\mathrm{F}} \approx 1.5$ eV for various Au thicknesses d_{Au}, which deviates from the FLT behavior. This anomaly in $\tau(E, d_{\mathrm{Au}})$ will be analyzed and discussed as next in section 4.4.

4.4. Anomaly in the relaxation time

The measured relaxation times in 4.3.2 for back- and front-side pumping tr-2PPE measurements are depicted in Figure **4-10**, **4-11** and **4-12**. For 30 and 70 nm Au thicknesses, the relaxation times τ_{FP} show a near-FLT behavior and no significant anomaly, as it is visible for the relaxation time in τ_{BP}. This non-monotonous feature depends on the excitation scheme, intermediate state energy $E - E_{\mathrm{F}}$ and the Au thickness d_{Au}, which appears due to the energy-dependent interplay among local and nonlocal relaxation dynamics of hot electrons. To understand this thickness- and energy-dependent anomaly in τ_{BP}, the study focuses on the results accomplished by back-side pumping time-resolved 2PPE, also known as Fe-side pumping experimental configuration on Au/Fe/MgO(001) heterostructure.
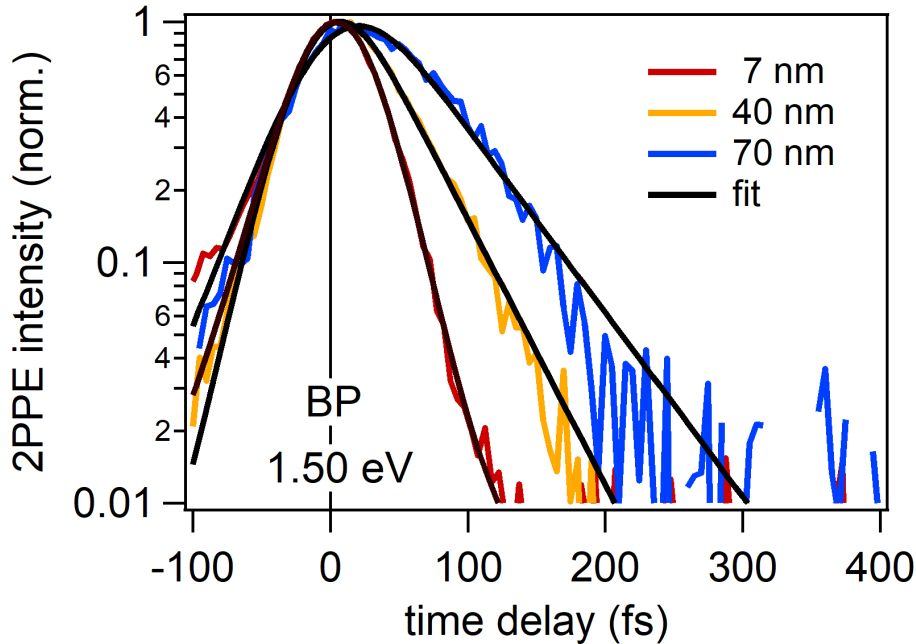
Figure 4-18: Time-dependent 2PPE yields with fits (black solid line) obtained by Fe-side pumping (BP) configuration for various Au thicknesses at $E - E_{\mathrm{F}} = 1.50$ eV.

To investigate the anomaly in the relaxation times in more detail, transient XC traces for $d_{\mathrm{Au}} = 7$, 40 and 70 nm at $E - E_{\mathrm{F}} = 1.50$ eV are plotted in Figure **4-18**. If one compares the transient population dynamics, one sees the slower relaxation and temporal broadening for thicker Au thicknesses, which have already been shown. However, the transient population dynamics for 70 nm Au show a non-common relaxation behavior in the time-resolved XC

trace at 1.50 eV. The peak seems to be broadened so that the decay probably starts with a later time delay. Additionally, an issue in the fitting process seems to be present, which leads to an overestimation of the relaxation times for 70 nm around $E - E_F \approx 1.5$ eV. Due to this fact and the desire to further understand this observation, a closer look is taken at the transient population dynamics for MgO(001)/ 7nm Fe/ 70 nm Au at different energies, see Figure **4-19**.
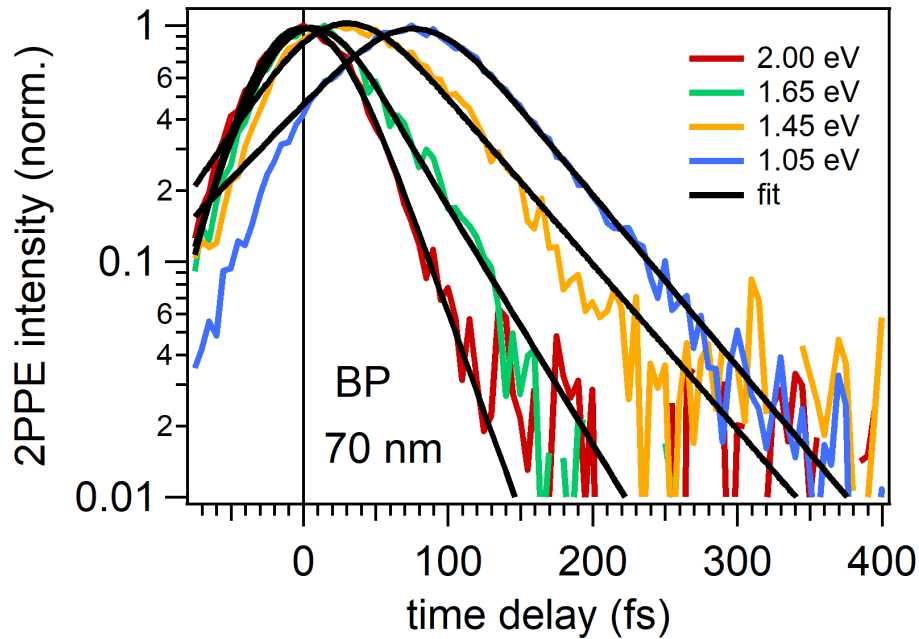
Figure 4-19: Time-dependent 2PPE yields obtained by Fe-side pumping (BP) configuration for various intermediate state energies at $d_{Au} = 70$ nm.

Comparing the transient population dynamics for $E - E_F = 2.00 - 1.05$ eV shows the temporal broadening and the slower relaxation toward lower-lying energies. A peculiar behavior is seen at 1.65 eV, where the decay does not follow the typical convolution of a Gaussian with an exponential decay curve. It resembles a later starting decay process. This behavior is strongly pronounced for the time-resolved 2PPE yield distribution at 1.45 eV. In contrast, at 1.05 eV, a typical exponential decay behavior is observable. The fits overestimate the hot electron relaxation processes at $E - E_F = 1.25 - 1.7$ eV, which is the reason for the relaxation times τ_{70nm}^{BP} in Figure **4-12**. Thus, as an outlook for future analysis, a more appropriate fitting procedure is needed to reach the proper relaxation times.

The later appearing decay refers to the surface later arrived electrons due to scattering processes. This is also observed in the time offset t_0 in thicker samples; see Figure **4-11** and **4-12**. The thicker the Au layer, the earlier the temporal shift starts ($t_0 > 0$ fs) at higher intermediate state energies, as discussed in subsection 4.3.2.

The intriguing behavior observed in the transient population dynamics of hot electrons in Fe/Au heterostructures can be attributed to the peculiar band structure properties of the thin Fe and Au films and to the underlying interplay between hot electron transport and inelastic e-e scattering processes. The pump pulse, with a photon energy of 2.10 eV, excites the Fe layer first, leading to the occupation of unoccupied states by hot electrons in the Fe layer. The presence of exchange-split energy bands in the d-bands of Fe further contributes to the excitation of hot electrons from occupied d-bands to unoccupied sp- and d-band states. Therefore, the optical pumping of the Fe layer results in the excitation of majority and minority electrons with different binding energies, lifetimes, and velocities, which in turn affect the local and nonlocal relaxation dynamics of the hot electrons.

To fully comprehend the spatiotemporal transport dynamics and local relaxation of hot majority and minority electrons in thin MgO(001)/Fe/Au films, further detailed measurements that are energy-, spin-, and time-resolved are necessary. These measurements will pave the way for more advanced theoretical models that can provide a better understanding of the elementary processes responsible for the relaxation dynamics of non-equilibrated hot electrons in metallic heterostructures. Markus Heckschen, under the guidance of Prof. Björn Sothmann, has developed a theory that accurately describes our results obtained with Au-side pumped geometry. This marks the initial steps toward unraveling how the interaction of local and nonlocal relaxation dynamics occurs in the energy-resolved time domain. The theoretical model is based on the Boltzmann transport equation and will be expanded to explain the tr-2PPE results that we acquired with the Fe-side pump geometry.

5. Conclusions and outlook

Conclusion

The ultrafast hot electron local and nonlocal relaxation dynamics in epitaxially grown Au/Fe/MgO(001) thin films have been investigated by femtosecond time-resolved 2PPE spectroscopy. Two different experimental configurations are established; (i) the FP geometry performed by Au-side pumping and Au-side probing, and (ii) the BP technique by Fe-side pumping and Au-side probing.

Employing the tr-2PPE with the Au-side pumping (FP) geometry allowed the observation of the first image potential state IPS ($n =1$) at the Au(001) surface with a binding energy of 0.8 eV to vacuum E_{vac}. In contrast to the FP experimental approach, a photoexcited state in Fe at $E - E_{\mathrm{F}} = 1.8$ eV was observed by the Fe-side pumping (BP) method, which appears in the density of states (DOS) of Fe as unoccupied d-band minority states. Thus, the Fe-side pumping geometry shows a buried media sensitive experimental approach.

The tr-2PPE analysis as a function of Au thickness $d_{\mathrm{Au}} = 5 - 70$ nm with both experimental configurations has shown that with the Fe-side pumping geometry a temporal shift in the intensity built-up of the XC traces is observed. The increasing temporal shift of the intensity built-up with the Au thickness d_{Au} is assigned to the transport effects of hot electrons. The ultrafast hot electrons experience a few inelastic e-e scattering events during the spatiotemporal transport from the Fe layer toward the Au surface across the Fe/Au interface, which is attributed to a superdiffusive propagation behavior. Additionally, the energy-dependent scattering rates in Fe and Au are distinguished by using the optical pumping of Fe and detection at the Au surface by time-resolved two-photon photoemission. While the separation of electron dynamics in the constituents was successful with the BP experimental setup, it failed in the case of the conventional FP geometry. In addition to the opposite direction of the pump-induced transport of hot electrons, we have shown that the spatially distributed optical excitation density plays a strong role in distinguishing Fe- and Au-side pumping.

All in all, the time-resolved 2PPE with the BP experimental configuration represents spectroscopy which accesses buried interfaces or media and provides energy-dependent information on electron dynamics. This novel experimental approach may provide highly desired insight into heterostructures in general.

Outlook

Back-side pumping and front-side probing tr-2PPE experiments on Au/Fe/MgO metallic heterostructures shed light on energy-dependent hot electron relaxation and transport processes in FM/NM heterostructures. Previous studies and the work within this thesis demonstrated the relevance of spin in electron dynamics [34,35,81]. Using the BP geometry with time- and spin-resolved PES might provide compelling insights into the energy-dependent spatiotemporal relaxation dynamics of hot charge carriers in FM/NM heterostructures. Distinguishing hot majority and minority electrons in the transient energy-dependent population dynamics could provide information about spin-dependent transport. Furthermore, theoretical transport approaches are proposed to understand the underlying microscopic hot electron relaxation processes.

An exciting material system for many researchers represents the stacked 2D material system, such as molybdenum disulfide (MoS_2), black phosphorus (bP), hexagonal boron nitride (hBN) and tantalum disulfide ($1T - TaS_2$). Due to their ultrathin nature of few monolayers and high interface quality, they are promoted as a possible alternative for silicon (Si) in electronic devices [12, 24, 25]. Thus, spin-resolved local and nonlocal relaxation measurements with the BP geometry could be applied to different material systems, such as 2D materials [25], ferromagnetic metal/2D material heterostructure [138], and organic spin valve structures [139]. This could provide new ways to understand and manipulate the microscopic processes of energy- and spin-dependent relaxation dynamics of majority and minority charge carriers in condensed matter and at heterostructure interfaces. A current ongoing project within our research group is the application of tr-2PPE experiments with BP geometry on $Fe/Au/MoS_2$ heterostructures. The aim is to elucidate the microscopic transport mechanisms governing the dynamics of hot charge carriers in stacked 2D materials, which can occur via either Bloch band transport or hopping across energy barriers. Furthermore, we propose utilizing energy-resolved time-domain spectroscopy, specifically time-resolved linear photoemission measurements, to investigate the energy-dependent hole relaxation dynamics in nonequilibrium states.

In summary, by investigating the energy- and spin-dependent dynamics of hot charge carriers in the constituents or interfaces of heterostructures, it may be possible to control material properties and develop cutting-edge technologies such as advanced solar batteries and spintronics. These findings have the potential to significantly impact the fields of materials science and technology.

A. Basics in ultrashort laser pulse dispersion

The following description of dispersion effects in ultrashort laser pulses is based on [118, 119]: The electric field of an ultrashort laser pulse in the time domain can be described by

$$E(t) = \varepsilon(t)e^{-i\phi(t)}, \tag{A-1}$$

where $\varepsilon(t)$ is the envelope and $\phi(t) = \omega_0 t + \varphi(t)$ is the temporal phase with the carrier frequency ω_0. The instantaneous angular frequency $\omega_{\text{inst.}}$ of the electrical pulse can be derived by the time derivative of the temporal phase $\phi(t)$

$$\omega_{\text{inst.}} = \omega_0 + \frac{d\varphi(t)}{dt}. \tag{A-2}$$

The time-dependent electric field $E(t)$ is equivalent to the pulse electric field in the frequency domain $E(\omega)$ which is mathematically connected by the Fourier transformation ($\mathcal{F}$)

$$E(\omega) = \mathcal{F}[E(t)] = \int_{-\infty}^{\infty} E(t)e^{-i\omega t}\, dt = \varepsilon(\omega)e^{i\psi(\omega)}, \tag{A-3}$$

with $\varepsilon(\omega)$ as the envelope in the frequency domain and $\psi(\omega)$ as the spectral phase. Quantifying CD is based on a Taylor expansion of the spectral phase as a function of the angular frequency ω around the carrier frequency ω_0 of the pulse

$$\psi(\omega) \approx \sum_{m=0}^{\infty} \frac{1}{m!}\psi_m(\omega - \omega_0)^m \tag{A-4}$$

with $\psi_m = \frac{d^m\psi(\omega)}{d\omega^m}\big|_{\omega_0}$. The terms with different m-order have different meanings regarding the dispersion of the laser pulse. The zero-order term ψ_0 describes a typical phase shift, while the first-order term ψ_1 refers to the group delay (GD). Both terms express the time delay without affecting the pulse shape in the time domain. In contrast, second- or higher-order dispersion is more interesting since they cause frequency-dependent shifts. The second-order dispersion is the change in the GD with respect to frequency known as group delay dispersion (GDD).

The different spectral components of the pulse propagate through a dispersive medium at different speeds due to frequency-dependent refractive indices $n(\omega)$. Resulting in a non-zero GDD, the pulse is broadened in time and thus linearly chirped. The frequency rises or falls with time, known as up-chirped or down-chirped pulses. The GDD is calculated by the second derivative of the spectral phase

$$\text{GDD} = \psi_2 = \left. \frac{d^2\psi}{d\omega^2} \right|_{\omega_0} \tag{A-5}$$

and given in the unit fs^2. Note that the GDD per unit length is the group velocity dispersion (GVD) described by the second derivative of the wavenumber $k(\omega)$

$$\text{GVD} = \left. \frac{d^2k}{d\omega^2} \right|_{\omega_0} = -\frac{1}{v_\text{g}} \frac{dv_\text{g}}{d\omega}, \tag{A-6}$$

in which v_g represents the group velocity of the envelope of the electrical pulse. Occasionally, in the literature and in scientific usage, the term GVD is often mistakenly used for ψ_2. To avoid confusion, one should therefore pay attention to the units in which the corresponding quantity for GVD is given by fs^2/m for optical pulses.

The third-order phase component corresponds to a cubic phase in the pulse, which is known as the third-order dispersion (TOD), given in units of fs^3 and determined by

$$\text{TOD} = \psi_3 = \left. \frac{d^3\psi}{d\omega^3} \right|_{\omega_0}. \tag{A-7}$$

The spectral phase dominated by TOD leads to GD with quadratic dependence on frequency, and consequently high and low frequencies are shifted in the same direction in time. Therefore, TOD causes after or before the main optical pulse additional low-intensity pulses in the temporal domain, as observed in Figure **3-12**. In this thesis work, the higher-order phase components beyond the third-order are negligible. One goal in ultrafast pump-probe measurement is the achievement of ultrashort pulses as close as to the BWL. Thus, minimizing the higher-order dispersion with the help of suitable designed optical pulse compressor systems is essential, as shown in section 3.5.

B. Continuum approach for scattering along the heterostructure

Separation of interface properties by film thickness dependent analysis is well established and was used, e.g., in Sokolowski-Tinten et al. [140] and Farle [141], Eq. 27. The underlying concept is in both cases the different spatial dimensions for bulk and interface contributions, which is the different energy density for bulk and interface of the magnetic anisotropy energy in the work by Farle and the interface scattering in the work by Sokolowski-Tinten et al. In both cases the bulk contributions vanish for thin films of thickness d, which suggests the scaling $A + B/d$ used in Equation 4-3. For sufficiently small d the interface contribution B/d dominates over the bulk contribution A. In the case of the magnetic anisotropy energy density the bulk contribution A has the unit J/m^3 while the interface contribution B has the unit J/m^2. In case of the interface and bulk scattering rates relevant in the present study it is assumed a Matthiesen's rule approach. In this case the bulk contribution A assumes an integral scattering probability over the film thickness increasing linearly with d, which reflects the analysis of scattering in bulk representing a homogeneous environment. In our back-side pumping front-side probing experiment, which analyzes the propagation of electrons injected from the Fe layer into the Au layer across the Fe-Au interface along the z direction, the scattering probability integrated over the layer stack becomes

$$\int\limits_0^{d_{\mathrm{Au-Fe}}+\,d_{\mathrm{Au}}} \tau^{-1}\,dz = \tau_{\mathrm{Au-Fe}}^{-1} \cdot d_{\mathrm{Au-Fe}} + \tau_{\mathrm{Au}}^{-1} \cdot d_{\mathrm{Au}}. \tag{B-1}$$

Here $d_{\mathrm{Au-Fe}}$ is the spatial extent of the Au-Fe interface and d_{Au} is the Au film thickness along z. A potential interface scattering rate can be expected to be revealed by suppressing the bulk scattering for sufficiently thin films, as shown by Sokolowski-Tinten et al. [140]. In our work, we assume two scattering rates which add up to the total measured relaxation rate. The thickness dependent analysis reported in Figure **4-13** and Figure **4-14** reveals that A and B/d agree with the known e-e scattering rates for bulk Au and Fe, respectively. Given the construction of Equation 4-3 with B as an interface contribution this indeed might be surprising and requires further discussion. Formally B has the unit m/s, i.e. a velocity. This originates from the construction as an interface contribution but can be misleading because B/d actually represents a scattering rate. The question which remains to be answered is why the interface scattering rate B/d is given by the bulk scattering rate

of Fe. Consider Equation B-1 above rephrased for two bulk integral scattering probabilities which increase linearly with independent film thicknesses of Au and Fe constituents, d_{Au} and d_{Fe}, respectively. Consider in addition an interface scattering contribution. The scattering probability integrated along the layer stack in z direction is

$$\int\limits_{0}^{d_{\mathrm{Fe}}+d_{\mathrm{Au-Fe}}+d_{\mathrm{Au}}} \frac{dz}{\tau(z)} = \frac{d_{\mathrm{Fe}}}{\tau_{\mathrm{Fe}}} + \frac{d_{\mathrm{Au-Fe}}}{\tau_{\mathrm{Au-Fe}}} + \frac{d_{\mathrm{Au}}}{\tau_{\mathrm{Au}}}. \tag{B-2}$$

Since in our experiment d_{Fe} is kept constant we determine by variation of d_{Au} the sum of the first two contributions. Since within our experimental uncertainty this sum agrees with the literature values of the e-escattering rate in bulk Fe it was concluded that the interface scattering rate is absent within experimental uncertainty and the electrons propagate without scattering across the epitaxial Fe-Au interface.

In case of non-epitaxial interfaces an additional scattering channel will occur locally at the interface. The model leading to Equation 4-3 can be, for example, extended to include such interface scattering by an additional term besides the bulk scattering contributions, as considered already in Equation B-2. One way to determine the respective interface scattering rate is the variation of the thicknesses d_a and d_b of both constituents of the heterostructure. Equation 4-3 becomes

$$\frac{1}{\tau(d_a, d_b)} = A + \frac{1}{d_a} \left(d_b \, B_{\mathrm{bulk}} + B_{\mathrm{int}} \right) \tag{B-3}$$

The term B/d from Equation 4-3 has here been split into two components $d_b \, B_{\mathrm{bulk}}/d_a$ and B_{int}/d_a, which represent the scattering probabilities in bulk and at the interface, respectively. Equation B-3 shows that increasing the thickness of one layer leads to a decrease in the weight of scattering probability in the other layer. In contrast, a systematic decrease in both thicknesses d_a and d_b highlights the interface scattering contribution.

Interface scattering of electrons can also be expected to occur by interaction with electronic interface states. Such interface scattering is expected to lead to resonant scattering and anomalies in the rather smooth energy dependent relaxation times reported in Figure **4-14**.

Bibliography

[1] U. N. F. C. on Climate Change, *Kyoto protocol to the united nations framework convention on climate change.* Kyoto, Japan: United Nations, 1998.

[2] U. N. F. C. on Climate Change, *Adoption of the Paris Agreement, 21st Conference of the Parties.* Paris, France: United Nations, 2015.

[3] S. Oberthür and L. Groen, "Explaining goal achievement in international negotiations: the EU and the Paris Agreement on climate change," *Journal of European Public Policy*, vol. 25, pp. 708–727, 2018.

[4] J. Hofer and K. Stratmann, "Fördermittel in Milliardenhöhe: Habeck will Chipproduktion nach Europa zurückholen," *Handelsblatt*, 2021.

[5] J. Bardeen and W. H. Brattain, "The Transistor, A Semi-Conductor Triode," *Physical Review*, vol. 74, pp. 230–231, 1948.

[6] B. K. Bose, "Global Warming: Energy, Environmental Pollution, and the Impact of Power Electronics," *IEEE Industrial Electronics Magazine*, vol. 4, pp. 6–17, 2010.

[7] Nature Electronics Editor, "A two-dimensional outlook," *Nature Electronics*, vol. 4, pp. 767–767, 2021.

[8] I. S. Amiri, H. Mohammadi, and M. Hosseinghadiry, *Invention and Evaluation of Transistors and Integrated Circuits.* Cham, Switzerland: Springer, 2019.

[9] G. E. Moore, "Cramming more components onto integrated circuits," *IEEE Solid-State Circuits Society Newsletter*, vol. 11, pp. 33–35, 2006.

[10] R. Dennard, F. Gaensslen, H.-N. Yu, V. Rideout, E. Bassous, and A. LeBlanc, "Design of ion-implanted MOSFET's with very small physical dimensions," *IEEE Journal of Solid-State Circuits*, vol. 9, pp. 256–268, 1974.

[11] B.-S. Liang, "Entrepreneurship-driven growth in the integrated circuit design industry," *Nature Electronics*, vol. 4, pp. 234–236, 2021.

[12] K. Zhu, C. Wen, A. A. Aljarb, F. Xue, X. Xu, V. Tung, X. Zhang, H. N. Alshareef, and M. Lanza, "The development of integrated circuits based on two-dimensional materials," *Nature Electronics*, vol. 4, pp. 775–785, 2021.

[13] S. M. Yakout, "Spintronics: Future Technology for New Data Storage and Communication Devices," *Journal of Superconductivity and Novel Magnetism*, vol. 33, pp. 2557–2580, 2020.

[14] E. V. Chulkov, A. G. Borisov, J. P. Gauyacq, D. Sánchez-Portal, V. M. Silkin, V. P. Zhukov, and P. M. Echenique, "Electronic Excitations in Metals and at Metal Surfaces," *Chemical Reviews*, vol. 106, pp. 4160–4206, 2006.

[15] M. Wolf and M. Aeschlimann, "Femtosekunden-Dynamik in Metallen - das kurze Leben heißer Elektronen," *Physikalische Blätter*, vol. 54, pp. 145–148, 1998.

[16] P. S. Kirchmann, L. Rettig, X. Zubizarreta, V. M. Silkin, E. V. Chulkov, and U. Bovensiepen, "Quasiparticle lifetimes in metallic quantum-well nanostructures," *Nature Physics*, vol. 6, pp. 782–785, 2010.

[17] U. Bovensiepen and P. Kirchmann, "Elementary relaxation processes investigated by femtosecond photoelectron spectroscopy of two-dimensional materials," *Laser & Photonics Reviews*, vol. 6, pp. 589–606, 2012.

[18] S. M. Sze, C. R. Crowell, G. P. Carey, and E. E. LaBate, "Hot-Electron Transport in Semiconductor-Metal-Semiconductor Structures," *Journal of Applied Physics*, vol. 37, pp. 2690–2695, 1966.

[19] E. Pop, "Energy dissipation and transport in nanoscale devices," *Nano Research*, vol. 3, pp. 147–169, 2010.

[20] A. Block, M. Liebel, R. Yu, M. Spector, Y. Sivan, F. J. G. de Abajo, and N. F. van Hulst, "Tracking ultrafast hot-electron diffusion in space and time by ultrafast thermomodulation microscopy," *Science Advances*, vol. 5, p. eaav8965, 2019.

[21] F. Turker, S. Rajabpour, and J. A. Robinson, "Material considerations for the design of 2D/3D hot electron transistors," *APL Materials*, vol. 9, p. 081103, 2021.

[22] J. Walowski and M. Münzenberg, "Perspective: Ultrafast magnetism and THz spintronics," *Journal of Applied Physics*, vol. 120, p. 140901, 2016.

[23] M. Hofherr, P. Maldonado, O. Schmitt, M. Berritta, U. Bierbrauer, S. Sadashivaiah, A. J. Schellekens, B. Koopmans, D. Steil, M. Cinchetti, B. Stadtmüller, P. M. Oppeneer, S. Mathias, and M. Aeschlimann, "Speed and efficiency of femtosecond spin current injection into a nonmagnetic material," *Physical Review B*, vol. 96, p. 100403, 2017.

[24] G. Fiori, F. Bonaccorso, G. Iannaccone, T. Palacios, D. Neumaier, A. Seabaugh, S. K. Banerjee, and L. Colombo, "Electronics based on two-dimensional materials," *Nature Nanotechnology*, vol. 9, pp. 768–779, 2014.

[25] N. Li, Q. Wang, C. Shen, Z. Wei, H. Yu, J. Zhao, X. Lu, G. Wang, C. He, L. Xie, J. Zhu, L. Du, R. Yang, D. Shi, and G. Zhang, "Large-scale flexible and transparent electronics based on monolayer molybdenum disulfide field-effect transistors," *Nature Electronics*, vol. 3, pp. 711–717, 2020.

[26] G. Tagliabue, J. S. DuChene, M. Abdellah, A. Habib, D. J. Gosztola, Y. Hattori, W.-H. Cheng, K. Zheng, S. E. Canton, R. Sundararaman, J. Sá, and H. A. Atwater, "Ultrafast hot-hole injection modifies hot-electron dynamics in $Au/p - GaN$ heterostructures," *Nature Materials*, vol. 19, pp. 1312–1318, 2020.

[27] S. D. Brorson, J. G. Fujimoto, and E. P. Ippen, "Femtosecond electronic heat-transport dynamics in thin gold films," *Physical Review Letters*, vol. 59, pp. 1962–1965, 1987.

[28] E. Beaurepaire, J.-C. Merle, A. Daunois, and J.-Y. Bigot, "Ultrafast Spin Dynamics in Ferromagnetic Nickel," *Physical Review Letters*, vol. 76, pp. 4250–4253, 1996.

[29] A. Alekhin, *Ultrafast hot carrier driven magnetization dynamics.* PhD thesis, Freie Universität Berlin, 2016.

[30] G. Malinowski, N. Bergeard, M. Hehn, and S. Mangin, "Hot-electron transport and ultrafast magnetization dynamics in magnetic multilayers and nanostructures following femtosecond laser pulse excitation," *The European Physical Journal B*, vol. 91, p. 98, 2018.

[31] G. Malinowski, F. Dalla Longa, J. H. H. Rietjens, P. V. Paluskar, R. Huijink, H. J. M. Swagten, and B. Koopmans, "Control of speed and efficiency of ultrafast demagnetization by direct transfer of spin angular momentum," *Nature Physics*, vol. 4, pp. 855–858, 2008.

[32] M. Battiato, K. Carva, and P. M. Oppeneer, "Superdiffusive Spin Transport as a Mechanism of Ultrafast Demagnetization," *Physical Review Letters*, vol. 105, p. 027203, 2010.

[33] T. Kampfrath, M. Battiato, P. Maldonado, G. Eilers, J. Nötzold, S. Mährlein, V. Zbarsky, F. Freimuth, Y. Mokrousov, S. Blügel, M. Wolf, I. Radu, P. M. Oppeneer, and M. Münzenberg, "Terahertz spin current pulses controlled by magnetic heterostructures," *Nature Nanotechnology*, vol. 8, pp. 256–260, 2013.

[34] A. Melnikov, I. Razdolski, T. O. Wehling, E. T. Papaioannou, V. Roddatis, P. Fumagalli, O. Aktsipetrov, A. I. Lichtenstein, and U. Bovensiepen, "Ultrafast Transport of Laser-Excited Spin-Polarized Carriers in Au/Fe/MgO(001)," *Physical Review Letters*, vol. 107, p. 076601, 2011.

[35] A. Alekhin, I. Razdolski, N. Ilin, J. P. Meyburg, D. Diesing, V. Roddatis, I. Rungger, M. Stamenova, S. Sanvito, U. Bovensiepen, and A. Melnikov, "Femtosecond Spin Current Pulses Generated by the Nonthermal Spin-Dependent Seebeck Effect and Interacting with Ferromagnets in Spin Valves," *Physical Review Letters*, vol. 119, p. 017202, 2017.

[36] I. Razdolski, A. Alekhin, N. Ilin, J. P. Meyburg, V. Roddatis, D. Diesing, U. Bovensiepen, and A. Melnikov, "Nanoscale interface confinement of ultrafast spin transfer torque driving non-uniform spin dynamics," *Nature Communications*, vol. 8, p. 15007, 2017.

[37] A. Alekhin, I. Razdolski, M. Berritta, D. Bürstel, V. Temnov, D. Diesing, U. Bovensiepen, G. Woltersdorf, P. M. Oppeneer, and A. Melnikov, "Magneto-optical properties of Au upon the injection of hot spin-polarized electrons across Fe/Au(001) interfaces," *Journal of Physics: Condensed Matter*, vol. 31, p. 124002, 2019.

[38] T. Seifert, S. Jaiswal, U. Martens, J. Hannegan, L. Braun, P. Maldonado, F. Freimuth, A. Kronenberg, J. Henrizi, I. Radu, E. Beaurepaire, Y. Mokrousov, P. M. Oppeneer, M. Jourdan, G. Jakob, D. Turchinovich, L. M. Hayden, M. Wolf, M. Münzenberg, M. Kläui, and T. Kampfrath, "Efficient metallic spintronic emitters of ultrabroadband terahertz radiation," *Nature Photonics*, vol. 10, pp. 483–488, 2016.

[39] O. Gückstock, L. Nádvorník, T. S. Seifert, M. Borchert, G. Jakob, G. Schmidt, G. Woltersdorf, M. Kläui, M. Wolf, and T. Kampfrath, "Modulating the polarization of broadband terahertz pulses from a spintronic emitter at rates up to 10 kHz," *Optica*, vol. 8, pp. 1013–1019, 2021.

[40] N. Bergeard, M. Hehn, S. Mangin, G. Lengaigne, F. Montaigne, M. L. M. Lalieu, B. Koopmans, and G. Malinowski, "Hot-Electron-Induced Ultrafast Demagnetization in Co/Pt Multilayers," *Physical Review Letters*, vol. 117, p. 147203, 2016.

[41] J. Sung, C. Schnedermann, L. Ni, A. Sadhanala, R. Y. S. Chen, C. Cho, L. Priest, J. M. Lim, H.-K. Kim, B. Monserrat, P. Kukura, and A. Rao, "Long-range ballistic propagation of carriers in methylammonium lead iodide perovskite thin films," *Nature Physics*, vol. 16, pp. 171–176, 2020.

[42] R. Fischer, S. Schuppler, N. Fischer, T. Fauster, and W. Steinmann, "Image states and local work function for Ag/Pd(111)," *Physical Review Letters*, vol. 70, pp. 654–657, 1993.

[43] T. Fauster, C. Reuß, I. L. Shumay, and M. Weinelt, "Femtosecond two-photon photoemission studies of image-potential states," *Chemical Physics*, vol. 251, pp. 111–121, 2000.

[44] W. S. Fann, R. Storz, H. W. K. Tom, and J. Bokor, "Direct measurement of nonequilibrium electron-energy distributions in subpicosecond laser-heated gold films," *Physical Review Letters*, vol. 68, pp. 2834–2837, 1992.

[45] W. S. Fann, R. Storz, H. W. K. Tom, and J. Bokor, "Electron thermalization in gold," *Physical Review B*, vol. 46, pp. 13592–13595, 1992.

[46] M. Lisowski, P. A. Loukakos, U. Bovensiepen, and M. Wolf, "Femtosecond dynamics and transport of optically excited electrons in epitaxial Cu films on $Si(111) - 7 \times 7$," *Applied Physics A*, vol. 79, pp. 739–741, 2004.

[47] M. Aeschlimann, M. Bauer, S. Pawlik, R. Knorren, G. Bouzerar, and K. H. Bennemann, "Transport and dynamics of optically excited electrons in metals," *Applied Physics A*, vol. 71, pp. 485–491, 2000.

[48] J. Cao, Y. Gao, H. E. Elsayed-Ali, R. J. D. Miller, and D. A. Mantell, "Femtosecond photoemission study of ultrafast electron dynamics in single-crystal Au(111) films," *Physical Review B*, vol. 58, pp. 10948–10952, 1998.

[49] M. Lisowski, P. A. Loukakos, U. Bovensiepen, J. Stähler, C. Gahl, and M. Wolf, "Ultrafast dynamics of electron thermalization, cooling and transport effects in Ru(001)," *Applied Physics A*, vol. 78, pp. 165–176, 2004.

[50] J. Gauyacq, A. Borisov, and M. Bauer, "Excited states in the alkali/noble metal surface systems: A model system for the study of charge transfer dynamics at surfaces," *Progress in Surface Science*, vol. 82, pp. 244–292, 2007.

[51] M. Aeschlimann, M. Bauer, S. Pawlik, W. Weber, R. Burgermeister, D. Oberli, and H. C. Siegmann, "Ultrafast Spin-Dependent Electron Dynamics in fcc Co," *Physical Review Letters*, vol. 79, pp. 5158–5161, 1997.

[52] S. Crampin, "Fe on Au(001): magnetism and band formation," *Journal of Physics: Condensed Matter*, vol. 5, pp. 4647–4664, 1993.

[53] Y. Suzuki, T. Katayama, A. Thiaville, K. Sato, M. Taninaka, and S. Yoshida, "Magneto-optical properties of Au/Fe/Ag and Ag/Fe/Au(001) sandwich films," *Journal of Magnetism and Magnetic Materials*, vol. 121, pp. 539–541, 1993.

[54] F. Kühne, Y. Beyazit, B. Sothmann, J. Jayabalan, D. Diesing, P. Zhou, and U. Bovensiepen, "Ultrafast transport and energy relaxation of hot electrons in Au/Fe/MgO(001) heterostructures analyzed by linear time-resolved photoelectron spectroscopy," *Physical Review Research*, vol. 4, p. 033239, 2022.

[55] P. E. Hopkins and D. A. Stewart, "Contribution of d-band electrons to ballistic transport and scattering during electron-phonon nonequilibrium in nanoscale Au films using an ab initio density of states," *Journal of Applied Physics*, vol. 106, p. 053512, 2009.

[56] T. Rangel, D. Kecik, P. E. Trevisanutto, G.-M. Rignanese, H. Van Swygenhoven, and V. Olevano, "Band structure of gold from many-body perturbation theory," *Physical Review B*, vol. 86, p. 125125, 2012.

[57] P. M. Echenique and J. B. Pendry, "The existence and detection of Rydberg states at surfaces," *Journal of Physics C: Solid State Physics*, vol. 11, p. 2065, 1978.

[58] D. Straub and F. J. Himpsel, "Identification of Image-Potential Surface States on Metals," *Physical Review Letters*, vol. 52, pp. 1922–1924, 1984.

[59] K. Giesen, F. Hage, F. J. Himpsel, H. J. Riess, and W. Steinmann, "Two-photon photoemission via image-potential states," *Physical Review Letters*, vol. 55, pp. 300–303, 1985.

[60] U. Bovensiepen, H. Petek, and M. Wolf, *Dynamics at Solid State Surfaces and Interfaces, Volume 2: Fundamentals*. Wiley-VCH, 2012.

[61] T. Fauster and W. Steinmann, "Chapter 8 - Two-Photon Photoemission Spectroscopy of Image States," in *Photonic Probes of Surfaces*, pp. 347–411, Elsevier, 1995.

[62] E. Chulkov, V. Silkin, and P. Echenique, "Image potential states on metal surfaces: binding energies and wave functions," *Surface Science*, vol. 437, pp. 330–352, 1999.

[63] T. Nakazawa, R. Arafune, N. Takagi, and M. Kawai, "Linewidth analysis of image potential states on noble metal surfaces with high-energy resolved two-photon photoemission spectroscopy," *Surface and Interface Analysis*, vol. 48, pp. 1194–1198, 2016.

[64] A. Zangwill, *Physics at Surfaces*. Cambridge: University Press, 1988.

[65] H. Ilbach and H. Lüth, *Solid-State Physics: An Introduction to Principles of Materials Science*. Springer, 4th ed., 2009.

[66] J. Schäfer, M. Hoinkis, E. Rotenberg, P. Blaha, and R. Claessen, "Fermi surface and electron correlation effects of ferromagnetic iron," *Physical Review B*, vol. 72, p. 155115, 2005.

[67] R. Knorren, K. H. Bennemann, R. Burgermeister, and M. Aeschlimann, "Dynamics of excited electrons in copper and ferromagnetic transition metals: Theory and experiment," *Physical Review B*, vol. 61, pp. 9427–9440, 2000.

[68] T. Valla, A. V. Fedorov, P. D. Johnson, and S. L. Hulbert, "Many-Body Effects in Angle-Resolved Photoemission: Quasiparticle Energy and Lifetime of a Mo(110) Surface State," *Physical Review Letters*, vol. 83, pp. 2085–2088, 1999.

[69] M. Bauer, A. Marienfeld, and M. Aeschlimann, "Hot electron lifetimes in metals probed by time-resolved two-photon photoemission," *Progress in Surface Science*, vol. 90, pp. 319–376, 2015.

[70] P. S. Kirchmann, *Ultrafast Electron Dynamics in Low-Dimensional Materials*. PhD thesis, Freie Universität Berlin, 2009.

[71] L. D. Landau, "On the theory of the Fermi liquid," *Sov. Phys. JETP*, vol. 8, p. 70, 1959.

[72] D. Pines and P. Nozieres, *The Theory of Quantum Liquids, Vol. I of Advanced Book Classic Series*. W. A. Benjamin, Inc., 1966.

[73] J. J. Quinn and R. A. Ferrell, "Electron Self-Energy Approach to Correlation in a Degenerate Electron Gas," *Phys. Rev.*, vol. 112, pp. 812–827, Nov 1958.

[74] J. J. Quinn, "Range of Excited Electrons in Metals," *Physical Review*, vol. 126, pp. 1453–1457, 1962.

[75] M. J. Lisowski, *Elektronen- und Magnetisierungsdynamik in Metallen untersucht mit zeitaufgelöster Photoemission*. PhD thesis, Freie Universität Berlin, 2005.

[76] J. Hohlfeld, S.-S. Wellershoff, J. Güdde, U. Conrad, V. Jähnke, and E. Matthias, "Electron and lattice dynamics following optical excitation of metals," *Chemical Physics*, vol. 251, pp. 237–258, 2000.

[77] L. Wittenbecher, E. Viñas Boström, J. Vogelsang, S. Lehman, K. A. Dick, C. Verdozzi, D. Zigmantas, and A. Mikkelsen, "Unraveling the Ultrafast Hot Electron Dynamics in Semiconductor Nanowires," *ACS Nano*, vol. 15, pp. 1133–1144, 2021.

[78] T. Juhasz, H. E. Elsayed-Ali, G. O. Smith, C. Suárez, and W. E. Bron, "Direct measurements of the transport of nonequilibrium electrons in gold films with different crystal structures," *Physical Review B*, vol. 48, pp. 15488–15491, 1993.

[79] C. Suárez, W. E. Bron, and T. Juhasz, "Dynamics and Transport of Electronic Carriers in Thin Gold Films," *Physical Review Letters*, vol. 75, pp. 4536–4539, 1995.

[80] V. P. Zhukov, E. V. Chulkov, and P. M. Echenique, "Lifetimes and inelastic mean free path of low-energy excited electrons in Fe, Ni, Pt, and Au: Ab initio GW + T calculations," *Physical Review B*, vol. 73, p. 125105, 2006.

[81] A. Eschenlohr, M. Battiato, P. Maldonado, N. Pontius, T. Kachel, K. Holldack, R. Mitzner, A. Föhlisch, P. M. Oppeneer, and C. Stamm, "Ultrafast spin transport as key to femtosecond demagnetization," *Nature Materials*, vol. 12, pp. 332–336, 2013.

[82] M. Battiato, K. Carva, and P. M. Oppeneer, "Theory of laser-induced ultrafast superdiffusive spin transport in layered heterostructures," *Physical Review B*, vol. 86, p. 024404, 2012.

[83] D. M. Nenno, B. Rethfeld, and H. C. Schneider, "Particle-in-cell simulation of ultrafast hot-carrier transport in Fe/Au heterostructures," *Physical Review B*, vol. 98, p. 224416, 2018.

[84] Y. Beyazit, J. Beckord, P. Zhou, J. P. Meyburg, F. Kühne, D. Diesing, M. Ligges, and U. Bovensiepen, "Local and Nonlocal Electron Dynamics of Au/Fe/MgO(001) Heterostructures Analyzed by Time-Resolved Two-Photon Photoemission Spectroscopy," *Physical Review Letters*, vol. 125, p. 076803, 2020.

[85] A. Einstein, "Über einen die Erzeugung und Verwandlung des Lichtes betreffenden heuristischen Gesichtspunkt," *Annalen der Physik*, vol. 322, pp. 132–148, 1905.

[86] H. Hertz, "Ueber einen Einfluss des ultravioletten Lichtes auf die electrische Entladung," *Annalen der Physik*, vol. 267, pp. 983–1000, 1887.

[87] P. Lenard, "Ueber die lichtelektrische Wirkung," *Annalen der Physik*, vol. 313, pp. 149–198, 1902.

[88] H. Petek and S. Ogawa, "Femtosecond time-resolved two-photon photoemission studies of electron dynamics in metals," *Progress in Surface Science*, vol. 56, pp. 239–310, 1997.

[89] S. Hüfner, *Photoelectron Spectroscopy Principles and Applications*. Berlin: Springer, 3rd ed., 2003.

[90] J. Pendry, "Theory of photoemission," *Surface Science*, vol. 57, pp. 679–705, 1976.

[91] M. Ligges, I. Avigo, D. Golež, H. U. R. Strand, Y. Beyazit, K. Hanff, F. Diekmann, L. Stojchevska, M. Kalläne, P. Zhou, K. Rossnagel, M. Eckstein, P. Werner, and U. Bovensiepen, "Ultrafast Doublon Dynamics in Photoexcited $1T - \mathrm{TaS}_2$," *Physical Review Letters*, vol. 120, p. 166401, 2018.

[92] L. Perfetti, P. A. Loukakos, M. Lisowski, U. Bovensiepen, H. Berger, S. Biermann, P. S. Cornaglia, A. Georges, and M. Wolf, "Time Evolution of the Electronic Structure of $1T - \mathrm{TaS}_2$ through the Insulator-Metal Transition," *Physical Review Letters*, vol. 97, p. 067402, 2006.

[93] T. Frigge, B. Hafke, T. Witte, B. Krenzer, C. Streubühr, A. Samad Syed, V. Mikšić Trontl, I. Avigo, P. Zhou, M. Ligges, D. von der Linde, U. Bovensiepen, M. Horn-von Hoegen, S. Wippermann, A. Lücke, S. Sanna, U. Gerstmann, and W. G. Schmidt, "Optically excited structural transition in atomic wires on surfaces at the quantum limit," *Nature*, vol. 544, pp. 207–211, 2017.

[94] N. V. Smith, "Inverse photoemission, journal = Reports on Progress in Physics," vol. 51, pp. 1227–1294, 1988.

[95] W. Steinmann, "Spectroscopy of image-potential states by two-photon photoemission," *Applied Physics A*, vol. 49, pp. 365–377, 1989.

[96] A. Hotzel, *Elektronendynamik der Adsorbatbedeckten Cu(111)-Oberfläche.* PhD thesis, Freie Universität Berlin, 1999.

[97] A. B. Schmidt, M. Pickel, M. Donath, P. Buczek, A. Ernst, V. P. Zhukov, P. M. Echenique, L. M. Sandratskii, E. V. Chulkov, and M. Weinelt, "Ultrafast Magnon Generation in an Fe Film on Cu(100)," *Physical Review Letters*, vol. 105, p. 197401, 2010.

[98] M. Sandhofer, *Elektron-Phonon Kopplung und impulsaufgelöste elektronische Eigenschaften des Pb/Si(111) Hybridsystems.* PhD thesis, Universität Duisburg-Essen, 2015.

[99] R. Loudon, *Quantum Theory of Light.* New York: Oxford University Press, 1983.

[100] Y. Beyazit, F. Kühne, D. Diesing, P. Zhou, J. Jayabalan, B. Sothmann, and U. Bovensiepen, "Ultrafast electron dynamics in Au/Fe/MgO(001) analyzed by Au- and Fe-selective pumping in time-resolved two-photon photoemission spectroscopy: Separation of excitations in adjacent metallic layers," *Physical Review B*, vol. 107, p. 085412, 2023.

[101] T. Mühge, A. Stierle, N. Metoki, H. Zabel, and U. Pietsch, "Structural properties of high-quality sputtered Fe films on $Al_2O_3(1120)$ and MgO(001) substrates," *Applied Physics A*, vol. 59, pp. 659–665, 1994.

[102] D. T. Dekadjevi, P. A. Ryan, B. J. Hickey, B. D. Fulthorpe, and B. K. Tanner, "Experimental Evidence for Electron Channeling in Fe/Au(100) Superlattices," *Physical Review Letters*, vol. 86, pp. 5787–5790, 2001.

[103] M. Mattern, A. von Reppert, S. P. Zeuschner, J.-E. Pudell, F. Kühne, D. Diesing, M. Herzog, and M. Bargheer, "Electronic energy transport in nanoscale Au/Fe heterostructures in the perspective of ultrafast lattice dynamics," *Applied Physics Letters*, vol. 120, p. 092401, 2022.

[104] F. Kühne, *Local and non-local relaxation dynamics of hot carriers by linear photoemission*. Master thesis, Universität Duisburg-Essen, 2020.

[105] J. C. Vickerman, "Secondary ion mass spectrometry–basic concepts, instrumental aspects, applications and trends," *Surface and Interface Analysis*, vol. 10, pp. 435–435, 1987.

[106] S. Hofmann, "Sputter depth profile analysis of interfaces," *Reports on Progress in Physics*, vol. 61, pp. 827–888, 1998.

[107] IONTOF-GmbH, "TOFSIMS^5 - Manual," 2022.

[108] L. Rettig, *Ultrafast Dynamics of Correlated Electrons*. PhD thesis, Freie Universität Berlin, 2012.

[109] E. Knoesel, *Ultrakurzzeit-Dynamik elektronischer Anregungen auf Metalloberächen*. PhD thesis, Freie Universität Berlin, 1997.

[110] P. S. Kirchmann, L. Rettig, D. Nandi, U. Lipowski, M. Wolf, and U. Bovensiepen, "A time-of-flight spectrometer for angle-resolved detection of low energy electrons in two dimensions," *Applied Physics A*, vol. 91, pp. 211–217, 2008.

[111] D. Strickland and G. Mourou, "Compression of amplified chirped optical pulses," *Optics Communications*, vol. 55, pp. 447–449, 1985.

[112] I. Agarwal, *Electron Transfer Dynamics in Halobenzenes at Ice and Metal Interfaces*. PhD thesis, Universität Duisburg-Essen, 2017.

[113] R. W. Boyd, *Nonlinear Optics*. New York: American Press, 3rd ed., 2008.

[114] G. I. Stegeman and R. A. Stegeman, *Nonlinear Optics: Phenomena, Materials and Devices*. New Jersey: John Wiley & Sons, 2012.

[115] F. Zernike and J. E. Midwinter, *Applied Nonlinear Optics*. Dover Publications Inc., 1973.

[116] W. Demtröder, *Laser Spectroscopy Vol. 1: Basic Principles*. Berlin: Springer, 4th ed., 2008.

[117] E. Knoesel, A. Hotzel, and M. Wolf, "Ultrafast dynamics of hot electrons and holes in copper: Excitation, energy relaxation, and transport effects," *Physical Review B*, vol. 57, pp. 12812–12824, 1998.

[118] R. Trebino, K. W. DeLong, D. N. Fittinghoff, J. N. Sweetser, M. A. Krumbügel, B. A. Richman, and D. J. Kane, "Measuring ultrashort laser pulses in the time-frequency domain using frequency-resolved optical gating," *Review of Scientific Instruments*, vol. 68, pp. 3277–3295, 1997.

[119] R. Trebino, *Frequency-Resolved Optical Gating: The Measurement of Ultrashort Laser Pulses*. New York: Springer, 2000.

[120] N. Karasawa, L. Li, A. Suguro, H. Shigekawa, R. Morita, and M. Yamashita, "Optical pulse compression to 5.0 fs by use of only a spatial light modulator for phase compensation," *Journal of the Optical Society of America B*, vol. 18, pp. 1742–1746, 2001.

[121] J. E. Beckord, "Femtosecond electron dynamics in Au/Fe/MgO(001) analyzed with two photon photoemission in front pump and back pump geometry," master thesis, Universität Duisburg-Essen, 2018.

[122] M. A. Krumbügel and R. Trebino, *The FROG Algorithm*. Boston: Springer, 2000.

[123] R. Szipöcs, K. Ferencz, C. Spielmann, and F. Krausz, "Chirped multilayer coatings for broadband dispersion control in femtosecond lasers," *Optics Letters*, vol. 19, pp. 201–203, 1994.

[124] N. Matuschek, F. Kartner, and U. Keller, "Theory of double-chirped mirrors," *IEEE Journal of Selected Topics in Quantum Electronics*, vol. 4, pp. 197–208, 1998.

[125] E. Treacy, "Optical pulse compression with diffraction gratings," *IEEE Journal of Quantum Electronics*, vol. 5, pp. 454–458, 1969.

[126] O. E. Martinez, J. P. Gordon, and R. L. Fork, "Negative group-velocity dispersion using refraction," *Journal of the Optical Society of America A*, vol. 1, pp. 1003–1006, 1984.

[127] B. Nourozi, A. Aminian, N. Fili, Y. Zangeneh, A. Boochani, and P. Darabi, "The electronic and optical properties of MgO mono-layer: Based on GGA − mBJ," *Results in Physics*, vol. 12, pp. 2038–2043, 2019.

[128] T. Hertel, E. Knoesel, M. Wolf, and G. Ertl, "Ultrafast Electron Dynamics at Cu(111): Response of an Electron Gas to Optical Excitation," *Physical Review Letters*, vol. 76, pp. 535–538, 1996.

[129] M. Aeschlimann, M. Bauer, and S. Pawlik, "Competing nonradiative channels for hot electron induced surface photochemistry," *Chemical Physics*, vol. 205, pp. 127–141, 1996.

[130] D. L. Windt, "IMD - Software for modeling the optical properties of multilayer films," *Computers in Physics*, vol. 12, pp. 360–370, 1998.

[131] L. D. Landau and E. M. Lifshitz, *Electrodynamics of Continuous Media*. Amsterdam: Pergamon, 2nd ed., 1984.

[132] E. Palik, *Handbook of Optical Constants of Solids*. New York: Academic Press, 1985.

[133] D. Straub and F. J. Himpsel, "Spectroscopy of image-potential states with inverse photoemission," *Physical Review B*, vol. 33, pp. 2256–2262, 1986.

[134] E. Chulkov, A. Leonardo, I. Nechaev, and V. Silkin, "Decay of electronic excitations in bulk metals and at surfaces," *Surface Science*, vol. 600, pp. 3795–3802, 2006.

[135] J. D. Koralek, J. F. Douglas, N. C. Plumb, J. D. Griffith, S. T. Cundiff, H. C. Kapteyn, M. M. Murnane, and D. S. Dessau, "Experimental setup for low-energy laser-based angle resolved photoemission spectroscopy," *Review of Scientific Instruments*, vol. 78, p. 053905, 2007.

[136] M. P. Seah and W. A. Dench, "Quantitative electron spectroscopy of surfaces: A standard data base for electron inelastic mean free paths in solids," *Surface and Interface Analysis*, vol. 1, pp. 2–11, 1979.

[137] C. A. Schmuttenmaer, M. Aeschlimann, H. E. Elsayed-Ali, R. J. D. Miller, D. A. Mantell, J. Cao, and Y. Gao, "Time-resolved two-photon photoemission from Cu(100): Energy dependence of electron relaxation," *Physical Review B*, vol. 50, pp. 8957–8960, 1994.

[138] L. Cheng, X. Wang, W. Yang, J. Chai, M. Yang, M. Chen, Y. Wu, X. Chen, D. Chi, K. E. J. Goh, J.-X. Zhu, H. Sun, S. Wang, J. C. W. Song, M. Battiato, H. Yang, and E. E. M. Chia, "Far out-of-equilibrium spin populations trigger giant spin injection into atomically thin MoS_2," *Nature Physics*, vol. 15, pp. 347–351, 2019.

[139] X. Zhang, S. Mizukami, T. Kubota, Q. Ma, M. Oogane, H. Naganuma, Y. Ando, and T. Miyazaki, "Observation of a large spin-dependent transport length in organic spin valves at room temperature," *Nature Communications*, vol. 4, p. 1392, 2013.

[140] K. Sokolowski-Tinten, R. K. Li, A. H. Reid, S. P. Weathersby, F. Quirin, T. Chase, R. Coffee, J. Corbett, A. Fry, N. Hartmann, C. Hast, R. Hettel, M. H. von Hoegen, D. Janoschka, J. R. Lewandowski, M. Ligges, F. M. zu Heringdorf, X. Shen, T. Vecchione, C. Witt, J. Wu, H. A. Dürr, and X. J. Wang, "Thickness-dependent electron–lattice equilibration in laser-excited thin bismuth films," *New Journal of Physics*, vol. 17, p. 113047, 2015.

[141] M. Farle, "Ferromagnetic resonance of ultrathin metallic layers," *Reports on Progress in Physics*, vol. 61, pp. 755–826, 1998.

List of publications

Published Papers

- M. Ligges, I. Avigo, D. Golež, H. U. R. Strand, Y. Beyazit, K. Hanff, F. Diekmann, L. Stojchevska, M. Kalläne, P. Zhou, K. Rossnagel, M. Eckstein, P. Werner, and U. Bovensiepen: Ultrafast Doublon Dynamics in Photoexcited $1T - \mathrm{TaS_2}$. Phys. Rev. Lett. 120, 166401 (2018)

- Y. Beyazit, J. Beckord, P. Zhou, J.P. Meyburg, F. Kühne, D. Diesing, M. Ligges, and U. Bovensiepen: Local and Nonlocal Electron Dynamics of Au/Fe/MgO(001) Heterostructures Analyzed by Time-Resolved Two-Photon Photoemission Spectroscopy. Phys. Rev. Lett. 125, 076803 (2020)

- Florian Kühne, Yasin Beyazit, Björn Sothmann, J. Jayabalan, Detlef Diesing, Ping Zhou, and Uwe Bovensiepen: Ultrafast transport and energy relaxation of hot electrons in Au/Fe/MgO(001) heterostructures analyzed by linear time-resolved photoelectron spectroscopy. Phys. Rev. Research 4, 033239 (2022)

- Y. Beyazit, F. Kühne, D. Diesing, P. Zhou, J. Jayabalan, B. Sothmann, and U. Bovensiepen: Ultrafast electron dynamics in Au/Fe/MgO(001) analyzed by Au- and Fe-selective pumping in time-resolved two-photon photoemission spectroscopy: Separation of excitations in adjacent metallic layers. Phys. Rev. B 107, 085412 (2023)

Ultrafast Doublon Dynamics in Photoexcited 1T-TaS$_2$

M. Ligges,[1,*] I. Avigo,[1] D. Golež,[2] H. U. R. Strand,[2] Y. Beyazit,[1] K. Hanff,[3] F. Diekmann,[3] L. Stojchevska,[1]
M. Kalläne,[3] P. Zhou,[1] K. Rossnagel,[3] M. Eckstein,[4] P. Werner,[2] and U. Bovensiepen[1]

[1]*Faculty of Physics, University of Duisburg-Essen, 47048 Duisburg, Germany*
[2]*Department of Physics, University of Fribourg, 1700 Fribourg, Switzerland*
[3]*Institute of Experimental and Applied Physics, University of Kiel, 24098 Kiel, Germany*
[4]*Max Planck Research Department for Structural Dynamics, University of Hamburg-CFEL, 22761 Hamburg, Germany*

Strongly correlated materials exhibit intriguing properties caused by intertwined microscopic interactions that are hard to disentangle in equilibrium. Employing nonequilibrium time-resolved photoemission spectroscopy on the quasi-two-dimensional transition-metal dichalcogenide 1T-TaS$_2$, we identify a spectroscopic signature of doubly occupied sites (doublons) that reflects fundamental Mott physics. Doublon-hole recombination is estimated to occur on timescales of electronic hopping $\hbar/J \approx 14$ fs. Despite strong electron-phonon coupling, the dynamics can be explained by purely electronic effects captured by the single-band Hubbard model under the assumption of weak hole doping, in agreement with our static sample characterization. This sensitive interplay of static doping and vicinity to the metal-insulator transition suggests a way to modify doublon relaxation on the few-femtosecond timescale.

Complex matter is characterized by strong interactions between different microscopic degrees of freedom, often resulting in rich phase diagrams where tiny variations of controllable parameters can lead to significant changes of the macroscopic material properties [1]. This competition or coexistence often occurs on comparable energy scales, and thus is only partly accessible in the spectral domain. The dynamics of such systems, driven out of equilibrium by an external stimulus, can shed new light on the underlying short- and long-range interactions because different coupling mechanisms result in dynamics on experimentally distinguishable femto- to picosecond timescales [2]. In contrast to materials with well-defined quasiparticles, the theoretical description and analysis of nonequilibrium phenomena in strongly correlated electron systems is challenging [3]. Model studies have predicted intriguing effects of electron-phonon coupling [4–6], spin excitations [7–9], and dynamical screening [10], but connecting these insights to measurements on real materials has rarely been attempted. In this Letter, we analyze the photoinduced electron dynamics in a quasi-two-dimensional system with strong electron-electron and electron-phonon interaction and a finite density of defects. Our combined theoretical and experimental study shows how to disentangle such competing processes in the time domain, and how the nature of photoexcited carriers and the dominant relaxation pathways can be identified.

1T-TaS$_2$ is a layered crystal that exhibits a manifold of electronically and structurally ordered phases [11–13], recently amended by quantum spin liquid properties [14]. In its high-temperature state ($T > 542$ K), the system is undistorted and metallic, while cooling results in the formation of various charge density waves (CDW) with an increasing degree of commensurability and a transition to semiconductorlike behavior. Below the critical temperature of 180 K, a commensurate periodic lattice distortion is formed, giving rise to the formation of "David star"-shaped 13-Ta-atom cluster sites. This structural distortion is accompanied by a rearrangement of the partially filled Ta 5d band into submanifolds. The uppermost half-filled band is prone to a Mott-Hubbard transition, forming an occupied lower Hubbard band (LHB) representing a single particle population per cluster and an unoccupied upper Hubbard band (UHB) indicating a double population of cluster sites. On-site Coulomb interaction acts on these doublons and leads to an energy gap of 350–420 meV between the LHB and UHB [15]. This widely accepted picture was recently challenged [16]. It was proposed that the formation of an energy gap can be explained by orbital texturing, which implies that Mott physics is not primarily responsible for the insulating state. Our combined theoretical and experimental effort shows how such ambiguity can be addressed under nonequilibrium conditions. We identify a hierarchy of timescales which allows for specific studies of electronic correlation effects in complex materials.

Time- and angle-resolved photoemission spectroscopy is a powerful tool for exploring the ultrafast electronic response of 1T-TaS$_2$ on femto- to picosecond timescales [17–20]. Our present studies were carried out in a pump-probe scheme in normal emission geometry (which probes electronic states at the center of the Brillouin zone) on *in situ* cleaved single crystals, which exhibit nonperfect stoichiometric ratios

($1T$-Ta$_{(1-x)}$S$_2$ with $x \leq 0.03$) [21] (see Supplemental Material for sample characterization [22]). The samples were excited with 50 fs laser pulses from a regenerative Ti:Sa laser amplifier ($\hbar\omega_{\text{pump}} = 1.55$ eV) operating at a 250 kHz repetition rate and probed by direct photoemission using frequency-quadrupled pulses ($\hbar\omega_{\text{probe}} = 6.2$ eV). The pump-probe cross-correlation width was determined to be 110 ± 5 fs (Gaussian full width at half maximum) through the fastest observed response, and the corresponding maximum was set as time zero. The spectral resolution of 80 meV was determined by analyzing the width of the high-temperature Fermi edge (assumed to be rigid). Incident excitation fluences F were kept well below the critical energy density necessary to drive the system thermally into the nearly commensurate CDW phase [23].

We present data obtained in a weak excitation limit and at a base temperature of $T = 30$ K, a situation in which we expect only minor modifications of the CDW-ordered state. Assuming that every absorbed pump photon excites one valence electron on one cluster site once, the excited electron density in the first atomic layers is estimated to be $< 3\%$ for $F = 100\ \mu\text{J/cm}^2$ [24]. Under such conditions, we observe a photoemission peak at $E - E_F \approx 175$ meV [Fig. 1(a)] that is barely visible for higher F and T, even when the transient spectra are averaged over the relevant delay range, as displayed in Figs. 1(b) and 1(c). The contrast between this photoemission peak and the

FIG. 1. (a) False-color representation of the time-dependent photoelectron intensity above E_F at 30 K for $F = 60\ \mu\text{J/cm}^2$ in normal emission. Besides an excitation continuum, the upper Hubbard band is observed at $E - E_F \approx 175$ meV in the vicinity of $t = 0$. (b) and (c) show photoemission spectra after excitation for selected T and F, respectively. The spectra were averaged within $\Delta t = -95 \ldots -35$ fs. Curves in (b) are offset for better visibility.

underlying background differs between samples of different growth batches, a finding that we assign to minute variations of stochiometric composition, and thus, hole doping (see Supplemental Material for details [22]). The general behavior, however, is the same for all samples under investigation. Figure 1(a) shows a false-color representation of time-dependent photoemission spectra. Upon pumping, a broad excitation continuum is generated that reaches up to $E - E_F \approx 1.5$ eV. The population decay of this continuum is resolved, and the closer to E_F the intensity is analyzed, the longer the relaxation times become—a behavior well known for electronic excitations at metal surfaces [27]. In contrast, the sharp spectral signature at 175 meV responds significantly faster. Due to its femtosecond dynamics, we interpret this feature as the UHB that directly reflects double occupation of cluster sites. This assignment is corroborated by the observed energy of the feature, which is in agreement with recent scanning tunneling microscopy studies [15]. It is furthermore observed that the UHB intensity decreases with increasing temperature [Fig. 1(b)], which is consistent with the emergence of a macroscopic coexistence of insulating and conducting domains (corresponding to the different CDW states) up to the critical temperature of 542 K, where the full transition to the normal metallic phase occurs [12].

The distinct response of the UHB becomes evident when the transient energy distribution curves are considered [Fig. 2(a)]. The UHB spectral weight reaches its maximum around $t = 0$ and is lost after 100 fs. This loss is accompanied by ultrafast filling of the gapped region around $E - E_F \approx -0.2 \ldots 0.2$ eV. At later delays, only the intensity of the broad continuum remains.

In order to further discuss the temporal evolution of the UHB and separate its dynamics from the underlying continuum, we decomposed both spectral contributions by fitting the energy distribution curves with an exponential background and a Lorentzian line, as shown exemplarily in Fig. 2(b). The fit results are shown in Fig. 2(c) and reveal the ultrafast response of the UHB in contrast to the slower dynamics of the spectral background that exhibits a population decay time of 277 fs. This background is still present at positive delays, when the UHB intensity has disappeared. Correspondingly, the UHB is not populated by secondary excitations, and we conclude that the photoinduced dynamics cannot be described by incoherent scattering processes considering rigid bands. The temporal evolution of the UHB intensity is the fastest response observed in our experiments, and we set its maximum to time zero. Analyzing the dynamics [Fig. 2(c)], we estimate the timescale of doublon-hole recombination to be < 20 fs due to the absence of an exponential decay component within experimental uncertainties (see Supplemental Material for details [22]). This timescale matches approximately the electronic hopping $\hbar/J \approx 14$ fs estimated by dynamic mean field theory [18]. The fast response is furthermore confirmed by the fact
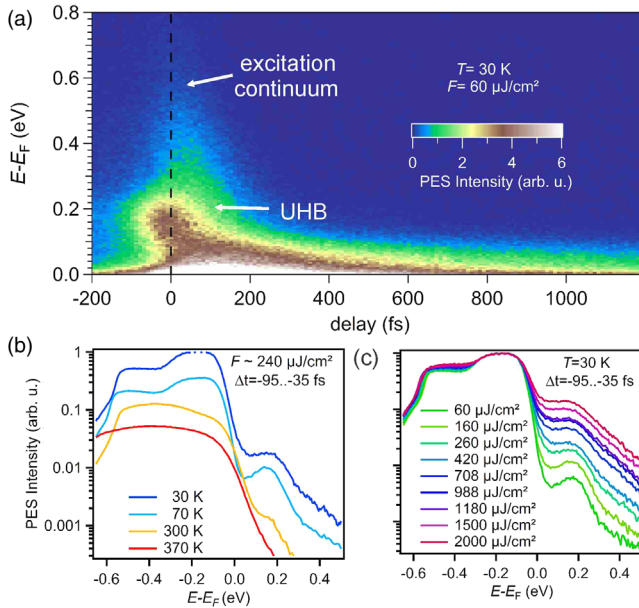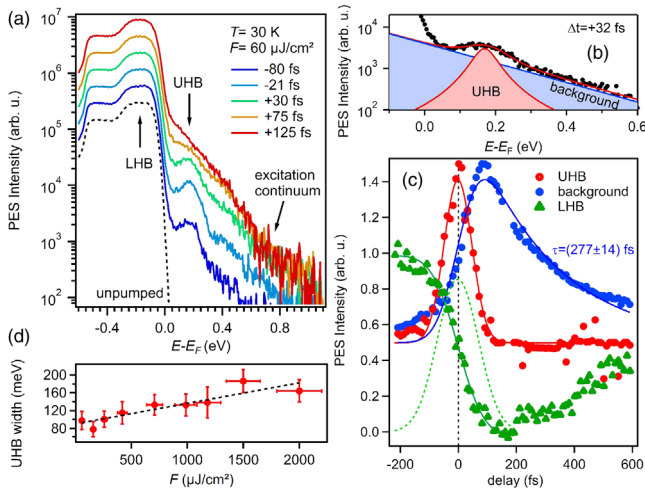
FIG. 2. (a) Transient photoemission spectra obtained for $T = 30$ K and $F = 60$ μJ/cm^2. The curves are offset for better visibility. (b) Exemplary fit to the transient energy distribution curve obtained at $\Delta t = +32$ fs. The superposition of the continuum and the Lorentzian line was convoluted with the instrumental energy resolution function. (c) Temporal evolution of the UHB spectral signature in direct comparison to the underlying continuum and electronic gap, as well as the LHB intensity loss that can be described by an error function (solid green line). The temporal derivative $-(dI/dt)$ of the least mean square fit of the LHB dynamics is shown as a dashed line for comparison with the UHB signal. Curves are rescaled for better visibility. (d) Spectral width of the UHB signature as a function of excitation fluence F.

that the temporal evolution of the UHB coincides with the decrease of the LHB signature that is instantaneously depopulated by the pump pulse [19], and thus can be well described by the temporal integral of the laser pulse cross correlation as shown in Fig. 2(c). This temporal coincidence does not imply a direct optical transition between the LHB and the UHB, whose energy difference of approximately 350 meV in our experiments is largely exceeded by the pump photon energy (1.55 eV). We consider a simultaneous depopulation of the LHB by excitation into higher-lying bands and a population of the UHB due to an excitation from lower-lying states. A corresponding initial state at $E - E_F \approx -1.3$ eV was earlier identified using static ARPES [28,29]. Reducing the pump photon energy to 0.92 eV and 1.04 eV was found to suppress the UHB signature (see Supplemental Material [22]).

For a given excitation fluence, we find that the UHB line profile is independent of t (see Supplemental Material [22]), indicating that the population of the UHB thermalizes on a timescale that cannot be resolved in our experiments. We observe that the energetic width of the UHB signature increases linearly with F [Fig. 2(d)], which excludes the possibility that the photoemission line arises from an unoccupied rigid band populated by the 6 eV probe pulse. We also find that the energy of the UHB line is independent of t (see Supplemental Material [22]), which

indicates that the signature is not related to polaronic excitations discussed in the literature [30]. Our finding rather demonstrates the ultrafast decoupling of electronic and lattice degrees of freedom, since polaron formation would result in an energetic stabilization on phononic timescales. Indeed, the response of the UHB is faster than a quarter period of the highest-frequency phonons in 1T-TaS$_2$ of 11.9 THz [31], which also implies a decoupling of the doublon dynamics from the periodic lattice distortion associated with CDW formation. We stress that the doublon recombination measured here is related to the dynamics of the occupation, while all-optical experiments probe the dynamics of the joint density of states [32]. In a non-equilibrium situation, there is no simple relation between the two, so both experimental approaches provide complementary information.

Our experimental findings are partly incompatible with the recently proposed energy gap formation based on orbital texturing [16]. Optical excitation of an orbitally ordered system could in principle result in the loss of order due to increased entropy and scattering. The fastest timescale we can imagine is determined by electron-electron scattering which leads to the relaxation dynamics of the excitation continuum; see Figs. 1(a) and 2(a). However, the observed loss of the UHB occurs earlier than that, a fact explained in the present study by local electron-electron correlations. We thus conclude that, while orbital order as well as layer stacking might play a role in electronic band formation, a discussion of the experimentally observed ultrafast electronic response in close vicinity to E_F requires a scenario where electron-electron correlation is considered.

In the following, we discuss a simple theoretical picture based on a purely electronic model and demonstrate how strong interaction is crucial for describing the ultrafast dynamics. We simulate the dynamics of a single-band Hubbard model on a two-dimensional triangular lattice:

$$H = \sum_{i\delta\sigma} J c_{i+\delta,\sigma}^{\dagger} c_{i+\delta,\sigma} + \mu n_i + U \sum_i \left(n_{i\uparrow} - \frac{1}{2} \right) \left(n_{i\downarrow} - \frac{1}{2} \right),$$
$$(1)$$

where $c_{i\sigma}^{\dagger}$ denotes the creation operators for a Fermion on lattice site i with spin σ, J is the hopping integral between neighboring sites, μ is the chemical potential, n_i is the number of carriers on site i, and U is the on-site Coulomb repulsion. The electric field of the pump laser $E(t)$ is applied along the (1,1) direction and is incorporated via the Peierls substitution. The parameters were chosen such that, in the absence of an external perturbation [$E(t) = 0$], this Hamiltonian mimics the equilibrium spectral function of single-layer 1T-TaS$_2$ [15,17] with a bandwidth of $W = 0.36$ eV. Since $U \approx W$, the material is close to the metal-insulator transition, which leads to short recombination times.

The dynamics after optical excitation is modeled by perturbing the system with a Gaussian pulse of the form $E(t) = E_0 \exp[-4.6(t-t_0)^2/t_0^2] \sin[\omega(t-t_0)]$, where the duration of the pulse t_0 is chosen such that it accommodates a single optical cycle. The frequency ω was chosen to be $\omega/J = 8.0$, and the pulse amplitude was $E_0/(Je) = 2.0$. While this pulse frequency generates direct transitions between the LHB and UHB, we have also checked the scenario of photo-doping from lower-lying bands by temporarily coupling an occupied (empty) electron bath to the UHB (LHB). The relaxation dynamics for both protocols is consistent, since it is mainly governed by the excess kinetic energy of the excited doublons. The amplitude of the excitation does not alter the qualitative dynamics as long as one restricts the scenario to the weak excitation regime. To solve the electron dynamics, we use the nonequilibrium dynamical mean field theory [3], which maps a correlated lattice problem onto a self-consistently determined impurity problem [33]. To treat the impurity problem, we use the lowest-order strong coupling expansion, the noncrossing approximation (NCA). To confirm that the resulting dynamics is qualitatively correct, and not sensitive to the details of the band structure, we also employ the one-crossing approximation (OCA) on the Bethe lattice. Realistic gap sizes are obtained for $U = 0.36$ eV in NCA, and $U = 0.43$ eV in OCA.

The transient occupation dynamics is analyzed in terms of the partial Fourier transform of the lesser component of the Green's function $A^<(t,\omega) = \mathrm{Im}[\int_t^{t+t_{\max}} dt' e^{i\omega(t'-t)} G^<(t',t)]$ (occupied density of states). We will first discuss the response of the ideal Mott insulator at half band filling ($n = 1$); see Fig. 3(a). The optical excitation leads to a partial
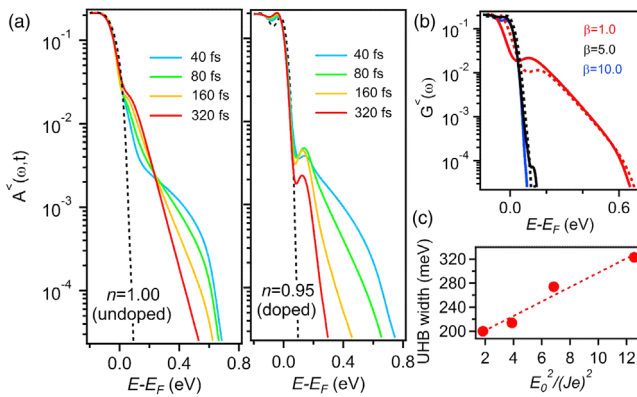
occupation of the UHB that relaxes within the band and results in a slow population buildup at the lower edge. This prediction of a monotonically increasing UHB population is inconsistent with the experimental observation. It is, however, in agreement with previous studies [34], which show that the thermalization in an isolated small-gap insulator can lead to an increase in double occupation on the timescale of a few inverse hoppings. We note that in contrast to the previous theoretical interpretations [17,18], but in agreement with the experimental data (and recent arguments based on high-temperature expansions [35]), our simulations do not predict a substantial gap filling after photoexcitation.

A more realistic description is obtained if one considers an effectively hole-doped system $1T\text{-}Ta_{(1-x)}S_2$. Taking into account the indications reported in the Supplemental Material [22], we estimate that the effective filling of the subband straddling E_F can range from half filled ($x = 0$, $n = 1$) to almost empty ($x = 0.03$, $n = 0.17$). To discuss the general influence on the UHB dynamics, we assume a small doping level of $n = 0.95$ [Fig. 3(b)]. In contrast to the half-filled case, the occupation function in the doped case shows a transient increase of the doublon spectral weight, which quickly vanishes. This evolution is in qualitative agreement with the experimental finding.

In agreement with previous works [34,36], the Hubbard band in the small-gap regime thermalizes on the timescale of several inverse hoppings, which we confirmed by checking that the fluctuation-dissipation theorem is fulfilled. Therefore, we can compare the results in the long-time limit with the thermal states at elevated temperatures; see Fig. 3(b). In the half-filled case, the UHB of this small-gap system is always substantially occupied due to the finite overlap of the high-temperature Fermi-Dirac distribution function with the UHB. In the doped case, the Fermi-Dirac distribution is shifted to lower energies, and the overlap with the UHB is exponentially suppressed. In such a situation, a significant population in the UHB can only be achieved at extremely high electron temperatures. This also explains the experimental requirement of low excitation densities to observe the ultrafast reduction of the UHB population and is reflected in the experimental finding that the spectral width of the UHB increases linearly with excitation fluence [Fig. 2(d)], which is also reproduced in the calculation [Fig. 3(c)]. We note that even though electron-phonon coupling is important in $1T\text{-}TaS_2$, we can neglect the phonon dynamics on electronic timescales. In any event, the effect of electron-phonon interactions, as well as short-ranged spin excitations, would be to speed up the relaxation and thermalization [37,38]. This likely explains the faster dynamics in the experiment, compared to the simulations which neglect this physics.

In summary, we identified in a combined experimental and theoretical study the double electron population of cluster sites in $1T\text{-}TaS_2$ and estimated their relaxation time

FIG. 3. (a) Time evolution of the occupation function $G^<(\omega,t)$ for a half-filled band ($n = 1$, left panel) and in the hole-doped case ($n = 0.95$, right panel). The dashed lines show the equilibrium situation before excitation. (b) Equilibrium occupation function $G^<(\omega)$ for $n = 0.98$ (solid lines) and $n = 0.95$ (dashed lines) at different temperatures $\beta = (k_B T)^{-1}$, given in units of W ($\beta = 1$ corresponds to a temperature of 32 300 K). (c) Spectral width of the UHB signature at $E - E_F \approx 175$ meV as a function of excitation density E_0^2. The dashed line indicates a linear dependence.

to be on the order of the electronic hopping $\hbar/J$. Essential was the time domain approach, which facilitated the detection of doublons before further excitations like secondary electrons or phonons set in. We emphasize the importance of static and photoexcited holes, which enable the ultrafast relaxation on hopping timescales. Our results suggest a tunability of femtosecond dynamics in the vicinity of the Fermi level, which has potential impact for high-frequency applications. More generally, the identification of nonequilibrium signatures of strong electron correlations has led to an improved microscopic understanding of complex materials with competing interactions.

---

[*]manuel.ligges@uni-due.de

[1] E. Dagotto, Science **309**, 257 (2005).

[2] C. Giannetti, M. Capone, D. Fausti, M. Fabrizio, F. Parmigiani, and D. Mihailovic, Adv. Phys. **65**, 58 (2016).

[3] H. Aoki, N. Tsuji, M. Eckstein, T. Oka, and P. Werner, Rev. Mod. Phys. **86**, 779 (2014).

[4] M. Eckstein and P. Werner, Phys. Rev. Lett. **110**, 126401 (2013).

[5] D. Golež, J. Bonca, L. Vidmar, and S. A. Trugman, Phys. Rev. Lett. **109**, 236402 (2012).

[6] P. Werner and M. Eckstein, Europhys. Lett. **109**, 37002 (2015).

[7] D. Golež, J. Bonca, M. Mierzejewski, and L. Vidmar, Phys. Rev. B **89**, 165118 (2014).

[8] J. Kogoj, Z. Lenarcic, D. Golež, M. Mierzejewski, P. Prelovsek, and J. Bonca, Phys. Rev. B **90**, 125104 (2014).

[9] M. Eckstein and P. Werner, Phys. Rev. Lett. **113**, 076405 (2014).

[10] D. Golež, M. Eckstein, and P. Werner, Phys. Rev. B **92**, 195123 (2015).

[11] J. A. Wilson, F. J. DiSalvo, and S. Mahajan, Adv. Phys. **24**, 117 (1975).

[12] B. Sipos, A. F. Kusmartseva, A. Akrap, H. Berger, L. Forro, and E. Tutis, Nat. Mater. **7**, 960 (2008).

[13] L. Stojchevska, I. Vaskivsky, T. Mertelj, D. Svetin, S. Brazovskii, and D. Mihailovic, Science **344**, 177 (2014).

[14] M. Klanjšek, A. Zorko, R. Žitko, J. Mravlje, Z. Jagličić, P. K. Biswas, P. Prelovšek, D. Mihailovic, and D. Arčon, Nat. Phys. **13**, 1130 (2017).

[15] D. Cho, S. Cheom, K.-S. Kim, S.-H. Lee, Y.-H. Cho, S.-W. Cheong, and H. W. Yeom, Nat. Commun. **7**, 10453 (2015).

[16] T. Ritschel, J. Trinckauf, K. Koepernik, B. Buchner, M. v. Zimmermann, H. Berger, Y. I. Joe, P. Abbamonte, and J. Geck, Nat. Phys. **11**, 328 (2015).

[17] L. Perfetti, P. A. Loukakos, M. Lisowski, U. Bovensiepen, H. Berger, S. Biermann, P. S. Cornaglia, A. Georges, and M. Wolf, Phys. Rev. Lett. **97**, 067402 (2006).

[18] L. Perfetti, P. A. Loukakos, M. Lisowski, U. Bovensiepen, M. Wolf, H. Berger, S. Biermann, and A. Georges, New J. Phys. **10**, 053019 (2008).

[19] J. C. Petersen *et al.*, Phys. Rev. Lett. **107**, 177402 (2011).

[20] S. Hellmann *et al.*, Nat. Commun. **3**, 1069 (2012).

[21] T. Endo, S. Nakao, W. Yamaguchi, T. Hasegawa, and K. Kitazawa, Solid State Commun. **116**, 47 (2000).

[22] See Supplemental Material at http://link.aps.org/supplemental/10.1103/PhysRevLett.120.166401 for additional data and details on sample growth and characterization.

[23] S. Hellmann *et al.*, Phys. Rev. Lett. **105**, 187401 (2010).

[24] This estimation is based on the optical properties reported in Ref. [25] and a geometrical site density of $n = 7 \times 10^{13}$ cm^{-2} [26].

[25] A. R. Beal, H. P. Hughes, and W. Liang, J. Phys. C **8**, 4236 (1975).

[26] A. Yamamoto, Phys. Rev. B **27**, 7823 (1983).

[27] M. Bauer, A. Marienfeld, and M. Aeschlimann, Prog. Surf. Sci. **90**, 319 (2015).

[28] N. Smith, S. Kevan, and F. DiSalvo, J. Phys. C **18**, 3175 (1985).

[29] M. Arita, H. Negishi, K. Shimada, F. Xu, A. Ino, Y. Takeda, K. Yamazako, A. Kimuar, S. Qiao, S. Negishi, M. Sasaki, H. Namatame, and M. Taniguchi, Physica (Amsterdam) **351B**, 265 (2004).

[30] N. Dean, J. C. Petersen, D. Fausti, R. I. Tobey, S. Kaiser, L. V. Gasparov, H. Berger, and A. Cavalleri, Phys. Rev. Lett. **106**, 016401 (2011).

[31] L. V. Gasparov, K. G. Brown, A. C. Wint, D. B. Tanner, H. Berger, G. Margaritondo, R. Gaál, and L. Forró, Phys. Rev. B **66**, 094301 (2002).

[32] A. Mann, E. Baldini, A. Odeh, A. Magrez, H. Berger, and F. Carbone, Phys. Rev. B **94**, 115122 (2016).

[33] A. Georges, G. Kotliar, W. Krauth, and M. J. Rozenberg, Rev. Mod. Phys. **68**, 13 (1996).

[34] P. Werner, K. Held, and M. Eckstein, Phys. Rev. B **90**, 235102 (2014).

[35] E. Perepelitsky, A. Galatas, J. Mravlje, R. Žitko, E. Khatami, B. Shastry, and A. Georges, arXiv:1608.01600.

[36] M. Eckstein and P. Werner, Phys. Rev. B **84**, 035122 (2011).

[37] Z. Lenarčič and P. Prelovšek, Phys. Rev. Lett. **111**, 016401 (2013).

[38] Z. Lenarčič and P. Prelovšek, Phys. Rev. B **90**, 235136 (2014).

Local and Nonlocal Electron Dynamics of Au/Fe/MgO(001) Heterostructures Analyzed by Time-Resolved Two-Photon Photoemission Spectroscopy

Y. Beyazit[ ],[1] J. Beckord[ ],[1,*] P. Zhou,[1] J. P. Meyburg,[2] F. Kühne,[2] D. Diesing,[2] M. Ligges,[1,†] and U. Bovensiepen[ ][1,‡]

[1]*Faculty of Physics and Center for Nanointegration (CENIDE), University of Duisburg-Essen,*
Lotharstrasse 1, 47057 Duisburg, Germany
[2]*Faculty of Chemistry, University of Duisburg-Essen, Universitätsstrasse 5, 45141 Essen, Germany*

Employing femtosecond laser pulses in front and back side pumping of Au/Fe/MgO(001) combined with detection in two-photon photoelectron emission spectroscopy, we analyze local relaxation dynamics of excited electrons in buried Fe, injection into Au across the Fe-Au interface, and electron transport across the Au layer at 0.6 to 2.0 eV above the Fermi energy. By analysis as a function of Au film thickness we obtain the electron lifetimes of bulk Au and Fe and distinguish the relaxation in the heterostructure's constituents. We also show that the excited electrons propagate through Au in a superdiffusive regime and conclude further that electron injection across the epitaxial interface proceeds ballistically by electron wave packet propagation.

Excited charge carriers relax in metals and semiconductors on femtosecond to picosecond timescales due to the large phase space for electron-electron (*e*-*e*) and electron-phonon scattering [1,2]. Microscopic insight into these processes was developed by combined efforts of static spectroscopy, spectroscopy in the time domain, and *ab initio* theory [3]. Early optical experiments used schemes in which the back side of the sample is pumped and the front side is probed and analyzed the propagation dynamics through the bulk of thin films [4]. Time- and angle-resolved two-photon photoelectron spectroscopy exploited the sensitivity to electron energy and momentum and was key to develop a comprehensive understanding of the microscopic nature of the engaged elementary processes which hot electrons experience [5–9]. In heterostrutures such an analysis is challenging but highly desired given the widespread application of these material systems. The surface sensitivity of photoelectron spectroscopy is a severe limitation for heterostructures and buried media which can be overcome by using hard x-ray photons in photoemission [10,11]. Also, photoelectrons with low kinetic energy are reported to probe the bulk [12] or buried interface electronic structure [13,14] in selected cases.

Hot electrons are characterized by their energy above the Fermi energy $E - E_F \gg k_B T$, where T is the equilibrium temperature, and their momentum **k**. For a component $k_\perp$ directed from the surface into bulk, transport effects occur. So far, local dynamics at the surface and nonlocal contributions due to, e.g., transport were distinguished indirectly by analyzing relaxation at surfaces [15–19]. Particular systems allowed a microscopic description of electron propagation through a molecular layer [20] and resonant tunneling across a dielectric film [13].

Electronic transport properties are essential in condensed matter. Besides transport in Bloch bands at E_F, problems like incoherent hopping in molecular wires [21] and two-dimensional materials [22,23], superdiffusive spin currents [24], and attosecond phenomena at surfaces [25] are important. The relevance of spin-dependent charge carrier transport in femtosecond magnetization dynamics has spurred the use of back side pumping in optical pump-probe experiments [26–28], which provide energy and momentum integrated information. Also, detection in microscopes provides insight into carrier propagation [29] and plasmon dynamics [30]. Back side pump–front side probe photoelectron spectroscopy might have considerable impact, since it promises energy- and momentum-dependent information [29].

In this Letter we report such a back side pump–front side probe photoemission experiment for the model system Au/Fe/MgO(001). While for thin films the electronic relaxation agrees for front and back side pumping, we identify electron transport for thicker Au films upon back side pumping. We are aware that the dynamics has a spin-dependent contribution [26]. The experiment performed here is spin integrating and we focus on the charge dynamics. By analyzing the relaxation time dependence on the Au film thickness d_{Au} we distinguish the electron dynamics in the Au and Fe constituents.

Figure 1, top, depicts the experimental configuration. Femtosecond laser pulses are generated by a commercial regenerative Ti:sapphire amplifier (Coherent RegA 9040) combined with a noncollinear optical parametric amplifier (NOPA, Clark-MXR) operating at 250 kHz repetition rate. We use pairs of 2 and 4 eV pulses each of 50 fs pulse duration as pump and probe pulses, respectively. Pump pulses are sent to the Au/Fe/MgO(001) sample kept at
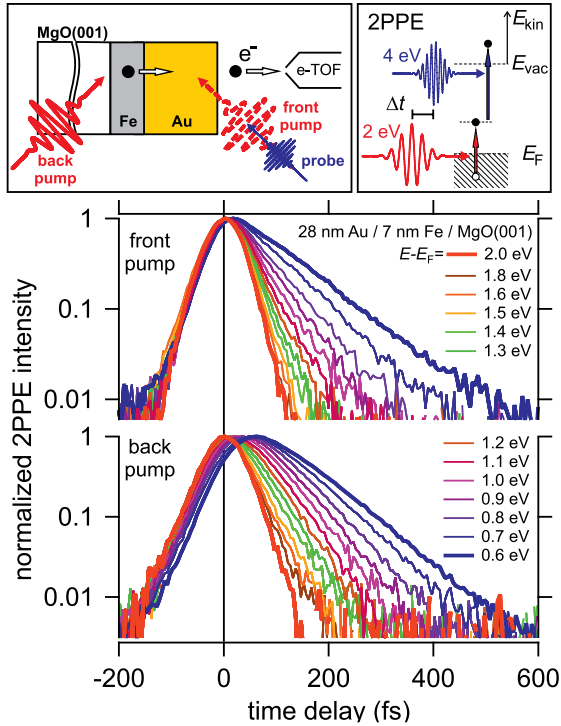
FIG. 1. Top: Schematic experimental configuration for front or back side pumping depicting the photoelectron analysis and the two-color 2PPE process for absorption of one 2 and 4 eV photon each. Bottom: Time-dependent 2PPE intensity on a logarithmic scale for front (top) and back side pumping (bottom) at indicated energies above the Fermi level.

room temperature with $\pm 45°$ angle of incidence, see Fig. 1, and reach at first the Au surface in the case of front side pumping or are transmitted through MgO(001) and excite electrons of Fe in back side pumping. The incident pump fluence was 50 $\mu J/cm^2$. Probe pulses are in both configurations sent to the Au surface close to 45° and probe electrons in intermediate, excited states (i) at the surface in case of front side pumping or (ii) propagating through Au for back side pumping. The time-delayed probe pulse photoemits electrons from the excited state by absorption of one 4 eV photon, see Fig. 1, top right, and generates the two-color two-photon photoemission (2PPE) signal discussed here. Photoelectrons are analyzed by a time-of-flight (e-TOF) analyzer [31] and collected within $\pm 11°$ off the surface normal; see Fig. 1. For a discussion of one- and two-color 2PPE, see Supplemental Material [32]. The Au/Fe/MgO(001) system was chosen due to its epitaxial structure [33] and inert surface. Samples are grown by molecular beam epitaxy, stored under Ar atmosphere, transferred in ambient conditions to the photoemission chamber, and cleaned by heating to 80 °C. Crystalline order and layer thickness were analyzed on a twin sample by cross-sectional transmission electron microscopy, magnetometry, profilometry, and atomic force microscopy; see Refs. [28,32,34].

Figure 1 shows the time-dependent 2PPE intensity for back and front side pumping at selected energies $E - E_F$ for 28 nm Au/7 nm Fe/MgO(001). Time zero is defined by the fastest signal given by the intensity maximum of electrons at the maximum kinetic energy; see $E - E_F = 2.0$ eV in Fig. 1 [35]. The upper panel depicts front side pump 2PPE data. The lower panel shows results for back side pumping which exhibit a shift in time delay of the intensity built up and maximum increasing with decreasing $E - E_F$. This effect is assigned to delayed arrival of excited electrons at the Au-vacuum interface. Both datasets exhibit slower intensity relaxation for lower $E - E_F$ due to the respective increase in hot electron lifetime [2].

Figure 2 compares back side pump 2PPE for different Fe thickness d_{Fe} [Fig. 2(a)] and for different d_{Au} [Fig. 2(b)]. While in the case of larger d_{Au} transport effects are identified through a time shift in arrival at the Au surface, increasing of d_{Fe} results essentially in a loss of intensity. Note that such loss of intensity is also observed with increasing d_{Au}, see Supplemental Material [32], because only electrons which reach the Au-vacuum interface are detected. These observations support the following concept. The Fe layer acts as the optically excited electron emitter and the Au layer serves as the acceptor hosting electron propagation as depicted by the scheme in Fig. 1.

Time-dependent 2PPE intensities are fitted by a single exponential decay $\propto \exp \frac{t-t_0}{\tau}$ convolved with the cross-correlation (XC) of the laser pulses as determined by 2PPE at maximum kinetic energy. Examples of such fits are plotted as insets in Figs. 3(a) and 3(b). This fitting determines energy-dependent, inelastic relaxation times $\tau(E)$ and time offsets $t_0(E)$, at which the relaxation starts. Figure 3 shows $\tau(E)$ and $t_0(E)$ obtained for $d_{Au} = 28$ nm [Fig. 3(a)] and 5 nm [Fig. 3(b)] at $d_{Fe} = 7$ nm. We find a decrease in τ with increasing energy and—if compared at identical energies—τ is larger for the thicker than for the thinner Au layer. Front and back side pumping lead to small differences in $\tau(E)$ near 1.2 eV for $d_{Au} = 28$ nm. Such differences were not obtained for $d_{Au} = 5$ nm, neither in τ nor in t_0. For sufficiently thin films transport effects become negligible [17] and $d_{Au} = 5$ nm provides a
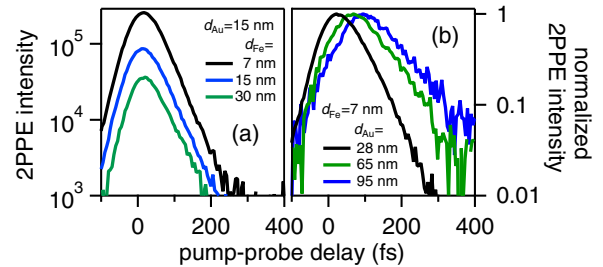

FIG. 2. Time-dependent 2PPE intensity upon back side pumping at $E - E_F = 1.0$ eV shown in (a) for different d_{Fe} and constant d_{Au} and vice versa in (b). In the latter case the 2PPE intensity is normalized to the intensity maximum.
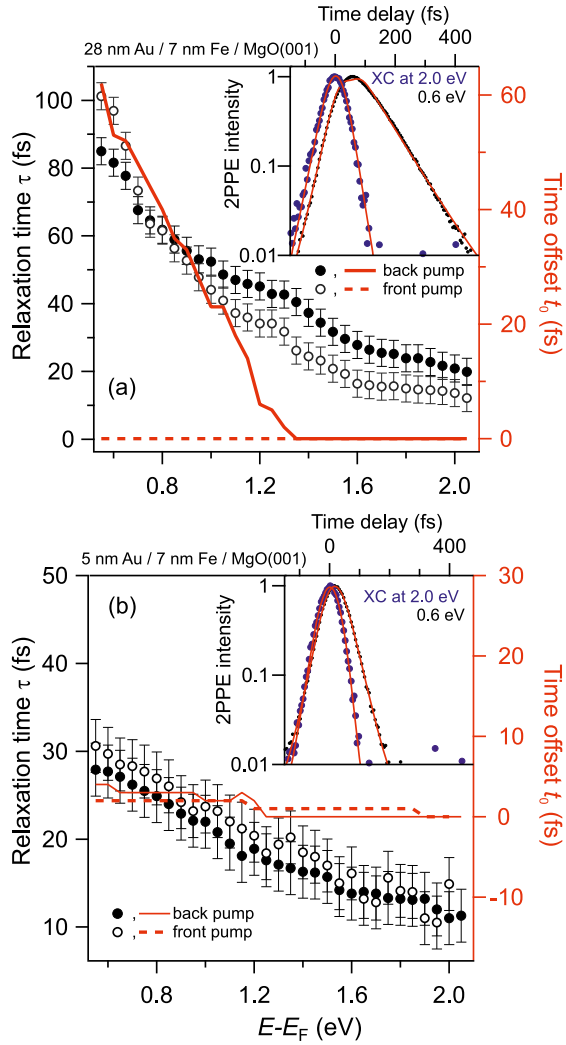
FIG. 3. Left axis: Relaxation times τ of hot electrons at energies $E - E_F$ for 28 nm (a) and 5 nm (b) thick Au films on 7 nm Fe on a MgO(001) substrate. Right axis: Time offset t_0; see text. Both quantities are determined by fitting and are given for front and back side pumping as indicated. Error bars for t_0 are ± 6 fs at 0.7 eV and decrease to ± 3 fs at 2.0 eV.

reasonable reference value in this regard. For $d_{Au} = 28$ nm we identify for back side pumping variations in $t_0(E)$ up to 60 fs while $t_0(E)$ does not vary for front side pumping. The observed $t_0 > 0$ for back side pumping is a nonlocal effect and quantifies the time required for transport of electrons excited in Fe, injected into Au across the Fe-Au interface, and propagation through Au toward the Au-vacuum interface, where they are probed in 2PPE. Following bulk optical constants [36], 95% of the absorbed pump pulse intensity excites the 7 nm Fe layer and the 2PPE signal detected for 28 nm Au/7 nm Fe/MgO(001) is dominated by electrons propagating through Au. This assignment is supported by the increase in t_0 and τ for the larger d_{Au} compared to the thinner one; see Fig. 3. Since relaxation times of hot electrons in metals at few eV energy above E_F are determined by inelastic e-e scattering [2], the similar

trend of increasing t_0 and τ with decreasing energy indicates that t_0 is determined by inelastic e-e scattering as well. On this basis the electron transport through Au is concluded to proceed in a superdiffusive regime, which occurs before hot electrons have thermalized by subsequent e-e scattering events [37]. As discussed in Supplemental Material [32], reaching the limit of diffusion would require many scattering processes, which we exclude due to the observation $t_0(E_0) < \tau(E_0)$, which implies individual events. Ballistic propagation, on the other hand, would occur for absent relaxation, which disagrees with the observed temporal broadening in time-dependent 2PPE intensities while the electrons propagate through Au; see Fig. 2(b). Given the weak variation of the electron group velocity with respect to the Fermi velocity in Au [38], ballistic propagation is also incompatible with the increase in t_0 observed with decreasing energy. Scattering might increase the covered distance to the surface and a determination of the electron's propagation velocity $v = d_{Au}/t_0$ which results for $d_{Au} = 28$ nm at $E - E_F = 1.0$ eV in $v = 1.3$ nm/fs—a value close to v_F in Au—has to be treated with care. We note that we cannot exclude ballistic propagation of electrons $E - E_F \geq 1.3$ eV where we find $t_0 = 0$ fs, which is set by the time zero determination.

We investigate $d_{Au} = 5$–95 nm and identify a thickness-dependent $\tau = \tau(d_{Au})$, see Figs. 2 and 3. The obtained τ are for thinner films smaller than in bulk Au [2]. Figure 4, top, shows $\tau(d_{Au})^{-1}$ for different energy. To understand this thickness dependence we consider a continuum approach to scattering in the heterostructure, which assumes that the individual thicknesses d_{Au}, d_{Fe} and the extension of the interface d_{Au-Fe} are comparable with the respective scattering lengths $\lambda_i \approx \tau_i v_{F,i}$, which are ≈ 50 nm in Au and ≈ 2 nm in Fe [28,39]. The integral scattering probability of electrons propagating in the interface normal direction z increases linearly with d_{Au}, d_{Fe}, and d_{Au-Fe}:

$$\int_0^{d_{Fe}+d_{Au-Fe}+d_{Au}} \frac{dz}{\tau(z)} = \frac{d_{Fe}}{\tau_{Fe}} + \frac{d_{Au-Fe}}{\tau_{Au-Fe}} + \frac{d_{Au}}{\tau_{Au}}. \quad (1)$$

In our 2PPE back side pump–front side probe experiment, the variation of d_{Au} allows separation of two independent processes, see Supplemental Material [32], described by

$$\frac{1}{\tau(d_{Au})} = \frac{1}{\tau_1} + \frac{1}{\tau_2} = A + \frac{B}{d_{Au}}. \quad (2)$$

Figure 4, top, depicts fits following Eq. (2) with A and B being the intercept with the ordinate and slope as a function of $1/d_{Au}$, respectively. Note that both A and B/d have the dimension of a rate. Our analysis determines relaxation times τ_1 and τ_2 which are plotted in Fig. 4, bottom, in comparison with literature values for hot electron lifetimes in bulk Au and Fe τ_{Au}, τ_{Fe}, respectively, taken from
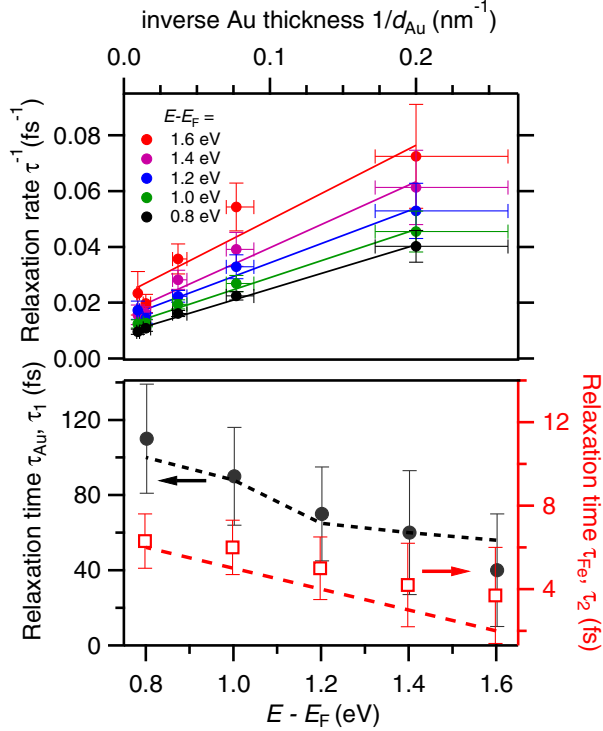
FIG. 4. Top: Relaxation rates τ^{-1} as a function of d_{Au}^{-1} for different electron energies above E_F. Lines represent linear fits. Slopes and intercepts determine the two relaxation rates discussed in the text. Bottom panel: The determined relaxation times τ_1 (•) and τ_2 (□) as a function of $E - E_F$ in comparison with literature data for hot electron lifetimes τ_{Au} and τ_{Fe} from Ref. [2] shown by dashed lines.

Ref. [2]. Given the agreement of our data with these values, we conclude to have distinguished the electron dynamics in the two constituents and thereby demonstrate sensitivity to the buried Fe film.

The observation of τ_{Au} is straightforward to understand. A hot electron injected into Au at the Fe-Au interface propagates through the Au film and reaches the surface where it is photoemitted. During the propagation it experiences inelastic e-e scattering with rates of bulk Au and transfers energy to a secondary electron. We detect this scattering by the time-dependent reduction of 2PPE intensity at the energy of interest at which the electrons were injected into Au. We did not take secondary electrons into account because we restricted the energy scale to rather high values $E - E_F$, where primary electrons dominate [17]. Secondary electrons start to contribute at half the primary energy [2], which is $E - E_F < 1$ eV for the highest energy electrons at 2 eV studied here. For sufficiently thick Au films, the second term in Eq. (2) vanishes and scattering in Au dominates.

Understanding the determination of τ_{Fe} in buried Fe requires consideration of all processes that may contribute to B in Eq. (2). Following Eq. (1) we take scattering in Fe and at the Au-Fe interface into account. Since we find within the experimental uncertainty $\tau_2 = \tau_{Fe}$, we conclude

that the scattering at the interface does not contribute. In the investigated epitaxial heterostructure electron injection across the interface can be assumed to proceed by coherent propagation of a wave packet in Bloch states which conserves energy and momentum across the interface [18,34]. Therefore, the injection process across the Au-Fe interface is ballistic and violates our above assumption $d_{Au-Fe} \approx \lambda_{Au-Fe}$, which might be reason for not detecting it.

In addition, the reported approach provides opportunities to analyze scattering at buried interfaces originating from (i) electronic interface states and (ii) scattering at nonepitaxial interfaces for heterostructures in general. While (i) might be investigated in an analysis following Eq. (2) through the appearance of anomalies in the energy-dependent relaxation times and lead to deviations from the smooth variation reported in Fig. 4, the impact of (ii) can be determined by changing the thickness of both constituents as introduced in Eq. (1). As detailed in Ref. [32], this would lead to an additional term in Eq. (2) representing scattering at the interface.

In conclusion, we demonstrate a time-domain analysis of electron dynamics in epitaxial Au/Fe/MgO(001) heterostructures with a total thickness of 12–102 nm. We distinguish the energy-dependent scattering rates in Fe and Au using optical pumping of Fe and detection at the Au surface by two-photon photoemission. We also identify the electron propagation to proceed in a superdiffusive regime. This separation of electron dynamics in the individual heterostructure constituents showcases the impact our approach might have on future work. A spectroscopy which accesses buried interfaces or media and provides energy-dependent information on electron dynamics is rarely available and may provide highly desired insight into heterostructures in general. We expect that this approach will bridge conventional transport measurements and time-domain spectroscopy. Implementing angle- and spin-resolved detection of photoelectrons will provide momentum- and spin-dependent information and a more comprehensive understanding of electron dynamics in complex materials. We expect further that this approach to electron transport dynamics will be applied to semiconducting or insulating material systems due to its sensitivity to excited electronic states.

Note added in proof.—We mention a recent report of spin- and time-resolved photoemission of spin currents, see [40].

[*]Present address: University of Zurich, 8057 Zurich, Switzerland.

†Present address: Fraunhofer IMS, 47057 Duisburg, Germany.

‡uwe.bovensiepen@uni-due.de

[1] J. Shah, *Ultrafast Spectroscopy of Semiconductors and Semiconductor Nanostructures*, 2nd ed. (Springer, Berlin, 1999).

[2] M. Bauer, A. Marienfeld, and M. Aeschlimann, Hot electron lifetimes in metals probed by time-resolved two-photon photoemission, Prog. Surf. Sci. **90**, 319 (2015).

[3] P. M. Echenique, R. Berndt, E. Chulkov, T. Fauster, A. Goldmann, and U. Höfer, Decay of electronic excitations at metal surfaces, Surf. Sci. Rep. **52**, 219 (2004).

[4] S. D. Brorson, J. G. Fujimoto, and E. P. Ippen, Femtosecond Electronic Heat-Transport Dynamics in Thin Gold Films, Phys. Rev. Lett. **59**, 1962 (1987).

[5] N.-H. Ge, C. M. Wong, R. L. Lingle, J. D. McNeill, K. J. Gaffney, and C. B. Harris, Femtosecond dynamics of electron localization at interfaces, Science **279**, 202 (1998).

[6] M. Weinelt, M. Kutschera, T. Fauster, and M. Rohlfing, Dynamics of Exciton Formation at the Si(100) c(4×2) Surface, Phys. Rev. Lett. **92**, 126801 (2004).

[7] J. Güdde, M. Rohleder, T. Meier, S. W. Koch, and U. Höfer, Time-resolved investigation of coherently controlled electric currents at a metal surface, Science **318**, 1287 (2007).

[8] *Dynamics at Solid State Surfaces and Interfaces*, edited by U. Bovensiepen, H. Petek, and M. Wolf (Wiley-VCH, Berlin, 2012), Vol. 1.

[9] X. Cui, C. Wang, A. Argondizzo, S. Garrett-Roe, B. Gumhalter, and H. Petek, Transient excitons at metal surfaces, Nat. Phys. **10**, 505 (2014).

[10] J. C. Woicik, *Hard X-Ray Photoelectron Spectroscopy* (Springer, Heidelberg, 2016).

[11] L.-P. Oloff, M. Oura, K. Rossnagel, A. Chainani, M. Matsunami, R. Eguchi, T. Kiss, Y. Nakatani, T. Yamaguchi, J. Miyawaki *et al.*, Time-resolved HAXPES at SACLA: Probe and pump pulse-induced space-charge effects, New J. Phys. **16**, 123045 (2014).

[12] T. Kiss, F. Kanetaka, T. Yokoya, T. Shimojima, K. Kanai, S. Shin, Y. Onuki, T. Togashi, C. Zhang, C. T. Chen *et al.*, Photoemission Spectroscopic Evidence of Gap Anisotropy in an f-Electron Superconductor, Phys. Rev. Lett. **94**, 057001 (2005).

[13] M. Rohleder, W. Berthold, J. Güdde, and U. Höfer, Time-Resolved Two-Photon Photoemission of Buried Interface States in Ar/Cu(100), Phys. Rev. Lett. **94**, 017401 (2005).

[14] L. Rettig, P. S. Kirchmann, and U. Bovensiepen, Ultrafast dynamics of occupied quantum well states in Pb/Si(111), New J. Phys. **14**, 023047 (2012).

[15] M. Aeschlimann, M. Bauer, S. Pawlik, R. Knorren, G. Bouzerar, and K. H. Bennemann, Transport and dynamics of optically excited electrons in metals, Appl. Phys. A **71**, 485 (2000).

[16] M. Lisowski, P. A. Loukakos, U. Bovensiepen, J. Stähler, C. Gahl, and M. Wolf, Ultra-fast dynamics of electron thermalization, cooling and transport effects in Ru(001), Appl. Phys. A **78**, 165 (2004).

[17] M. Lisowski, P. A. Loukakos, U. Bovensiepen, and M. Wolf, Femtosecond dynamics and transport of optically excited electrons in epitaxial Cu films on Si(111) $- 7 \times 7$, Appl. Phys. A **79**, 739 (2004).

[18] J. P. Gauyacq, A. G. Borisov, and M. Bauer, Excited states in the alkali/noble metal surface systems: A model system for the study of charge transfer dynamics at surfaces, Prog. Surf. Sci. **82**, 244 (2007).

[19] P. S. Kirchmann, L. Rettig, X. Zubizarreta, V. M. Silkin, E. V. Chulkov, and U. Bovensiepen, Quasiparticle lifetimes in metallic quantum-well nanostructures, Nat. Phys. **6**, 782 (2010).

[20] J. Stähler, M. Meyer, D. O. Kusmierek, U. Bovensiepen, and M. Wolf, Ultrafast electron transfer dynamics at NH_3/Cu (111) interfaces: determination of the transient tunneling barrier, J. Am. Chem. Soc. **130**, 8797 (2008).

[21] A. A. Kocherzhenko, S. Patwardhan, F. C. Grozema, H. L. Anderson, and L. D. A. Siebbeles, Mechanism of Charge Transport along Zinc Porphyrin-Based Molecular Wires, J. Am. Chem. Soc. **131**, 5522 (2009).

[22] A. S. Ngankeu, S. K. Mahatha, K. Guilloy, M. Bianchi, C. E. Sanders, K. Hanff, K. Rossnagel, J. A. Miwa, C. Breth Nielsen, M. Bremholm *et al.*, Quasi-one-dimensional metallic band dispersion in the commensurate charge density wave of $1T - TaS_2$, Phys. Rev. B **96**, 195147 (2017).

[23] S.-H. Lee, J. S. Goh, and D. Cho, Origin of the Insulating Phase and First-Order Metal-Insulator Transition in $1T - TaS_2$, Phys. Rev. Lett. **122**, 106404 (2019).

[24] M. Battiato, K. Carva, and P. M. Oppeneer, Superdiffusive Spin Transport as a Mechanism of Ultrafast Demagnetization, Phys. Rev. Lett. **105**, 027203 (2010).

[25] Z. Tao, C. Chen, T. Szilvási, M. Keller, M. Mavrikakis, H. Kapteyn, and M. Murnane, Direct time-domain observation of attosecond final-state lifetimes in photoemission from solids, Science **353**, 62 (2016).

[26] A. Melnikov, I. Razdolski, T. O. Wehling, E. T. Papaioannou, V. Roddatis, P. Fumagalli, O. Aktsipetrov, A. I. Lichtenstein, and U. Bovensiepen, Ultrafast Transport of Laser-Excited Spin-Polarized Carriers in Au/Fe/MgO(001), Phys. Rev. Lett. **107**, 076601 (2011).

[27] N. Bergeard, M. Hehn, S. Mangin, G. Lengaigne, F. Montaigne, M. L. M. Lalieu, B. Koopmans, and G. Malinowski, Hot-Electron-Induced Ultrafast Demagnetization in Co/Pt Multilayers, Phys. Rev. Lett. **117**, 147203 (2016).

[28] I. Razdolski, A. Alekhin, N. Ilin, J. P. Meyburg, V. Roddatis, D. Diesing, U. Bovensiepen, and A. Melnikov, Nanoscale interface confinement of ultrafast spin transfer torque driving non-uniform spin dynamics, Nat. Commun. **8**, 15007 (2017).

[29] J. Sung, C. Schnedermann, L. Ni, A. Sadhanala, R. Y. S. Chen, C. Cho, L. Priest, J. M. Lim, H.-K. Kimand, B. Monserrat *et al.*, Long-range ballistic propagation of carriers in methylammonium lead iodide perovskite thin films, Nat. Phys. **16**, 171 (2020).

[30] A. Klick, M. Großmann, M. Beewen, P. Bittorf, J. Fiutowski, T. Leißner, H.-G. Rubahn, C. Reinhardt, H.-J. Elmers, and M. Bauer, Femtosecond time-resolved photoemission electron microscopy operated at sample illumination from the rear side, Rev. Sci. Instrum. **90**, 053704 (2019).

[31] P. S. Kirchmann, L. Rettig, D. Nandi, U. Lipowski, M. Wolf, and U. Bovensiepen, A time-of-flight spectrometer for angle-resolved detection of low energy electrons in two dimensions, Appl. Phys. A **91**, 211 (2008).

[32] See Supplemental Material at http://link.aps.org/supplemental/10.1103/PhysRevLett.125.076803 for detailed information on the samples, the experimental method, and the continuum model for electron transport.

[33] M. Rickart, B. F. P. Roos, T. Mewes, J. Jorzick, S. O. Demokritov, and B. Hillebrands, Morphology of epitaxial metallic layers on MgO substrates: Influence of submono-layer carbon contamination, Surf. Sci. **495**, 68 (2001).

[34] A. Alekhin, I. Razdolski, N. Ilin, J. P. Meyburg, D. Diesing, V. Roddatis, I. Rungger, M. Stamenova, S. Sanvito, U. Bovensiepen *et al.*, Femtosecond Spin Current Pulses Generated by the Nonthermal Spin-Dependent Seebeck Effect and Interacting with Ferromagnets in Spin Valves, Phys. Rev. Lett. **119**, 017202 (2017).

[35] In case of ballistic electron propagation through Au the back side optical excitation would occur at negative time delays given by the Fermi velocity, which is for Au $v_F \approx 1.4$ nm/fs [4,36], multiplied with d_{Au}.

[36] J. H. Weaver, C. Krafka, D. W. Lynch, and E. E. Koch, *Optical Properties of Metals*, Physics Data (Fachinformationszentrum, Karlsruhe, 1981), Vols. 18–1,18–2.

[37] M. Battiato, K. Carva, and P. M. Oppeneer, Theory of laser-induced ultrafast superdiffusive spin transport in layered heterostructures, Phys. Rev. B **86**, 024404 (2012).

[38] D. M. Nenno, B. Rethfeld, and H. C. Schneider, Particle-in-cell simulation of ultrafast hot-carrier transport in Fe/Au heterostructures, Phys. Rev. B **98**, 224416 (2018).

[39] V. P. Zhukov, E. V. Chulkov, and P. M. Echenique, Lifetimes and inelastic mean free path of low-energy excited electrons in Fe, Ni, Pt, and Au: Ab initio $GW + T$ calculations, Phys. Rev. B **73**, 125105 (2006).

[40] K. Bühlmann, G. Saerens, A. Vaterlaus, and Y. Acremann, Detection of femtosecond spin injection into a thin gold layer by time and spin resolved photoemission, Sci. Rep. **10**, 12632 (2020).

Ultrafast transport and energy relaxation of hot electrons in Au/Fe/MgO(001) heterostructures analyzed by linear time-resolved photoelectron spectroscopy

Florian Kühne,[1] Yasin Beyazit [ORCID],[1] Björn Sothmann,[1] J. Jayabalan [ORCID],[1] Detlef Diesing,[2] Ping Zhou,[1] and Uwe Bovensiepen [ORCID][1,*]

[1]*Faculty of Physics and Center for Nanointegration (CENIDE), University of Duisburg-Essen, Lotharstr. 1, 47057 Duisburg, Germany*
[2]*Faculty of Chemistry, University of Duisburg-Essen, Universitätsstr. 5, 45711 Essen, Germany*

In condensed matter, scattering processes determine the transport of charge carriers. In case of heterostructures, interfaces determine many dynamic properties such as charge transfer and transport, and spin current dynamics. Here, we discuss optically excited electron dynamics and their propagation across a lattice-matched, metal-metal interface of single crystal quality. Using femtosecond time-resolved linear photoelectron spectroscopy upon optically pumping different constituents of the heterostructure, we establish a technique that probes the electron propagation and its energy relaxation simultaneously. In our approach, a near-infrared pump pulse excites electrons directly either in the Au layer or in the Fe layer of epitaxial Au/Fe/MgO(001) heterostructures while the transient photoemission spectrum is measured by an ultraviolet probe pulse on the Au surface. Upon femtosecond laser excitation, we analyze the relative changes in the electron distribution close to the Fermi energy and assign characteristic features of the time-dependent electron distribution to transport of hot and nonthermalized electrons from the Fe layer to the Au surface and vice versa. From the measured transient electron distribution, we determine the excess energy, which we compare with a calculation based on the two-temperature model that takes diffusive electron transport into account. On this basis, we identify a transition with increasing Au layer thickness from a superdiffusive to a diffusive transport regime at 20–30 nm.

I. INTRODUCTION

The propagation of electric currents in metals and semiconductors is on a microscopic level determined by scattering of charge carriers with themselves, with crystal defects, and with phonons. At interfaces the electronic structure changes abruptly and the necessary energy and/or momentum transfer of charge carriers is mediated by interaction with secondary charge carriers and/or phonons. In case of pseudomorphic interfaces without defects, hybrid electronic wave functions develop, which conserve energy and momentum at selected points in the electronic band structure $E(\mathbf{k})$ across the interface. In the more general case with defects, electron and momentum changes across the interface are compensated by inelastic and elastic scattering processes, respectively. Therefore, charge injection and charge carrier multiplication across interfaces is an interesting problem, which is relevant in various energy conversion applications [1]. In case of spin-polarized currents across such interfaces, generated by, e.g., charge carriers excited in ferro- or ferrimagnetic emitters, spin-dependent dynamic properties occur and spin filter effects are a typical example [2].

Analysis of the femto- to picosecond dynamics of optically excited, hot charge carriers in condensed matter provides microscopic information on the interaction processes, which these charge carriers experience in the relaxation process [3–5]. To achieve such a quantitative understanding, it is essential to distinguish transport effects, which spatially redistribute the excited electron density leading to transient inhomogeneous situations, and spatially homogeneous relaxation.

Transport phenomena arise from driving forces such as gradients in occupation number. A gradient in the hot electron density, which can be excited by optical absorption of femtosecond laser pulses within the optical absorption depth, drives electron currents. The latter can be either ballistic or diffusive depending on the ratio between scattering length and sample size. A gradient in temperature results in heat flow [6,7]. Such transport effects have been observed in early studies [8], and were empirically [6] as well as microscopically [9] taken into account in theoretical modeling. While these effects are particularly relevant in surface sensitive experiments, e.g.. time-resolved photoemission [10–13] and surface second harmonic generation [6], they also facilitated separation of transport from relaxation effects in linear optical experiments due to differences in depth sensitivity of the real and imaginary part of the optical response [14].

Brorson *et al.* [8] have established a direct experimental approach to distinguish transport (nonlocal effects) from relaxation (local effects) in pump-probe experiments by pumping and probing at opposite or identical sides of the sample of interest, respectively. The resulting transient electronic

---

population can modify chemical bonding of molecules on surfaces in catalytic surface reactions [11,15]. The back-side excitation geometry allows to pump the system exclusively by hot electrons contrary to optical excitations, which involve initial states in, e.g., HOMO-LUMO transitions of adsorbed molecules. More recently, this backside pump approach was used by Melnikov *et al.* to investigate spin currents in Fe/Au heterostructures [16–19] by linear and nonlinear optical pump-probe experiments and by Bergeard *et al.* [20] to analyze hot electron induced demagnetization of Co/Pt heterostructures by linear optical means. In a more recent work, ballistic charge carrier propagation has been investigated in such a configuration in perovskite thin films [5], however, without energy-dependent information on the scattering processes. Such spectroscopy was demonstrated in time-resolved two-photon photoemission experiments on epitaxial heterostructures Au/Fe/MgO(001) in which the pump pulse excited the Fe and the photoelectrons were emitted from the Au surface [21]. In this work, we demonstrated that achieving ballistic currents in these samples is challenging because the time scale for ballistic propagation through the sample at the Fermi velocity is close to the average electron-electron scattering time, which were reported earlier [4,22]. In such a case, the electronic transport is considered to be super-diffusive rather than ballistic [9]. Moreover, the spin-dependent dynamics in such heterostructures consisting out of ferromagnetic metals and heavy metals are exploited as THz emitters due to the spin-dependent currents across these interfaces [23]. Understanding the spatiotemporal electron distribution might facilitate a microscopic understanding in these emission processes and help to distinguish spin-polarized charge vs. magnon currents.

In this paper, we report our results on time-resolved linear photoemission spectroscopy (*tr*-PES) performed on epitaxial Au/Fe/MgO(001) heterostructures of different Au thicknesses. In these measurements, the photoemission spectrum of the Au layer in the vicinity of the Fermi energy (E_F) was probed while carriers were excited either directly in the same Au layer or in the nearby Fe layer. We analyze the dependence of the hot-electron dynamics as a function of the Au layer thickness and identify signatures of electronic transport in the nonequilibrium electron distribution function, which we discuss on the basis of the time-dependent excess energy.

II. EXPERIMENTAL DETAILS

The samples under study are epitaxial Au-Fe heterostructures grown on a transparent MgO(001) substrate using molecular beam epitaxy. A schematic of the sample is shown in Fig. 1(a). In a preparation chamber, Fe(001) was grown on the MgO(001) substrate, which was followed by growth of Au(001). Note that the in-plane axes of both layers are rotated by $\pi/4$ with respect to each other to minimize the lattice mismatch between Fe and Au and facilitate pseudomorphic growth [24,25]. The MgO allows for an almost transparent path for direct optical excitation of the Fe layer in the pump-probe measurements. The thickness of the layers was determined by AFM and depth analysis of grooves through the whole film stack, which was prepared by a needle. In this work, three different Au layers of thickness $d_{Au} = 5$ nm,
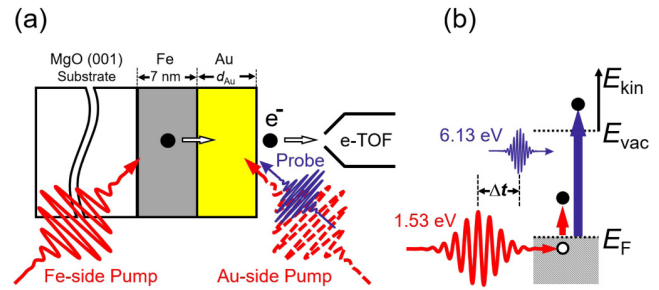

FIG. 1. (a) Schematic of the sample configuration along with the two pump and probe configurations used in the measurement of the *tr*-PES with an electron time of flight spectrometer (e-TOF). A 1.53 eV infrared pump beam excites carriers directly either in the Au layer (Au side) or in the Fe layer (Fe side) while a 6.13 eV UV pulse always probes the Au surface. (b) Energy diagram of the *tr*-PES measurement with a time delay Δt between the pump and probe pulses, E_{vac} is the vacuum energy, E_F is the Fermi energy of the metallic heterostructure and E_{kin} the kinetic energy of the photoelectrons.

15 nm, and 28 nm were investigated. The Fe layer was kept at a fixed thickness $d_{Fe} = 7$ nm. The time-resolved photoelectron spectroscopy measurements were carried out after sample transfer through ambient conditions into the vacuum chamber equipped with the photoelectron spectrometer under ultrahigh vacuum conditions in two different pump configurations, see Ref. [26] for a detailed description of the photoemission setup. The schematic of the pump and probe configurations are shown Fig. 1(a). In the Au-side configuration, both the pump and probe pulses arrive directly on the Au surface. In the Fe-side configuration, the pump pulse reaches the Fe layer by entering through the MgO substrate while the probing is still done on the Au surface, spatially separating the electron excitation from the probe at the surface. The infrared pump pulses at 1.53 eV used in the *tr*-PES measurements were obtained directly from the output of a Ti:Sapphire amplifier (Coherent RegA 9040) operating at a repetition rate of 250 kHz. The spectral width of the pump pulse was 70 meV full width at half-maximum (FWHM). The 6.13 eV probe pulses were obtained by generating the fourth harmonic of the fundamental 1.53 eV beam using two consecutive second-harmonic generations in a Beta barium borate crystal (β-BBO). Both the pump and probe beams were *p* polarized. The angle of incidence of both the pump and probe beams on the sample were close to 45°. In the Fe-side pump configuration, the pump beam has an incidence angle of 45° towards the sample and 90° with respect to the probe beam. The pump fluence used in all the measurements was about 100 μJcm^{-2}. It was limited by photoelectron emission due to multiphoton absorption of the pump pulse. The typical FWHM of the pump beam was usually between 100–150 μm with the probe beam focus being roughly 30% smaller to ensure homogeneous excitation. The kinetic energy of the photoelectrons emitted by the sample within an angle $\pm 11°$ to the surface normal was collected and measured using a time-of-flight electron spectrometer (e-TOF). The photoemission process in the Au layer is illustrated by Fig. 1(b). All the measurements were carried out at room temperature. The time resolution of the

FIG. 3. Photoemission intensity $I_{PES}(E)$ measured on the Au surface of the Au/Fe/MgO(001) heterostructure with $d_{Au} = 5\,\text{nm}$ at two different time delays for Fe-side (black) and Au-side (red) excitations. The photoemission spectra measured much before the arrival of the pump pulse are shown in light colors while the spectra obtained at time zero are shown in full colors. The spectra are normalized at $E - E_F = -0.1\,\text{eV}$. The incident pump fluence used in the experiment was about $100\,\mu\text{Jcm}^{-2}$.

pump photon energy $E = 1.53\,\text{eV}$, the angle of incidence $\theta = 45°$, the p polarization of the light, the refractive indices $n_{Au}(1.53\,\text{eV}) = 0.08$, $n_{Fe}(1.53\,\text{eV}) = 3.02$ and the extinction coefficients $k_{Au}(1.53\,\text{eV}) = 4.69$ $k_{Fe}(1.53\,\text{eV}) = 3.72$ [28]. We find that in case of Fe-side pumping the absorption is almost exclusively occurring inside the Fe layer: 99% for $d_{Au} = 5\,\text{nm}$ and 94% for $d_{Au} = 28\,\text{nm}$. The case for Au-side pump is more involved. In the bottom panel of Fig. 2 we recognize a strong variation in the relative intensity at the Fe-Au interface because of the change in refractive index. The thicker the Au layer is, the stronger the light field is attenuated in Au when it reaches Fe. The intensity that reaches Fe decreases with d_{Au}. At $d_{Au} = 5\,\text{nm}$, 11% of the pump is absorbed in Au, while the majority is absorbed in the Fe layer. For $d_{Au} = 28\,\text{nm}$, the absorption of the pump mostly occurs in the Au layer and for $d_{Au} = 15\,\text{nm}$ around 40% is absorbed in Au and 60% in Fe. We note that a systematic comparison of the pump-induced dynamics as a function of d_{Au} should be done for comparable pump conditions, i.e., Fe-side pumping. Au-side pumping distributes the pump energy in a nontrivial manner across the layer stack.

III. EXPERIMENTAL RESULTS

Figure 3 shows the recorded photoelectron spectra $I_{PES}(E)$ for $d_{Au} = 5\,\text{nm}$ well before the pump pulse arrival $\Delta t = -\infty$, which we term $I_{PES}^0(E)$, and at temporal pump-probe overlap $\Delta t = 0$. Results for the cases of Fe- and Au-side excitation are depicted. The measured photoemission spectra contain signatures of photoexcited holes at $E - E_F < 0\,\text{eV}$ for both configurations. However, in the present paper we discuss the changes above E_F due to the better statistics of the data, which allows for a detailed analysis. For energies above E_F, the spectrum at $\Delta t = -\infty$ follows a Fermi-Dirac distribution taking into account spectral broadening due to the ultraviolet femtosecond probe laser pulse with a bandwidth $\Delta E = 60\,\text{meV}$ and room temperature, where the data were recorded. The difference in the low-energy cutoff near $E - E_F < -1\,\text{eV}$,
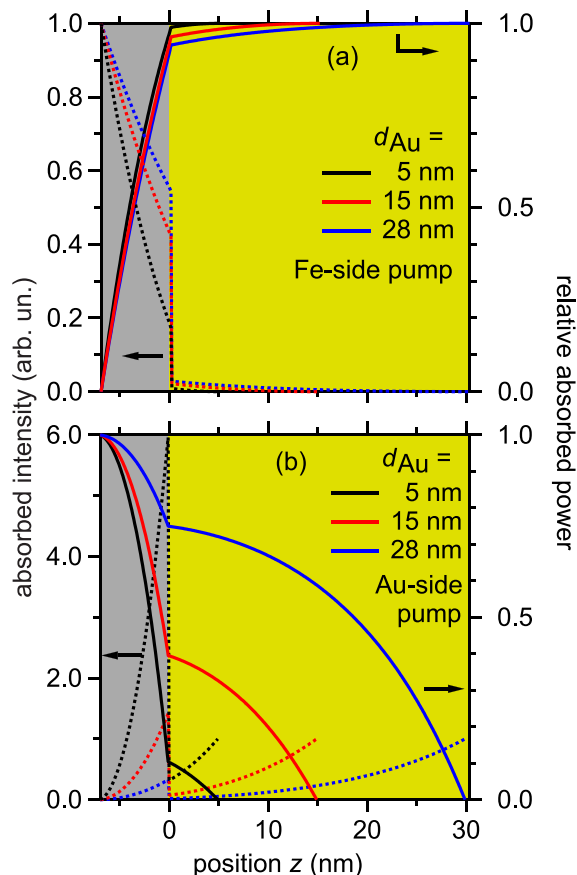

FIG. 2. The calculated relative pump light intensity with respect to the incident light field (dashed lines, left axis) and the relative absorbed pump light intensity (solid lines, right axis) as a function of Au layer thickness for (a) Fe-side and (b) Au-side pumping. The Fe layer thickness is fixed at 7 nm. The maximum in absorption intensity in (b) is higher at the interface because of the change in optical constants for a change in layer sequence.

setup was determined by measuring the temporal width of the highest electrons in the correlated photoemission signal, which was found to be below 100 fs.

To understand to what degree absorption of the pump pulse occurs in the Au and Fe layers, we calculate the electric field inside the material in both pump configurations using the IMD software [27] and derive the absorbed power $P(z)$ in the different constituents

$$P(z) = n(z)I(z) = n(z)|E(z)|^2 = n(z)I_t e^{-\alpha z}, \quad (1)$$

with z being the distance from the Fe-Au interface along the normal direction, α the absorption coefficient, $I(z)$ the intensity, $E(z)$ the electric field and $n(z)$ the refractive index of the material. The power in the layer stack is given by the real part of the Poynting vector. Figure 2 depicts the relative intensities for Fig. 2(a) Au-side and Fig. 2(b) Fe-side pumping, as well as the relative absorbed power, which we obtained by subtracting the transmitted field and normalizing the incoming intensity to 1 because we are only interested in the attenuation of the field by absorption. To determine the spatial distribution of the optical absorption in the heterostructure, we used the
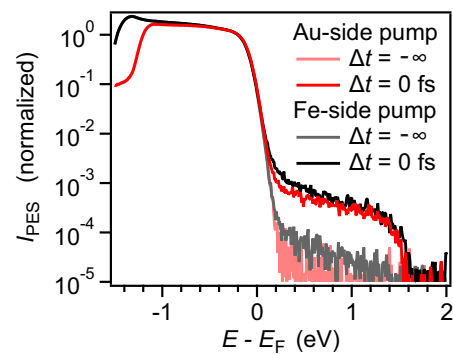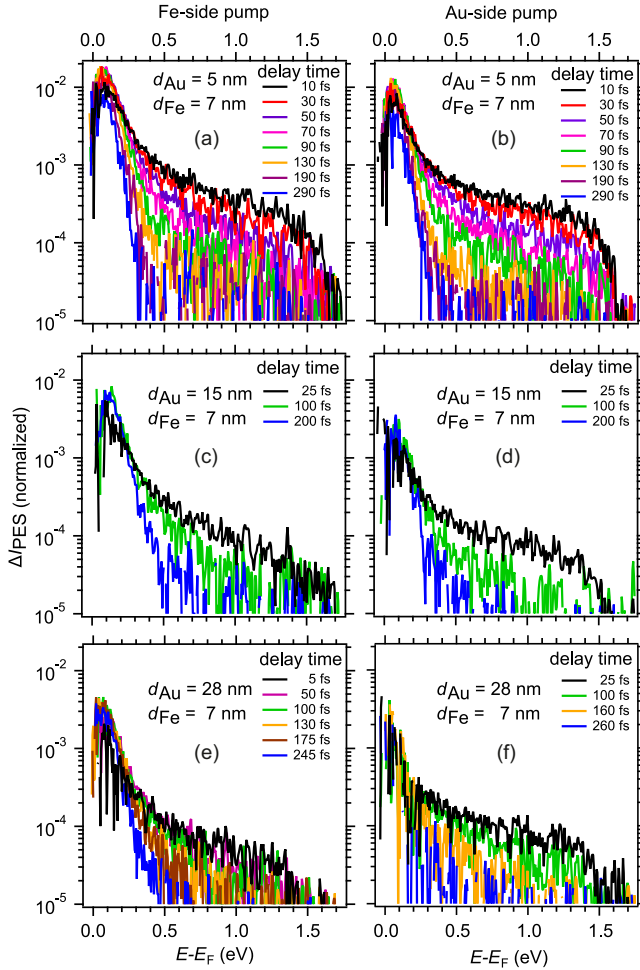
FIG. 4. Pump-induced changes in the time-resolved photoemission intensity $\Delta I_{PES}(\Delta t)$ at energies above the Fermi level for Fe-side (a), (c), (e) and Au-side (b), (d), (f) pumping for the three different Au layer thicknesses $d_{Au} = 5, 15,$ and 28 nm. The incident pump fluence was $100\,\mu Jcm^{-2}$. Spectra recorded at delay times in between the depicted ones were averaged symmetrically to improve the statistics and the variation in the time delays between the depicted spectra represent the statistics of the original data sets.
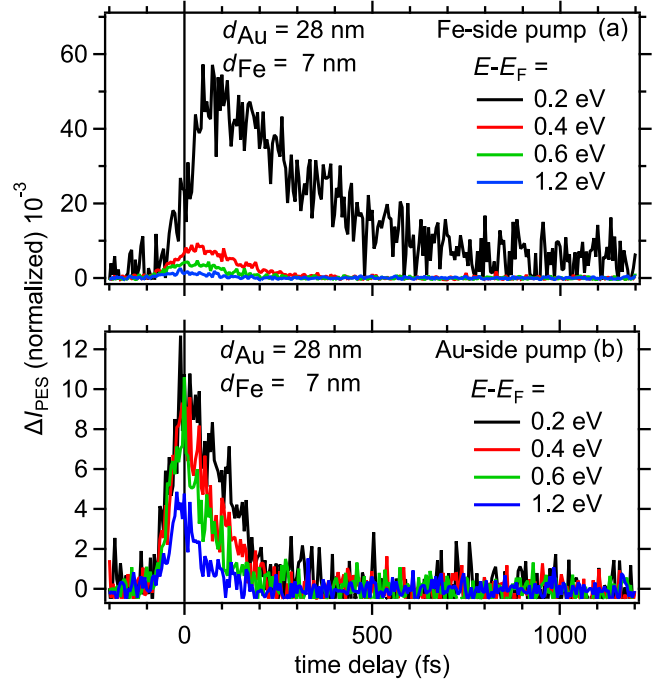

FIG. 5. Time-dependent change in photoemission intensity $\Delta I_{PES}(\Delta E)$ upon laser excitation at energies above the Fermi level for a Au layer thickness d_{Au} of 28 nm in both (a) Fe-side as well as (b) Au-side pumping. The intensities were integrated over an energy ΔE of 200 meV. Only selected energies in the 1.55 eV high pump induced change are shown for visibility.

which is determined by the work function, is explained by the different positions on the Au surface at which the spectra were recorded and local variation in the work function. With the absorption of the infrared pump pulse, electrons in the states up to 1.53 eV below E_F are excited to states up to 1.53 eV above E_F. One can clearly recognize this absorption by the increase in photoemission intensity relative to before the pump-pulse arrival by an order of magnitude to 10^{-4} at $\Delta t = 0$ in that energy range. Note that the spectra at $\Delta t = 0$ for Fe- and Au-side pumping are found to be almost identical for the 5 nm thick Au layer. For the further discussion the pump-induced changes in the photoelectron spectra $\Delta I_{PES}(E, \Delta t) = I_{PES}(E, \Delta t) - I_{PES}^0(E)$ are calculated.

In Figs. 4(a), 4(b) we show $\Delta I_{PES}(E, \Delta t)$ at selected delay times for Fe- and Au-side excitation of the heterostructure with $d_{Au} = 5$ nm. Such measurements were also performed for $d_{Au} = 15, 28$ nm and are also shown in Fig. 4. In all the

samples and independent of the side of excitation, the absorption of the pump pulse causes significant changes in ΔI_{PES} in the energy range of 0–1.5 eV at $\Delta t = 0$. The time-dependent evolution $\Delta I_{PES}(\Delta t)$ strongly depends on the electron energy and proceeds differently above and below $E-E_F = 0.5$ eV. We distinguish two contributions. At higher energies, the transient electron distribution depends exponentially on energy and relaxes with increasing Δt. The second contribution occurs for $E - E_F < 0.5$ eV and contains about one order of magnitude more electrons per energy. Further, up to nearly 100 fs the overall distribution is clearly nonthermal, i.e., it deviates from a Fermi-Dirac distribution.

In order to compare the difference in the temporal response at various energies, we plot the time-dependent change in photoemission intensity, $\Delta I_{PES}(E, \Delta t)$, for selected energies in Fig. 5 for Fe- and Au-side excitations of the heterostructure with $d_{Au} = 28$ nm and $d_{Fe} = 7$ nm. We observe that the magnitude of ΔI_{PES} of the low-energy electrons of the Fe-side pump case is much higher, it increases slowly reaching a maximum at a delay time of 100 fs, relaxes within 800 fs, and has a weak pedestal at longer delays. In the Au-side pump case, Fig. 5(b), the change in photoemission intensity is much weaker compared to the Fe-side case, even though we are directly probing the pumped region. Further, the maximum ΔI_{PES} at all energies are reached almost at zero time delay and they all decay faster. Thus, the behavior of the low-energy electrons of the Fe-pumped case is very different from all others. To investigate this effect in more detail, we calculate the time-dependent
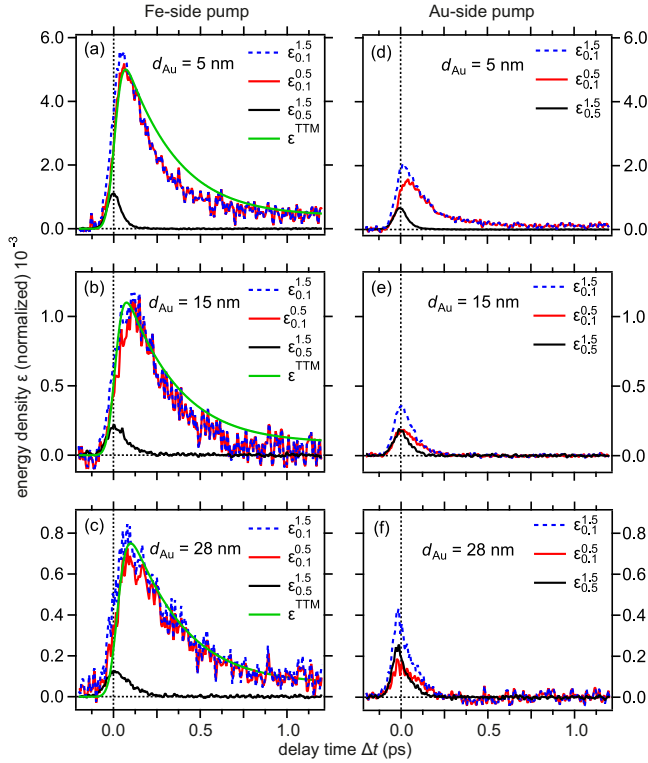
FIG. 6. The time dependence of the energy densities ϵ calculated at different energy ranges using Eq. (2) for the Fe-side (a)–(c) and Au-side (d)–(f) excitation. The determined ϵ can be compared quantitatively for the different experimental datasets. The green traces are energy densities calculated by an adapted two-temperature model (TTM) and convolved with a 80 fs FWHM Gaussian pulse. They are scaled to the experimental data by a factor, see text for details.

energy content at low- and high-energy regimes from these data.

The energy and time-dependent relative change in the electron population $\Delta n(E, \Delta t)$ is assumed to be proportional to the measured ΔI_{PES}. The time-dependent energy content in a given energy range E_1 to E_2 is then calculated by [11],

$$\epsilon_{E_1}^{E_2}(\Delta t) = \mathcal{C} \int_{E_1}^{E_2} \Delta n(E, \Delta t)(E - E_{\text{F}})dE, \qquad (2)$$

where $\mathcal{C}$ is a proportionality constant, which depends on photoelectron detection efficiency. It is determined by the photoemission matrix element and geometric factors of the setup. Since the probing geometry and photon energy are kept constant for all measurements reported here, the integrals in Eq. (2) resulting for the different data sets can be compared among each other. Therefore, $\epsilon_{E_1}^{E_2}$ represents a normalized quantity, which provides access to the relative excess energy content.

In Fig. 6, we show these time-dependent energy densities, the total measured energy density $\epsilon_{0.1}^{1.5}$ in the full energy range (0.1–1.5 eV), $\epsilon_{0.1}^{0.5}$ for the lower-energy excited electrons, and $\epsilon_{0.5}^{1.5}$ for the higher-energy excited electrons of all samples and both pump configurations. In all the cases, the $\epsilon_{0.1}^{1.5}$ plotted in Fig. 6 shows a rise of the excited carriers at time zero with the arrival of the pump pulse followed by a decay at later times.
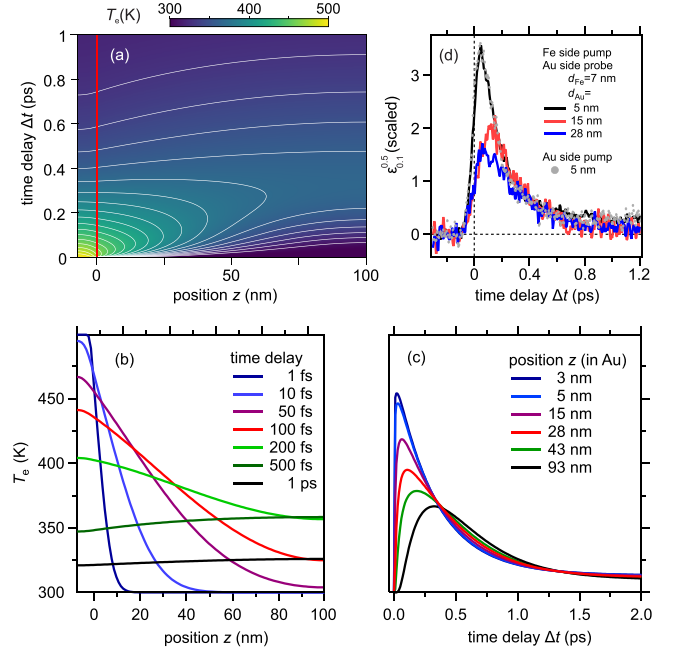

FIG. 7. (a) Combined false color and contour plot of the calculated electron temperature by using the two-temperature model (TTM) as detailed in the text for $d_{\text{Fe}} = 7$ nm and $d_{\text{Au}} = 100$ nm. Two contour lines are separated by 10 K. The horizontal axis describes the position z along the interface normal; $z < 0$ represents Fe and $z > 0$ the Au layer. The change with Δt is plotted along the vertical axis. The electronic heat is generated by an instantaneous increase of T_e in Fe from 300–500 K. (b) Temperature transients at indicated values of z as a function of Δt. $z = 0$ refers to the Fe/Au interface. (c) Time evolution of the electron temperature at selected z. (d) Low-energy density $\epsilon_{0.1}^{0.5}$ for Fe-side pumping of $d_{\text{Au}} = 5, 15, 28$ nm and Au-side pumping of $d_{\text{Au}} = 5$ nm. The data sets are scaled to each other to match at $\Delta t = 0.5$ ps.

A comparison of the measured total energy density shows that for one selected pumping geometry the maximum $\epsilon_{0.1}^{1.5}$ reduces with the increase in the Au layer thickness. Further, the maximum $\epsilon_{0.1}^{1.5}$ is always higher for the Fe-side pumping if compared to that of corresponding data for Au-side excitation. These observations are well explained by the absorption calculations discussed earlier in Fig. 2. The pump absorption is much larger if electrons are excited in Fe compared with Au-side pumping. Apart from the case of $d_{\text{Au}} = 5$ nm, the decay is slower for the Fe-side excitation when compared to that of Au-side excitation. In case of $d_{\text{Au}} = 5$ nm the decay occurs on identical time scales for both pumping configurations, see Fig. 7(d) for a direct comparison. These slower decaying cases always show a delayed maximum in $\epsilon_{0.1}^{0.5}$ with respect to time zero. Further, we find that for all d_{Au} in the Fe-side pump configuration $\epsilon_{0.5}^{1.5}$ decays faster and is lower in magnitude when compared to that of the corresponding $\epsilon_{0.1}^{0.5}$ (Fig. 6). Thus, after a buildup of low-energy electrons due to scattering of high-energy electrons, the low-energy electrons (< 0.5 eV) comprise the majority of the measured energy density.

IV. TWO-TEMPERATURE MODEL

We compare the observed electron-propagation dynamics in case of Fe-side pumping with model predictions in the limit of thermalized electron distributions as a function of Δt and position z along the interface normal direction. To this end, we adopted the two-temperature model (TTM) by Anisimov *et al.* [29] by (i) considering Au and Fe films of thicknesses d_{Au} and d_{Fe}, respectively, and (ii) assuming that the optical excitation occurs exclusively in Fe following the dominant pump absorption in the Fe layer for Fe-side pumping, see Fig. 2. We, furthermore, assume that the electrons in Fe instantaneously reach an electron temperature $T_e = 500$ K. We obtained this value by fitting a Fermi-Dirac distribution function to the time-dependent photoemission spectra in Fig. 4 at $\Delta t = 100$ fs. We take material parameters for Au and Fe into account as detailed below. The TTM takes e-ph interaction and diffusive heat transfer into account as described by the coupled differential equations [15,29,30],

$$C_e(T_e)\frac{\partial T_e}{\partial t} = S(\Delta t, z) - g(T_e - T_l) + \frac{\partial}{\partial z}\left(\kappa \frac{\partial T_e}{\partial z}\right), \quad (3)$$

$$C_l \frac{\partial T_l}{\partial t} = g(T_e - T_l), \quad (4)$$

where $C_e = \gamma T_e$ and C_l are the electron and lattice specific heat capacities, respectively, κ is the electronic part of the thermal conductivity which is responsible for diffusive electronic transport in the Au layer. The e-ph interaction is modeled by e-ph coupling constants g taken from literature: $g_{\mathrm{Au}} = 2.3 \times 10^{16}$ Wm^{-3}K^{-1} [8] and $g_{\mathrm{Fe}} = 9 \times 10^{17}$ Wm^{-3}K^{-1} [31]. The difference in the e-ph coupling constants is linked to the larger electronic density of states at the Fermi energy in iron compared to gold [32]. Diffusive heat transport driven by the gradient $\partial T_l/\partial z$ is discarded because it proceeds on time scales >100 ps, which are not discussed here. The reason is that T_l and $\partial T_l/\partial z$ are considerably smaller than the respective values for T_e. $S(z, t)$ is the source term determined by the energy $C_e T_e$ deposited in Fe. The electronic thermal conductivity κ is taken as temperature dependent [15]: $\kappa(T_e) = \kappa_0 T_e/T_l$. Since the Debye temperature of Au is 165 K, we used the high-temperature value of $C_l^{\mathrm{Au}}(T \to \infty) = 33$ Jmol^{-1}K^{-1} [33]. For Fe, whose Debye temperature is 460 K, we take the room temperature value $C_l^{\mathrm{Fe}}(T = 300$ K$) = 26$ Jmol^{-1}K^{-1} [34]. Using further literature values for Au and Fe $\kappa_0^{\mathrm{Au}} = 317$ Wm^{-1}K^{-1}, $\gamma^{\mathrm{Au}} = 71$ Jm^{-3}K^{-2}, $\kappa_0^{\mathrm{Fe}} = 80$ Wm^{-1}K^{-1}, $\gamma^{\mathrm{Fe}} = 764$ Jm^{-3}K^{-2} [35], the transient electron temperature was calculated. Figures 7(a)–7(c) depict the results of this calculation for a gold thickness of $d_{\mathrm{Au}} = 100$ nm, which enables us to simultaneously discuss the experimental results of different gold thickness.

With increasing time delay, we observe the cooling of the electron system in Fe driven by e-ph coupling which is very efficient and occurs already around 100 fs, see $z < 0$ in Fig. 7(a). Simultaneously, electron diffusion is driven by $\partial T_e/\partial z$ across the Fe-Au interface and increases T_e in Au, see $z > 0$ in Figs. 7(a), 7(b). The cooling of T_e in Au is slower than in Fe because the e-ph coupling in Au is almost 40 times weaker than in Fe. The combination of diffusive electron transport and e-ph coupling determines effective finite time and length scales of diffusive electron transport, which in-

crease T_e within 200 fs and 100 nm by approximately 50 K as discussed in the following. Since in Au the electron transport is faster than e-ph coupling, T_e increases on a second, longer time scale for larger distance to the Fe-Au interface and for later delays, see the data for 0.5 and 1.0 ps in Fig. 7(b). In agreement with this interplay between e-ph coupling end electron diffusion, Fig. 7(c) indicates that the maximum T_e shifts to later Δt with increasing z. At a distance of 43 nm to the Fe-Au interface the maximum T_e is found at $\Delta t = 190$ fs, while it occurs at 28 nm distance at 110 fs.

A more detailed look suggests to distinguish two regimes of the relaxation dynamics, i.e., the cooling of T_e, in Au as a function of z. First, for $z \lesssim 20$ nm, i.e., within Au close to the Fe-Au interface, the relaxation in Au is almost as fast as in Fe, which is explained by electron transport from Au back to Fe. This is driven by the faster e-ph coupling in Fe compared to Au, which reduces T_e in Fe and results in $\partial T_e/\partial z$ of the opposite sign compared to initial diffusive electron transport into the Au. Within these spatial and temporal regimes diffusive electron transport from Au to Fe occurs and the excess energy in Fe decays too fast for the electrons to couple to phonons in Au and electrons in Au transfer back to Fe and couple to phonons in Fe. This explains why T_e in Au very close to the interface relaxes much faster than in bulk Au [6] and emphasizes that for $z \lesssim 20$ nm the relaxation of T_e, and ϵ, is determined by electronic transport effects. Second, for $z > 70$ nm, the electron temperature reaches a maximum in Au at 300 fs and e-ph coupling in Au is a relevant channel for energy dissipation because at these larger z the distance to Fe is too large to compete by diffusive electron transport to Fe with the local e-ph coupling in Au. Third, in between, for 20 nm $< z < 70$ nm, there is a transition from the low-z to the high-z regime.

V. DISCUSSION

Since the probing occurs at the Au surface for both pump geometries, the experimental results reported above for Au-side and Fe-side pumping allow for a direct comparison of hot electron dynamics that is driven by electrons injected at a defined distance into the Au layer with dynamics that is optically excited at the Au surface. The measured energy distribution of the photoexcited electrons above E_{F}, see Fig. 4, exhibits two interesting features for $d_{\mathrm{Au}} = 15, 28$ nm. (i) The results for Au-side pumping is characterized by an electron population loss at $E - E_{\mathrm{F}} > 0.5$ eV. For Fe-side pumping the population relaxes above 0.5 eV as well, but below 0.3 eV the population increases during the first few 10 fs, in contrast to data for Au-side pumping. (ii) The distribution change with increasing Δt indicates a stronger trend towards a thermalized electron distribution for Fe-side than for Au-side pumping. Both observations are in good agreement with the assignment of an excess energy loss of hot electron distributions to transport effects in previous time-resolved photoemission studies on Ru(001) [11]. The hot electrons excited at the Au surface propagate into the depth of the Au film and into Fe, which leads to a loss in the time-resolved photoelectron intensity since photoemission is a surface sensitive probe. In case of the Fe-side pumping, the hot electrons scatter with other electrons while they propagate through the whole Au layer and are

monitored in the spectrum at a lower electron energy, closer to a thermalized distribution. Nevertheless, the observed electron distributions still feature nonthermal contributions up to $\Delta t = 300$ fs. The case of $d_{Au} = 5$ nm differs characteristically from this behavior because the optical transmission of the pump pulse through the very thin Au layer for Au-side pumping and its absorption in Fe still induces the dominant hot electron fraction, see Sec. II.

This scenario is in good agreement with our analysis of the time-dependent energy density shown in Fig. 6. For Au-side pumping and $d_{Au} = 15, 28$ nm, the excited energy density is completely dissipated within 250 fs while for Fe-side pumping a remnant pedestal at 1 ps is found, that we assign to phonons excited by e-ph coupling. Moreover, in case of Au-side pumping the high-energy fraction of the energy density, i.e., $\epsilon_{0.5}^{1.5}$, accounts for about half of the total $\epsilon_{0.1}^{1.5}$, while for Fe-side pumping this fraction is with about 20% much weaker. This behavior confirms the dominant contribution of scattered electrons in case of Fe-side pumping and motivates the comparison of the experimental results for Fe-side pumping with the TTM calculations introduced in Fig. 7. In Figs. 6(a)–6(c), we compare the measured energy densities with those determined by the two-temperature model, which were calculated by using a thermalized pump-induced change in the population change Δn in Eq. (2) for the d_{Au} investigated in the experiment. The temperature of that population change was taken from the two-temperature model calculations and are depicted by the green lines. The relaxation of measured time-dependent energy densities $\epsilon_{0.1}^{1.5}$ follows the modeled transient behavior. We find that the smaller d_{Au} is, the larger the deviations between experiment and the model become. For $d_{Au} = 28$ nm, experiment and model match quantitatively. We conclude that for $d_{Au} = 5, 15$ nm the scattering pathway through the Au layer is not sufficient to reach a diffusive limit and we consider that electronic transport processes from Au to Fe, see above, which are faster than the purely diffusive contribution in Eq. (3), are responsible for this behavior. In this limit, our observations agree with reports in the literature by Battiato *et al.* that conclude on the importance of superdiffusive transport under similar conditions as discussed here [9] and our own previous work [21]. For $d_{Au} = 28$ nm, the agreement between experiment and the model suggests that the transport proceeds diffusively and scattering in these thicker films is found to be sufficient to reach this limit.

In Fig. 7(d) we replot the measured $\epsilon_{0.1}^{0.5}$ for all d_{Au} after multiplication with factors such that the data match at $\Delta t = 0.5$ ps, which works well within the experimental uncertainty. Due to the rather small changes in T_e, we discard here the resulting variation in the temperature-dependent electronic specific heat and compare the scaled energy density in Fig. 7(d) with the calculated electron temperature in Fig. 7(c).

We find that the experimental and theoretical results agree well qualitatively regarding the coinciding transient behavior for different d_{Au} at $\Delta t \geqslant 0.5$ ps. Also, the maxima in $\epsilon_{0.1}^{0.5}(\Delta t, d_{Au})$ recede to almost half for a change in d_{Au} from 5–28 nm in good agreement with the prediction of the calculation. However, the time delay at which the maxima in $\epsilon_{0.1}^{0.5}(\Delta t, d_{Au})$ occur for different d_{Au} show a monotonous increase in Δt in case of the calculations. In the experimental results the time delay of the maxima for ϵ with increasing d_{Au} appears as nonmonotonous. Such deviations from the model behavior could indicate transport effects beyond the diffusive limit for the two thinner layers in agreement with the conclusions above from the energy relaxation. We expect that future experiments will allow more gradual variation in d_{Au}, an improved time resolution to monitor the primary energy injection from Fe to Au, and usage of higher pump fluences to provide improved data quality in order to distinguish diffusive and superdiffusive regimes more rigorously.

VI. CONCLUSION

In this work we reported experimental results obtained in linear femtosecond time-resolved photoelectron spectroscopy of epitaxial heterostructures Au/Fe/MgO(001) for different pump excitation geometries. The pump pulse either reaches the Au or the Fe-side of the heterostructure while probing always occurs at the Au surface. We draw conclusions from the measured time-dependent photoelectron emission spectra regarding the transient electron distribution and scattering. In addition, we determined the transient excess energy density from these distributions, which is dissipated to the largest extent within 1 ps for Fe-side pumping and within 300 fs for Au-side pumping. The Fe-side pumping results are compared to a calculation by the TTM, which predicts spatiotemporal dynamics under the consideration of e-ph coupling and diffusive electron transport. We conclude that electron transport dynamics proceeds close to a diffusive limit, but at a Au layer thickness of 20–30 nm a transition from a superdiffusive to a diffusive regime was identified based on the comparison of the modeled and the measured energy relaxation. Our experimental approach gives clear insight that hot electrons propagate through the sample.

ACKNOWLEDGMENTS

[1] A. Hagfeldt and M. Graetzel, Light-induced redox reactions in nanocrystalline systems, Chem. Rev. **95**, 49 (1995).

[2] F. Hellman, A. Hoffmann, Y. Tserkovnyak, G. S. D. Beach, E. E. Fullerton, C. Leighton, A. H. MacDonald, D. C. Ralph, D. A. Arena, H. A. Dürr, P. Fischer, J. Grollier, J. P. Heremans, T. Jungwirth, A. V. Kimel, B. Koopmans, I. N. Krivorotov, S. J. May, A. K. Petford-Long, J. M. Rondinelli *et al.*, Interface-induced phenomena in magnetism, Rev. Mod. Phys. **89**, 025006 (2017).

[3] J. Shah, *Ultrafast spectroscopy of semiconductors and semiconductor nanostructures*, 2nd ed. (Springer, Berlin, 1999)

[4] E. V. Chulkov, A. G. Borisov, J. P. Gauyacq, D. Sánchez-Portal, V. M. Silkin, V. P. Zhukov, and P. M. Echenique, Electronic

excitations in metals and at metal surfaces, Chem. Rev. **106**, 4160 (2006).

[5] J. Sung, C. Schnedermann, L. Ni, A. Sadhanala, R. Y. S. Chen, C. Cho, L. Priest, J. M. Lim, H.-K. Kimand, B. Monserrat, and P. Kukur, Long-range ballistic propagation of carriers in methylammonium lead iodide perovskite thin films, Nature Phys. **16**, 171 (2020).

[6] J. Hohlfeld, S. S. Wellershoff, J. Güdde, U. Conrad, V. Jähnke, and E. Matthias, Electron and lattice dynamics following optical excitation of metals, Chem. Phys. **251**, 237 (2000).

[7] X. Liu, R. Stock, and W. Rudolph, Ballistic electron transport in Au films, Phys. Rev. B **72**, 195431 (2005).

[8] S. D. Brorson, J. G. Fujimoto, and E. P. Ippen, Femtosecond electronic heat-transport dynamics in thin gold films, Phys. Rev. Lett. **59**, 1962 (1987).

[9] M. Battiato, K. Carva, and P. M. Oppeneer, Theory of laser-induced ultrafast superdiffusive spin transport in layered heterostructures, Phys. Rev. B **86**, 024404 (2012).

[10] M. Aeschlimann, M. Bauer, S. Pawlik, R. Knorren, G. Bouzerar, and K. H. Bennemann, Transport and dynamics of optically excited electrons in metals, Appl. Phys. A **71**, 485 (2000).

[11] M. Lisowski, P. A. Loukakos, U. Bovensiepen, J. Stähler, C. Gahl, and M. Wolf, Ultra-fast dynamics of electron thermalization, cooling and transport effects in Ru(001), Appl. Phys. A **78**, 165 (2004).

[12] M. Lisowski, P. A. Loukakos, U. Bovensiepen, and M. Wolf, Femtosecond dynamics and transport of optically excited electrons in epitaxial Cu films on Si(111) − 7 × 7, Appl. Phys. A **79**, 739 (2004).

[13] A. Klick, M. Großmann, M. Beewen, P. Bittorf, J. Fiutowski, T. Leißner, H. G. Rubahn, C. Reinhardt, H. J. Elmers, and M. Bauer, Femtosecond time-resolved photoemission electron microscopy operated at sample illumination from the rear side, Rev. Sci. Instrum. **90**, 053704 (2019).

[14] J. Wieczorek, A. Eschenlohr, B. Weidtmann, M. Rösner, N. Bergeard, A. Tarasevitch, T. O. Wehling, and U. Bovensiepen, Separation of ultrafast spin currents and spin-flip scattering in Co/Cu(001) driven by femtosecond laser excitation employing the complex magneto-optical kerr effect, Phys. Rev. B **92**, 174410 (2015).

[15] M. Bonn, D. N. Denzler, S. Funk, M. Wolf, S.-S. Wellershoff, and J. Hohlfeld, Ultrafast electron dynamics at metal surfaces: Competition between electron-phonon coupling and hot-electron transport, Phys. Rev. B **61**, 1101 (2000).

[16] A. Melnikov, I. Razdolski, T. O. Wehling, E. T. Papaioannou, V. Roddatis, P. Fumagalli, O. Aktsipetrov, A. I. Lichtenstein, and U. Bovensiepen, Ultrafast transport of laser-excited spin-polarized carriers in Au/Fe/MgO(001), Phys. Rev. Lett. **107**, 076601 (2011).

[17] I. Razdolski, A. Alekhin, N. Ilin, J. P. Meyburg, V. Roddatis, D. Diesing, U. Bovensiepen, and A. Melnikov, Nanoscale interface confinement of ultrafast spin transfer torque driving non-uniform spin dynamics, Nature Commun. **8**, 15007 (2017).

[18] A. Alekhin, I. Razdolski, N. Ilin, J. P. Meyburg, D. Diesing, V. Roddatis, I. Rungger, M. Stamenova, S. Sanvito, U. Bovensiepen, and A. Melnikov, Femtosecond Spin Current Pulses Generated by the Nonthermal Spin-Dependent Seebeck Effect and Interacting with Ferromagnets in Spin Valves, Phys. Rev. Lett. **119**, 017202 (2017).

[19] A. Alekhin, I. Razdolski, M. Berritta, D. Bürstel, V. Temnov, D. Diesing, U. Bovensiepen, G. Woltersdorf, P. M. Oppeneer, and A. Melnikov, Magneto-optical properties of Au upon the injection of hot spin-polarized electrons across Fe/Au(001) interfaces, J. Phys.: Condens. Matter **31**, 124002 (2019).

[20] N. Bergeard, M. Hehn, S. Mangin, G. Lengaigne, F. Montaigne, M. L. M. Lalieu, B. Koopmans, and G. Malinowski, Hot-electron-induced ultrafast demagnetization in Co/Pt multilayers, Phys. Rev. Lett. **117**, 147203 (2016).

[21] Y. Beyazit, J. Beckord, P. Zhou, J. P. Meyburg, F. Kühne, D. Diesing, M. Ligges, and U. Bovensiepen, Local and nonlocal electron dynamics of Au/Fe/MgO(001) heterostructures analyzed by time-resolved two-photon photoemission spectroscopy, Phys. Rev. Lett. **125**, 076803 (2020).

[22] M. Bauer, A. Marienfeld, M. Aeschlimann, Hot electron lifetimes in metals probed by time-resolved two-photon photoemission, Prog. Surf. Sci. **90**, 319 (2015).

[23] T. Kampfrath, M. Battiato, P. Maldonado, G. Eilers, J. Nötzold, S. Mährlein, V. Zbarsky, F. Freimuth, Y. Mokrousov, S. Blügel, M. Wolf, I. Radu, P. M. Oppeneer, and M. Münzenberg, Terahertz spin current pulses controlled by magnetic heterostructures, Nature Nanotechnol. **8**, 256 (2013).

[24] T. Mühge, A. Stierle, N. Metoki, H. Zabel, and U. Pietsch, Structural properties of high-quality sputtered Fe films on Al$_2$O$_3$(1120) and MgO(001) substrates, Appl. Phys. A **59**, 659 (1994).

[25] M. Mattern, A. von Reppert, S. P. Zeuchner, J.-E. Pudell, F. Kühne, D. Diesing, M. Herzog, and M. Bargheer, Electronic energy transport in nano scale Au/Fe heterostructures in the perspective of ultrafast lattice dynamics, Appl. Phys. Lett. **120**, 092401 (2022).

[26] M. Sandhofer, I. Sklyadneva, V. Sharma, V. M. Trontl, P. Zhou, M. Ligges, R. Heid, K.-P. Bohnen, E. Chulkov, and U. Bovensiepen, Unoccupied electronic structure and relaxation dynamics of Pb/Si(111), J. Electron Spectrosc. Relat. Phenom. **195**, 278 (2014).

[27] D. L. Windt, IMD software for modeling the optical properties of multilayer films, Comput. Phys. **12**, 360 (1998).

[28] J. H. Weaver, C. Krafka, D. W. Lynch, and E. E. Koch, *Optical properties of metals* (Fachinformationszentrum, Karlsruhe, 1981)

[29] S. I. Anisimov, B. L. Kapeliovich, and T. L. Perel'man, Electron emission from metal surfaces exposed to ultrashort laser pulses, Sov. Phys. JETP **39**, 375 (1974).

[30] U. Bovensiepen, Coherent and incoherent excitations of the Gd(0001) surface on ultrafast timescales, J. Phys.: Condens. Matter **19**, 083201 (2007).

[31] K. Kang and G.-M. Choi, Electron-phonon coupling parameter of ferromagnetic metal Fe and Co, Materials **14**, 2755 (2021).

[32] A. Eiguren, B. Hellsing, E. V. Chulkov, and P. M. Echenique, Phonon-mediated decay of metal surface states, Phys. Rev. B **67**, 235423 (2003).

[33] J. W. Arblaster, Thermodynamic properties of gold, J. Phase Equilib. Diffus. **37**, 229 (2016).

[34] P. D. Desai, Thermodynamic properties of iron and silicon, J. Phys. Chem. Ref. Data **15**, 967 (1986).

[35] C. Kittel, *Introduction to Solid State Physics*, 8th ed. (Wiley, New York, 2005).

Ultrafast electron dynamics in Au/Fe/MgO(001) analyzed by Au- and Fe-selective pumping in time-resolved two-photon photoemission spectroscopy: Separation of excitations in adjacent metallic layers

Y. Beyazit,[1] F. Kühne,[1] D. Diesing,[2] P. Zhou,[1] J. Jayabalan ®,[1] B. Sothmann ®,[1] and U. Bovensiepen ®[1,3,*]

[1]*Faculty of Physics and Center for Nanointegration (CENIDE), University of Duisburg-Essen, Lotharstraße 1, 47057 Duisburg, Germany*
[2]*Faculty of Chemistry, University of Duisburg-Essen, Universitätsstraße 5, 45711 Essen, Germany*
[3]*Institute for Solid State Physics, The University of Tokyo, Kashiwa, Chiba 277-8581, Japan*

The transport of optically excited, hot electrons in heterostructures is analyzed by femtosecond, time-resolved two-photon photoelectron emission spectroscopy (2PPE) for epitaxial Au/Fe/MgO(001). We compare the temporal evolution of the 2PPE intensity upon optically pumping Fe or Au, while the probing occurs on the Au surface. In the case of Fe-side pumping, assuming independent relaxation in the Fe and Au layers, we determine the hot electron relaxation times in these individual layers by an analysis of the Au layer thickness dependence of the observed, effective electron lifetimes in the heterostructure. We show in addition that such a systematic analysis fails for the case of Au-side pumping due to the spatially distributed optical excitation density, which varies with the Au layer thickness. This paper extends a previous study [Beyazit *et al.*, Phys. Rev. Lett. **125**, 076803 (2020)] with data leading to reduced error bars in the determined lifetimes and by a nonlinear term in the Au thickness-dependent data analysis which contributes to similar Fe and Au film thicknesses.

I. INTRODUCTION

Excited electrons in Bloch bands of condensed matter scatter on femtosecond to picosecond timescales due to the strong interaction with bosons and other electrons by e-boson and e-e scattering, respectively [1–4]. Due to the filled valence band in semiconductors, e-phonon coupling dominates the relaxation dynamics in the conduction bands of these materials. In metals, the half-filled bands provide a large phase space for e-e scattering. In addition to the scattering rates as a function of electron energy E and momentum $\mathbf{k}$, the propagation of such excitations in real space is important to consider from a fundamental point of view as well as in device applications. Finally, gradients in real space induce currents of free charges [1,5] which will heat up the crystal lattice and the device structure by e-ph coupling.

While the decay rates of electronic excitations in metals are by now rather well understood [3,4], the nature of currents on femtosecond and picosecond timescales are a topic of current research, and fundamental questions are of interest. In a seminal study using femtosecond laser pulses in a pump-probe experiment on freestanding Au films, Brorson *et al.* [1] concluded on the ballistic nature of electron currents. On the other hand, it was shown more recently that the analysis of propagation velocities calculated by dividing the film thickness by the propagation time is not accounting for the actual electronic propagation pathway [6–8], and individual e-e scattering processes occur although the determined velocities along the normal direction of the film are close to the Fermi velocity [7].

Such transport phenomena can have considerable influence on the quantitative analysis of hot electron lifetimes [9,10] and transient electron distribution functions [11] centered at the Fermi energy if discarded in surface sensitive methods like photoelectron emission spectroscopy.

Ultrafast electron currents in metals can carry a spin polarization [12], and the resulting spin currents and their interaction with ferromagnetic layers in heterostructures have provided opportunities to control magnetic excitations mediated by spin-pumping, spin-accumulation, and spin-transfer torque [13–20]. These experimental studies rely on magneto-optical or terahertz probes which do not directly access the transient electron distributions. To complement those studies, it is therefore desired to provide energy- and time-resolved information on the propagating electrons.

In the context of spatiotemporal transport effects, it is useful to distinguish the decay dynamics of (i) individual electronic quasiparticles and (ii) hot electron distributions. In the first regime, the decay times measured in time-resolved experiments like two-photon photoelectron emission spectroscopy (2PPE) represent the interaction with further microscopic excitations in response to e-e, e-magnon, and e-ph scattering which is represented by the imaginary part of the self-energy [3,21]. Since no temperature is defined for a single particle, this regime describes by definition a nonthermal limit. In the second regime, the distribution of many electrons is analyzed, and single-particle properties are lost within the distribution. This regime provides insight into the time-dependent energy content of the excited electronic system as a whole and how it interacts with the magnetization or spin polarization [12]. Within simplifying assumptions, it is described, in principle, by the two-temperature model and its derivatives [5,22,23].

The effect of electron transport in time-resolved photoelectron spectroscopy in the first regime has been analyzed in Beyazit *et al.* [7]. A more recent publication by Kühne *et al.* [24] addresses the second regime and discusses transport effects within the two-temperature model, which allowed them to distinguish diffusive and superdiffusive electron transport. The specific time- and energy-dependent electron dynamics that extends Ref. [7] will provide input to works that so far assumed thermalized distributions [25] or lack sensitivity to nonthermal electrons [26].

In this paper, we report on time-resolved 2PPE results on epitaxial Au/Fe/MgO(001) heterostructures. We directly compare the 2PPE spectra detected on the Au surface in the cases of Fe- and Au-side pumping and analyze the energy-dependent relaxation and propagation times as a function of the Au layer thickness d_{Au}. In the case of Fe-side pumping, the determined relaxation times depend on the energy above the Fermi level $E - E_F$ and on d_{Au}, which is qualitatively explained by a sum of the decay rates in Fe and Au following Matthiesen's rule. In the case of Au-side pumping, this separation fails which is explained by the difference in the optical excitation profiles for Fe- and Au-side pumping. We complement our previous work, Ref. [7], by recently obtained results that are reported here in combination with an extension of the fitting model.

II. EXPERIMENTAL DETAILS

A. Sample Preparation and Characterization

Epitaxial Au-Fe heterostructures were grown on MgO(001) by molecular beam epitaxy. Fe(001) was prepared on the MgO(001) substrate followed by Au(001). As described in Refs. [14,27,28], the in-plane axes of both layers are rotated by $\pi/4$ with respect to each other to minimize the lattice mismatch between Fe and Au which facilitates pseudomorphic growth with an atomically sharp interface. Our earlier work directly analyzes the structure of the buried Fe-Au interface by scanning transmission electron microscopy. It shows that the interface is atomically sharp [14] and that, in the case of more complex heterostructures, the interdiffusion is limited to a few lattice constants [29]. The MgO(001) substrates of 10×10 mm^2 were cleaned in ultrasonic baths of ethanol, isopropanol, and acetone. Subsequently, they were put into ultrahigh vacuum and exposed to O_2 at a partial pressure of 2×10^{-3} mbar at a temperature of 540 K to remove carbon contamination. The Fe layer and the first nanometer of Au were evaporated at 460 K. Then the sample was cooled to room temperature, and the remaining Au was evaporated in the following step-wedge structure. We varied d_{Au} systematically from 5 to 70 nm by growing a wedge-shaped Au layer with 17 steps on a 7-nm-thick Fe layer. Each step is 0.4 mm wide and can be accessed specifically by the laser pulses focused to a spot of $140 \pm 30\,\mu$m diameter full width at half maximum (FWHM) for the visible pump and $90 \pm 30\,\mu$m FWHM for the ultraviolet probe. The thicknesses of the Au and Fe layers were determined by secondary ion mass spectroscopy (SIMS), and the depths of the craters induced in SIMS were confirmed subsequently by an independent analysis using a profilometer. The position of the Fe/Au interface could be determined by a decrease of the SIMS signal to 50% of the Au, while the Fe signal increased to 50%. The thickness of the Fe layer was determined in the same way with the signal increase of the Mg and the signal decrease of the Fe. The error in the film thickness determination is $\pm 10\%$ for all films except for $d_{Au} = 7$ nm, where it is $\pm 20\%$.

B. Time-Resolved 2PPE

Femtosecond laser pulses are generated by a commercial regenerative Ti : sapphire amplifier (Coherent RegA 9040) combined with a noncollinear optical parametric amplifier (NOPA, Clark-MXR) operating at a 250-kHz repetition rate tuned to a signal photon energy of $h\nu = 2.1$ eV, which we frequency-doubled in a BBO crystal subsequently. We use these pairs of femtosecond pulses at 2.1 and 4.2 eV with pulse durations <40 fs at a time delay Δt as pump and probe pulses, respectively. The probe pulses reach the Au surface at a 45° angle of incidence. Since the transparent MgO(001) substrate allows direct optical excitation of the Fe layer, the pump pulse can be sent to either the Au or the Fe side of the sample by different pathways, also at a 45° angle of incidence. Thereby, pump and probe laser pulses propagate within their foci simultaneously over the sample which avoids a deterioration of time resolution. Typical incident fluences are 50 and 1 μJ/cm^2 for pump and probe, respectively. The sample was kept in ultrahigh vacuum and at room temperature. Photoelectrons are detected in normal emission direction from the Au surface by a self-built electron time-of-flight spectrometer [30]. The concept of the 2PPE experiment with a direct comparison of Fe- and Au-side pumping of the Au/Fe/MgO(001) heterostructure is illustrated in Fig. 1(a).

Optical absorption of the pump pulses in the heterostructure differs for Fe- and Au-side pumping since the absorption coefficient of 2-eV photons in Fe is considerably larger than in Au. We have calculated the absorption of the pump pulse in Au/Fe by the electric field inside the material in both pump configurations using IMD software [31] and derived the pump power $P(z)$ in the different constituents with z being the interface normal direction; $z = 0$ is set to the Fe-Au interface:

$$P(z) = n(z)I(z) = n(z)|E(z)|^2 = n(z)I_0 e^{-\alpha z}, \quad (1)$$

Here, α is the absorption coefficient, $I(z)$ the intensity, $E(z)$ the electric field, and $n(z)$ the refractive index in the respective material. The power in the layer stack is given by the real part of the Poynting vector. Figure 1 depicts the normalized intensity (dashed lines, left axes) for (b) Fe-side and (c) Au-side pumping. The relative absorbed power $P_a(z)$ was obtained by subtracting the transmitted power and normalizing to the absorbed power because we focus on the attenuation of the field by absorption (solid lines, right axes). $P_a(z) = [P(z) - P_T]/(P_I - P_T)$, where P_I and P_T are the incident and transmitted pump power, respectively. We considered the pump photon energy of 2.1 eV, the angle of incidence $\theta = 45°$, the p-polarization of the light, the refractive indices $n_{Au}(2.1$ eV$) = 0.25$, $n_{Fe}(2.1$ eV$) = 2.91$, and the extinction coefficients $k_{Au}(2.1$ eV$) = 3.07$, $k_{Fe}(2.1$ eV$) = 3.02$ [32] with $\alpha = 4\pi k/\lambda$; λ is the optical wavelength. We find that, in the case of Fe-side pumping, the absorption is dominated by the Fe layer: 96% for
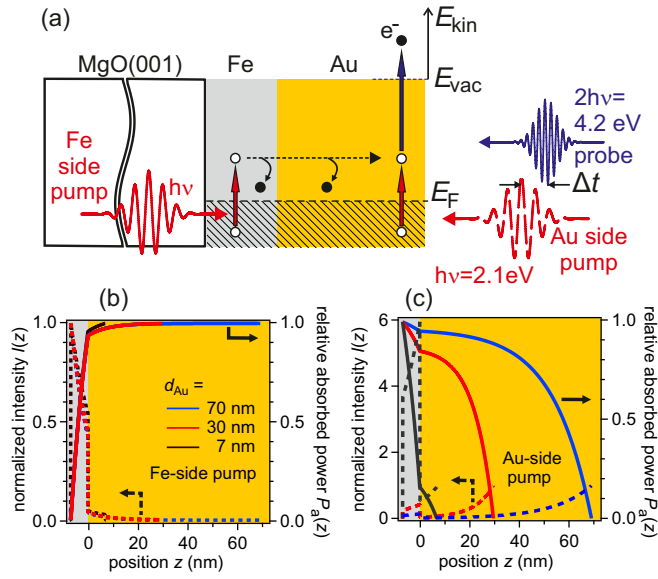
FIG. 1. (a) Experimental geometry of the pump-probe experiment with Fe- and Au-side pumping of Au/Fe/MgO(001) heterostructures by visible femtosecond laser pulses at $h\nu = 2.1$ eV photon energy. Probing occurs by analysis of the two-photon photoelectron emission spectrum at the Au surface induced by $2h\nu = 4.2$ eV. In the case of Fe-side pumping, electrons must propagate to the Au surface before being probed. Spatial distribution of the excitation density by the calculated pump intensity $I(z)$ with respect to the incident light field (dashed lines, left axes) and the relative absorbed pump power $P_a(z)$ (solid lines, right axes) as a function of Au layer thickness for (b) Fe-side and (c) Au-side pumping. Please see the text for details. The thickness of the Fe layer is 7 nm (gray area). Note that the nominal maximum intensity in (c) is higher at the interface than in (b) because of the change in optical constants for a change in layer sequence.

$d_{Au} = 7$ nm and 94% for $d_{Au} = 70$ nm. In the case of Au-side pumping, the situation is diverse. A pronounced variation in the relative intensity occurs at the Fe-Au interface, where the refractive index changes and the light field is attenuated in Au before it reaches Fe. Note, that for $d_{Au} = 7$ nm, the dominant absorption occurs in Fe though it reaches Au first. For thicker Au layers, the pump absorption is distributed over the Au layer.

III. EXPERIMENTAL RESULTS AND DATA ANALYSIS

The time-resolved 2PPE intensity was measured as a function of d_{Au} on the step-wedged sample, and representative results are shown in Fig. 2 after subtraction of time-independent contributions originating from multiphoton photoemission within a single pump or probe pulse, which is typically 10% of the time-dependent intensity. Characteristic changes with increasing d_{Au} for Fe-side pumping are a reduced intensity at $E - E_F = 1.7$ eV and a shift of the intensity maximum at lower energy near $E - E_F = 0.6$ eV to later Δt. For Au-side pumping, the maximum intensity is found at a peak close to the top end of the spectrum at 1.7 eV independent of d_{Au}. This peak is assigned to image potential states in front of the Au surface [33]. Since these states are
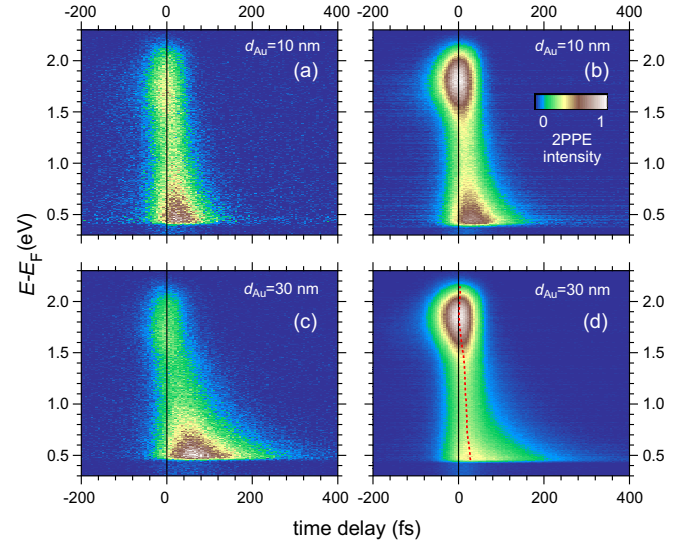

FIG. 2. Representative two-photon photoelectron emission spectroscopy (2PPE) intensity as a function of time delay and energy above the Fermi level in a false color representation for $d_{Fe} = 7$ nm and $d_{Au} = 10$ and 30 nm, as indicated; (a) and (c) Fe-side pumping, (b) and (d) Au-side pumping. The red, dashed line in (d) indicates the 2PPE intensity maxima for different energies with time delay.

bound to the vacuum energy at the Au surface and not the Fermi energy of the layer stack, they will not be discussed further here.

For all datasets, an increase in intensity toward lower $E - E_F$ and later Δt is recognized, which can be weaker or stronger depending on d_{Au} or the pumping geometry. This effect has two origins. (i) The hot electron lifetime increases according to Fermi-liquid theory $\propto (E - E_F)^{-2}$ [3,4]. (ii) At electron energies $E - E_F$ below half of the pump photon energy, secondary electrons will contribute to the 2PPE intensity [10]. In this paper, we focus on the analysis of the hot electron lifetimes, i.e., the inverse rate of the primary inelastic scattering event, for which 2PPE is the appropriate method. Thereby, we analyze nonthermal transport since electron thermalization has not yet taken place. The contribution of secondary electrons, effects toward electron thermalization upon Fe- and Au-side pumping, and thermal electron transport were reported recently in Ref. [24] based on time-resolved linear photoelectron emission spectroscopy.

For both pump geometries, $\Delta t = 0$ was determined for consistency by the 2PPE intensity maximum at the highest energy at the top end of the spectrum. We note that there is a certain ambiguity in this choice of time zero. For Fe-side pumping, a certain propagation time of the excited electron through the layer stack before the electron is detected at the Au surface occurs. For Au-side pumping, the spectrally broad image potential state feature could extend up to the top end of the spectrum. As a consequence, the chosen $\Delta t = 0$ would be shifted to negative time delays since the finite decay time of the image potential states convoluted with the pulse duration results in an effective shift of the intensity maximum since the trailing part of the probe laser pulse contributes to the signal. To estimate this potential inaccuracy in the determination of $\Delta t = 0$, we indicate in Fig. 2(d) the intensity maxima
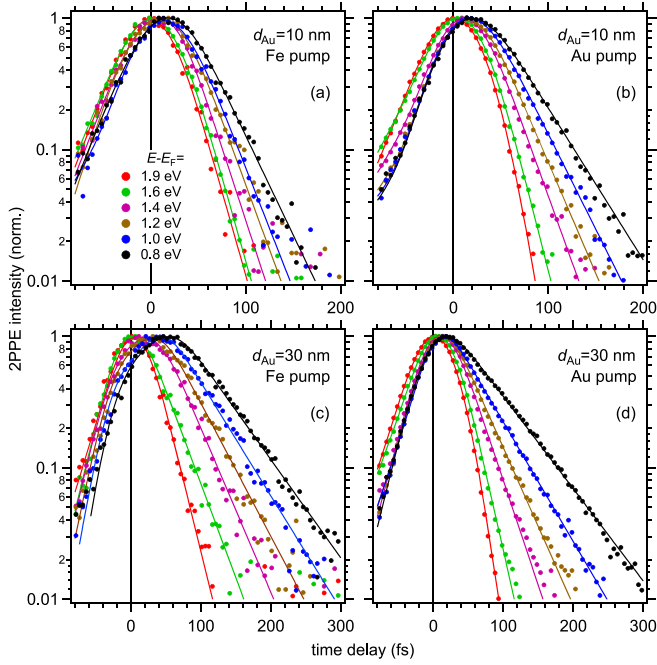
FIG. 3. Normalized two-photon photoelectron emission spectroscopy (2PPE) intensity as a function of time delay at different energies $E - E_F$ for $d_{Fe} = 7$ nm and d_{Au} and pumping as indicated in (a)–(d). The dots are experimental data, the lines represent least-square fits using an exponential relaxation convoluted with a Gaussian, see text for details. Note that different intervals in time delay are depicted in (a), (b) and (c), (d).
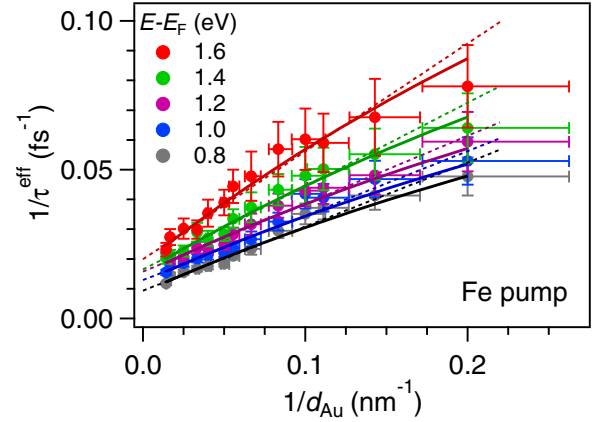

FIG. 4. The relaxation rates determined from the inverse hot electron lifetimes in the case of Fe-side pumping are plotted as filled circles for energies above E_F as a function of the inverse Au layer thickness. The solid (dotted) lines depict nonlinear (linear) functions fitted to the relaxation rates at the energy represented by the indicated color code. See the text for details.

as a function of Δt for all energies by a dashed red line. At $E - E_F = 1.5$–1.0 eV, the maximum is shifted to $+15$ fs without a clear decay. We consider in the following that the actual time zero is uncertain within this interval of 0–15 fs.

Similar measurements were taken for 13 different d_{Au}'s in the case of Fe-side pumping and 7 different d_{Au}'s in the case of Au-side pumping. We analyzed the time-dependent 2PPE intensities at constant energy $E - E_F$ for all these measurements after normalization to the time-dependent peak maximum. Typical examples of such datasets are shown in Fig. 3 for the data of Fig. 2. A comparison of these traces for d_{Au} in panels (c) and (d) for both pumping geometries highlights that the time delays of the intensity maxima are shifted for Fe-side pumping toward later Δt much more than for Au-side pumping. This effect is attributed to propagation of the electronic excitation through the Au layer and quantified by a time offset t_0, see Ref. [7] for a discussion of the results on t_0. These traces are fitted for both pumping geometries with two exponential decays, one toward negative Δt to account for the contribution excited by 4.2 eV photons and one for the decay toward positive Δt excited by 2.1 eV photons shifted by t_0. All is convoluted with a Gaussian of $\sim$50 fs width to account for the cross-correlation of the laser pulses. The resulting fits are included in Fig. 3 by solid lines.

For a discussion of the determined lifetimes, it is important to consider that the excited electron can relax in the Fe or in the Au layer of the heterostructure. If it does not relax in Fe, we assume in the following analysis that the electron is injected elastically into the Au layer where it relaxes

subsequently. This is rationalized with the single-crystalline interface structure [14] and by the fact that no interface decay contribution is required to describe the data, as discussed below. For the Fe-side pumping and Au-side probing geometry, the detected electron has to propagate through the layer stack, and the probability for an electron to decay will increase in both layers with their respective thicknesses. In the limit of a sufficiently thin Fe layer, which is grown on the insulating MgO(001), transport effects can be neglected in Fe. Supposing that the Au layer grown on top of Fe is sufficiently thin that its contribution to the decay probability can be neglected, this experimental geometry would be expected to measure the relaxation dynamics in Fe. Vice versa, if the Fe layer is very thin and the Au layer is sufficiently thick, the relaxation dynamics in Au would be measured. As a function of d_{Au}, we can therefore expect to detect a combination of relaxation in the Fe and Au constituents as suggested by Mathiessens's rule. The data presented in Fig. 3 clearly show a faster relaxation for $d_{Au} = 10$ nm than $d_{Au} = 30$ nm for both Fe- and Au-side pumping. To test this hypothesis, we analyze the inverse relaxation times as a function of d_{Au} as a linear function of $1/d_{Au}$ to account for the variation of the decay contribution in Au by

$$\frac{1}{\tau^{\mathrm{eff}}(d_{Au})} = A + \frac{B}{d_{Au}}. \qquad (2)$$

In this empirical limit, $1/A = \tau_{Au}$ and $1/B = \tau_{Fe}/d_{Au}^0$, where d_{Au}^0 normalizes d_{Au} and is chosen as 1 nm. Figure 4 shows the respective analysis. The linear functions of Eq. (2) are included as dotted lines which fit the experimental data reasonably well within the error bars. At large $1/d_{Au}$, we observe systematic deviations of the linear fit from the experimental results. The fit tends to overestimate the measured relaxation rates. In the following, we derive a suitable nonlinear correction. The corresponding fits are plotted as solid lines in Fig. 4.

Under the approximation that the electronic velocity in Fe and Au is similar and that scattering at the Fe-Au interface
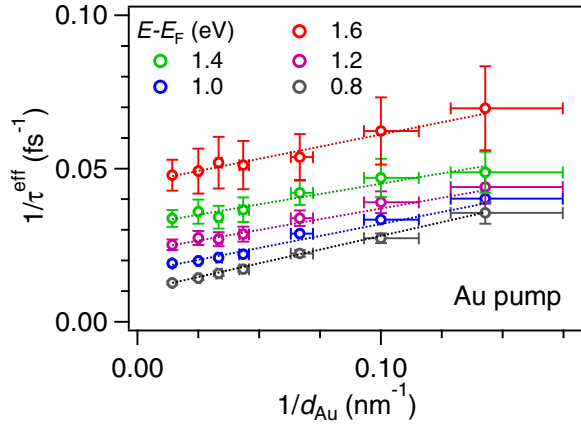
FIG. 5. The relaxation rates determined from the inverse hot electron lifetimes in the case of Au-side pumping, see text for details, are plotted as open circles for energies above E_F as a function of the inverse Au layer thickness. The dotted lines are linear fits to the relaxation rates at the energy represented by the indicated color code.

can be discarded, the scattering probability in the layer stack $1/\tau^{\text{eff}}$ is determined by d_{Au} and d_{Fe} [7] following

$$\frac{d_{Au} + d_{Fe}}{\tau^{\text{eff}}} = \frac{d_{Au}}{\tau_{Au}} + \frac{d_{Fe}}{\tau_{Fe}}. \tag{3}$$

Since d_{Au} was varied and d_{Fe} was kept constant at 7 nm,

$$\frac{1}{\tau^{\text{eff}}(d_{Au})} = \frac{d_{Au}}{d_{Fe}^{\text{eff}} + d_{Au}} \frac{1}{\tau_{Au}} + \frac{d_{Fe}^{\text{eff}}}{d_{Fe}^{\text{eff}} + d_{Au}} \frac{1}{\tau_{Fe}}. \tag{4}$$

As discussed below in Sec. IV, we introduce d_{Fe}^{eff} to account for the optical inhomogeneous pumping of Fe and for different electron velocities in Fe and Au. For $d_{Au} \gg d_{Fe}^{\text{eff}}$, the factor of the first term becomes one and the one of the second term tends to reduce to $1/d_{Au}$ as in Eq. (2). For $d_{Au} \approx d_{Fe}^{\text{eff}}$, the fitting by Eq. (4) overcomes the previous deviation between experimental data and improves the fitting using Eq. (2) for thin Au films, see Fig. 4.

This analysis potentially also holds for the experiments which employ Au-side pumping. To test this hypothesis, we plot $1/\tau^{\text{eff}}$ obtained for Au-side pumping as a function of $1/d_{Au}$ and fit the data by Eq. (2). The results are shown in Fig. 5. In this case, the linear fitting describes the data very well, but the quantitative behavior of the results for A and B as a function of $E - E_F$ differs from the results obtained for Fe-side pumping, c.f. Fig. 4. For Au-side pumping, the slope B increases with decreasing energy, while the opposite trend is found for Fe-side pumping. In addition, the offset A is about two times larger than for Fe-side pumping.

The results for τ_{Au} and τ_{Fe} obtained for the linear and nonlinear analysis in the Fe-side and for the linear analysis in the Au-side pumping geometry are compiled as a function of energy in Fig. 6. We also include literature data for hot electron lifetimes in bulk Au and Fe taken from Bauer *et al.* [4] for comparison. The findings for τ_{Au} and τ_{Fe} in the case of Fe-side pumping are in very good agreement with the literature data, which holds for both fitting models. We conclude that, for Fe-side pumping, a separation of the relaxation dynamics in the Fe and Au constituents is successful. We
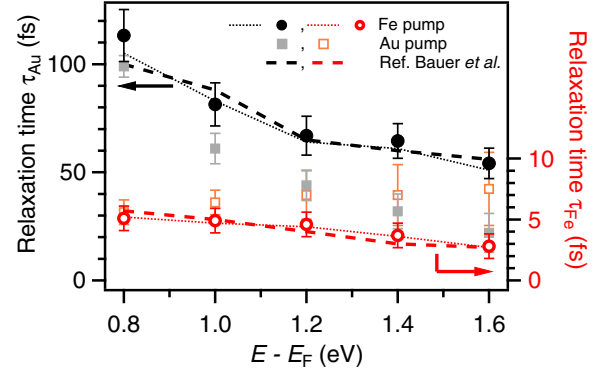

FIG. 6. Filled and open circles are the best fit results of τ_{Fe} and τ_{Au} by the Au thickness-dependent analysis of the hot electron lifetimes in the case of Fe-side pumping using the nonlinear fitting analysis. The results for the linear fitting are depicted by thin dotted lines. Open and filled squares are the corresponding results for Au-side pumping. Dashed lines represent literature data for hot electron lifetimes for bulk Fe and Au [4]. Black and gray data for τ_{Au} are referred to the left axis, red and orange data for τ_{Fe} to the right axis.

note that the nonlinear fitting required to assume a value of $d_{Fe}^{\text{eff}} = 1.3 \pm 0.2$ nm which is much smaller than the actual Fe film thickness of $d_{Fe} = 7$ nm to obtain this agreement. This result is discussed in the Sec. IV below. In the case of Au-side pumping, the deviation of the experimental data points and the literature data is significant for $E - E_F > 0.8$ eV. In this experimental geometry, the separation of the dynamics in the two constituents fails.

IV. DISCUSSION

Hot electron transport phenomena have been widely identified and discussed in the literature of pump-probe experiments in which pump and probe pulses impinge at the sample surface from the identical side, see, e.g., Refs. [5,9–11,13,19,34–36]. We showed in this paper that profound differences occur in the quantitative analysis for two experimental configurations in which pump and probe pulses arrive at the same or opposite sides of the sample surface. These differences are not primarily related to the analysis of the transport phenomenon itself but have effects on the determined hot electron lifetimes. This aspect might be particularly relevant in heterostructure samples where electrons can be transferred among different constituents. We explain these differences between Fe- and Au-side pumping by the different pump absorption profiles in the heterostructure. As shown in Figs. 1(b) and 1(c), the absorption profile is very different for the two pumping geometries. For the Fe-side pumping, the hot electrons are primarily excited in Fe and propagate a well-defined distance to the Au surface, where the photoelectrons are detected. In the Au-side pumping situation, the electrons are excited in Fe and Au with different spatial profiles depending on d_{Au}. Since the electronic transport processes are determined by gradients in excitation density and electronic temperature [5], the velocity distributions and the corresponding transient electron densities will differ for the two pumping geometries. Therefore, it is not only the opposite direction of the pump-induced transport that distinguishes Au- and Fe-side pumping. The quantitative difference in the absolute values of

the spatial gradients of the excitation density leads to spatial redistribution of transient electron density which was already recognized to result in misleading lifetime analysis [9,10]. The wider spatial distribution of the excited electrons that cover Fe and Au in the case of Au-side pumping inhibits the separation of the dynamics in this case. So far, the back-side pump and front-side probe configuration proved to be a very suitable approach to analyze electron scattering and transport for the material system under study.

The nonlinear fitting approach in the analysis of the hot electron lifetimes for Fe-side pumping resulted in the finding that $d_{Fe}^{eff} = 1.3$ nm is much thinner than the actual $d_{Fe} = 7$ nm. Here, we discuss two aspects in this context to rationalize this result. (i) Figure 1(b) depicts the variation of absorbed pump intensity which changes two times across the Fe layer. A corresponding spatial distribution of excited electrons is injected from Fe to Au. Consequently, the average distance an electron has to travel before it reaches the Fe-Au interface is 3–4 nm. (ii) In deriving Eq. (4), we assumed that the electronic velocities in Fe and Au are similar. In fact, they differ at the relevant energies considerably according to GW calculations [37]. For most electrons in Fe, the velocity is 0.6 of the one in Au at $E - E_F = 1.5$ eV. To compensate for this difference in velocity, a correspondingly thinner Fe sheet might be considered as effective since, in the time interval before scattering occurs, an electron can cover a shorter pathway at a lower velocity. We discard here minority electrons in Fe since the injection probability across the Fe-Au interface favors injection of majority electrons [29]. Both these effects reduce the effective Fe film thickness in hot electron injection to Au, and the result obtained for d_{Fe}^{eff} is very plausible.

The model considers quasiparticle lifetimes of individual excited electrons. It is accounting for nonthermal electrons because electron thermalization is the result of the decay of these electrons and their interaction with other electrons. Since these lifetimes are dominated by the e-e scattering probability, the secondary electrons generated in this scattering form a thermalized distribution in the vicinity of the Fermi energy. Considering the incident pump fluence of 50 μJ/cm^2, a corresponding hot electron temperature increase is on the order of 100 K, see Kühne *et al.* [24] for further discussion of this aspect. In the present 2PPE experiment, electrons at the Fermi energy are not detected. As such, we do not discuss thermal transport here but in Ref. [24]. Therefore, the timescales in this paper are considerably shorter than those reported in Ref. [26] and experiments in similar regimes.

Finally, we discuss the potential impact of our work on other problems. In this paper, we quantify the energy-dependent electron dynamics upon Au- and Fe-side optical excitation, which complements a recently published study [24] which used linear time-resolved photoelectron detection to study the electron distribution near E_F. Both these works might serve as input for electron dynamics in the description of optically excited spin currents in metallic heterostructures. A description of these currents by thermal models can be considered as simplified, though they potentially describe the spin currents reasonably well.

An extension of the presented approach to spin-resolved photoelectron spectroscopy appears as promising given the recent development of efficient spin-resolved photoelectron

analysis [38]. A 2PPE experiment will very likely be more suitable than detection in time-resolved linear photoelectron emission [26] since it provides higher count rates of photoelectrons that carry time-resolved information.

Previous interest in time-resolved spectroscopic information in layered perovskite systems upon optical excitation at the opposite sample side [39] suggests an extension of the approach reported in this paper to further material systems. Our study can be considered to address a rather favorable problem since, due to the excellent interface structure, the scattering centers at the interface were sufficiently small in density that they did not have to be considered explicitly. For other material systems, this might be different, particularly for structures that promise technological relevance like, e.g., the mentioned perovskite systems. In such a situation, interface scattering could be analyzed by variation of the two film thicknesses separately [7]. Another potential direction of experiments that builds on our demonstration is the use of Au/Fe/MgO(001) as electrodes for hot electrons injected into solid layers prepared on top of Au. This is a promising future research opportunity for solid layered materials. It is also interesting to consider this approach in combination with liquid electrolytes. In this case, the detection of photoelectrons could be very challenging, but the detection by a surface sensitive nonlinear optical technique might be viable [14].

V. CONCLUSIONS

The ultrafast transport of optically excited hot electrons in epitaxial Au/Fe/MgO(001) heterostructures is studied by systematically varying the Au layer thickness. The results presented here extend our earlier study on this heterostructure and enabled a determination of hot electron lifetimes for the Fe and Au constituents separately with reduced error. This analysis implies a nonlinear dependence of the effective relaxation rate on the Au layer thickness. It was successful in attributing a systematic deviation at smaller Au layer thickness, in the range of the Fe layer thickness, from its dependence on thicker Au layers for the Fe-side pumping configuration. The success of the analysis in the case of Fe-side pumping is attributed to its ability to excite carriers in a specific part in the heterostructure independently on the propagation pathway before detection. Front- and back-side pumping studies are commonly used for studying transport-induced effects in nanostructures; however, we showed here that the spatial distribution of the excitation density plays a strong role in modifying the measured results. The results presented here will serve as input for electron dynamics in the description of spin currents in metallic heterostructures, their interfaces, and hot electrons injected into other coupled systems which are of technological importance.

[1] S. D. Brorson, J. G. Fujimoto, and E. P. Ippen, Phys. Rev. Lett. **59**, 1962 (1987).

[2] J. Shah, *Ultrafast Spectroscopy of Semiconductors and Semiconductor Nanostructures*, 2nd ed. (Springer, Berlin, Heidelberg, 1999).

[3] E. V. Chulkov, A. G. Borisov, J. P. Gauyacq, D. Sánchez-Portal-Portal, V. M. Silkin, V. P. Zhukov, and P. M. Echenique, Chem. Rev. **106**, 4160 (2006).

[4] M. Bauer, A. Marienfeld, and M. Aeschlimann, Prog. Surf. Sci. **90**, 319 (2015).

[5] J. Hohlfeld, S. S. Wellershoff, J. Güdde, U. Conrad, V. Jähnke, and E. Matthias, Chem. Phys. **251**, 237 (2000).

[6] X. Liu, R. Stock, and W. Rudolph, Phys. Rev. B **72**, 195431 (2005).

[7] Y. Beyazit, J. Beckord, P. Zhou, J. P. Meyburg, F. Kühne, D. Diesing, M. Ligges, and U. Bovensiepen, Phys. Rev. Lett. **125**, 076803 (2020).

[8] A. Melnikov, L. Brandt, N. Liebing, M. Ribow, I. Mertig, and G. Woltersdorf, Phys. Rev. B **106**, 104417 (2022).

[9] M. Aeschlimann, M. Bauer, S. Pawlik, R. Knorren, G. Bouzerar, and K. H. Bennemann, Appl. Phys. A: Mater. Sci. Process. **71**, 485 (2000).

[10] M. Lisowski, P. A. Loukakos, U. Bovensiepen, and M. Wolf, Appl. Phys. A **79**, 739 (2004).

[11] M. Lisowski, P. A. Loukakos, U. Bovensiepen, J. Stähler, C. Gahl, and M. Wolf, Appl. Phys. A: Mater. Sci. Process. **78**, 165 (2004).

[12] M. Battiato, K. Carva, and P. M. Oppeneer, Phys. Rev. Lett. **105**, 027203 (2010).

[13] G. Malinowski, F. D. Longa, J. H. H. Rietjens, P. V. Paluskar, R. Huijink, H. J. M. Swagen, and B. Koopmans, Nat. Phys. **4**, 855 (2008).

[14] A. Melnikov, I. Razdolski, T. O. Wehling, E. T. Papaioannou, V. Roddatis, P. Fumagalli, O. Aktsipetrov, A. I. Lichtenstein, and U. Bovensiepen, Phys. Rev. Lett. **107**, 076601 (2011).

[15] N. Bergeard, M. Hehn, S. Mangin, G. Lengaigne, F. Montaigne, M. L. M. Lalieu, B. Koopmans, and G. Malinowski, Phys. Rev. Lett. **117**, 147203 (2016).

[16] I. Razdolski, A. Alekhin, N. Ilin, J. P. Meyburg, V. Roddatis, D. Diesing, U. Bovensiepen, and A. Melnikov, Nat. Commun. **8**, 15007 (2017).

[17] F. Hellman, A. Hoffmann, Y. Tserkovnyak, G. S. D. Beach, E. E. Fullerton, C. Leighton, A. H. MacDonald, D. C. Ralph, D. A. Arena, H. A. Dürr *et al.*, Rev. Mod. Phys. **89**, 025006 (2017).

[18] D. M. Nenno, B. Rethfeld, and H. C. Schneider, Phys. Rev. B **98**, 224416 (2018).

[19] J. Chen, U. Bovensiepen, A. Eschenlohr, T. Müller, P. Elliott, E. K. U. Gross, J. K. Dewhurst, and S. Sharma, Phys. Rev. Lett. **122**, 067202 (2019).

[20] V. H. Ortiz, S. Coh, and R. B. Wilson, Phys. Rev. B **106**, 014410 (2022).

[21] M. Weinelt, J. Phys.: Condens. Matter **14**, R1099 (2002).

[22] U. Bovensiepen, J. Phys.: Condens. Matter **19**, 083201 (2007).

[23] B. Koopmans, G. Malinowski, F. D. Longa, D. Steiauf, M. Fähnle, T. Roth, M. Cinchetti, and M. Aeschlimann, Nat. Mater. **9**, 259 (2010).

[24] F. Kühne, Y. Beyazit, B. Sothmann, J. Jayabalan, D. Diesing, P. Zhou, and U. Bovensiepen, Phys. Rev. Res. **4**, 033239 (2022).

[25] M. Beens, R. A. Duine, and B. Koopmans, Phys. Rev. B **105**, 144420 (2022).

[26] K. Bühlmann, G. Saerens, A. Vaterlaus, and Y. Acremann, Sci. Rep. **10**, 12632 (2020).

[27] Th. Möhge, A. Stierle, N. Metoki, H. Zabel, and U. Pietsch, Appl. Phys. A **59**, 659 (1994).

[28] M. Mattern, A. von Reppert, S. P. Zeuschner, J.-E. Pudell, F. Kühne, D. Diesing, M. Herzog, and M. Bargheer, Appl. Phys. Lett. **120**, 092401 (2022).

[29] A. Alekhin, I. Razdolski, N. Ilin, J. P. Meyburg, D. Diesing, V. Roddatis, I. Rungger, M. Stamenova, S. Sanvito, U. Bovensiepen *et al.*, Phys. Rev. Lett. **119**, 017202 (2017).

[30] P. S. Kirchmann, L. Rettig, D. Nandi, U. Lipowski, M. Wolf, and U. Bovensiepen, Appl. Phys. A **91**, 211 (2008).

[31] D. L. Windt, Comput. Phys. **12**, 360 (1998).

[32] E. D. Palik, *Handbook of Optical Constants of Solids*, 1st ed., Vol. III (Academic Press, San Diego, 1997).

[33] This peak is assigned to image potential states in front of the Au surface [40] in response to the sequence of pumping with 4.2 eV and probing with 2.1 eV, opposite compared with the sequence discussed in this paper. This sequence leads to population decay with nominally negative time delays. The energy of the peak corresponds therefore to $E - E_F = 3.8$ eV, which is obtained by adding the photon energy to the energy indicated in Fig. 2. The observed spectral linewidth indicates inhomogeneous broadening due to the remaining surface inhomogeneity. Within the temporal overlap of the ultrashort pump and probe pulses, the time-dependent, nonlinear polarization and the population buildup, which is mediated by dephasing of the polarization, both lead to 2PPE intensity but with different intermediate state energy [21,41]. These two contributions overlap since their final state energy detected in the electron spectrometer is identical.

[34] A. J. Schellekens, K. C. Kuiper, R. de Wit, and B. Koopmans, Nat. Commun. **5**, 4333 (2014).

[35] J. Wieczorek, A. Eschenlohr, B. Weidtmann, M. Rösner, N. Bergeard, A. Tarasevitch, T. O. Wehling, and U. Bovensiepen, Phys. Rev. B **92**, 174410 (2015).

[36] J. Chen, J. Wieczorek, A. Eschenlohr, S. Xiao, A. Tarasevitch, and U. Bovensiepen, Appl. Phys. Lett. **110**, 092407 (2017).

[37] V. P. Zhukov, E. V. Chulkov, and P. M. Echenique, Phys. Rev. B **73**, 125105 (2006).

[38] G. Schönhense, K. Medjanik, and H.-J. Elmers, J. Electron Spectrosc. Relat. Phenom. **200**, 94 (2015).

[39] J. Sung, C. Schnedermann, L. Ni, A. Sadhanala, R. Y. S. Chen, C. Cho, L. Priest, J. M. Lim, H.-K. Kimand, B. Monserrat *et al.*, Nat. Phys. **16**, 171 (2020).

[40] P. M. Echenique, R. Berndt, E. Chulkov, T. Fauster, A. Goldmann, and U. Höfer, Surf. Sci. Rep. **52**, 219 (2004).

[41] H. Petek and S. Ogawa, Prog. Surf. Sci. **56**, 239 (1997).

DuEPublico

Duisburg-Essen Publications online